

Improvement of the oxygen reduction cathodes of microbial fuel cells designed to treat municipal wastewater

A dissertation presented
by

Richard John Burkitt

to

the department of Chemical Engineering and Advanced Materials

In partial fulfilment of the requirements for a degree of

Doctor of Philosophy

In the field of Chemical and Process Engineering

Newcastle University

United Kingdom

Accepted 19th March 2014

Thesis committee**Thesis supervisor**

Dr Eileen Hao Yu

Lecturer

Newcastle University

Thesis co-supervisor

Prof. Keith Scott

Professor of electrochemical engineering

Newcastle University

Viva panel chair

Prof. Justo Lobato Bajo

Chemical Engineering Department Campus Universitario, Ciudad Real. Spain.

Viva panel internal examiner

Prof. Sudipta Roy

Professor of electrochemistry and nano-materials

Newcastle University

This research was conducted under a grant from the
Engineering and Physical Sciences Research Council

Richard John Burkitt

Improvement of the oxygen reduction cathodes of microbial fuel cells designed to treat municipal
wastewater,

281 pages.

Thesis, Newcastle University, Newcastle upon Tyne, UK (2014) ©

All rights reserved. This thesis may not be reproduced in whole or in part, by photocopy or other means,
without the permission of the author.

Abstract

The Microbial Fuel Cell is a technology for self-powered pollution remediation, receiving widespread academic interest only since the turn of the 21st century. The device centres on immobilised anaerobic microbes that oxidise organic pollutants in industrial or domestic wastewater and generate an electrical charge. To generate useful energy from this charge, oxygen is commonly used as an electron acceptor at a cathode to complete the cell. This oxygen reduction reaction (ORR) requires catalysis and is thought to produce H₂O at pH7. High cost materials such as Platinum and energy inefficient materials such as activated carbon are typically used to catalyse this reaction in MFC's. The majority of ORR catalysis research is based in acid or alkali media. To facilitate MFC commercialisation the project aim was to enhance cathode performance by developing an active, selective, stable and low cost oxygen reduction catalyst. Presented within this thesis is a fundamental study of the enzyme mimic catalyst Iron Phthalocyanine (FePc). With the addition of a novel anion selective binder and membranes, the low cost cathodes are applied to laboratory scale single chamber MFC's fed with primary clarifier influent wastewater.

With use of a rotating ring disc electrode, the O₂ reduction mechanism was found to produce OH⁻ and the O₂ adsorption step was not rate limiting. The mechanism with the lowest overpotential proceeds through an intermediary of strongly adsorbed peroxide. Unfortunately, partial release of this H₂O₂, ranging from 0.5 to 7%, caused catalyst destabilisation. The traditional approach of catalyst pyrolysis was found to be ineffective remedy, reducing the number of viable sites (by 96%) and overall activity.

It was hypothesised that pH splitting from OH⁻ production could be reduced with anion selective materials. A Quaternary-1,4-diazabicyclo-[2.2.2]-octane Polysulfone (QDPSU) anion exchange ionomer utilising a Dabco anion exchange group was implemented in thin films and MFC cathodes as a substitute for Nafion. A facile tafel slope of 25.4 mV per decade of current implied a decrease in the overall activation energy for ORR. Oxygen diffusivity was comparable with Nafion and in real wastewater the air cathodes producing an average of 34% more power in MFC's. An impedance spectroscopy study identified a numerical way of quantifying the poisoning of anion exchange groups. The addition of ion selective membranes increased the

resistance showing this process to be related to ion diffusion, thin membranes with quaternary ammonium produced the best results.

Acknowledgements

This thesis would not have been possible without the assistance of many good people; I cannot name them all here, but I am thankful for their contributions.

Firstly, I would like to acknowledge my advisor, Dr Eileen Yu, for providing the resources to make this work possible, for allowing me the latitude of pursuing my own avenues of interests, for attempting to improve my writing skills. Next, special thanks goes to Dr Xu Wang, for synthesis and the explanation behind a novel material, without which half of my thesis would disappear. Good luck to him in his new post.

I'd like to thank James Merotra for working it out together in the early years, and to the other members of the Yu research group, Orlando, Ed and Jing for sharing a lab, a chat and a showing a remarkable tolerance to some of the more pungent aspects of my research. Special thanks to Anisah Hussein for being a good friend, and for providing me with the cakes and calories needed by a PhD student in the write up. Thanks goes to the MSc students I guided and who guided me; Thom Whiffen, Vasileios Tsintavis, Kerem Irfan, Saud Ramadan, Sheau Voon (Bell) and David Ardid.

For technical advice and support thanks goes to Brian Glover, his experience with materials will soon be missed. I'd like to express appreciation to the other members of the workshop team, for Simon Daley for feedback on all things electronic, Stewart Latimer for being accommodating, Rob Dixon, Paul Sterling and Dr Kumar for instruction during the formative years.

For my parents John and Dorothy,

1. Table of Contents

Abstract	ii
Acknowledgements	iv
List of Figures	ix
List of Tables	xiii
Nomenclature	xiv
Chapter 1. Background on principles of bioelectrochemical systems.....	1
1.1 Sustainable treatment of wastewater	2
1.2 Established technologies and the monetary case for MFCs	3
1.3 The microbial fuel cell	4
1.3.1 Anode	6
1.3.2 Polarisation of electrogenic biofilms	7
1.3.3 Electrolyte	7
1.3.4 Membrane	8
1.3.5 Cathode Assembly	9
1.4 Electrochemistry in electrocatalysis	9
1.4.1 Heterogeneous catalysts and electrochemical catalysts	9
1.4.2 E^0 , $E^{0'}$ and Open Circuit Potential	10
1.4.3 The cathode and the electron acceptor	11
1.5 Motivation of study	13
1.5.1 Justification and aims of research in chapter 5	13
1.5.2 Justification and aims of research in chapter 6	13
1.5.3 Justification and aims of research in chapter 7	14
1.5.4 Justification and aims of research in chapter 8	14
Chapter 2. Theory of electron transfer analysis and laws governing experimental systems.....	15
2.1 Potential ramping techniques for studying electron transfer	16
2.1.1 Staircase voltammetry for assessing electron transfer	16
2.2 Theory of electron transfer	16
2.2.1 Energy barriers of single electron transfer to an adsorbed reactant	16
2.2.2 Multiple electron transfer to an adsorbed reactant	19
2.2.3 Capacitance	21
2.2.4 Relevance of tafel slopes.....	23
2.3 Mixed Potential theory	24
2.3.1 Application to MFC electrodes as cross-over	24
2.4 Oxygen and H_2O_2 and H_2O/OH^-	26
2.4.1 Oxygen adsorption and reduction pathways	26
2.4.2 Methods of peroxide destruction.....	28
2.4.3 Transients and the Cottrell equation in unstirred solution	29
2.4.4 Randles-Ševčík analysis of unstirred solutions.....	33
2.5 Methods of substrate diffusion control and peroxide detection	33
2.5.1 Methods of peroxide detection – RDE and RRDE	33
2.4.2. Levich Equation	35
2.4.3. Koutecky-Levich (K-L) Equation and kinetic current.....	37
2.4.4. $2/4 e^-$ ratio calculation	40
2.4.5. Wroblowa analysis for distinction of k_1 from $k_2 \rightarrow k_3$	40
2.6 Capacitance, charge motion and the redox polymer electrode.....	48
2.6.1 Rate limiting conditions in porous redox polymer thin films analysis	48
2.6.2 Assessment of electrode constrained redox active species	49
2.6.3 Trumpet plot of redox active film	51

2.6.4	Anson plot for surface coverage and charge carrier concentration.....	52
2.7	Electrochemical impedance spectroscopy	53
2.7.1	Impedance	53
2.7.2	Equivalent circuit components modelling physical processes	54
2.7.3	Farradic reactions in EIS	57
2.7.4	Analysis of intersecting time constants in EIS.....	59
2.7	Analysis of ion exchange materials and redox polymers with EIS	59
Chapter 3. Literature Review of Electrocatalysis of O₂, Ion exchange polymers, Bioelectrochemical systems and their materials.....		63
3.1	Summary of Electron Acceptor Performances in MFCs	64
3.2	Oxygen reduction catalysts	66
3.2.1	Pure metals	66
3.2.2	Alloys	67
3.2.3	MeOx with and without graphite support	67
3.2.4	Graphite with and without chemical or thermal treatments	68
3.2.5	Chemical treatment/pyrolysis of graphite.....	69
3.2.6	Enzymes	71
3.2.7	Biocathodes	72
3.3	Transition metal macrocycles for ORR	72
3.3.1	Approaches to enhancing ORR through macrocycle modification.....	77
3.3.2	Approaches to enhancing stability through macrocycle modification	81
3.4	Anion Exchange Materials	83
3.4.1	Anion exchange material implemented in MFC	83
3.4.2	Anion exchange groups.....	83
3.4.3	Dabco chemistry.....	83
3.5	Anion exchange membranes in bioelectrochemical systems	85
3.6	Analysis of ion exchange materials and redox polymers with EIS	87
3.7	MFC systems – Architecture and Substrate Treatment.....	88
3.7.1	Anode biofilm dispersion and models.....	88
3.7.2	Wastewater and coulombic efficiencies	88
3.7.3	Cathodic limitation.....	89
3.7.4	MFC lab scale designs	90
Chapter 4. Experimental methodologies.....		92
4.1	Chapter 5 and 6 Experimental	93
4.1.1	Catalyst Preparation	93
4.1.2	Unsupported iron phthalocyanine films	93
4.1.3	Binder materials	94
4.1.4	Ink preparation for thin films	94
4.1.5	Deposition of thin films on glassy carbon disc electrode	95
4.1.6	Air cathode preparation for Gas Diffusion Cell	95
4.1.7	Electrochemical experiments	96
4.1.8	Air cathode half-cell.....	98
4.1.9	Determination of kinetic current	98
4.1.10	QDPSU redox peak analysis	98
4.1.11	Koutecký-Levich analysis of film with different binder.....	98
4.1.12	RRDE methodology	99
4.3	Chapter 7 Experimental.....	99
4.3.1	Air cathode preparation for MFC.....	99
4.3.2	MFC polarisations and batch cycle	100
4.3.3	EIS analysis on thin films	102
4.3.4	EIS analysis of Air cathodes	102

4.3.5	Data analysis	102
4.4	Experimental – Chapter 8.....	103
4.4.1	Physical parameters of membranes	103
4.4.2	Method for membrane fixation	104
4.4.3	Batch performance and polarisation of MFCs with MEA.	105
4.4.4	EIS evaluation of membrane electrode assembly	105
Chapter 5. Results - oxygen reduction catalysed by carbon supported iron phthalocyanine at neutral pH.....		106
5.1	Introduction	107
5.2	Catalyst activity	107
5.2.1	Carbon supports in phosphate buffer	107
5.2.2	Unsupported FePc films in phosphate buffer – electron transfer activity	109
5.2.3	Unsupported FePc films in phosphate buffer – activity in O ₂	110
5.2.4	Confocal microscopy of carbon supported FePc films	111
5.2.5	O ₂ diffusion limitation in carbon supported FePc films.....	112
5.2.6	PBS effect of pH buffering and adsorption for FePc activity	114
5.2.7	Peroxide generation of FePc	115
5.3	Catalyst kinetics	117
5.3.1	Kinetic rate of ORR quinone activity in the support	117
5.3.2	Unsupported FePc	118
5.3.3	Kinetic performance of carbon supported FePc/Nafion films	121
5.3.4	FePc – influence of rotation on kinetic current	125
5.3.5	Wroblowa analysis of intermediates and heterogeneous rate constants ..	126
5.3.6	The rate limiting step	131
5.4	Iron Phthalocyanine stability.....	133
5.4.1	De-activation of FePc - Consecutive cyclic voltammetry in O ₂	133
5.4.2	Pyrolysis effect on active site	136
5.4.3	Pyrolysis effect on potential of the ORR wave	137
5.4.4	Peroxide generation of pyrolysed FePc	138
5.5	Conclusions	139
Chapter 6. Results - Improved kinetic performance of Iron Phthalocyanine from a novel anion exchange ionomer		141
6.1	Background - inspiration from alkali membrane fuel cells	142
6.2	QDPSU binder in thin carbon black films.....	143
6.2.1	An O ₂ related redox peak in QDPSU electrodes.....	143
6.2.2	Redox peak geometry.....	144
6.2.3	Electrolyte effect on QDPSU	147
6.2.4	Redox mechanism of QDPSU O ₂ fixation.....	149
6.2.5	QDPSU interaction with ORR active carbon sites.....	149
6.3	QDPSU binder in thin films of FePc/KJB and Pt/C.....	151
6.3.1	Binder influence on kinetics in thin films	152
6.3.2	Binder influence on kinetics in air cathodes	159
6.3.3	Anion influence on QDPSU and FePc in de-aerated medium	160
6.3.4	Anion influence on QDPSU and FePc in oxygenated medium	164
6.4	Stability	167
6.4.1	FePc/KJB QDPSU stability in PBS	167
6.4.2	FePc/KJB QDPSU stability in other electrolytes.....	169
6.5	Conclusions	170

Chapter 7. Results - Performance and stability of cation and anion exchange binder in wastewater half cells and Microbial Fuel Cells.....	172
7.1 Introduction	173
7.1.1 EIS analysis of cathodes.....	173
7.2 Results and Discussion	173
7.2.1 Impedance response of thin film electrodes in N ₂ and O ₂	173
7.2.2 High frequency ion diffusion through thin films	176
7.2.3 AC field phase lag in Nafion/QDPSU air cathodes	180
7.2.4 High frequency ion diffusion in pores of Nafion and QDPSU	181
7.2.5 Phosphate and Chloride effect on diffusive resistance	185
7.2.6 Impedance spectra of QDPSU and Nafion air cathodes in PBS	187
7.3 Nafion and QDPSU binders for MFC air cathodes	190
7.3.1 Impedance of QDPSU air cathodes in buffered wastewater.....	190
7.3.2 Wastewater pollutant and R _{ct} of QDPSU and Nafion air cathodes.....	191
7.3.3 Equivalent circuit in PBS WW for QDPSU and Nafion.....	192
7.3.4 MFCs polarisation with QDPSU air cathodes in artificial wastewater...	195
7.3.5 MFCs polarisation using QDPSU FePc air cathodes in wastewater.....	198
7.3.6 Batch performance of MFCs with QDPSU air cathodes	199
7.3.7 QDPSU/FePc interaction with organics in wastewater.....	201
7.4 Conclusions	204
Chapter 8. Results - Cation and anion exchange membranes for Microbial Fuel Cells...	...206
8.1 Background – Factors affecting membranes in MFCs	207
8.2 Results - Analysis of MEA impedance spectra	207
8.2.1 General Nyquist plot response of MEA in pure electrolyte	207
8.2.2 Membrane ionic resistance (R _m)	209
8.2.3 High Frequency response of MEA in pure electrolyte.....	211
8.2.4 Resistance from diffusive elements in MEA	214
8.2.5 General Equivalent Circuit.....	215
8.3 MEA performance in artificial wastewater	216
8.3.1 Polarisation curves	216
8.3.2 EIS spectra of batch fed MFC.....	217
8.3.3 Membrane SCMFC batch performance	219
8.3.4 EIS half-cell as a predictor of MFC batch performance	221
8.4 Conclusion.....	222
Chapter 9. Conclusions and recommendations for further work.....	223
9.1 Recommendations for further work.....	224
9.2 Capital cost of materials	225
9.3 Closing comments on cathode development	226
9.4 Closing comments on balance of the MFC	226
Chapter 10. Appendices.....	228
10.1 Derivations	229
10.1.1 Derivation of tafel slope equation	229
10.1.2 Derivation of Cottrell equation.....	229
10.1.3 Derivation of the Levich equation.....	231
10.2 Calculations and estimates	234
10.2.1 FePc/KJB Nafion film thickness for EIS calculation on TFE	234
10.2.2 FePc/KJB QDPSU air cathode thickness for EIS calculation.....	234
10.2.3 Cost calculation for QDPSU synthesis	234

10.2.4	Non-precious cathodes and MEA	235
10.2.5	Schmidt number of O ₂ in aqueous solution	235
10.3	Tables	236
10.4	Chemical de-activation of FePc catalyst	240
10.5	Method Justification	242
10.5.1	Iron Phthalocyanine films, deposition solvent and support	242
10.5.2	Electroanalysis of redox polymer catalyst	243
10.5.3	RRDE methodology	246
10.5.4	RRDE data	252
10.5.5	QDPSU interaction with Pt and carbon surface	254
10.6	EIS	255
10.6.1	Nova arc fitting software for EIS	255
10.6.2	High frequency arc with FePc films/air cathodes	256
10.6.3	Warburg impedance of QDPSU FePc/KJB air cathode in wastewater... ..	256
10.7	Physical characterisation data	258
10.7.1	X-ray Photoemmission Spectroscopy of FePc catalyst	258
10.7.2	Confocal microscopy on thin film.....	258
10.8	Stability of Ag AgCl reference electrodes	259
10.9	MFC components	261
	Conferences and Publications	263
	References	265

List of Figures

Figure 1-1.	Representation of an MFC utilising anode biocatalysis.....	6
Figure 1-2.	Biocatalysed <i>OCP</i> or $E^{0'}$ of common redox couples in nature relevant to MFC.	12
Figure 2-1.	E vs t plot for staircase voltammetry.....	16
Figure 2-2.	Effect of cathodic polarisation on free energy barriers of 1e ⁻ electron transfer.	17
Figure 2-3.	Model tafel plot of reversible 1e ⁻ transfer at $\eta=0V=E^{0'}$ as $f(\alpha)$	18
Figure 2-4.	Standard free energy change in a cathodically polarised reduction reaction.	19
Figure 2-5.	Potential profile across the double-layer and diffuse layer region.....	20
Figure 2-6.	Capacitance of a porous electrode in mono-anionic dilute electrolyte in the absence of a faradic reaction.	22
Figure 2-7.	Mixed Potential theory for an unpolarised electrode	25
Figure 2-8.	Oxygen reduction pathways of surface adsorbed O ₂ in a catalyst layer.....	27
Figure 2-9.	Initial oxygen adsorption orientations onto an Iron Phthalocyanine.....	28
Figure 2-10.	Example concentration profile for reactant depletion at the electrode surface	30
Figure 2-11.	i - E response of a strongly adsorbed metal based electrocatalyst in the presence (red) or absence (black) of dissolved reactant.....	31
Figure 2-12.	(B) Schematic of a Rotating Ring Disc Electrode (RRDE) tip	34
Figure 2-13.	Model of (B) laminar flow regime and (A) co-ordinates approaching disc reaction site in axially rotated electrode.	34
Figure 2-14.	Example Levich plot of transition between kinetic and diffusion control	36
Figure 2-15.	Example K-L plot of transition between kinetic and diffusion control.....	38
Figure 2-16.	Validity of slope and intercept data CE^*i_D/i_R vs $\tilde{\omega}^{-0.5}$ as a function of potential....	44
	Expressed an example trend in R^2 as $f(E)$	44
Figure 2-17.	Model of porous thin film on GC disc utilising carbon supported redox polymer for ORR.	49
Figure 2-18.	i - E response of a strongly adsorbed metal based electrocatalyst in the absence of dissolved reactant.....	50
Figure 2-19.	Potentiostatic input (A) and corresponding current output (B) of an AC perturbation in applied potential (EIS).....	53

Figure 2-20. Model of $R_{ct}[C]$ circuit as a function of potential.....	58
Figure 2-21. Model of finite reflective diffusion as (A)(B) Nyquist plot, or (C) Randles plot...	60
Figure 2-22. Model of finite open-ended diffusion (A) Nyquist plot, (B)(C) Randles plot.....	60
Figure 3-1. Forms of commercial carbon electrode.....	68
Figure 3-2. Illustration of edge plane active quinone groups on edge plane graphite	70
Figure 3-3. Similarities between Haemoglobin and Iron Phthalocyanine	73
Figure 3-4. A schematic representation of the types of FePc deposition on graphite planes,.....	75
Figure 3-5. Approaches to modifying Me Phthalocyanine activity for ORR;	78
Figure 3-6. Types of nucleophilic degradation recorded in literature.....	84
Figure 3-7. Lab-scale MFC designs of continuous flow configuration.	91
Figure 4-1. Gas Diffusion Cell (GDC) used in assessment of air cathodes	96
Figure 4-2. Diagram of (A) Half Cell used in EIS or (B) MFC used in batch or polarisation curve evaluation of air cathodes.....	100
Figure 4-3. Diagram of Half Cell assembly used to assess membrane performance with EIS.	105
Figure 5-1. (A)(B) Steady state i - E curve ($v=1\text{mV/s}$) or (B)(C) stable CV ($v=20\text{mV/s}$) of carbon materials used in this thesis.....	108
Figure 5-2. (A) Scan rate effect on Fe(II)→Fe(III) peak of FePc adsorbed onto Glassy carbon	109
Figure 5-3. CV of unsupported FePc film in N_2 or O_2 saturated electrolyte.....	111
Figure 5-4. Confocal microscope image of (A) FePcKJB powder and (B)(C)(D) FePcKJB film on GC disc.....	112
Figure 5-5. Influence of electrode rotation on CV for FePc/KJB film with Nafion binder.	113
Figure 5-6. Localised pH shift in catalyst layer from ORR in (A) 1 st and (B) 2 nd consecutive CV.	114
Figure 5-7. RRDE study of disc modifications of FePc/MON or FePc film from DMF. (A)(C) i_R vs. E and (B)(D) i_D vs. E	115
Figure 5-8. % H_2O_2 vs. E profile from RRDE study on FePc films and Pt benchmark.....	116
Figure 5-9. Potentiostatic sweep of Monarch 1000, used as received or with pyrolysis prior to thin film modification of GC tip.	117
Figure 5-10. Potentiostatic scan of a) 20% wt. Pt/C (Nafion) or b) unsupported FePc.	118
Figure 5-11. (A) i - E data of ORR on unsupported FePc films as a function of scan rate.....	120
Figure 5-12. Trumpet plot of Fe(II)↔Fe(III) redox of FePcKJB Na-Nafion thin film	121
Figure 5-13. Trumpet plot same FePcKJB Nafion electrode in the presence of O_2 . Two E_{pc} are present; ORR (orange) and Fe(III)→Fe(II) (red).....	122
Figure 5-14. Tafel slope of KJB and FePc/KJB films on GC.....	124
Figure 5-15. Influence of ω on kinetic control region of J vs E plot in thin films; (a) unsupported FePc ($\Gamma=4\times10^{-9}$ Moles cm^{-2}) or (b) FePc/KJB Nafion,	125
Figure 5-16. $i_{D,L}/(i_{D,L}-i_D)$ vs $\tilde{\omega}^{-1/2}$ plot for unsupported FePc film	127
Figure 5-17. CE^*i_D/i_R vs $\tilde{\omega}^{-0.5}$ plot for unsupported FePc film	127
Figure 5-18. Intercept and R^2 fit of data from the CE^*i_D/i_R over $\omega^{-1/2}$ plot of the film in Figure 5-17	128
Figure 5-19. S vs J plot of unsupported FePc film.....	129
Figure 5-20. S/J vs. E plot of the data from Figure 5-19.	130
Figure 5-21. FePc stability in de-aerated PBS.	133
Figure 5-22. FePc stability from ROS production in FePc/KJB Nafion thin films	134
Figure 5-23. Redox properties of moieties generated from ORR induced FePc de-activation.	135
Figure 5-24. Redox potential of Fe chelate. The effect of pyrolysis on the Fe(II)/Fe(III) redox potential of FePc/KJB,.....	136
Figure 5-25. Components of current (J_{ORR} and Fe(II)/Fe(III)) in thin FePc/KJB films with Nafion binder,	137
Figure 5-26. Effect of pyrolysis on % H_2O_2 vs. E profile of thin films	138
Figure 6-1. Structure of QDPSU repeating unit [276, 277].	143
Figure 6-2. Redox active Dabco/ O_2 moiety. CV of KJB carbon with (A) Nafion or (B) QDPSU binder	143
Figure 6-3. Redox active Dabco/ O_2 moiety – influence of scan rate.....	145
Figure 6-4. J_p vs. $v^{1/2}$ plot for redox peak of O_2 insertion in Dabco (A).	146
Figure 6-5. Redox activity of Dabco/ O_2 moiety – role of Cl^- and PO_4^{3-} anion.	147

Figure 6-6. Quasi-reversible O ₂ insertion into Dabco group in QDPSU.	149
Figure 6-7. (A) <i>i</i> - <i>E</i> response showing interaction between Dabco in QDPSU with KJB.	150
Figure 6-8. K-L plots of current obtained with thin films of KJB with binders of (A) Nafion or (A)(B) QDPSU at (A) <i>E</i> =-0.4 or (B) various <i>E</i>	150
Figure 6-9. (A) LSV of FePc/KJB with QDPSU, PTFE or Nafion binders - quiescent solution.	152
Figure 6-10. Thin RRDE films on a GC disk using a binder of H ⁺ -Nafion (dotted), or QDPSU (solid line) for main MFC catalyst materials; Pt/C, FePc/KJB and KJB.	153
Figure 6-11. K-L plots of limiting current obtained with FePc/KJB (left) or Pt/C (right) thin films with binders of a) Nafion b) QDPSU and c) PTFE at <i>E</i> =-0.4V.	154
Figure 6-12. K-L plot gradient for thin films.	155
Figure 6-13. Effect of binder on %H ₂ O ₂ released from ORR thin films of (A) Pt or FePc or (B) KJB.	156
Figure 6-14. K-L plot of FePc/KJB QDPSU thin film.	157
Figure 6-15. <i>S</i> - <i>C</i> Wroblowa plot from N^*i_D/i_R over $\omega^{-1/2}$ data recorded for FePc/KJB (QDPSU) of thin films.	158
Figure 6-16. Potentiostatic scan of FePc/KJB air cathodes using Na ⁺ -Nafion, PTFE or QDPSU binder.	159
Figure 6-17. CH ₃ COO ⁻ and Cl ⁻ anion binding to FePc with QDPSU or Nafion binder.	161
Figure 6-18. (A) Anion adsorption in the CV response of FePc/KJB (QDPSU) thin films.	162
Figure 6-19. Effect of binder on pH swing from ORR in non-buffered electrolytes.	164
Figure 6-20. Solution anion effect on (A) <i>i</i> _D vs. <i>E</i> and (B) <i>i</i> _R vs. <i>E</i> plots during ORR catalysed by FePc/KJB QDPSU thin films.	166
Figure 6-21. FePc stability in FePc/QDPSU thin film from (A) polarisation in N ₂ or (B) ROS production.	168
Figure 6-22. Tafel plot of 2 nd and 100 th CV scan from data in Figure 6-21.	169
Figure 6-23. Anion and Binder influence on FePc deactivation in O ₂	170
saturated electrolytes described in Figure 6-18. Potential recorded at <i>J</i> =-300 mA cm ⁻² during consecutive CV (100 scans). ω =0rpm, v =50mV/s.	170
Figure 7-1. LF Impedance spectra of thin FePc/KJB Nafion film in (A) de-aerated (B) or aerated PBS media.	174
Figure 7-2. (A) High and (B) Mid frequency complex plane response, invariant of applied potential in FePc/KJB-QDPSU thin film in de-aerated media.	177
Figure 7-3. Corresponding warburg plot to data in Figure 7-2.	177
Figure 7-4. (A) <i>Z'</i> vs. $\tilde{\omega}^{-0.5}$ and (B) $-Z''$ vs. $\tilde{\omega}^{-0.5}$ plot to illustrate diffusive control in thin FePc/KJB Nafion film.	178
Figure 7-5. HF linear regions of <i>Z</i> vs. $\tilde{\omega}^{-0.5}$ plot in thin FePc/KJB Nafion film.	178
Figure 7-6. Binder influence on $(-\phi)$ as a function of log(<i>f</i>) in air cathodes.	181
Figure 7-7. Total electrode impedance, <i>Z</i> vs. $\tilde{\omega}^{-0.5}$, for high frequency diffusion related impedance of air cathodes as a function of binder.	182
Figure 7-8. HF warburg parameter (A) σ vs <i>E</i> , and (B) <i>f</i> ₁ vs. <i>E</i> and <i>f</i> ₂ vs. <i>E</i> , in FePc/KJB QDPSU air cathodes.	186
Figure 7-9. $-Z''$ vs. <i>Z'</i> plots of air cathodes in Figure 7-6.	187
Figure 7-10. Equivalent circuit (C) fit to mid frequency (A) or low frequency (B) data in NOVA software for FePc/KJB (Nafion) air cathodes poised at <i>E</i> =0.28V.	189
Figure 7-11. Nyquist plot of air cathodes described in legend, in a WW-PBS filled cube half-cell.	190
Figure 7-12. (<i>R</i> _{ct} ⁻¹) vs <i>E</i> plot for FePc/KJB air cathodes with binders of a) QDPSU or b) Nafion in WW-PBS.	191
Figure 7-13. Equivalent circuit used to model FePc/KJB QDPSU air cathodes with contamination and blocking from adsorption of species in PBS buffered wastewater.	193
Figure 7-14. Nafion FePc/KJB air cathode, low frequency impedance in wastewater.	195
Figure 7-15. Steady state polarisation curves of MFCs with FePc/KJB air cathodes containing QDPSU or Nafion binders.	196
Figure 7-16. <i>E</i> _{cat} of QDPSU or Nafion binder. Obtained during polarisation curves of MFC's.	197

Figure 7-17. (A) V_{cell} and Power density vs J and (B) E_{an} and E_{cat} vs J in polarisation of SCMFC's with air cathodes of Pt/C (Nafion), or FePc/KJB (QDPSU). Electrolyte; primary clarifier influent,	198
Figure 7-18. Batch performance of FePc/KJB in single chamber MFCs using air cathodes with a) QDPSU or b) Nafion ionomer.	200
Figure 7-19. Batch performance of single chamber MFCs using Pt/C-Nafion or FePc/KJB-QDPSU air cathodes. Electrolyte; Unbuffered Wastewater,	200
Figure 7-20. Batch performance of MFCs fed with acetate (1 or 2g/L).	201
Figure 7-21. Binder and catalyst effect on COD removal.	203
Figure 8-1. Nyquist plot of typical MEA impedance data.	208
Figure 8-2. Nyquist plot of typical MEA impedance data.	209
Figure 8-3. Area specific resistances and thickness normalised ASR of several membranes. .	210
Figure 8-4. Characteristics of HF arc of MEA as a function of applied potential	212
Figure 8-5. Example Warburg plot for MEA.....	214
Figure 8-6. Equivalent circuit (B) and fit of data (A) of FePcKJB-QDPSU air cathodes.	215
Figure 8-7. E_{cat} vs J polarisation curves of MFC utilising MEA listed in Table 4-1 and FePc/KJB QDPSU air cathodes.	216
Figure 8-8. Nyquist plot of full MFC utilising MEA.....	218
Figure 8-9. Comparison of half-cell R_{AC} obtained from EIS and the batch MFC performance using identical MEA.	221
Figure A-1. FePc demetallation during storage in pH2 air sat. H ⁺ Nafion/ethanol ink.	241
Figure A-2. Effect of concentration polarisation and scan rate on tafel behaviour of an FePc/KJB film and correction techniques.....	244
Figure A-3. Fitting a polynomial baseline (6-order) to obtain integratable charge of Fe(II)Pc/Fe(III)Pc redox	244
Figure A-4. Fe(II)↔Fe(III) redox peaks (A) with adjustment of cathodic scan baseline.	245
Figure A-5. Trumpet plot unsupported FePc film. Cathodic peak relates to ORR	246
Figure A-6. RRDE experimental apparatus	246
Figure A-7. The (A) i_D vs. E and (B) i_R vs. E profile for RRDE experiments on Synthetic Graphite/Nafion thin films.	247
Figure A-8. Effect of RRDE tip rotation speed on experimentally determining ring CE	248
Figure A-9. I_R vs E_{disc} recorded during LSV scan. Components of current	251
Figure A-10. S vs. C plot of $CE*i_D/i_R$ vs. $k_{D,H2O2}^{-1}$ data of FePc film (4×10^{-9} Moles cm^{-2}) on GC disc.	251
Figure A-11. Slope and R^2 fit of data from Figure 5-16	252
Figure A-12. $CE*i_D/i_R$ over $\tilde{\omega}^{-1/2}$ plot for FePc/KJB film with QDPSU binder,	252
Figure A-13. Intercept and R^2 fit of data from Figure A-12	252
Figure A-14. $CE*i_D/i_R$ over $\tilde{\omega}^{-1/2}$ plot for pyrolysed (750°C) FePc/KJB film with Nafion binder,	253
Figure A-15. Intercept and R^2 fit of data from Figure A-14	253
Figure A-16. CV of Pt/C-surface chemistry with Nafion or QDPSU	254
Figure A-17. CV of Pt/C-surface chemistry with Nafion or QDPSU	254
Figure A-18. Arc fitting and linear regression of Warburg element in Nova software.	255
Figure A-19. Example of determination of Electron/Ion hopping/diffusion resistance in reflective finite diffusion.....	255
Figure A-20. Effect of wastewater on Bode Plot ($-\phi$ vs. f) of Nafion and QDPSU binders.	257
Figure A-21. $ Z $ vs. $\tilde{\omega}^{0.5}$ plot illustrating the effect of solution electrolytes on diffusion control at mid frequency.	257
Figure A-22. XPS N1s spectra of FePc/MON. Demonstration of effective loading or Nitrogen signal in support relative to FePc.	258
Figure A-23. Confocal microscope surface image of FePcKJB QDPSU film on GC disc.....	259
Figure A-24. Ag AgCl reference electrode protected from wastewater bacteria and chemical poisoning by salt bridge tip.....	260
Figure A-25. Parasitic biofilm growth on air cathode.....	262
Figure A-26. SCMFC with parafilm cover	262
Figure A-27. Carbon felt supported biofilm (A); CV, $v=2mV/s$. (B); Potentiostatic $E=-0.3V$. Electrolyte; anaerobic WW-PBS, pH 7.0.....	263

List of Tables

Table 1-1. Typical make-up of wastewater.....	8
Table 2-1. Individual elements of equivalent circuits models of electrodes.....	54
Table 3-1. Electron acceptor and associated catalysts previously studied in MFCs.....	64
Table 3-2; Summary of ORR kinetic studies on Iron Phthalocyanine.....	80
Table 3-3. Studies on cathode design improvements.....	90
Table 4-1. Physical and chemical properties of commercial membranes used.....	104
Table 5-1. Various catalyst ORR activity in thin films-Nafion binder.....	123
Table 5-2. Peak characteristics of Figure 5-24.....	136
Table 6-1. Various catalyst ORR activity in thin films-QDPSU or PTFE binder.....	151
Table 6-2. Influence of anion and binder on features of Fe(II)/Fe(III) redox.....	163
Table 6-3. ORR influence by anion for FePc/KJB QDPSU thin films.....	165
Table 7-1. Influence of applied potential on C_{Σ} and R_{ct} for FePc/KJB Nafion thin film in O_2 and N_2	175
Table 7-2. Air cathode binder effect on high frequency Warburg co-efficient.....	182
Table 7-3. Utilising data obtained in Table 7-2 and testing various species that may cause a diffusion limiting scenario.....	183
Table 7-4. Summary of linear regions in Z vs. $f^{-0.5}$ plots at high frequency, EIS of half-cells at potentials approximate to OCP	185
Table 7-5. Characteristics of high and mid frequency region displayed in Figure 7-9.....	188
Table 7-6. Characteristics of LF region displayed in Figure 7-10.....	189
Table 7-7. FePc QDPSU electrodes in WW-PBS, parameters of fitted circuit Figure 7-13,....	194
Table 7-8. Summary of repeated MFC performance at fixed external load (left column) or steady-state polarisation (right column).....	196
Table 7-9. MFC performance in batch mode ($\Omega_{ext}=300\Omega$) or steady-state polarisation. Electrolyte; Unbuffered Wastewater.....	199
Table 8-1. Peak E_{cat} and V_{cell} obtained under fixed external resistance with FePc/KJB (QDPSU) air cathodes and a membrane strapped down with SS304 mesh.....	219
Table 8-2. Averaged peak E_{cat} and V_{cell} obtained over batch cycles over two MFC.....	220
MFC with FePc/KJB (QDPSU) air cathodes and membrane.....	220
Table 9-1. Cost analysis of materials discussed in this thesis.....	225
Table A-1. Preparation procedure for all catalysts prepared in-house.....	236
Table A-2. Physical constants of 50mM PBS used in this study.....	237
Table A-3. Dissolved O_2 in air equilibrated 50mM Na^+ PBS, pH 7.0.....	237
Table A-4. Physical constants of ions in 50mM PBS at $T = 20^{\circ}C$	238
Table A-5. Reported qualities of carbons from manufacturer and academic sources.....	238
Table A-6. Collection Efficiency for Pt ring used in Wroblowa analysis.....	238
Table A-7. Ingredients of biofilm growth nutrient supplement.....	239
Table A-8. Reproducibility of electro-active FePc loading from 6 μ l aliquots of new catalyst inks.....	239
Table A-9. Membranes thickness in $NaHCO_3$ PBS or $NaCl$ solution and % swelling vs dry state.....	240
Table A-10. Quantification of random sources of error in thin film experiment.....	240

Nomenclature

Electrochemical and physical parameters

Symbol	Meaning	Usual Unit
A	Geometric Area	cm^2
A	Pre-exponential factor in Arrhenius equation	
a	Diameter of species (subscript)	m
B	Diffusion limit of finite diffusion	$\text{s}^{0.5}$
b_c	Slope of $\log_{10}(I)$ vs E plot	V decade^{-1}
C	Capacitance	F, F cm^{-2}
C_{dl}	Double Layer Capacitance	
C_{ads}	Adsorption/surface state capacitance	
C_{diff}	Differential capacitance	
C_s	Surface concentration of reactant	Mol cm^{-3}
C_{cl}	Catalyst layer concentration of reactant	
C_a	Adsorbed concentration of reactant	
C_0	Bulk concentration of reactant	
C_z	Total electrode capacitance – from CV or EIS at low freq.	
CE	Collection Efficiency (RRDE)	%
d	Diffusion distance	cm
D	Diffusivity co-efficient	$\text{m}^2 \text{s}^{-1}$
D_O	Diffusivity co-efficient of oxidised couple	
D_R	Diffusivity co-efficient of reduced couple	
E	Measured Potential	V, mV
E_a	Activation Energy	kJ mole^{-1}
E_{an}	Anode Potential	V, mV
E_{cat}	Cathode Potential	
E_{onset}	Onset Potential - current switching direction in LSV	
E^0	Standard Potential of a redox couple	
$E^{0'}$	Formal Potential of a redox process or faradic reaction	
E_{pa}	Potential of anodic peak during forward sweep CV	
E_{pc}	Potential of cathodic peak during reverse sweep CV	
$E_{p/2}$	Potential at half wave height (E at $J = 0.5J_L$)	
$E_{1/2}$	Half wave potential	
E_{Onset}	Potential in LSV where current changes direction ($J=0$)	
E_{ORR}	Potential of the start of ORR ($ J_{ORR} >0$)	
E_{pzc}	Potential at which the net surface charge is zero	
E_{step}	Step Potential during staircase cyclic voltammetry	
F_{improv}	Improvement factor relative to control	-
f	AC frequency in EIS	Hz, Rads s^{-1}
f_p	Peak frequency in capacitive arc in EIS	
f_1	High frequency limit of warburg behaviour in EIS	
f_2	Low frequency limit of warburg behaviour in EIS	
ΔG	Change in gibbs free energy (Chemical)	kJ, kJ mol^{-1}
ΔG^\ddagger	Gibbs free energy of activation	
\overline{G}	Electrochemical free energy	
i	Current	A, mA
i_0	Exchange current	

i_D	Disc Current	
$i_{D,L}$	Limiting Disc Current from substrate diffusion limitation	
i_L	Limiting current (any system)	
$i_{L,c}$	Limiting cathodic current	
i_{dl}	Charging current	
i_R	Ring Current	
i_{R-BG}	Ring current associated only with H ₂ O ₂ oxidation	
j	Complex plane component ($\sqrt{-1}$), used in EIS	
J	Intercept of $CE*I_D/I_R$ vs $\omega^{-0.5}$ plot	
J_{flux}	Planar flux of reactant to electrode	Mole cm ⁻² s ⁻¹
J	Current Density (geometric area)	A m ⁻² , A cm ⁻²
J_{an}	Anode/Anodic Current	
J_{cat}	Cathode/Cathodic Current	
J_k	Kinetic Current Density (no η_{ohm} or η_{conc})	
J_0	Exchange current density (at steady state <i>OCP</i>)	
J_L	Diffusion limited current density	
J_p	Peak height of a) electron redox or b) catalytic wave	
J_{ORR}	Oxygen reduction current $J(O_2-N_2)$	
k_E	Rate-constant of electron reaction in film	s ⁻¹
$k_{E,h}$	Heterogenous rate constant of electron reaction in film	cm s ⁻¹
k	Heterogenous rate constant of reaction (subscript specifies)	
k^0	Heterogenous rate constant of Irreversible faradic reaction at $\eta=0V$	
k_{app}	Overall rate-constant of electron transfer	
K_{app}	Reaction rate constant per active site.	M ⁻¹ s ⁻¹
K_a	Acid dissociation constant	Mole dm ⁻³
K_b	Base dissociation constant	
k_D	Mass transfer co-efficient of reactant	cm s ⁻¹
m	Linear gradient of graph ($y=\underline{m}x+C$)	Various
m	No. of protons	
n	No. of electrons	
n_c	No. of e ⁻ transferred prior to RDS	
n_i	No. of e ⁻ transferred during RDS	
N	Frequency power of constant phase element in EIS	-
N_{ORR}	The number of electron received per O ₂ molecule in ORR	-
<i>OCP</i>	Open Circuit Potential (obtained experimentally)	V, mV
Q	Charge	Coulomb
R_{AC}	Total resistance obtained from LF Z' axis intercept in EIS	Ω , Ω cm ²
R_s	Solution ionic resistance	
R_{ct}	Electrical charge transfer resistance	
R_{dl}	Electrochemical Double Layer resistance	
R_{dbl}	Diffusion layer Mass transfer resistance	
s	Laplace plane variable	
t_{step}	Time period of potential step in staircase cyclic voltammetry	
T	Absolute temperature	°K
VOL_{an}	Anode chamber volume	cm ³
VOL_{cat}	Cathode chamber volume	
V_{cell}	Cell Voltage	V, mV
$W_{1/2}$	Peak Width at Half Maximum height	X-axis scale
x	Distance from electrode surface	cm
Z	Charge of a particle or intermediary	

Z'	Real part of the impedance (resistive)	$\Omega, \Omega \text{ cm}^2$
Z''	Imaginary part of the impedance (capacitive)	
Z_W	Warburg Impedance (diffusive)	
Z_{dl}	Impedance of the double layer	
Z_0	Impedance value at low frequency end of an arc in EIS	
Z_∞	Impedance value at high frequency end of an arc in EIS	
α	Electron transfer co-efficient	-
β_C	The symmetry factor of the RDS	-
δ	Diffusion layer thickness	cm
δ_{film}	Film thickness of a modified electrode	cm
Δ_{COD}	Change in “COD” over MFC batch cycle	$\text{gO}_2 \text{ m}^{-3}$
ϵ_c	Columbic efficiency	%
κ	Solution conductivity	S cm^{-1}
ω	Electrode rotation speed	RPM
$\tilde{\omega}$	Electrode rotation speed / Radial frequency (in EIS)	Rads s^{-1}
η	Total overpotential, $E - E^0$	V, mV
η_{ct}	Charge transfer overpotential	
η_{conc}	Concentration overpotential	
Ω_{ext}	MFC external fixed resistance	Ω
ρ	Density	Kg dm^{-3}
σ	Warburg co-efficient in EIS	$\Omega \text{ cm}^2 \text{ s}^{0.5}$
τ	Descriptor of increased O_2 from recycled disproportionation	-
τ_D	Dielectric relaxation time in EIS	seconds
v	(a) Applied potential scan rate during CV (b) Scan rate intercept of E_p vs $\log_{10}(v)$ plot with subscript ca or an (c) Linear velocity of solution flow in direction subscript r, y, θ	V s^{-1} cm s^{-1}
$\theta_{FePc-X-}$	Adsorbed anion surface coverage	-
ϕ	(a) Phase angle of electrode (EIS) (b) Localised Potential	Degrees V
χ^2	Chi-squared “Goodness of fit” utilised in NOVA software	-
ν	Kinematic Viscosity	$\text{m}^2 \text{ s}^{-1}$
Γ	Calculated loading on surface from colloid or solution aliquot	Mol cm^{-2}
$\tilde{\Gamma}$	Electro-active loading of redox material on surface	Mol cm^{-2}
ζ	Zeta potential ($\phi_{OHP} - \phi_{bulk}$)	V

These symbols are used throughout the thesis to refer to the axis of the graph and the numerical treatment, e.g σ vs. E plot.

Material and chemical abbreviations

Abbreviation	Meaning
AEM	Anion Exchange Membrane
ASR	Area specific resistance
BDE	Bond Dissociation Energy
BES	Bio-electrochemical Systems
CV	Cyclic Voltammetry
CE	Counter Electrode
CEM	Cation Exchange Membrane
DABCO	Di-azobicyclo-[2.2.2]-octane
DMAC	Di-methyl Acetamide

DMSO	Di-Methyl Sulfoxide
DIW	De-ionised Water
DFT	Density Functional Theory
EIS	Electrochemical Impedance Spectroscopy
EPPG	Edge Plane Pyrolytic Graphite
emf	Electromotive Force
FePc	Iron Phthalocyanine
FWHM	Full Width Half Maximum
GC	Glassy Carbon
GDE/GDC	Gas Diffusion Electrode/Cathode
HF	High Frequency
LF	Low Frequency
NPc	Napthalocyanine
PBS	Phosphate Buffer Solution
PP	Porphyrin
GC	Glassy Carbon
HOPG	Highly Orientated Pyrolytic Graphite
IHP	Inner Helmholtz Plane
KJB	Ketjen Black ECJ300 (Carbon Black)
LSV	Linear Sweep Voltammetry
MON	Monarch 1000 (Carbon Black)
MEC	Microbial Electrolysis Cell
MFC	Microbial Fuel Cell
MeO_x	Transition Metal Oxides of varying oxidation state
NADH	Nicotinamide Adenine Dinucleotide
OCP	Open Circuit Potential
OHP	Outer Helmholtz Plane
ORR	Oxygen Reduction Reaction
PEM(FC)	Proton Exchange Membrane (Fuel Cell)
Pt	Platinum
QDPSU	Quaternary-1,4-diazabicyclo-[2.2.2]-octane Polysulfone
RDE	Rotating Disc Electrode
RE	Reference Electrode
RHE	Reversible Hydrogen Electrode
RRDE	Rotating Ring Disc Electrode
RDS	Rate Determining Step
SCE	Saturated Calomel Electrode
XPS	X-ray Photoemmission Spectroscopy
WE	Working Electrode
WW	Wastewater

Chapter

1

Chapter 1. Background on principles of bioelectrochemical systems

1.1 Sustainable treatment of wastewater

The demand placed upon water and power resources continually escalates as land use and population growth intensifies. Wastewater treatment allows sustainability of water resources but at the cost of high electricity consumption. Centralised collection of wastewater generated from the domestic wastewater of cities offers a unique opportunity for turning a source of pollution into a resource. Domestic wastewater contains approximately $9.5 \text{ kJ litre}^{-1}$ of unutilised energy in the form of oxidizable organic pollutants. The current treatment method of oxygenation and microbial remediation does not attempt any recovery of this energy. The processes involved in wastewater collection and treatment can incur 4% of the electricity output of a first world nation [1].

In terms of global warming, this electricity consumption relates to significant environmental damage. In addition, the anaerobic methods used to treat domestic wastewater release large quantities of N_2O and methane, a greenhouse gas 19 times as potent as CO_2 (20 year scale). An analysis of traditional wastewater treatment showed that 1 megalitre of wastewater produced 340g of CH_4 and 335kg of CO_2 [2]. The introduction of a technology that transforms all organic pollution to CO_2 and most importantly, avoids consuming 4% of the national grids consumption would significantly improve the green credentials of the wastewater treatment industry. Wastewater companies in a first world country such as the US would not consume ~\$18,000 million of electricity per year¹. Electricity current produced via means incurring CO_2 discharge.

In third world nations the electricity and construction cost can lead local government to discharge untreated effluent, resulting in a significant environmental cost. Eutrophication in freshwater streams and a reduction in freely available potable water are problems that are rife in landlocked third world countries, impacting human health and the ability to grow food. Attempts to cultivate food by using human sewage and industry wastewater result in cytotoxicity of the most basic and essential foodstuffs [3], toxins that show bio-accumulation effects.

¹ US consumes $28,714 \text{ TWh year}^{-1}$. Treatment stage needs 1.6% of US consumption. Industry price $\$0.06 \text{ kWh}^{-1}$

In first world nations the environmental impact of sewage is largely abated due to treatment. Some pollutants such as Estrogens [4], endocrine disruptors [5] and antibiotics [6] can survive traditional sewage treatment processes and require energy intensive tertiary treatment or are discharged into river courses. These can result in problems for animal reproduction and microbial imbalances favouring antibiotic tolerant pathogens. An approach that does not simply rely on anaerobic and aerobic bacteria may be more effective at removing these pollutants. Approaches such as contact adsorption, oxidising agents or electrochemical decomposition are areas of intense academic interest. These approaches are promising but can incur the problems of adsorption saturation and energy consumption when producing the oxidising agents, while the electrochemical approach lacks a direct power source of its own.

New sewage treatment technologies that can be applied on locally and at a small scale can potentially abate many of these environmental effects. Anaerobic digestion plants have been successfully applied to make nutrient rich earth in such settings as used mine pits and farming communities. They produce 40% CO₂ and up to 60% methane, a concentration high enough to burn for electricity generation. The cost of large reactor units is still high and mechanised equipment is required to handle the larger units. A scalable design with no moving parts or the need for mechanised equipment beyond the construction stage would improve quality of life around the world.

1.2 Established technologies and the monetary case for MFCs

The typical energy content of domestic wastewater is 1,750 kWh per mega-litre [2]. In England and Wales this means ~730,000 kW of unused energy finds its way to sewage treatment facilities in the UK. Remediation of this energy could also occur without centralised collection, such sources may include intensive agriculture, and select industries associated with organic products. This would have the combined benefit of remediating pollution and avoiding the construction of expensive centralised collection infrastructure to rural or remote locations.

The impact of the MFC has not yet been felt in the realm of popular science. The first full Life Cycle Analysis of MFCs, MECs and Gasification was carried out by Foley et al [7] in 2010, a Microbial Electrolysis Cell approach was recommended due to the transportable nature of the H₂. Established technologies for wastewater treatment

include Upstream anaerobic baffled tank reactor, Aeration tank, Gasification, Activated Sludge, Trickling filters, Membrane ultra-filtration (bacteria and micro-agglomerates), Electrochemical treatment and consumable oxidising agents.

1.3 The microbial fuel cell

A fuel cell can be defined as.. “An electrochemical device that oxidises a substrate, creating a diffusive chemical species and electrons which are captured by the electrode (anode) which is connected in an external circuit to an electrode (cathode), an electrode that is in the presence of an oxidising agent. This allows the diffusive chemical element created at the anode to recombine with electrons in the presence of the electron acceptor, thus creating a continual current.” [8]

A microbial fuel cell (MFC) fits this description by offering a unique way of harvesting the metabolic efforts of microbial life, utilising the potential difference across the periplasmic membrane.

In the simplest description, microbial metabolism relies on the diffusion of substrate through cellular membrane and the removal of metabolic product through the same avenue. The process requires a thermodynamically favourable net energy gain between the reaction of an electron donor and an electron acceptor. The oxidation of organic substrate produces electrons, initiating a chain of chemical conversions that result in a potential difference inside and outside the cell membrane. In an exocellular setting, the electron acceptor does not readily perform the reaction without catalysis, in the cell the reaction is broken into many steps.

The cell voltage (V_{cell}) ideal for an MFC is equated to the free energy liberated by full cell reaction with a thermodynamic energy change of ΔG (J mole⁻¹), illustrated in Eq.1-1. Where n = no. of electrons liberated/consumed, F = Faraday's constant, T is temperature (°K), $E^{0'}$ is the formal potential (V) and K is the concentration equilibrium value between reactants and products when net reaction rate is zero (variable units). For a full fuel cell reaction at two electrodes $E^{0'}$ approximates V_{cell} when the electrodes are electrically isolated. A full cell reaction is divisible into two half-cell reactions (a) anode, (b) cathode, where eq.1-1 applies to the ΔG_f change between reactants and products for either half-cell reaction, generating $E^{0'}$, a formal electrode potential.

$$\Delta G = -nFE^{o'} = -RT \ln K \quad (\text{Eq.1-1})$$

The first paper on a bioelectrochemical system was released in 1911 by Potter [9]. The study utilised a yeast anolyte and received little follow up interest due to the modest V_{cell} , of 0.32 Volts.

Some bacteria regulate metabolism by dumping electrons via transfer to redox proteins in the periplasmic membrane. From this point transfer to an extra-cellular acceptor is achieved with nano-wires, mediators or direct electron transfer from membrane bound redox enzymes to solid surface. These organisms are known as exo-electrogens and oxidise organic pollutants in an MFC [10]. The anode replaces oxygen as the electron acceptor under certain anerobic conditions. Exo-electrogens may be present in a consortia or a pure strain, thriving in anaerobic (no oxygen) and occasionally anoxic (low oxygen) environments.

Exoelectrogenic biocatalysis of acetate (a volatile fatty acid) at the anode produces protons, electrons, biomass and $\text{CO}_2/\text{HCO}_3^-$ by product. At the cathode, the protons and electrons from the anode reduce a suitable electron acceptor. This process is depicted in Figure 1-1. Protons typically diffuse along a concentration gradient against the direction of the electric field. Anaerobic conditions are maintained at the via (a) a sufficient microaerobic body of biotic electrolyte or (b) an electrolyte permeable barrier to O_2 diffusion [11]. The cathode reaction is biocatalysed (aerobic bacteria) or chemically catalysed (electro-catalyst).

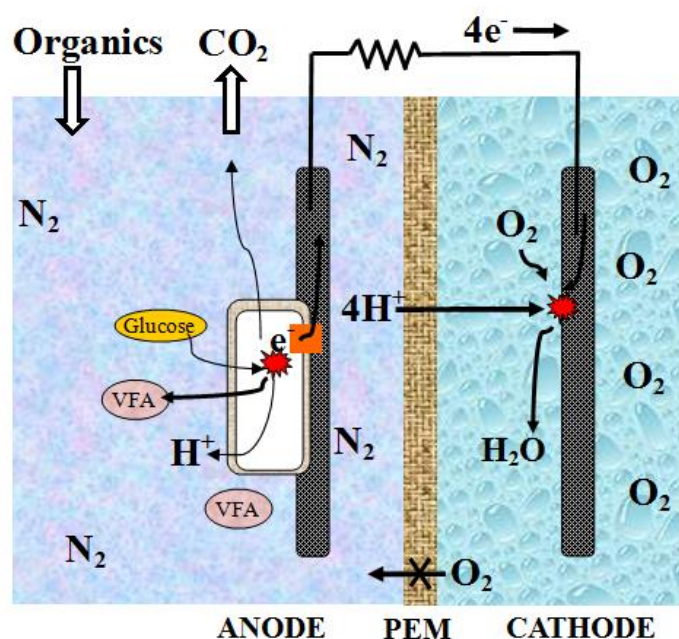


Figure 1-1. Representation of an MFC utilising anode biocatalysis. Glycolysis, fermentive and exoelectrogenic processes occur in the organism attached to a conductive electrode (grey/black) via a redox enzyme (orange). Key; VFA (Volatile Fatty Acid), PEM (Proton Exchange Membrane), red – reaction sites.

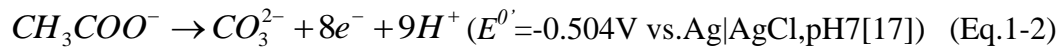
An MFC can be equipped with a biotic cathode, allowing reduction of solvated pollutants (ie. NO_3^- , SO_4^{2-} , ClO_4^- , CH_2Cl_2) at cathode potentials (E_{cat}) lower than obtainable with an electrocatalyst [12, 13]. The cathode may become the electron donor to the bacteria as it mimics a metal or mineral surface found in nature.

1.3.1 Anode

In a PEM fuel cell H_2 gas is pumped through a porous catalyst layer at overpressure (30-80°C), producing pure H^+ and e^- product at the anode. In an MFC this process does not require an acid and thermally resistant support material, but one that is bio-compatible, presenting a large conductive surface area for biofilm growth. Biofilms can form on substrates that include silica, minerals, some plastics, biopolymers, metals, carbons and alloys [14] but only conductive materials are able to support large electrogenic biofilms if a solvated electron acceptor is not present. Labscale MFCs primarily use graphite and activated carbons as passivity is not an issue.

Electrostatic repulsion between bacteria and support can result in slow biofilm formation. It originates from charge in bacterial outer membrane/lipopolysaccharide and

the columbic shielding from a charged double layer arrayed around the anode surface (see Figure 2-5). Therefore control of the electrical potential of the anode surface during the growth phase is commonplace [15]. The anode potential (E_{an}) has a profound effect on metabolic kinetics of acetate consumption [16]. The acetate oxidation reaction (Eq.1-2) produces 8 electrons, many of which are not utilised at the anode. Electrons are primarily lost to metabolic processes or cross-over. This effect is quantified by the anolyte coulombic efficiency (ε_c) for an MFC fed with acetate and using O_2 at the cathode (Eq.1-3) [17].



$$\varepsilon_c = 8.29 * 10^{-5} * \int_{t=0}^{t=\infty} i \partial t / [VOL_{an} * \Delta_{COD}] \quad (\text{Eq.1-3})$$

Where “ i ” is external electric cell current (amp), “ VOL_{an} ” is the anode chamber volume (cm^3), Δ_{COD} is the change in chemical oxygen demand (COD) content from the start of the batch cycle to the end (g of O_2 / cm^3).

1.3.2 Polarisation of electrogenic biofilms

The $E^{0'}$ in Eq.1-2 is set by the formal redox potential of the membrane protein or mediator delivering electrical charge [17, 18]. Imposing a more positive potential than this (anodic polarisation) causes the flow of electrical current and allows cell metabolism to increase. Acetate fed MFCs typically select for the nano-wire producing *Geobacter Sulfureducens* [19-22] with optimum polarisation potentials differing between co-species in consortia, electrode porosity, reactor geometry, electrolyte conditions and study. An applied upper potential limit on the terminal reductase is thought to be feasible [19]. Variance between studies in consortia is further compounded by synergistic effects from other bacteria, including removal of auto-inhibiting respiration products in the electrolyte (localised acidity and VFA).

1.3.3 Electrolyte

Wastewater plant influent (Table 1-1) contains a significant amount of dissolved organics, a large portion of which (40%) are soluble volatile fatty acids whose oxidation incurs little overpotential. 30 mg/L of acetic acid can be found in wastewater influent

from pre-treatment fermentation [23]. High COD removal values (60%) show that fermentation processes occur in wastewater fed MFC reactors as the VFA are consumed.

Table 1-1. Typical make-up of wastewater adapted from [24]

	Conc. mg/L	Conc. mM/L
Total Dissolved Solids	780	n/a
Bicarbonate Alkalinity, as CaCO ₃	240	n/a
Na ⁺	160	6.96
K ⁺	1.7	0.043
Calcium	76	1.9
Magnesium	33	3.1
Cl ⁻	220	6.2
SO ₄ ²⁻	88	0.916
Fl ⁻	0.48	0.025
NO ₃ ⁻	24	0.387
NO ₂ ⁻	~2.5	0.054
Phosphorus, as PO ₄	0.081	0.0026
pH	7.2-7.4	
Specific Conductance	2700 $\mu\text{S cm}^{-1}$	

If a large body of electrolyte separates the anode and cathode, an increase in MFC internal resistance, referred to as i-R drop or R_u (uncompensated resistance) occurs along the direction of current flow. The relationship between electrode separation and conductivity of the electrolyte is given in Eq.1-4.

$$R_u = L/A\kappa \quad (\text{Eq.1-4})$$

Where L is the distance, cm; A is the cross-sectional area (cm^2), over which the ionic conduction occurs; κ is the ionic conductivity of the electrolyte, S cm^{-1} .

1.3.4 Membrane

Ideally membranes for air cathodes would be both hydrophilic and an oxygen separator. Producing such membranes may rely on small diffusion channels capable of differentiating between polar and non-polar molecules. Such a membrane would be susceptible to pore clogging and high internal resistance.

Utilisation of cheap separator materials in mass production such as J-cloth have been attempted, but are susceptible biofilm fouling [25]. Materials such as visking tubing may not allow sufficient ionic current and remain susceptible to bio-corrosion, short circuiting the MFC. Detailed literature discussions are continued in chapter 3.

1.3.5 Cathode Assembly

A common configuration for the oxygen electrode is the air cathode. This design performs the oxygen reduction reaction (ORR) with minimal oxygen mass transfer limitation. Detailed discussion continues in further chapters. Briefly, a conductive catalyst layer (typically carbon) is bound to the solid surface an ionomer (charged) or binder (dispersing agent). The porous conductive layer may support an electrocatalyst. The design is optimised for electrochemical oxygen reduction. The substrates and products of ORR are pH dependent, as shown in Eq.1-5 and Eq.1-6, the opposing half-cell reactions to the anodic half-cell reaction (Eq.1-2). Cathode materials and design studies are reviewed in chapter 3.



1.4 Electrochemistry in electrocatalysis

Application of electrochemical engineering allows reactions which normally require large pressurised or high temperature vessels to overcome the activation energy, E_a (kJ mol⁻¹), when compared to heterogeneous catalysts without polarisation. Potentially explosive processes such Hydrazine oxidation can be controlled by polarisation and partially separating reactants into half-cells. The oxidation of a graphite electrode in contact with a water interface can be powered by a household battery (<1V vs Ag|AgCl) using H₂O as a substrate. The process of surface oxygen insertion would typically require 500°C in Solid-Gas reaction to dissociate the O=O bond. Anodic dehydrogenation reactions of alkane [26], CO oxidation [27] allow specific products to form. Researching reaction specificity and reducing E_a of individual steps will become increasingly important, in particular, those linked to the chemistry of the important oxidants such as O₂.

1.4.1 Heterogeneous catalysts and electrochemical catalysts

In heterogeneous catalysis the net balance of electrons in reactants and products is identical. In electrochemical catalysis electrons and protons can be used as substrate or are liberated as a reaction product in each half-cell reaction. As the half-cell reaction

occurs on the solid surface and not in the electrolyte a potential gradient is created between the two. Manipulation of the potential difference (polarisation) allows the reaction to occur in a net direction. When the electrode is unpolarised it is said to be in open circuit when no net rate of reaction or electron exchange occurs. Polarisation is effected by connection to the opposing electrode (counter electrode). The counter electrode is in the same process electrolyte as the working electrode. The unpolarised rate of reaction is defined as the exchange current density, J_0 (A cm^{-2}). It is akin to exchange rate of reaction at reactant-product equilibrium seen in heterogeneous catalysis, eg. k_f or k_b (variable units) with the same catalyst, substrate and electrolyte.

1.4.2 E^0 , $E^{0'}$ and Open Circuit Potential

Potentials are reported relative to a reference electrode (RE). The RE is situated in the electrolyte at close proximity to the electrode. On the metal wire surface of the RE a facile (non-polarisable) and reversible reaction involving an electron occurs with a high degree of reaction specificity. The metal surface and an ion (product or reactant) are in equilibrium with no net current flowing through the RE solution electrolyte (Appendix section 10.8).

For the reaction occurring on the surface of the working electrode most literature values for a given reaction are reported as the **standard redox potential** (E^0). The E^0 is defined as the midpoint in a reversible/quasi-reversible reaction on a Platinum surface where the concentration of each aqueous phase substrate and product are present in the pure aqueous solution at a concentration of 1M/litre under standard conditions (298°K). Substrates and products are seldom present at the ideal 1M concentration, in which case the **formal redox potential** ($E^{0'}$) is often applied. In this instance the concentration of reactants and products in the process electrolyte are factored into the equilibrium, as is ionic strength. In equations where H^+ or OH^- are involved in the reaction as substrate or product the $E^{0'}$ value shifts significantly from E^0 .

$$E^{0'} = E^0 + \ln \Pi * 2.303RT/nF \quad (\text{Eq.1-7})$$

$$\Pi = [S1]^a [S2]^b / [P1]^y [P2]^z \quad (\text{Eq.1-8})$$



In real world implementation of electrochemical cells it is usually the case that mixed reactions occur on the surface of an electrode, resulting in a mixture of formal potentials of each reaction [28]. In this case the **open circuit potential (OCP)** describes the observed equilibrium potential between each reaction. In an ideal electrochemical cell (pure electrolyte, single-anion, single reaction, chemically homogenous electrocatalyst surface, 100% selective electrocatalyst) the formal potential should equal the open circuit potential. The largest discrepancy between $E^{0'}$ and OCP in pure electrolyte is;

- 1) Non-selective catalyst producing different products. An example would be the mixture of $2e^-$ ORR ($E^{0'}=+0.074V$ vs. Ag|AgCl) and $4e^-$ ORR ($E^{0'}=+0.605V$ vs. Ag|AgCl) that occurs at pH7 on a catalyst supported on carbon electrode.
- 2) Exorogenic losses in non-electrochemical reactions acquiring electrical energy [29].
- 3) Differing ratios and concentrations of oxidised and reduced couple in the vicinity of the active site than in the process electrolyte.
- 4) Different local chemical environment for the electrocatalyst, such as ligands and substrate resulting in differing activation energy of rate limiting steps.
- 5) Difference in electrostatic repulsion between substrate or product [30]²
- 6) Impurities solvated in the electrolyte (eg. Carbonate from air, trace metals).

The relationship between $E^{0'}$ and pH in any process involving $m H^+/OH^-$ and n electrons is represented in Eq.1-10. A -59mV shift per pH unit is applicable for O_2 reduction to H_2O/OH^- or H_2O_2 . This affects any reactions involving an H^+ or OH^- .

$$\partial E^{0'}/\partial pH = -2.3RTm/nF \quad [31] \quad (\text{Eq.1-10})$$

1.4.3 The cathode and the electron acceptor

Strong cathodic electron acceptors facilitate continual organic degradation at the anode biofilm by increasing the proton concentration gradient. Figure 1-2 lists the biocatalysed electron donor and receptor reactions relevant to an MFC. Quick growing organisms efficiently biocatalyse terminal donor and acceptor reactions with the largest potential gap.

² Eg. If the product of ORR is OH^- it will bind strongly to a positively charged electrode, shifting $E^{0'}$. Additionally, $[O_2]$ at the site may differ from that in the electrolyte due to de/adsorption.

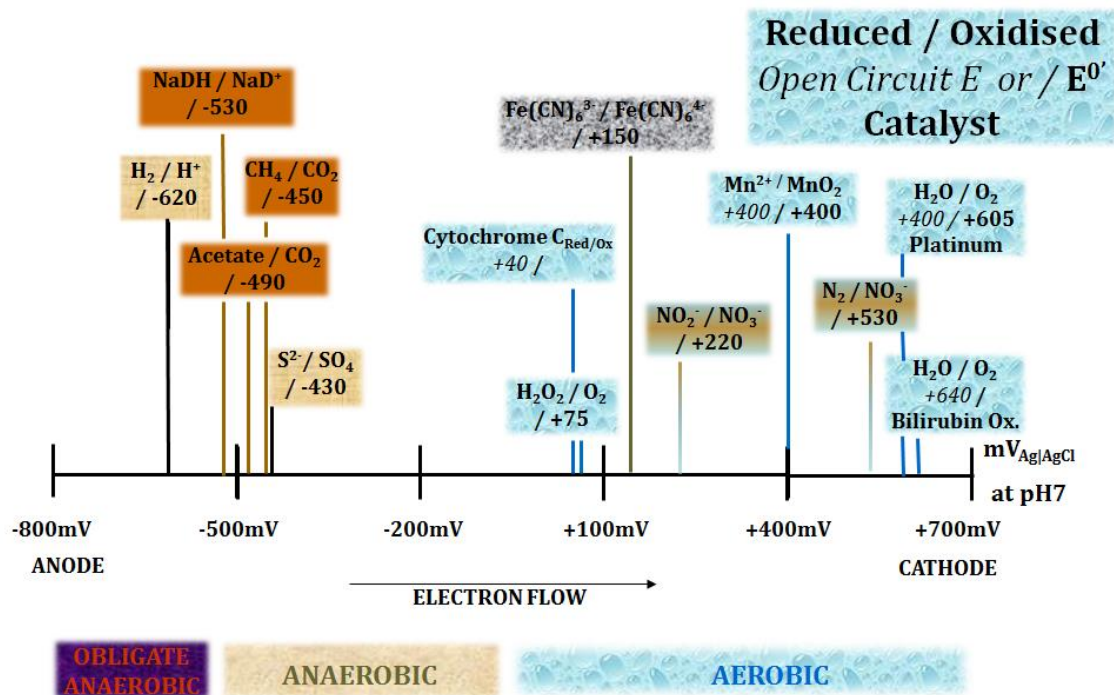


Figure 1-2. Biocatalysed OCP or E^0 of common redox couples in nature relevant to MFC. Light Brown (strictly anaerobic), dark brown (anaerobic), or blue (aerobic) for life or grey (chemical electron acceptor). pH 7.0. E vs Ag|AgCl 3MNaCl

Thermodynamic performance of an electron acceptor (E^0) is closely linked to the bond dissociation energy (BDE). The BDE of O-O in O₂ is 494 kJ mole⁻¹ [32]. The kinetic performance of an electro-catalyst is determined by the activation energy of the rate-determining step. In aqueous electrolytes the reaction proceeds via the rate constant k_{app} (cm s⁻¹) which when under electron transfer control obeys the Arrhenius form (eq.1-11), meaning $\ln(k_{app}) \propto 1/T$, and yielding plots with slope $\Delta G^\ddagger / R$ and intercept $\ln(A)$.

$$k_{app} = Ae^{-\Delta G^\ddagger / RT} \quad (\text{Eq.1-11})$$

Where ΔG^\ddagger is the standard free energy of activation (kJ mole⁻¹), reduced with polarisation, A is an Arrhenius prefactor constant (s⁻¹, 1st order). The rate constant of electron exchange (k^0) at OCP is related polarisation by Eq.1-12. Polarisation reduces the ‘hump’ of RDS activation energy increasing k_{app} . In the case of a single electron transfer at reasonably large overpotential (making k_b negligible) [33]...

$$k_{app} = k^0 e^{\left[\frac{(E-E^0)F}{RT} \right]} \quad (\text{Eq.1-12})$$

1.5 Motivation of study

1.5.1 *Justification and aims of research in chapter 5*

Primary aim

- To uncover the neutral pH electrochemical behaviour of a non-precious metal fuel cell cathode material of intense academic interest (Iron Phthalocyanine).
- To isolate and quantify the means of catalyst destruction in operating conditions.
- To improve the reaction kinetics of ORR.

Secondary benefits

- Phosphate is the main pH buffering anion in blood. Transplantable medical devices can utilise non-toxic haemoglobin like compounds for selective cathodes in bioelectrochemical sensor devices, oxidising target substrate at the anode. A parallel could be drawn between haemoglobin breakdown to bilirubin and the stability of Iron Phthalocyanine (FePc). The information may be useful to artificial blood design or anaemia treatment.
- Oxy-FePc is a moderately powerful oxidising agent that is inert to the majority of volatile fatty acids [28]. More powerful oxidising agents (such as H₂O₂) oxidise everything. While its anti-bacterial properties are not known, a fundamental study may be useful in designing devices with FePc adsorbed on a flat surface, scavenging selected solvated substances in biotic aerated streams [28].

1.5.2 *Justification and aims of research in chapter 6*

Primary aim

- To assess the effect of a novel anion exchange material on the ORR kinetics of FePc and other electrocatalytic surfaces at neutral pH.
- To assess O₂ interaction with and diffusion through the anion exchanger.

Secondary benefits

- Dabco is used in a variety of organic synthesis reactions, catalytic side reaction of use to chemical synthesis could be identified.

- New materials for selective dialysis membranes are required for medical and purification processes. Information of their selectivity and interaction with different electrolytes may find applications.

1.5.3 *Justification and aims of research in chapter 7*

Primary aim

- Evaluate the first application of an anion exchange material not to be based on quaternary ammonium or tri-methyl amine in MFC cathodes.
- Assessment of Dabco based anion exchange binder in real wastewater.
- The use of impedance spectroscopy to identify performance bottlenecks in catalyst layer design.

1.5.4 *Justification and aims of research in chapter 8*

Primary aim

- Assess membrane phase conductivity and interfacial resistances of ion exchange membranes in MEA form in neutral pH media.
- Compare manufacturer reported conductivity in NaCl to that obtained using impedance spectroscopy.
- Evaluate impedance spectroscopy method by comparing predicted performance of membranes to multiple batch tests of MFCs with the MEA.
- Recommend materials of interest and produce a finalised MEA representing the optimal balance of cost and performance.

Chapter

2

Chapter 2. Theory of electron transfer analysis and laws governing experimental systems

2.1 Potential ramping techniques for studying electron transfer

2.1.1 Staircase voltammetry for assessing electron transfer

Staircase voltammetry relies on steps in applied potential E_{step} (Volts) over a time period of t_{step} (seconds) to generate a profile of i vs E . Figure 2-1 indicates changes in E vs t over a portion of a staircase Cyclic Voltammogram (CV) or Linear Sweep Voltammogram (LSV).

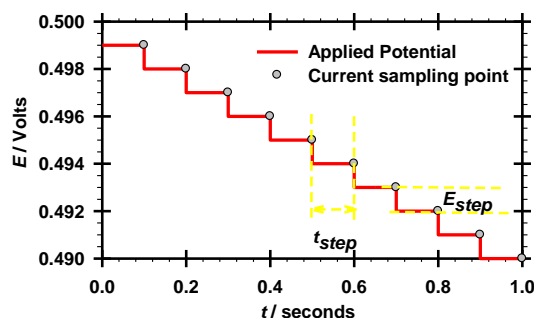


Figure 2-1. E vs t plot for staircase voltammetry. Used to obtain all i - E data in this thesis

The effective scan rate ν (V s^{-1}) is computer controlled and is used to calculate t_{step} via Eq.2-1.

$$E_{step} / \nu = t_{step} \quad (\text{Eq.2-1})$$

2.2 Theory of electron transfer

2.2.1 Energy barriers of single electron transfer to an adsorbed reactant

For the general case of $1e^-$ electron transfer...



In some cases it is useful to separate the heterogeneous rate constant into forward and backward components (k_f) and (k_b), varying as a function of overpotential (η), obtained from $E-E^{0'}$. In multi-step reactions, the change in Gibbs free energy of the adsorbed intermediary complexes before and after each step produces a series of $E^{0'}$ values, the median of which is akin to OCP . The same electro-catalyst is unlikely to be able to efficiently catalyse each stage and so the RDS must be found to identify process

bottlenecks. Julius Tafel identified a linear relationship between $\log_{10}|i|$ vs η . This has been used as the mark of kinetic current (i_k) of a polarised surface ever since.

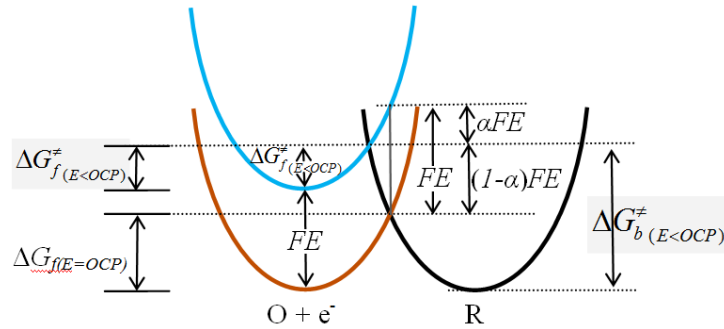


Figure 2-2. Effect of cathodic polarisation on free energy barriers of $1e^-$ electron transfer. Subscript 'b' 'f' represent forward and backward reaction. Cathodic polarisation (Blue) and $E=OCP$ (brown)

In Figure 2-2 the reduction of activation energy with overpotential can be visualised by viewing the transfer as a transition over an energy barrier. The x-plane represents a solvent co-ordinate. The term α is a measure of symmetry in the energy barrier. If the activation energy barrier of electron transition is located closer to the adsorbed oxidised couple then the electrocatalyst, α is increased. For a cathodic reaction ΔG_c^{\ddagger} (kJ mol^{-1}) is the activation energy is reduced with polarisation from that at $E^{0'}$ (ΔG_{0c}^{\ddagger})...

$$\Delta G_c^{\ddagger} = \Delta G_{0c}^{\ddagger} + \alpha F(E - E^{0'}) \quad (\text{Eq.2-3})$$

The effect of cathodic polarisation on an adsorbed oxidised couple causes the energy barrier to shift closer to the electrocatalyst, meaning α is a function of potential [34], though if the potential range is small α is relatively consistent. A change in the orientation of reactant can also affect energy barrier geometry, affecting α . The influence this reaction co-ordinate plays on the faradic current is depicted in Figure 2-3.

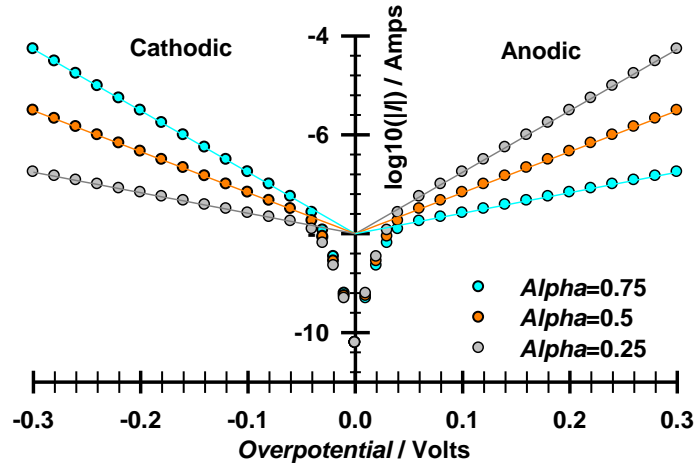


Figure 2-3. Model tafel plot of reversible $1e^-$ transfer at $\eta=0V=E^{0'}$ as $f(\alpha).C_{0,Red}=C_{0,Ox}$, $\alpha=0.5$, $A=1cm^2$, $i_0=1 \times 10^{-8}$ Amps, $T=298.15^\circ K$.

An electrode at equilibrium is known to take on an *OCP* relative to bulk concentration of Ox and Red (Eq.2-4). Large values of i_0 mean that the system attains equilibrium quickly. Under certain conditions $OCP \neq E^{0'}$, primarily when the reverse couple is not present in solution the reverse reaction becomes negligible...

$$\log_{10}(i_0) = \log_{10}(FAk^0) + (1-\alpha)\log_{10}(C_{0,Ox}) + \alpha\log_{10}(C_{0,Red}) \quad (\text{Eq.2-4})$$

$$i_0 = FAk^0 C_{0,Ox} \exp\left[-(OCP - E^{0'})\alpha F/RT\right] \quad (\text{Eq.2-5})$$

Eq.2-5 can be used to determine α by varying Red when Ox is kept consistent. In the case of ORR this may be problematic, as Red can correspond to H_2O or OH^- . For a reaction with a single step reversible reaction the kinetic current is obtained by the Butler-Volmer equation [35]...

$$i_k = i_0 \left(e^{[-\alpha n \eta / k_{app} T]} - e^{[(1-\alpha) n \eta / k_{app} T]} \right) \quad (\text{Eq.2-6})$$

A multi-step reaction may be thought of as a series of the steps governed by Eq.2-6. In multi-step reactions the *OCP* is a mixture of each step, whereby $k_{app}=0$ and $i_k=0$ but for each individual step $i_k \neq 0$ may occur if multiple pathways are present. The concentration of each reactant applies to intermediates. In this case, it could be assumed that an adsorbed intermediary controls the *OCP*, as described by Eq.2-7. The subscript 'a' describes this situation and the superscript 'RDS' denotes the oxidised or reduced couple of the RDS.

$$i = nFAk_{RDS}^0 \left[\left(C_{a,Ox}^{RDS}(0,t) \right) e^{-\left(OCP-E^0 \right) \alpha F / RT} - \left(C_{a,Red}^{RDS}(0,t) \right) e^{-\left(OCP-E^0 \right) (1-\alpha) F / RT} \right] \quad (\text{Eq.2-7})$$

2.2.2 Multiple electron transfer to an adsorbed reactant

For multiple electron transfers a series of energy barriers must be overcome. Plotting the change in Gibbs energy of formation between the reduced and oxidised couple of each step allows the rate determining step to be obtained. Figure 2-4 depicts a half-cell four electron reduction reaction. The Y-axis of Gibbs free energy includes all substrates.

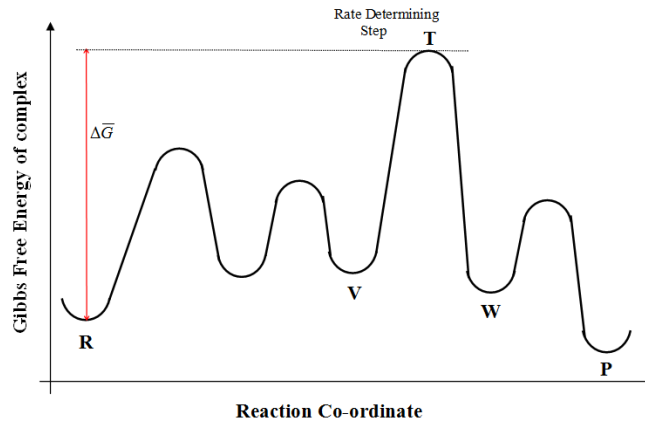


Figure 2-4. Standard free energy change in a cathodically polarised reduction reaction. Four step reduction reaction. Key; R–Reactants, P–Products, V–State of complex prior to RDS, W–state of complex after RDS

In this relationship the change in Gibbs free electrical energy incurred by the RDS ($\Delta \bar{G}^0$) if the reverse reaction is negligible is shown in Eq.2-8 [36]. This is related to the current under electron transfer control via Eq.2-9.

$$\Delta \bar{G}^0 = \sum_i Z_{RV} F \Delta \phi_{RV} + Z_{VW} F \Delta \phi_{VT} \quad (\text{Eq.2-8})$$

$$\Delta \bar{G}^0 = -RT \ln(i_k) + C \quad (\text{Eq.2-9})$$

Where Z_{RV} is the charge of an intermediary particle transferred from state R to V, $\Delta \phi_{VT}$ is the local potential difference (V) through which the particle moves travelling from state W to transition transition complex T. T is a transition complex, other subscripts correspond to points on Figure 2-4. This yields a generalised tafel equation, considering

the case where intermediaries remain adsorbed causes the values to deviate. Eq.2-10 is the corrected equation which involves the terms “ f ” to describe the fraction of the $\phi_S - \phi_{bulk}$ electrical field involved in the charge transfer process.

$$-b_c = \frac{2.303}{\sum_i Z_{RV} f_{IP} + Z_{VW} \beta_c f_{VW}} \frac{RT}{F} \quad (\text{Eq.2-10})$$

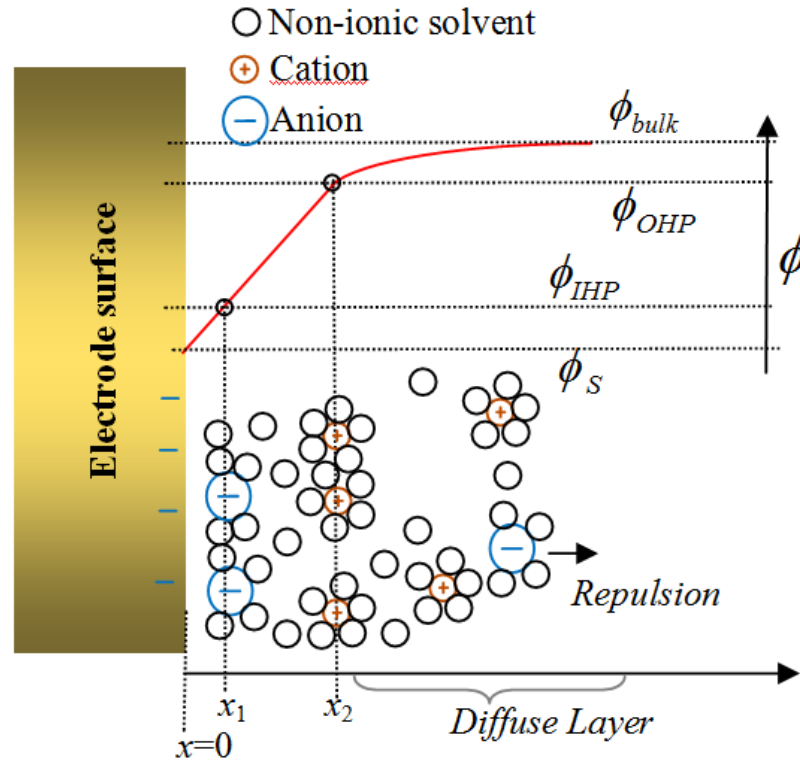


Figure 2-5. Potential profile across the double-layer and diffuse layer region without the case of adsorbing ions. Key; S-Surface, IHP-Inner Helmholtz Plane, OHP-Outer Helmholtz Plane

The double layer forms at the boundary between an electronic and ionic conductor. Anions tend to form the IHP, owing to their ability to strip elements of their solvation shell and form van der Waals interactions with the surface. Counter charges orientate around these charges, additional counter charges form the diffuse layer (section 2.2.3), producing a series of capacitors which charge and discharge over different time periods. The inner potential drop across the ϕ_S to ϕ_{OHP} region has previously been modelled as linear, or in more concise models the drop is most significant at the IHP.

The drop $\phi_{OHP} - \phi_{bulk}$ is referred to as the zeta potential (ζ). This form of columbic shielding controls agglomeration of particulates in colloidal suspension (eg. catalyst

inks) or flocculation of material onto electrodes (eg. early biofilm formation). For higher ionic strengths the diffuse layer compresses and ζ becomes nearly irrelevant and $E = \phi_{IHP} - \phi_{OHP}$.

2.2.3 Capacitance

Capacitance arises from the arrayed orientation of countercharges separated by a dielectric or relative permittivity with breakdown constant (ϵ_r) with plate-plate thickness (d). This is formalised in Eq.2-11, which is valid for perfect capacitor of two facing parallel plates with opposing charge.

$$C = \epsilon_r \epsilon_0 / d \quad (\text{Eq.2-11})$$

Typically ϵ_r is 80 for H₂O solvent (no units), ϵ_0 the permittivity of free space ($8.854 \times 10^{-12} \text{ F m}^{-1}$), and the separation of the plates is approximately half the diameter of a typical hydrate cation (c.a. 0.2nm). The orientation of counter charges around the IHP gives rise to the Helmholtz double layer capacitance (C_H) in which Eq.2-12 holds true.

$$Q_{IHP-OHP} = C_{IHP-OHP} (\phi_{IHP} - \phi_{OHP}) \quad (\text{Eq.2-12})$$

With the addition of the diffuse layer and the capacitance of dipole rotation (typically the majority of C_H) each capacitance can be measured in series (Eq.2-13). Considering the capacitance of the diffuse layer C_{dl} is produced from Eq.2-14. The influence of $C_{diffuse}$ on C_{dl} is greater in dilute solutions. In general C_{dl} is within the range $5\text{-}50 \mu\text{F cm}^{-2}$ for flat metal surfaces [35].

$$\frac{1}{C_H} = \frac{1}{C_{dipole}} + \frac{1}{C_{IHP-OHP}} = \frac{a_{H2O}}{\epsilon_0 \epsilon_{dipole}} + \frac{a_{ion}}{2 \epsilon_0 \epsilon_{IHP-OHP}} \quad (\text{Eq.2-13})$$

$$\frac{1}{C_{dl}} = \frac{1}{C_H} + \frac{1}{C_{diffuse}} \quad (\text{Eq.2-14})$$

$$C_{diffuse} = \kappa \epsilon_0 \epsilon_r \quad (\text{Eq.2-15})$$

a_{H2O} and a_{ion} is the diameter of a water molecule and hydrated ion diameter respectively. The term ϵ_{dipole} and $\epsilon_{IHP-OHP}$ refer to the relative dielectric constant (ϵ_r) of

electrolyte between surface-IHP and between IHP-OHP respectively, typically c.a. 6 and 30 respectively. κ is the bulk solution conductivity (S m^{-1}), for the diffuse layer $\epsilon_r \rightarrow 80$ for H_2O solutions. Adsorption may be weakened or strengthened by changes in potential. For anions van der Waals interact with the electrode. A precursor step to this process would be the stripping of co-ordinating solvent molecules in-between anion and solid surface. As anions are capable of direct electrode contact this gives rise to the inner Helmholtz plane. The potential where the surface charge on the electrode and adsorbed ion charge reaches a minimum (z_{IHP}) is termed the potential of zero charge (E_{pzc}). The corresponding counter charge orientates around the solid and IHP charge in the form of the OHP and diffuse layer and electroneutrality is maintained. At this point $E_{\text{pzc}} = \phi_{\text{IHP}} - \phi_{\text{bulk}}$ reflects the point where the net surface charge on the solid phase and IHP is zero.

For porous electrodes performing no reaction additional capacitance ($C_{\Sigma} > 5\text{--}50 \mu\text{F cm}^{-2}$) can appear in parallel rather than series with C_{dl} and can possess a separate time constant if both placed in parallel with a resistance. For this reason $C_{\Sigma} \neq 0$ at E_{pzc} in Figure 2-6. C_{dl} may be determined from electrochemical impedance spectroscopy, whilst C_{Σ} is simply obtained from linearly ramping dE/dt as in Figure 2-6. In Figure 2-6 the blue line at $E > E_{\text{pzc}}$ represent the relative affinity of anions to the anodic porous electrode surface. At $E < E_{\text{pzc}}$ the opposite relation is seen.

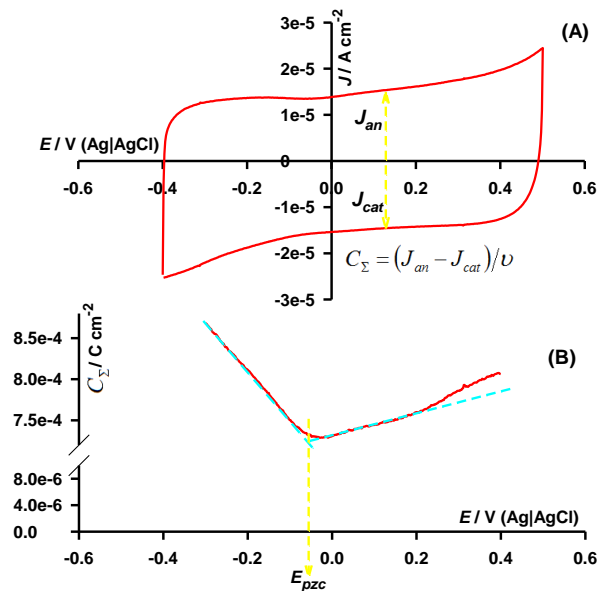


Figure 2-6. Capacitance of a porous electrode in mono-anionic dilute electrolyte in the absence of a faradic reaction. (A) Cyclic Voltammogram and (B) Derivate total capacitance (C_{Σ}) vs E . $u=20\text{mV/s}$.

The total capacitance (DC) of a porous electrode is calculated via Eq.2-16 from cyclic voltammetry.

$$C_{\Sigma} = 0.5(J_{an} - J_{cat})/\nu \quad (\text{Eq.2-16})$$

If an irreversible faradic reaction is present Eq.2-16 does not necessarily hold. If no faradic reaction or redox surface state change occurs then the surface may possess the ability to store charge with perturbation in applied potential, known as differential capacitance (C_{diff}). In mono-anionic solutions adsorbed charge may vary linearly with applied potential (Figure 2-6). The accumulation of surface charge (Q_{ads}) is obtained with the deviation from E_{pzc} . At E_{pzc} the capacitance from this charge should be 0.

$$Q_{ads} = C_{diff}(E - E_{pzc}) \quad (\text{Eq.2-17})$$

The total electrode capacitance C_{Σ} is typically dominated by differential capacitance C_{diff} in the absence of substrate. In the presence of a faradic reaction the large C_{Σ} values attached to porous electrodes can result in large potential dependent capacitances. This means in the presence of the reaction total steady state is not acquired at relatively low imposed potential scan rates (ν).

2.2.4 Relevance of tafel slopes

A tafel slope is the inherent polarisation arising from the process of electrical charge transfer across the double layer via a solvated diffusible reactant/product couple. Two factors must be compensated for accurate $\log_{10}(I)$ vs E values; 1) uncompensated ohmic resistance (R_u) due to potential from RE-WE separation in the field of ionic flow [35], 2) Concentration polarisation.

Tafel slopes can be expressed as the number of reaction steps involving an e^- , H^+ or OH^- that occur before the rate determining step (RDS) [37], as defined in Eq.2-18. Selective single step reactions incur uniform tafel slopes (-120, -60, -40 or -30mV dec^{-1}). However, contributions from steps before RDS [38], multiple pathways, and reaction reversibility can cause a variety of reported tafel slopes for similar reactions.

$$-b_c = 2.303v_jRT/[F(n_c + \beta_c n_j)] \quad (\text{Eq.2-18})$$

Where $-b_c$ is the tafel slope (V dec^{-1}), v_j is the no. of occurrences of the RDS that is required for one complete reaction (typically 1), n_c is the number of electrons transferred before the RDS. β_c is the symmetry factor of the RDS (c.a. 0.5 in precious metal catalysis) [39]. n_j is the number of electrons transferred in the RDS (usually 1 for an charge transfer RDS or 0 for a chemical step RDS) [36]. 2.303 is used as the interger to convert $\ln(I)$ vs E to $\log_{10}(I)$ vs E .

By this token, it is suggested that the improved tafel slopes occur when; the RDS occurs later in the reaction mechanism, the RDS preferably transfers two electrons as opposed to one (unlikely [39]), the RDS is not repeated in the same catalytic turnover (rarely the case). At 20°C this simplifies Eq.2-18 to Eq.2-19.

$$-b_c = 0.058148v_j/(n_c + \beta_c n_j) \quad (\text{Eq.2-19})$$

The symmetry factor ($0 < \beta < 1.0$) is defined as ‘the fraction of the electrical free energy ($G=nFE$) applied to the system which activates the complex,’ or ‘the fraction of overpotential that activates the forward reaction [40].’ Symmetry factor and electron activity co-efficient (α_c) of the RDS are related by Eq.2-20.

$$\alpha_c = n_c + (1 - \beta_c) \quad (\text{Eq.2-20})$$

2.3 Mixed Potential theory

2.3.1 Application to MFC electrodes as cross-over

Cross-over is the diffusion of a reducing agent to the cathode (ie. Formate or S^{2-}), or diffusion of an oxidising agent to the anode (ie. NO_3^- or O_2), thus reducing cell voltage. This is seldom a problem for MFC cathodes. Harnisch et al studies the effect of fermented organics on the *OCP* of Pt and pyrolysed Iron Phthalocyanine cathodes [28]. Platinum displayed poor selectivity for oxygen reduction as seen by a small decrease in *OCP* in the presence of ethanol, lactate and methanol and a large decrease with addition of Sulphide and Formate, indicating significant oxidation. At 1mM S^{2-} and CH_3COO^- decreased *OCP* of 52mV and 72mV respectively. Crucially to this thesis, they

demonstrated that carbon, iron macrocycle and platinum materials are not severely affected by acetate in phosphate buffer (see chapter 3 and 6).

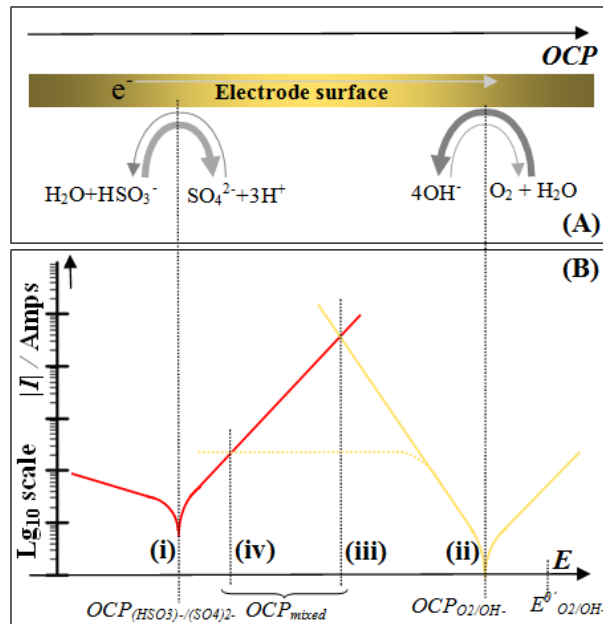


Figure 2-7. Mixed Potential theory for an unpolarised electrode with one cathodic and one anodic reaction occurring on the surface. (A) Relative potentials of either reaction, (B) simplified model of steady state polarisation of electrode in the presence of either O_2 (orange) or SO_3^{2-} (red). OCP in mixed solution when (i) $[O_2]=0$, (ii) $[(SO_3)_2]=0$, (iii) C_{O_2} and $[(SO_3)_2]$ are large, (iv) $[O_2]$ is small. Dotted line implies O_2 diffusion limitation.

An example is shown for a two mixed redox couples sulphite/sulphate ($E^0=0.172V$) and H_2O/O_2 reaction ($E^0=1.223V$) on a metal electrode. A similar situation could arise from organic oxidation on the cathode, such as formate/ CO_2 ($E^{0'}=-0.42V$) and H_2O/O_2 .

MFC anodes may suffer from cross-over of O_2 unless membranes or large electrode separation is used. Cross-over of strong electron acceptors other than O_2 is less of a problem due to their low molarity presence in wastewaters. However, dissolved O_2 may partially impede growth of anaerobic exoelectrogens. Cheng et al [41] found this to be a problem under batch configuration but not continuous flow. Dissolved oxygen concentrations³ of 0.005–0.01 mg/L were detected 2cm away from an air cathode operating a peak power density (P_{max}). This is relevant to the reactor design used in

³ The author calculates that such concentrations at the biofilm surface would reduce oxidation current by only $3.2mA\ m^{-2}$ in stagnant electrolyte. Based on 9.2mg/L equating to $3A\ m^{-2}$ limit at the cathode.

chapter 7, as air cathodes consume less O₂ than permitted to diffuse through to the electrolyte.

2.4 Oxygen and H₂O₂ and H₂O/OH⁻

2.4.1 Oxygen adsorption and reduction pathways

The basis of oxygen reduction catalysis is reduction in the strength of the O=O bond after adsorption onto a surface. Oxygen adsorption primarily occurs via Langmuir (isolated homogenous adsorption site), freundlich (inhomogeneous surface with distributed adsorption energies) or Temkin (adjacent inter-site interaction) isotherms describing surface coverage. The Langmuir model is described by Eq.2-21. The Langmuir isotherm accounts for a consistent adsorption site. The Temkin isotherm describes a situation where adsorption sites are located closely to one another (eg. Pt surface) and adsorption energies are affected by the occupancy of the adjacent site. The free energy change of adsorption ΔG_{ads} applies as Eq.2-22.

$$\Gamma = \frac{\Gamma_{max} K_{ads}[O]}{1 + K_{ads}[O]} \quad (\text{Eq.2-21})$$

$$\Delta G_{ads} = -RT \ln[K_{ads}] \quad (\text{Eq.2-22})$$

$$\theta = [O]_{surf} / [A] \quad (\text{Eq.2-23})$$

Where Γ is the actual surface coverage (in this instance Mole g⁻¹ site) and Γ_{max} is the maximum surface coverage (Mole g⁻¹ site) where species O is present in excess. The partial surface coverage then becomes Eq.2-23 in the case of Langmuir adsorption, where in a film or layer capable of adsorption of O the terms [O]_{surf} and [A] are the surface concentrations of adsorbed substrate and bare adsorption site (mole cm⁻³) respectively. In reality O₂ will not be the only molecule capable of adsorption. Many electrocatalysts are ionophores and the site may be partially occupied by ions or intermediaries from a reaction involving O₂.

Figure 2-8 describes the various pathways of electro-reduction of oxygen to water, from the reaction starting point (O_{2(bulk)}) to the desired end-point (OH_(cl)). The mechanism is not specific to a single catalyst and intermediate oxygen forms vary according to pH. 4e⁻ reduction is preferable to 2e⁻ reduction path, releasing almost twice the free energy [32]. k_l selective catalysts that either avoid k_{2f} or avoid H₂O₂ desorption k_{df} are preferable for

cathode energy efficiency. k_2 is less problematic, but in neutral media the bond between H_2O_2 and surface is weaker than that in alkali (HO_2^-) and has a tendency to desorb. The scheme considers a single electro-catalyst, though k_5 , k_7 and k_8 all describe H_2O_2 decomposition away from the original site of generation. In the light, the latter two may be indistinguishable from k_5 . Via a single electrocatalyst ($k_{D,O_2} \rightarrow k_{\delta C} \rightarrow k_1$ or $k_2 \rightarrow k_3$ or $k_2 \rightarrow k_{6f}$). Cleavage of the first O_2 double bond results in a peroxo intermediary with both the k_1 and k_2 pathways, the difference being that the peroxo species in k_1 is incapable of desorption. All heterogeneous rate constants refer to Figure 2-8.

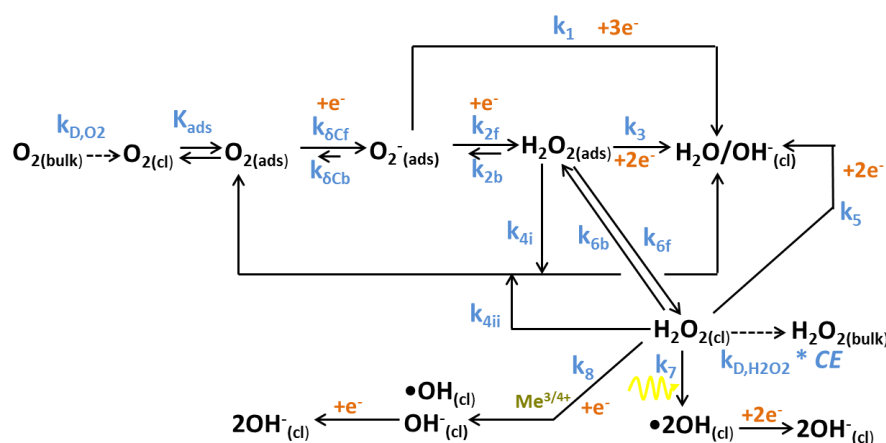


Figure 2-8. Oxygen reduction pathways of surface adsorbed O_2 in a catalyst layer. Electron transfer steps in orange, photocatalytic steps in yellow, rate constants in blue. Substrates such as H_2O or H^+ not included, catalyst (or co-catalyst) in brown. Key; Catalyst Layer (cl), Bulk Electrolyte (bulk), Adsorbed species (ads).

According to Appleby et al [42], all of the rate constants are a function of potential with the exception of chemical disproportionation steps (k_{4ii} and perhaps k_{4i}). The overall apparent rate constant (k_{app}) should be similar to the rate-constant of the Rate Determining Step (RDS). The dominant pathway of ORR is heavily influenced by the initial orientation of O_2 adsorption [32, 36].

‘Side on’ adsorption results in H_2O product whilst an ‘End on’ produces H_2O_2 unless present as a bridge adsorption between two sites and resulting in H_2O [32]. Deposition of organic catalyst multilayers between graphite sheets may allow bridge adsorption, see Figure 2-9 with co-facial and monolayer configurations of the organic catalyst FePc.

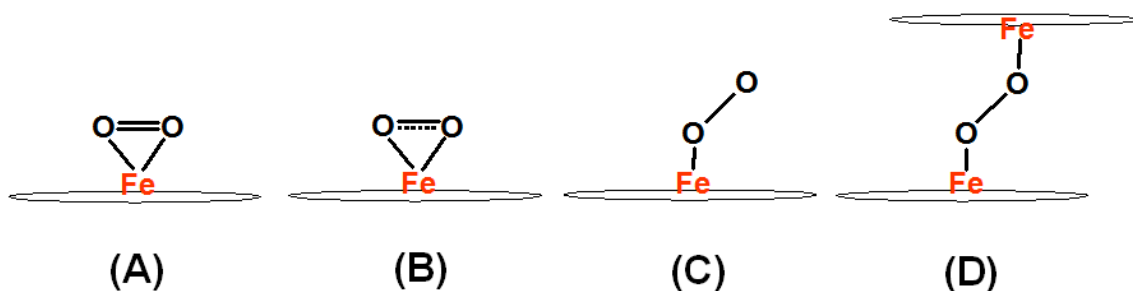
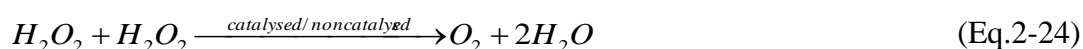


Figure 2-9. Initial oxygen adsorption orientations onto an Iron Phthalocyanine catalyst nucleus (a) and (b) side-on, (c) end on or (d) bridge. Adapted from [32]. Iron is displaced from the macrocycle plane with bound O_2

In bridge mechanism catalysis the Me-Me separation is of critical importance. In noble metal catalysis, ORR occurs via a bridge like mechanism, each oxygen bonds to adjacent metal atoms. Me-Me distance strongly influences activity so nano-particle geometry and crystal phase become important. The same is true of macrocycle catalysis (section 3.3) where Me-Me atomic distance is controlled by separation between layers in a polymeric film. Following deposition from a solvent the Me-Me separation is a fixed distance, dictated by π -bond overlap on FePc benzene atoms.

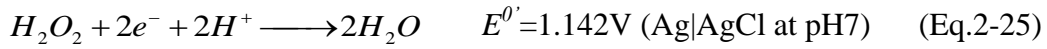
2.4.2 Methods of peroxide destruction

Peroxide is capable of self-oxidation in the solution phase (Eq.2-24) also known as disproportionation, k_{4ii} . This reaction is catalysed by trace metal contaminants (including ions) and is only inert in Pyrex, Quartz, some Plastics and Aluminium [43]. Decomposition occurs on graphite and is very quick on a noble metal surface [43], regenerating to chemisorbed O_2 , for this reason k_{4i} is included where absent in most schemes [44]. Where it is difficult to separate k_{4i} and k_{4ii} they are amalgamated, $k_{4i}+k_{4ii}=k_4$. The rate of k_{4ii} increases with T and solvated O_2 concentration. This is generally not a potential dependent process as no exogenous electrons are involved (Figure 2-8, rate k_{4ii}), though some materials perform improved disproportionation in either an oxidised or reduced form.



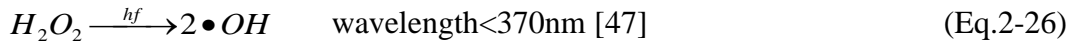
Critically to the scope of this thesis, H_2O_2 decomposition is not catalysed by Na^+ or Phosphate [45], indeed Phosphate ions partially stabilise H_2O_2 .

Another mechanism of removal of produced H_2O_2 is **electro-reduction** in an aqueous media (Eq.2-25) in the presence of a solid surface (k_3).



Eq.2-25 shows irreversible behaviour [35] and shifts by $|b_c| = 59\text{mV pH}^{-1}$. H_2O_2 is a strong electron acceptor with a short half-life in a catalyst layer. The ramifications for RRDE study are that a portion of $4e^-$ reduction is consecutive $2e^-$ to H_2O_2 followed by $2e^-$ to H_2O . Reducing H_2O_2 residence time in catalyst films by using thin films reduces the amount of subsequent peroxide reduction, making pathway determination less problematic.

Photo-homolysis (k_7) is typically the least significant pathway and is important in photocatalysis. Produced $\bullet OH$ would damage MFC components due to the strong oxidising capabilities of $\bullet OH$; $E^{0'} = 2.19V$ Ag|AgCl at pH7. $\bullet OH$ has a typical half-life of only 0.1-0.5 μs [46].



Chemical oxidation of organics may decrease H_2O_2 detection and affect the concentration of organics in wastewater and artificial wastewater electrolyte, particularly when a carbon cathode is employed.

2.4.3 Transients and the Cottrell equation in unstirred solution

In an unstirred solution, a model for the diffusion layer is seen in Figure 2-10. The flux of material to the surface, J_{flux} ($\text{Mol cm}^{-2} \text{ s}^{-1}$) is described by Fickian diffusion (Eq.2-27). As the scan proceeds from E_{ORR} in a cathodic direction, a concentration gradient increases as the surface concentration (C_s) tends to zero at E_p . At this point the Nernst diffusion layer thickness (δ) is still increasing by Eq.2-28 as reactant is depleted at the disc surface via concentration gradient in Eq.2-27. Transient decay is predicted in the absence of convection, natural or forced, this is never the case in real systems where natural convection produces only finite transient decay, producing J_L [48-51]. This results in the current decreases at potentials more negative than E_p (reduction).

$$J_{flux} = D(C_0 - C_s)/\delta \quad (\text{Eq.2-27})$$

$$\delta = (\pi Dt)^{1/2} \quad (\text{Eq.2-28})$$

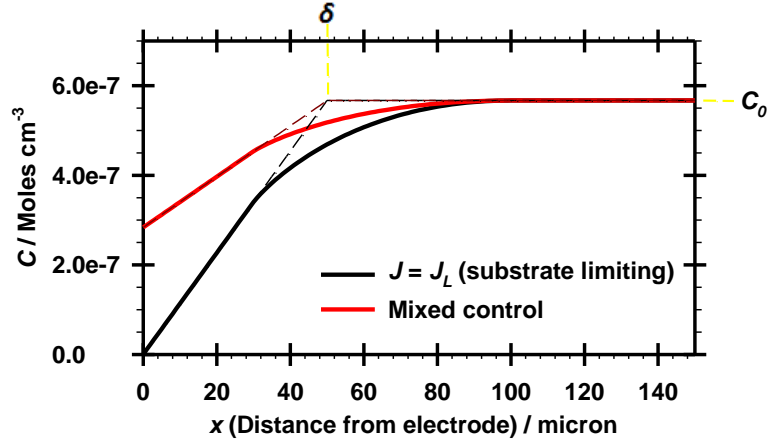


Figure 2-10. Example concentration profile for reactant depletion at the electrode surface($x=0$), creating Nernst Diffusion Layer. Two different electrode potentials, case of diffusion limited current (black) and mixed kinetic, diffusion control.

For a porous electrode C_s could be considered the inner portion of the film/solution interface. With small cathodic polarisation C_s does not decrease to 0 provided transport is sufficiently quick. The presence of natural convection assures that i_L and a steady δ are obtained. In a cathodic LSV sweep with and without dissolved oxygen (Figure 2-11) a peak is observed (J_p).

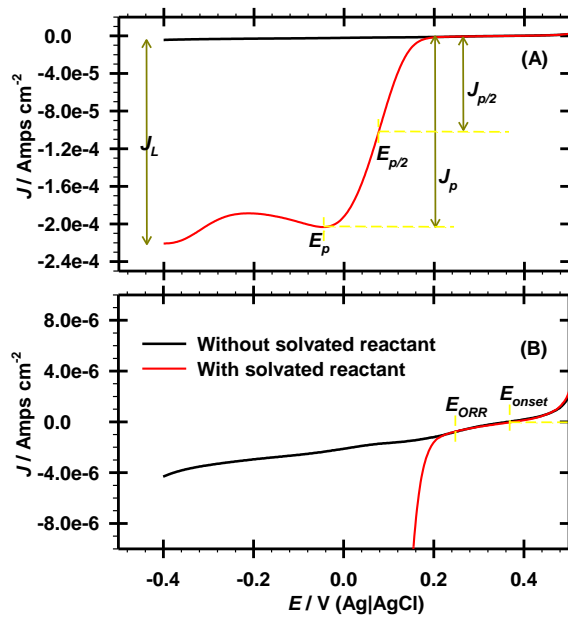


Figure 2-11. i - E response of a strongly adsorbed metal based electrocatalyst in the presence (red) or absence (black) of dissolved reactant. Example is for chelated $\text{Fe}^{2+}/\text{Fe}^{3+}$ redox flat film with competitive electrocatalyst adsorption between reactant and anion. Features used in analysis are annotated in (A) the raw data, and (B) enlargement of Y-axis. $\nu=5\text{mV/s}$.

For a totally irreversible $1e^-$ reduction reaction the wave possesses the following attributes [35]...

Cathodic

$$|E_p - E_{p/2}| = 1.857RT/\alpha F \quad (\text{Eq.2-29})$$

$$\frac{\partial E_p}{\partial \nu} = \frac{1.15RT}{\alpha F} = 0.03/\alpha (298^\circ K) \quad (\text{Eq.2-30})$$

In the more useful case of multi-electron transfer, provided the RDS is a single $1e^-$ heterogeneous transfer as the 1st step, the above equations can be used. Equations describing peak current must be multiplied by ' n ' in this case. Hence the result of Eq.2-34 changes for this case.

In Figure 2-11(A), J_L describes the ORR limiting current at $E=-0.4\text{V}$ in the case where an anion adsorption blocks the reaction site for ORR, but surface coverage of anion X ($\theta_{\text{FePc-X-}}$) decreases as the scan moves in a cathodic direction. The ORR diffusion limiting current (J_L) is strongly potential dependent. Without this effect, $J_L=J_p$ in stirred

solution approaching steady state (low v) and a J_L plateau is seen provided n is constant. It cannot be ascertained from extrapolation of a linear i - E response in the diffusion limiting region [52].

For unstirred solutions the Cottrell equation (Eq.2-34) is obtained from Laplace transform of the relationship between flux to surface and current (Eq.2-35). A derivation is found in section 10.1.2. A maximum occurs in k_D when $C_s=0$ and $C_0-C_s=ca$. C_0 . Though this is a function of applied potential if substrate is being converted upon contact with the disc at the maximum rate, Eq.2-31 holds if the reverse reaction is negligible, as is usually the case at i_L .

$$i_L = nFAk_D C_0 \quad (\text{Eq.2-31})$$

$$\frac{i}{nFA} = k_D [C_0 - C_s(x=0)] \quad (\text{Eq.2-32})$$

$$C_s(x=0) = \frac{i_L - i}{nFAk_D} \quad (\text{Eq.2-33})$$

Where k_D is the planar mass transfer co-efficient (cm s^{-1}). Eq.2-32 describes the volume flow of reactant per unit area per second. Using Eq.2-31 and substituting into Eq.2-31 produces Eq.2-33. It is shown that the concentration of the electroactive species is linearly related to the current, with $C_s \rightarrow 0 \text{ Mole cm}^{-3}$ when $i \rightarrow i_L$.

In substrate-less redox electrocatalyst electrodes the diffusion of electrons can be obtained from the gradient of i vs $t^{-0.5}$ which is linear for Fickian diffusion [53]. The charging current (i_{dl}) decays according to..

$$J(t) = \frac{nFD^{0.5}C_0}{\pi^{0.5}t^{0.5}} \quad (\text{Eq.2-34})$$

$$-J_{flux}(0,t) = \frac{i(t)}{nFA} = D \left[\frac{\partial C_0(x,t)}{\partial x} \right]_{x=0} \quad (\text{Eq.2-35})$$

In which π is the number pi, t is the time after the potential step (secs)

2.4.4 Randles-Ševčík analysis of unstirred solutions

As a result of the transient behaviour described at substrate depletion at the surface the Randles-Ševčík equation can be used to predict the peak current density in the presence of an increasing diffusion layer thickness in stationary electrolytes over time.

$$J_p = -0.496\sqrt{(n_c + \alpha_{n'})}nFC_0\sqrt{\frac{FvD}{RT}} \quad (\text{Eq.2-36})$$

$$\sqrt{(n_c + \alpha_{n'})} = J_p / \left(-0.496nFC_0\sqrt{\frac{FvD}{RT}} \right) \quad (\text{Eq.2-37})$$

$$D = RT \left[J_p / -0.496nFC_0\sqrt{(n_c + \alpha_{n'})} \right]^2 / Fv \quad (\text{Eq.2-38})$$

$$\frac{\partial \ln(i)}{\partial E} = \frac{(n_c + \alpha_{n'})F}{RT} \quad (\text{Eq.2-39})$$

The transposability factor between $d\ln(i)/dE$ and $d\log_{10}(i)/dE$ is a factor of $e=2.303$.

2.5 Methods of substrate diffusion control and peroxide detection

2.5.1 Methods of peroxide detection – RDE and RRDE

The Rotating Ring Disk Electrode (RRDE), Figure 2-12, is used to study ORR in aqueous or aprotic media. The RRDE allows quantification of substrate mass transport by disc rotation to force laminar convective flow. The axially rotating electrode assembly consists of a disc embedded into an insulating material. Around the disc is a concentric ring, allowing electrochemical detection of disc products. Electrical contact is made with between rotor and RRDE stator assembly through a conductive brush.

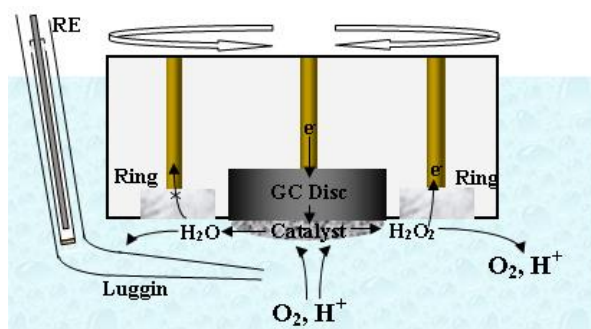


Figure 2-12. (B) Schematic of a Rotating Ring Disc Electrode (RRDE) tip for the evaluation of quantitative $2/4e^-$ electro-reduction of dissolved O_2

Hydrodynamic forces under a steady state produce a consistent velocity profile. At this stage the mass transfer can be explained in terms of cylindrical co-ordinates, velocity profiles in each dimension (x , y and ϕ) and the limiting conditions applied. Laminar flow velocities are divided into three dimensions (v_x , v_y and v_ϕ), which are expanded by hydrodynamic theory in section 10.1.3.

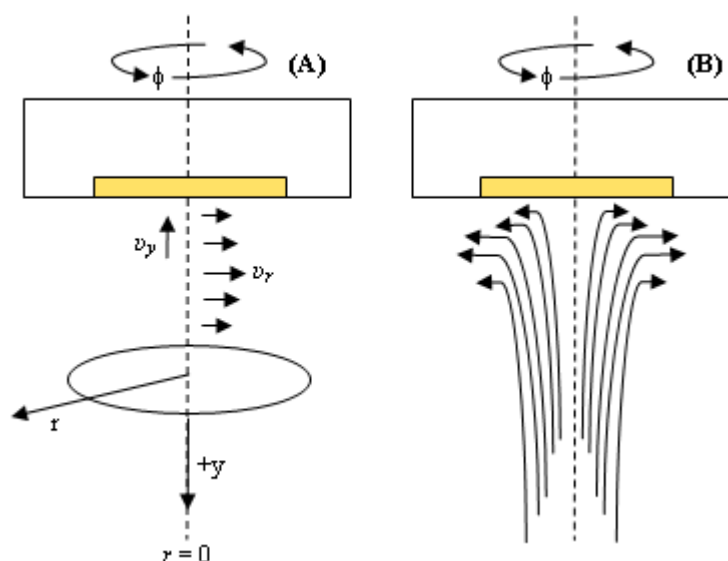


Figure 2-13. Model of (B) laminar flow regime and (A) co-ordinates approaching disc reaction site in axially rotated electrode.

With axial rotation a linear flow profile is produced (section 10.1.3). The fluid is dragged across the surface of the disc. Other substrates/products leave or enter the reaction site at rates influenced by rotation speed (Figure 2-12). The following conditions should exist;

(a) laminar flow, bearing solvated substrate towards a rotating reaction surface at fixed concentration

- (b) flow perpendicular to axis of rotation and
- (c) a first order reaction.

A similar equation to Eq.2-31 is valid even if only natural convection is present towards a stationary horizontal plate [51]. k_D is consistent with A provided A is large enough that only planar diffusion occurs, i.e. via $v_y > 0$ and $v_r \approx 0$, or $v_y \gg v_r$.

2.4.2. Levich Equation

Diffusion limiting current density (J_L) is a function of δ . As such in porous electrodes J_L lacks comparability between studies. Under steady state, the diffusion layer model is described by equation the Levich equation, which only applies to totally mass-transfer limited condition ($|\eta| \gg 0V$). The Levich equation derivation in the appendix (section 10.1.3.) is placed under the limiting condition of current $i = i_L$ and using Eq.A-30 and Eq.A-31 we obtain the Levich equation, Eq.2-40.

$$|J_L| = 0.62nFD^{2/3}\tilde{\omega}^{0.5}\nu^{-1/6}C_0 \quad (\text{Eq.2-40})$$

Where D is the diffusion co-efficient of electroactive species ($\text{cm}^2 \text{s}^{-1}$), ν is the kinematic viscosity of the electrolyte ($\text{cm}^2 \text{s}^{-1}$), $\tilde{\omega}$ is the radial velocity of the electrode (rad s^{-1}) and C_0 =Bulk Concentration of electroactive species (moles cm^{-3}). For diffusion to a planar electrode at steady state Eq.2-41 applies with substitution for $k_D = D/\delta$.

$$i_L = nFAk_D C_0 = nFA\left(\frac{D}{\delta}\right)C_0 \quad (\text{Eq.2-41})$$

Substituting Eq.2-41 into the Levich equation, the terms D/δ becomes equivalent to \tilde{m} producing Eq.2-42.

$$k_D = \frac{D}{\delta} = 0.62D^{2/3}\tilde{\omega}^{0.5}\nu^{-1/6} \quad (\text{Eq.2-42})$$

Re-arranging in terms of diffusion layer thickness (δ) produces Eq.2-43.

$$\delta = 1.61D^{1/3}\nu^{1/6}\tilde{\omega}^{-0.5} \quad (\text{Eq.2-43})$$

This equation has since been improved upon by correction for situations of large Schmidt numbers [54], where the fluid is viscous or migrating ions/substrate are physically large molecules. This impacts the original derivation of Levich [55], by a small amount, around 3% change in $i_{D,L}$ for $Sc=1000$.

Physical constants for O₂ saturated PBS at 20°C, are located see appendix Table A-2. Eq.2-43 shows that δ is proportional to $\omega^{-1/2}$. In addition to transition of the diffusion layer an additional concentration impedance can be resented from a non-electrocatalytic active coating of the film (J_{film}). This ionomer coating prevents obtaining δ from multiplying J_L by N_{ORR} , which can be isolated with a Koutecký-Levich (K-L) plot.

An example Levich plot (i vs $\omega^{0.5}$) are displayed in Figure 2-14. This case shows a transition between diffusion control and kinetic control in a solution containing one half of a redox couple.

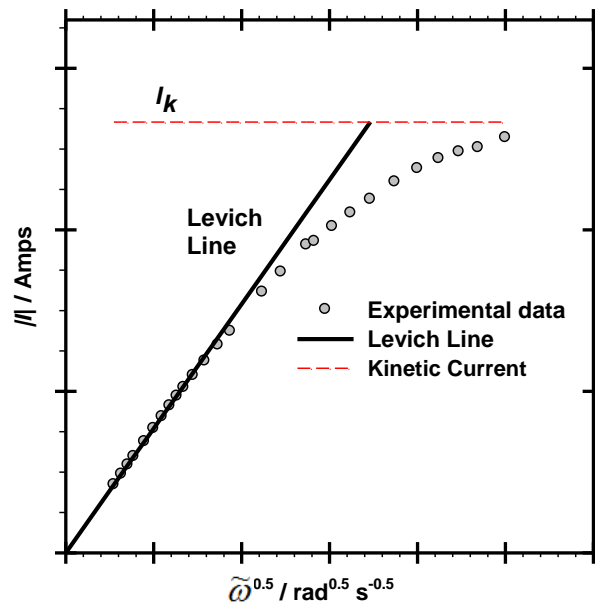


Figure 2-14. Example Levich plot of transition between kinetic and diffusion control at constant potential for dissolved substrate

The Levich gradient observes Eq.2-40 when the reaction is purely mass transfer limited.

2.4.3. Koutecký-Levich (K-L) Equation and kinetic current

Considering a totally irreversible reaction the Eq.2-44 and Eq.2-45 are valid from a change in integration limits of Eq.A-29, producing Eq.2-46.

$$i = F A k_f(E) C(y=0) \quad (\text{Eq.2-44})$$

$$k_f(E) = k^0 \exp\left[-(E - E^0) \alpha F / RT\right] \quad (\text{Eq.2-45})$$

$$C_0 - C(y=0) = \left(\frac{\partial C}{\partial y}\right)_{y=0} \int_0^\infty \exp\left(\frac{-y^3}{3B}\right) dy \quad (\text{Eq.2-46})$$

Where i is the measured current (Amps), k_f is the heterogeneous rate constant of the forward reaction (cm s^{-1}). Writing Eq.2-46 is written in terms of δ as defined by Eq.2-43 to yield Eq.2-47.

$$i = \frac{n F A D [C_0 - C(y=0)]}{\delta} = n F A k_D [C_0 - C(y=0)] \quad (\text{Eq.2-47})$$

Whilst from Eq.2-40..

$$i = i_{L,c} \left[\frac{C_0 - C(y=0)}{C_0} \right] \quad (\text{Eq.2-48})$$

Where $i_{L,c}$ is the limiting current in one direction (cathodic). Combining Eq.2-48, Eq.2-47 and Eq.2-44 produces Eq.2-49.

$$i = F A k_f(E) C_0 \left(1 - \frac{i}{i_{L,c}} \right) \quad (\text{Eq.2-49})$$

As a portion of equation represents the forward component of the reaction based on the heterogeneous rate constant, it can be expressed as a kinetic current.

$$i_k = F A k_f(E) C_0 \quad (\text{Eq.2-50})$$

Applying for multi-electron transfer, inclusion of “ n ” produces the Koutecký-Levich plot, with the terms from Eq.2-40 incorporated for the full equation. At diffusion

limitation the reverse reaction is negligible and $k_{app}=k_f$. Eq.2-51 is expressed as a linear function at axial rotations speeds where...

$$\frac{1}{i} = \frac{1}{i_k} + \frac{1}{i_{L,c}} = \left[\frac{1}{0.62nFAD^{2/3}v^{-1/6}C_{0,Ox}} \right] \frac{1}{\sqrt{\omega}} + \frac{1}{nFAk_{app}C_{0,Ox}} \quad (\text{Eq.2-51})$$

$$y = [m] * x + [C]$$

The most accurate extrapolation of a linear equation least squares fit is applied to the low rotation speed data as a linear equation $y=mx+c$ [33] as in Eq.2-51. For this equation to be universally applicable the reaction must occur at the solution/film interface. In terms of kinetic current density Eq.2-52 is in the form..

$$J_k = J / [1 - (J / J_L)] \quad (\text{Eq.2-52})$$

Figure 2-15 depicts a K-L plot in the case of electrocatalysis at a poised potential where high rotation speeds cause kinetic limitation (zero order) and low rotation cause mass transfer limitation (1st order).

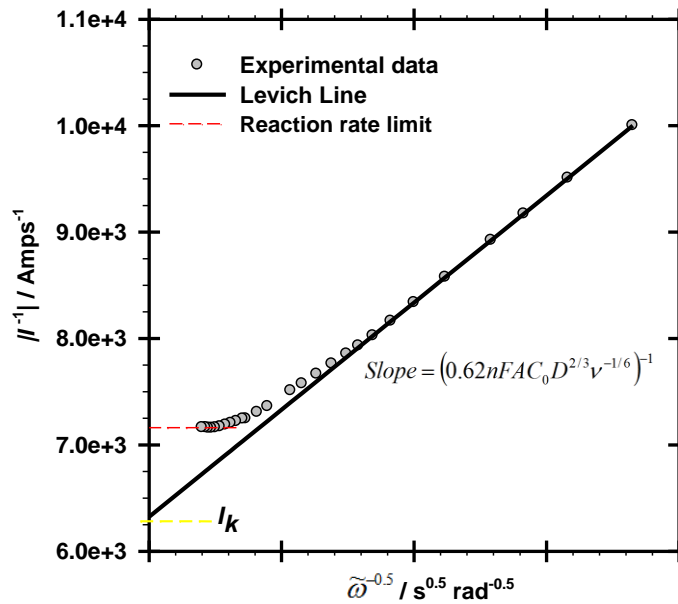


Figure 2-15. Example K-L plot of transition between kinetic and diffusion control at constant potential. Slope is typical of ORR in aqueous media, $n=4$, $A=0.24718\text{cm}^2$, $C_0=5.67 \times 10^{-7} \text{M cm}^{-3}$

The i^{-1} vs $\omega^{-0.5}$ plot is predicted to have a zero gradient at infinitely high rotation speeds in the case of a transition to total kinetic control. The true kinetic current (i_k) describes a

situation where mass transfer effects are absent. In other words, if reactant concentration in the vicinity of the reaction site is identical to that in bulk solution ($C=C_0$).

Extrapolation from the K-L plot is typically used to obtain i_K as in Figure 2-15. In certain limiting cases experimental data may deviate from the slope if a non electrochemical reaction limits electron transfer at high current [56]. In the case where the electrode surface is covered with a redox active electrocatalyst of loading $\tilde{\Gamma}$ (moles cm^{-2}) the relationship between i_k and the heterogeneous rate constant is described in Eq.2-53 [57].

$$i_k = nFkC_{a,O_2}\tilde{\Gamma}_{\text{Electrocatalyst}} \quad (\text{Eq.2-53})$$

To obtain n from K-L slopes, accurate estimations of viscosity and substrate diffusivity are required. Use of the RRDE with ultra-thin films allows intermediate detection prior to further decomposition in a thick film. In the case of ORR, the transfer co-efficient, K_{app} ($\text{cm}^3 \text{M}^{-1} \text{s}^{-1}$), relative to the no. of redox electrocatalyst active sites, is shown by Eq.2-54.

$$K_{app} = J_K / 4F\tilde{\Gamma}_{\text{electrocatalyst}}[O_2]_{\text{bulk}} \quad (\text{Eq.2-54})$$

The electro-active redox catalyst loading $\tilde{\Gamma}$ should be used as opposed to calculated loading Γ , as only the catalyst involved in the reaction should be considered.

In situations where electrode is modified with an inert non redox active film (no reaction) through which reactant must diffuse an additional term can be substituted into Eq.2-51[58]...

$$\frac{1}{i} = \frac{1}{i_k} + \frac{1}{i_{L,c}} + \frac{\delta_{\text{coating}}}{nFC_{\text{coating},Ox}D_{\text{coating},Ox}} \quad (\text{Eq.2-55})$$

Where δ_{coating} is the thickness of the inert coating, $C_{\text{coating},Ox}$ is the concentration of reactant (ie. O_2) in the inert coating (Moles cm^{-3}), and $D_{\text{coating},Ox}$ is the diffusion co-efficient of reactant in the inert coating ($\text{cm}^2 \text{s}^{-1}$). Should a reaction occur throughout the film and the position of reaction shift from the disc surface with potential a set of

criteria are present to determine i_k [59, 60]. For applicability of this criteria the film must be uniform and has not been applied to redox polymers coating carbon in porous electrodes. This criteria has not been applied in this thesis.

2.4.4. 2/4 e^- ratio calculation

Disc currents and disc mass transfer limited ring currents are separated into data sets grouped by the same applied disc potential (E). The sets are plotted as a function of rotation frequency (ω) to yield a mass balance on the RRDE tip. For the %H₂O₂ vs. E data, the proportional H₂O₂ production was assessed by Eq.2-56. i_{ORR} ($i_{O_2}-i_{N_2}$) has been used instead of i_D to remove non-faradic process currents.

$$X_{H_2O_2} = ((i_R - i_{R-BG})/CE)/(i_{D,[O_2]} - i_{D,[N_2]}) \quad (\text{Eq.2-56})$$

$$N_{ORR} = 4 - [X_{H_2O_2} * 2] \quad (\text{Eq.2-57})$$

Where $X_{H_2O_2}$ is no. of moles of H₂O₂ released from the catalyst layer per mole of O₂ electrochemically reduced, $i_{D,[O_2]}$ is the disc current obtained in O₂ at a specified potential, $i_{D,[N_2]}$ is the disc current obtained in N₂ at a specified potential, i_R is recorded ring current, i_{R-BG} is the ring background current recorded at the point during LSV immediately before detecting increased H₂O₂ oxidation. i_{R-BG} was habitually specified as 10nA lower than the lowest ring current recorded for each LSV (see appendix Figure A-9). Briefly, ring current was processed by removing mainly currents from H₂O oxidation and PtO formation (Eq.2-58). The remaining current arises from H₂O₂ oxidation.

$$i_R - i_{R-BG} = i_R - i_{dl} - i_{O_2, ev} - i_{Pt \rightarrow PtO} \quad (\text{Eq.2-58})$$

Where $i_{O_2, ev}$ is H₂O/OH⁻ oxidation current (A), i_{dl} is the double layer current (A), $i_{Pt \rightarrow PtO}$ is the PtO formation current after anodic polarisation is stopped.

2.4.5. Wroblowa analysis for distinction of k_1 from $k_2 \rightarrow k_3$

In oxygen reduction, k_1 passes the same current as $k_2 \rightarrow k_3$ (4e⁻). This poses an interesting experimental problem of how to differentiate between the two. If the k_2 intermediary is

capable of desorption then residence time becomes a function of electrode rotation. Therefore analysis of the %H₂O₂ vs E type plot at single rotation speed is insufficient to determine whether k_1 or $k_2 \rightarrow k_3$ is the dominant mechanism. Should an equilibrium adsorption of H₂O₂ on the surface of the electrocatalyst occur, then a lack of electrode rotation would cause a situation where it accumulates in the catalyst layer, potentially damaging the membrane.

A common analysis for mechanistic determination in Oxygen Reduction is the treatment originally derived by Wroblowa et al [61]. The guidelines are set out by Wroblowa et al [61] have been applied in neutral medium [62], tabulated as a simple summary by Hsueh et al [44] and then modified to include disproportionation effect on $i_{D,L}$ in porous electrodes in Appleby et al [42] with the addition of τ for O₂ recycled from disproportionation ($1 < \tau < 2$). Appleby's derivation makes consideration of H₂O₂ that is reduced elsewhere from the main electrocatalyst site (ie. carbon or trace metal or non-adsorbed reduction). This analysis is frequently applied to porous films [63-66], due to the consideration of the term k_4 , an attribute with strong dependence on film thickness and residence time from rotation.

The data is able to offer mechanistic information even when the disc current is not limited by rotation ($|i| < |i_{L,c}|$) [63, 67], occasionally being able to determine k_1 , k_2 and k_3 over the entire potential range [44]. In most instances k_1/k_2 ratios are obtained for the most active ORR mechanism for redox polymer electrocatalyst films [67].

Wroblowa derivation

In Wroblowa's paper k_6 , k_5 and diff are referred to as k_{6b} , k_{6f} and k_{D,H_2O_2} respectively for comparability with Appleby's study. Considering the electrocatalyst to contain an adsorbed portion of H₂O₂ C_{a,H_2O_2} in equilibrium with the concentration at the IHP or catalyst layer (C_{cl,H_2O_2}) whereby a portion is lost to the bulk C_{0,H_2O_2} and another portion oxidised by the ring. The situation where i_D is controlled by desorption or reduction of H₂O₂ can be examined. Applied in its entirety, this criteria can identify situations where the overall reaction rate (k_{app}) is controlled by k_1 , k_2 , k_3 or k_6 . At steady state..

A mass balance on C_{a,H_2O_2} under $i_{D,L} \dots$

$$k_2 C_{cl,O_2} = (-k_{2b} + k_3 + k_4 + k_{6f}) C_{a,H_2O_2} - k_{6b} C_{cl,H_2O_2} \quad (\text{Eq.2-59})$$

A mass balance on C_{a,H_2O_2} under $i_K \dots$

$$k_2 C_{a,O_2} = (-k_{2b} + k_3 + k_4 + k_{6f}) C_{a,H_2O_2} - k_{6b} C_{cl,H_2O_2} \quad (\text{Eq.2-60})$$

A mass balance on C_{cl,H_2O_2} under any condition...

$$k_{6f} C_{a,H_2O_2} - k_{6b} C_{cl,H_2O_2} = Z \omega^{0.5} C_{cl,H_2O_2} \quad (\text{Eq.2-61})$$

Where Z is the value obtained from the Levich Eq.2-40, though the H_2O_2 flow is now tangential to the disc surface...

$$Z = 0.62 D^{2/3} \nu^{-1/6} \quad (\text{Eq.2-62})$$

Note that the 0.62 value assumes laminar flow from disc to ring and is an approximation which does not account for the change in Schwartz number for dealing with solvated H_2O_2 . Very accurate determination of O_2 and H_2O_2 transport are required, otherwise, the diagnostic graph can shift left or right and yield inaccurate S or C values, which cause a misdiagnosis of the mechanism. Disc and ring currents are..

The current i_D under $i_{D,L} \dots$

$$i_D = 2AF [(2k_1 + k_2) C_{cl,O_2} + (k_3 - k_{2b}) C_{a,H_2O_2}] \quad (\text{Eq.2-63})$$

The current i_D under $i_K \dots$

$$i_D = 2AF [(2k_1 + k_2) C_{a,O_2} + (k_3 - k_{2b}) C_{a,H_2O_2}] \quad (\text{Eq.2-64})$$

i_R under any condition..

$$i_R = 2AF (CE) Z \omega^{0.5} C_{a,H_2O_2} \quad (\text{Eq.2-65})$$

It is clear that the disc current does not need to be under O_2 diffusion limitation for this analysis to be valid, though i_R must be under diffusion limitation of H_2O_2 from the disc. The ring potential must be selected accordingly to oxidise the amount of H_2O_2 passing over the surface (see appendix section 10.5.3.).

Making concentrations the subject, the following equations resolve to describe the condition at $i_{D,L}$; Eq.2-59, Eq.2-63, Eq.2-65 and Eq.2-61. Under the disc condition i_k Eq.2-60, Eq.2-64, Eq.2-65 and Eq.2-61. Irrespective of whether the situation is totally kinetically controlled or totally controlled both sets of equations combine to produce...

$$i_D/i_R = (1/N) \left[1 + 2k_1/k_2 + A + (k_{6b}/Z\omega^{0.5})A \right] \quad (\text{Eq.2-66})$$

$$\text{Where } A = (2k_1/k_2k_{6f})(k_{2b} + k_3 + k_4) + (2k_3 + k_4)/k_{6f} \quad (\text{Eq.2-67})$$

Making...

$$\frac{S}{J} = \frac{k_{6b}A}{Z(1 + A + 2k_1/k_2)} \quad (\text{Eq.2-68})$$

Substituting $k_I=0$ into Eq.2-66 reduces the equation to...

$$i_D/i_R = (1/N) \left[1 + (2k_3/k_4)/k_{6f} + (k_6/Z\omega^{0.5})(2k_3 + k_4)/k_{6f} \right] \quad (\text{Eq.2-69})$$

In this case the slope (S) and intercept (J) of this linear function show...

$$J = 1 + (Z/k_{6f})S \quad (\text{Eq.2-70})$$

For a linear portion of the $S J^{-1}$ plot of $\underline{k_I \neq 0}$ but $S J^{-1}$ is linear k_I and k_2 must have the same potential dependence. The intercept of the $S J^{-1}$ graph extrapolates to J' . If the $S J^{-1}$ graph is not linear then no easy conclusion can be drawn. If the graph is linear a trendline can be applied, reducing the situation to ...

$$J' = 1 + 2k_1/k_2 \quad (\text{Eq.2-71})$$

This criterion predicts a good fit of the data at high and low potential. At intermediate potential neither Eq.2-64 or Eq.2-63 applies as both as $i_D=f(C_{cl,O_2}, C_{a,O_2})$. The terms do not cancel out in this instance. Data may take the form of a minimum in R^2 of the i_D/i_R vs $\tilde{\omega}^{-0.5}$ plot at intermediate potentials, for example Figure 2-16. From an engineering

perspective, the low overpotential reaction is of most interest, for cell components susceptible to the prospect of H₂O₂ release.

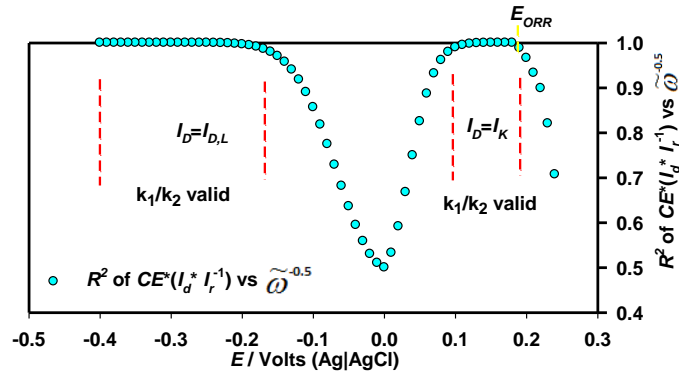


Figure 2-16. Validity of slope and intercept data CE^*i_D/i_R vs $\tilde{\omega}^{-0.5}$ as a function of potential. Expressed an example trend in R^2 as $f(E)$

Appleby derivation

An alternate method may find importance when considering O₂ diffusion limited current ($i_{D,L}$). The method derived by Appleby [42] examines H₂O₂ disproportionation to regenerate O₂ in the catalyst layer via k_4 . The additional current under $i_{D,L}$ is now considered. In addition Appleby considers H₂O₂ reduction at a site outside the initial reaction zone, k_5 . In this thesis the initial reaction zone is FePc. Carbon modification [66] or trace metals [68] remaining from pyrolysis or doping may perform k_5 . The mathematical treatment followed five similar steps to Wroblowa's criteria..

- 1) Perform mass balance on unadsorbed H₂O₂ in the catalyst layer, C_{cl,H_2O_2} , make it the subject of the equation.
- 2) Obtain balance relating the rate of H₂O₂ departure from the catalyst layer to the ring current via heterogeneous rate constant, ie. $i_R = f(C_{cl,H_2O_2}) * k_{D,H_2O_2}$ and integrate this equation into step (1).
- 3) Re-arrange the equation resulting from step (2) to make the precursor chemical step to electroreduction the subject, being C_{a,O_2} , C_{cl,O_2} depending on whether the disc current is under kinetic or diffusion control respectively.
- 4) Obtain relationship between disc current (i_D) to C_{a,O_2} , C_{cl,O_2} depending on whether disc current is under kinetic or diffusion control respectively. Re-arrange to make this term the subject.
- 5) Substitute step (4) into step (3) and re-arrange the resultant equation to obtain one in the form $i_D/i_R = f(k_{d,H_2O_2}^{-1})$.

Eq.2-72 links electrode rotation to the heterogeneous transport of H₂O₂ to the ring ($k_{D,H2O2}$), in a similar formulae Eq.2-62. According to Eq.2-72 the intercept value of $CE*i_D/i_R$ vs. $\tilde{\omega}^{-1/2}$ and $CE*i_D/i_R$ vs. $1/k_{D,H2O2}$ should be identical with a different value for the slope.

$$k_{D,H2O2} = 0.62D^{2/3}v^{-1/6}\tilde{\omega}^{1/2} \quad [42, 69] \quad (\text{Eq.2-72})$$

A mass balance on C_{cl,H_2O_2} under $i_{D,L}...$

$$C_{cl,H_2O_2} = k_{2f}C_{cl,O_2} / (k_3 + k_4 + k_{D,H2O2}) \quad (\text{Eq.2-73})$$

Substituting this into Eq.2-75 produces Eq.2-76. In this case k_2 is approximately equal to k_{2f} and can be substituted for simplicity. Eq.2-76 is valid for kinetic limitation or O₂ diffusion limitation into the disc layer, provided cathodic overpotential is high enough and k_{2b} negligible.

The Ring current expression is valid for all cases under study, “A” represents the disc area.

Under diffusion controlled oxidation of H₂O₂...

$$i_R = CE * 2AFk_{D,H2O2}C_{cl,H_2O_2} \quad (\text{Eq.2-74})$$

If $(k_3+k_4) < 5k_5$ and $k_{D,H2O2} \gg k_{5b}$ then the ring current is described by..

$$i_R = CE * 2Fk_{D,H2O2}C_{cl,H_2O_2} = CE * 2F \left(\frac{k_{5f}k_{D,H2O2}}{k_{5b} + k_{D,H2O2}} \right) C_{a,H_2O_2} \quad (\text{Eq.2-75})$$

This equation differs from that of Wroblowa's. In Appleby's instance, the case where the breakdown of adsorbed H₂O₂ becomes rate limiting can be evaluated using $CE*i_D/i_R$ and a mass balance around adsorbed H₂O₂. Characters are referred to in Figure 2-8. At pH7 O₂⁻(aq) is unstable [32], it is assumed all O₂⁻ in the catalyst layer is bound to the electrocatalyst, awaiting reduction. It is also assumed that K_{ads} is large at all potentials considered and $k_{\delta Cf}/k_{\delta Cb}$ is large as seen for FePc [70]. In Appleby's model k_{2b} is 1st order with respect to H₂O₂ and OH⁻. To make this term negligible only cases where the

potential is too cathodic for oxidation of H₂O₂ on the electrocatalyst will be considered ($E < 0.18V$). The mass balance around H₂O₂ becomes..

$$i_R = CE * 2AFC_{cl,O_2} \frac{k_2 k_{D,H_2O_2}}{k_3 + k_4 + k_{D,H_2O_2}} \quad (\text{Eq.2-76})$$

When considering i_D , the rate of O₂ entering the film at steady state equilibrium is given by Eq.2-77 for a single potential. The consequential steps of K_{ads} and $k_{\delta C}$ are irrelevant to the balance as they overwhelmingly favour the forward reaction. As long as k_{2b} is negligible....

$$\begin{aligned} I &= I_{D,L} & I &= I_k \\ k_{D,O_2} C_{0,O_2} &= (k_1 + k_2) C_{cl,O_2} = (k_1 + k_2) C_{a,O_2} \end{aligned} \quad (\text{Eq.2-77})$$

The disc current is provided from Eq.2-78. To modify for the unknown concentration of O₂ adsorbed on the electrocatalyst surface Eq.2-77 is used.

$$i_D = 4AF(k_1 + k_2) C_{a,O_2} \quad (\text{Eq.2-78})$$

If a descriptor (τ) is added with a value between 1 and 2 depending on ratio of H₂O₂ is recycled back to O₂ and OH⁻ from that reduced the mass balance on $i_{D,L}$ becomes Eq.2-79 under .

$$i_{D,L} = 2AF(2k_1 + \tau k_2) C_{cl,O_2} \quad (\text{Eq.2-79})$$

If $\tau=2$ then k_3 or k_4 predominate, whilst in $\tau=1$ the ring current k_{D,H_2O_2} dominates. k_4 is expected to be a function of ω but not E [71]. To perform the analysis recommended by Wroblowa and Appleby a $CE*i_D/i_R$ vs $\omega^{-0.5}$ plot is produced by re-arranging Eq.2-78 to make C_{a,O_2} the subject and inserting into Eq.2-76. This term can then be combined with that for i_R in Eq.2-76 to yield Eq.2-80. In the case of kinetic disc limitation $\tau=1$.

Y-axis X-axis | Gradient | + Y-axis intercept

$$\frac{CE * i_D}{i_R} = \frac{1}{k_{DH_2O_2}} \left[\left(\frac{2k_1}{k_2} + \tau \right) \left(\frac{(k_3 + k_4)k_{5b}}{k_{5f}} \right) \right] + \left(\frac{2k_1}{k_2} + \tau \right) \left(\frac{k_3 + k_4 + k_{5f}}{k_{5f}} \right) \quad (\text{Eq.2-80})$$

In the expanded version the intercept value is still equal to $2k_1/k_2+\tau$ provided k_3 and k_4 are insignificant compared to k_{5f} . Under O_2 diffusion limitation the k_1/k_2 the value of τ must be identified.

For further mechanism analysis the S/J values are plotted as a function of E to determine the kinetics of intermediary reduction/oxidation only, one term dominates with the \log_{10} plot being linear.

$$\frac{S}{J} = \frac{(k_3 + k_4)k_{5b}}{k_3 + k_4 + k_{5f}} \quad (\text{Eq.2-81})$$

If $2k_1/k_2+\tau=1$, as must be the case with $J'=1$ then Eq.2-80 reduces to..

$$S = (k_3 + k_4)k_{5b}/k_{5f} \quad (\text{Eq.2-82})$$

Electron transfer rate constants k_1 , k_2 and k_3 are expected to show tafel behaviour whilst k_5 and K_{ads} are only weakly dependent on potential whilst, k_{4ii} is potential independent [42].

Plots of CE^*i_D/i_R vs $\omega^{-0.5}$ are recommended by each model for diagnostic criterion [42, 44, 61, 62, 72] with additional data being provided by $CE^*(i_D-i_R)/i_R$ vs $\omega^{-0.5}$ [61] or the similar plots of $CE^*(i_{D,L}-i_D)/i_R$ vs $\omega^{-0.5}$ [73] or $CE^*i_{D,L}/(i_{D,L}-i_D)$ vs $\omega^{-0.5}$ with some authors claiming the latter method to be a simplification [74], though relies on fewer theoretical assumptions on the mechanism. To evaluate which model best applied the Iron Phthalocyanine case, the plot of CE^*i_D/i_R vs $\omega^{-0.5}$ was made.

The plot of $CE^*i_{D,L}/(i_{D,L}-i_D)$ vs $\omega^{-0.5}$ produces k_{app} , through Eq.2-84. Where Z_{O_2} refers to the use of O_2 limiting diffusion in Eq.2-83..

$$i_{D,L} = NFAZ_{O_2}\tilde{\omega}^{0.5} \quad (\text{Eq.2-83})$$

$$i_{D,L}/(i_{D,L}-i_D) = 1 + k_{app}/(Z_{O_2}\omega^{0.5}) \quad (\text{Eq.2-84})$$

Under kinetic disc limitation τ is neglected...

$$k_{app} = (2k_1 + k_2) \quad (\text{Eq.2-85})$$

Hsueh trialled a variety of models on the entire potential range [44] on a Pt electrode in H_2SO_4 , finding only a model omitting disproportionation to fit the entire range. They report S/C data up to 100mV of cathodic overpotential. All methods of analysis [44, 61, 75] report the intercept of $CE i_D/i_R$ vs. $\tilde{\omega}^{-0.5}$ to be equivalent to k_1/k_2 in some form. The general method applied to cases in neutral media [61, 75] contains a term for the intercept that could equate to 0 making the intercept $1+2k_1/k_2$.

2.6 Capacitance, charge motion and the redox polymer electrode

2.6.1 Rate limiting conditions in porous redox polymer thin films analysis

Ion diffusion through ionomer coated pores may become a limiting case in certain conditions in then thin film. The criterion of several limiting cases of the K-L plot are outlined by Andrieux et al [59, 60, 76], Anson et al [77] and Lyons [78]. All models pertain to analysis of systems under steady state [78], which may not be present in cyclic voltammetry. Electron movement in semi-conductive electrodes can be modelled as a diffusive process, loosely obeying Fick's law [60]. A model has yet to be produced for counter-ion diffusion dependent electro catalysis in a porous electrode with a non-homogenous coating of redox polymer electro-catalyst (ie. FePc) at potentials higher than limiting current. The effect of counter-ion on electron hopping has been conveyed [79] but not adapted to K-L plots. A graphical representation of the major processes is shown in Figure 2-17. In this figure two scenarios of electrocatalysis occurring a) at film-electrolyte interface or b) at the electrode-film interface.

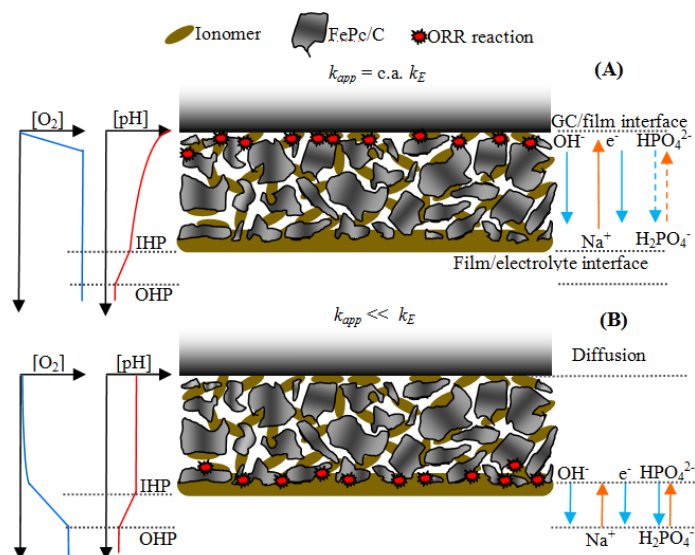


Figure 2-17. Model of porous thin film on GC disc utilising carbon supported redox polymer for ORR. (A) $E < E^{0'}$ ($\eta < 100\text{mV}$) kinetic control with slow e^- percolation (B) $E \ll E^{0'}$ O_2 diffusion control with fully reduced film.

2.6.2 Assessment of electrode constrained redox active species

When a faradic reaction is catalysed by a redox electrocatalyst a study of the CV response in the absence of substrate can yield useful information on loading, dispersion and layer conductivity. The equations used to analyse an electrode modified with a redox material where both the oxidised and reduced state are strongly adsorbed is outlined by Laviron [80]. The dependence of factors such as E_{pa} , E_{pc} , J_p and $W_{1/2}$ on scan rate and pH yields kinetic data. These factors are obtained by treatment of the experimental data as in Figure 2-18(A) with baseline subtraction of contributions from charging current in Eq.2-16 to produce Figure 2-18(B). Generally, a widening and flattening of the peak points to a distribution of ionization energies for the adsorbed redox active material. A shift in the value $E_{pa}-E_{pc}$ with increasing scan rate allows the value of rate of surface electron exchange reaction k_E (s^{-1}) to be determined.

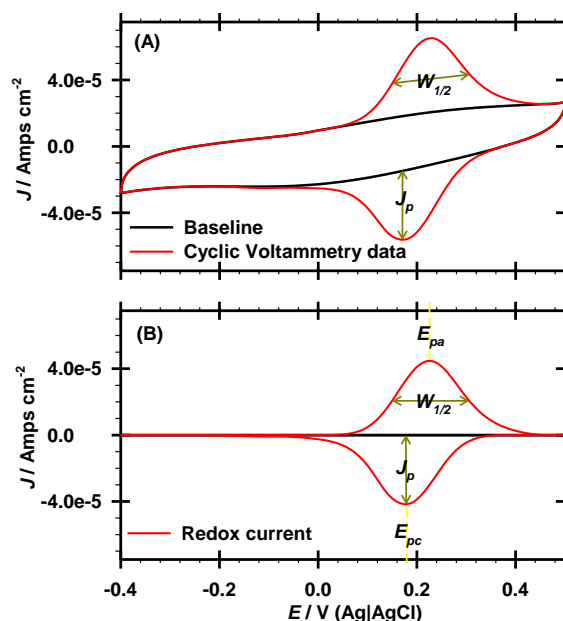


Figure 2-18. i - E response of a strongly adsorbed metal based electrocatalyst in the absence of dissolved reactant. Example is for chelated $\text{Fe}^{2+}/\text{Fe}^{3+}$ redox. Features used in analysis are presented for (A) the raw data, and (B) after subtraction of capacitive current. $\nu=20\text{mV/s}$.

In the case of FePc, the amount which is electroactive, $\tilde{\Gamma}_{\text{FePc}}$ (moles cm^{-2}) is calculated from the $\text{Fe(II)Pc} \rightarrow \text{Fe(III)Pc}$ redox peak area during CV in quiescent de-aerated solution $\nu=20\text{mV/s}$. The actual redox area was obtained by fitting a 6 order polynomial baseline to purely capacitive currents ($0.45 < E < 0.5$ and $-0.4 < E < 0$) using the NOVA software package (autolab) as in the example in appendix, Figure A-3. The resulting current for each reading was multiplied by the time period, obtained by the change in E for each reading divided by ν , thus producing the total charge passed. Eq.2-87 is produced by integrating the recorded current for each t_{step} time period. Each time period is then multiplied for each current then integrating the time between each recorded current. Integration of the charge passed in oxidising the redox polymer ($i_{\text{Red} \leftrightarrow \text{Ox}}$) via applying Eq.2-87 to Figure 2-18(B) was deemed more accurate than peak height as peaks become non-Gaussian at high scan rate [80].

Laviron's equation for electrodes bearing films of surface confined species [80] allows modelling of electroactive coverage using Eq.2-86. For this equation to be valid the oxidised and reduced state are irreversibly adsorbed. This equation is valid when no diffusive element is present in the cell and electron removal/insertion occurs reversibly.

$$J_p = n^2 F^2 \nu \tilde{\Gamma} / 4RT = nFQ\nu / 4RT \quad (\text{Eq.2-86})$$

$$A\tilde{\Gamma}F = t_{step} \int_{t=0\% Ox}^{t=100\% Ox} i_{Red \leftrightarrow Ox} \quad (\text{Eq.2-87})$$

Where J_p is the current density at the redox peak (A cm^{-2}), n =no. of electrons involved in the exchange, F =Faradays Constant, ν =Scan Rate (V s^{-1}), $\tilde{\Gamma}$ =Surface loading of redox active material (mole cm^{-2}), Q =total charge passed during redox (C cm^{-2}).

The electron insertion mechanism of a strongly adsorbed species is calculated using the width of the peak at half the maximum peak height ($W_{1/2}$). In an ideal situation with Gaussian peaks with no steric hindrance, peak splitting from a subsequent slow step or a lag caused by large ν , the $W_{1/2}$ can be calculated using Eq.2-88 [81].

$$W_{1/2} = (2RT/nF) * \ln(3 + 2\sqrt{2}) \quad (\text{Eq.2-88})$$

Assuming $T=293^\circ\text{K}$ the ideal $W_{1/2}$ value would be 0.0445V for $n=2$ and 0.089V for $n=1$. This method was used to the ease of electron transfer from co-ordinated Iron moieties and peak splitting. Additionally it has been utilised in chapter 6 to assess O_2 chelation by QDPSU binder.

2.6.3 Trumpet plot of redox active film

In the absence of substrate plotting E_p vs $f(\log_{10}\nu)$ produces a trumpet shaped plot with linear section at high ν with gradient $-2.3RT/\alpha nF$ for the anodic branch and $2.3RT/(1-\alpha)nF$ for the cathodic branch [82]. When these branches are extended to $E^{0'}$ they produce scan rates ν_{an} and ν_{ca} respectively...

$$k_E = \alpha nF \nu_{ca} / RT = (1-\alpha) nF \nu_{an} / RT \quad (\text{Eq.2-89})$$

k_E (s^{-1}) is the rate constant for the reaction of a single redox moiety in the film where $\tilde{\Gamma}_{Ox} = \tilde{\Gamma}_{Red}$ and $E=E^{0'}$ for $n=1$ [83]. This electron exchange rate describes how quickly the film can be oxidised/reduced. To convert k_E to a heterogeneous rate constant $k_{E,h}$ Eq.2-90 is used...

$$k_{E,h} = \delta_{film} k_E \quad (\text{Eq.2-90})$$

2.6.4 Anson plot for surface coverage and charge carrier concentration

The Anson plot of bolometric data (ΣQ vs $t^{0.5}$) of current decay following a potential step is governed by Eq.2-91.

$$\Sigma Q = \frac{2nFAC(Dt)^{0.5}}{\pi^{0.5}} + Q_{ads} + Q_{dl} \quad (\text{Eq.2-91})$$

$$Q_{ads} = nFA\Gamma \quad (\text{Eq.2-92})$$

In this case Q_{ads} is the charge injected into the electrode to compensate for specific adsorption onto the electrocatalyst surface of substrate or counter-ion. Repeating this experiment with and without solvated substrate produces information on partial surface coverage. The approximation of Q_{dl} can be obtained from impedance spectroscopy using $C_{dl} = Q_{dl} / (\phi_{IHP} - \phi_{OHP})$. In situations where $Q_{ads} \gg Q_{dl}$ the intercept of the Anson plot ($\gg 50 \mu\text{F cm}^{-2}$) in de-aerated and aerated electrolyte provides relative surface coverage of anion adsorption and O_2 adsorption via Eq.2-93 [84].

$$Q_{ads} = (nFA\Gamma_{FePc}) (\theta_{FePc-X-} + \theta_{FePc-O_2}) \quad (\text{Eq.2-93})$$

Due to the issues highlighted in section 5.2.5 two distinct terms are used in this thesis where a faradic reaction occurs on an electrode possessing large C_z .

- 1) E_{onset} (Onset Potential). “A potential during voltammetry where net current changes direction.”
- 2) E_{ORR} (Potential of ORR). “The potential where faradic current recorded in aerated electrolyte increases relative to non-faradic current in de-aerated electrolyte, indicating ORR.”

2.7 Electrochemical impedance spectroscopy

2.7.1 Impedance

Impedance is composed of a real part Z' , and an imaginary part Z'' , associated with capacitance. The resulting complex plane impedance is defined by Eq.2-94.

$$Z = Z' + jZ'' = \sqrt{(Z')^2 + (Z'')^2} \quad (\text{Eq.2-94})$$

Where j is $\sqrt{-1}$, a complex term in the imaginary plane, typically solved by Laplace transform and Nyquist or complex plane plots (Z' vs. $-Z''$) can be generated. Following an AC perturbation over a DC signal the resulting phase lag (capacitance) and reduction in amplitude (resistance) generate a complex plane plot. Typical input and output signals for a system are shown in Figure 2-19.

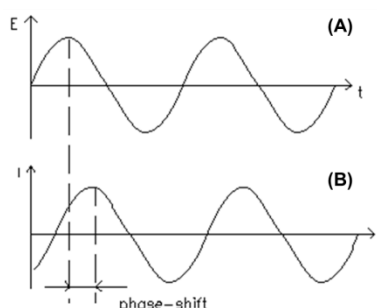


Figure 2-19. Potentiostatic input (A) and corresponding current output (B) of an AC perturbation in applied potential (EIS).

The decrease in anticipated current (ohm's law) provides the real component, whilst the lag in phase angle (ϕ) quantifies the degree of capacitance. In the absence of solvated substrate or surface reaction a purely capacitive response ($\phi = -90^\circ$) is obtained where the electrode is charged but e^- are not conveyed to the solution via reaction or consumed in a surface confined reaction (etc. corrosion). The thermodynamic lag associated with bond-reorganisation and energy barriers means that over certain time scales (AC frequencies) capacitance is observed in the response. The time scale for bonds to break and form produces an arc, where the HF limit (Z'_0) and LF limit (Z'_∞) describe the timescales at which the reaction is complete and unable to be affected by changing surface conditions. The difference $Z'_0 - Z'_\infty$ is akin to the amount of electrical energy lost in the process of bond reorganisation.

Several elementary components are used to generate equivalent circuits of electrochemical processes. The total impedance as a function of frequency (f), phase angle and the obtainable kinetic information from the individual unit in series are shown in Table 2-1. The equations are frequently expressed as radial frequency $\tilde{\omega}$ (rad s^{-1}) as opposed to Hz frequency (f), the relation between them as in Eq.2-95. The relationship between $f^{-0.5}$ vs. $\tilde{\omega}^{-0.5}$ and f^{-1} vs. $\tilde{\omega}^{-1}$ are also linear. The conversion factor is written in Eq.2-96 and 4-4 respectively.

$$0.159155 \tilde{\omega} = f \quad (\text{Eq.2-95})$$





$$0.398942 \tilde{\omega}^{-0.5} = f^{-0.5} \quad (\text{Eq.2-96})$$

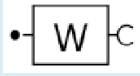
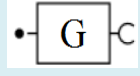
$$6.28318306 \tilde{\omega}^{-1} = f^{-1} \quad (\text{Eq.2-97})$$

2.7.2 Equivalent circuit components modelling physical processes

Table 2-1 describes the phase discrepancy between bias voltage and corresponding current, the overall impedance of the unit as a function of DC perturbation frequency and the obtainable kinetic parameters of circuit elements connected in series. When connected in parallel other kinetic information is obtained.

Table 2-1. Individual elements of equivalent circuits models of electrodes.

Element	Overall Impedance	Phase Discrepancy (φ)	Obtainable Kinetic Info
 Resistor	$Z = R$	0°	N/A
 Capacitor	$Z = 1/(j * \tilde{\omega} * C)$	-90°	N/A
 Constant Phase Element	$Z_{CPE} = 1/C(j\tilde{\omega})^N$	$f(N)$, when; $N = 0, \quad 0^\circ$ $N = 0.5, \quad -45^\circ$ $N = 1, \quad -90^\circ$	Low frequency limit on capacitive response. Slope indicates Pseudocapacitance.
 Inductance	$Z = 1/(j * \tilde{\omega} * L)$	$+90^\circ$	N/A

 <p>Warburg Impedance</p>	<p>Infinite;</p> $Z_w = \sigma(\tilde{\omega})^{-1/2} - j\sigma(\tilde{\omega})^{-1/2}$ <p>Finite reflective (general);</p> $Z_w = \sigma(\tilde{\omega})^{-1/2} \coth\left(\delta\left(\frac{j\tilde{\omega}}{D}\right)^{0.5}\right)$ <p>Open ended diffusion [85];</p> $Z_w = \sigma(\tilde{\omega})^{-1/2} \tanh\left(\frac{\delta}{D^{0.5}} j\tilde{\omega}\right)$	<p>Infinite; -45°</p> <p>Reflective finite; A -45° region changing to a -90° region</p> <p>Open ended diffusion; -45° region and gradual approach to 0°</p>	<p>Reflective finite; Low f lim. $Z' = (\delta/Y^0 \sqrt{D})/3$</p> <p>Open ended finite; $f_p = 0.4/(\delta/\sqrt{D})^2$</p> <p>Low f lim. $Z' = \delta/Y^0 \sqrt{D}$</p>
 <p>Gerischer Impedance</p>	$Z = 1/Y^0(k_a + j\tilde{\omega})^{0.5}$	<p>-45° region and gradual approach to 0°</p>	<p>Low f lim. $Z' = 1/Y^0 k_a^{0.5}$</p>

N is the exponent of the constant phase element, d is the distance of diffusion and can be used interchangeably as the Nernst diffusion layer δ (cm) or film thickness δ_f (cm) in cases of reactions at the electrode/film interface. D is a general diffusion co-efficient of the diffusing species ($\text{cm}^2 \text{s}^{-1}$), Y^0 ($\Omega^{-1} \text{cm}^{-2}$) is the equivalent admittance at $\tilde{\omega}=1 \text{ rad s}^{-1}$, k_a is the rate of a preceding chemical reaction in the bulk (s^{-1}), C is capacitance associated with that unit (F cm^{-2}) and Z , Z_w or Z_{CPE} are total impedances associated with the various units (Ohm cm^2). The Warburg diffusion co-efficient σ ($\text{Ohm cm}^2 \text{s}^{-0.5}$) is described in Eq.2-98.

$$\sigma = \sigma_O + \sigma_R = \left(RT/n^2 F^2 \sqrt{2} \right) \left(1/(C_{0,ox} \sqrt{D_O}) + 1/(C_{0,Red} \sqrt{D_R}) \right) \quad (\text{Eq.2-98})$$

The diffusion factor σ , has mainly been amalgamated from the reduced (σ_R) and oxidised (σ_O) form ($\Omega \text{cm}^2 \text{s}^{-0.5}$). Symbols D_O and D_R relate to the individual diffusion co-efficient ($\text{cm}^2 \text{s}^{-1}$) and A is electrode area (cm^2). The oxidised and reduced parts of the couple can be amalgamated into a single diffusion co-efficient D present at concentration $[X]$. This equation can be used to model reversible and quasi-irreversible reactions such as ion diffusion and adsorption. Most equivalent circuit fit programmes return Y^0 of a diffusion unit as opposed to σ , the two are related by Eq.2-99.

$$\sigma = 1/Y^0 \sqrt{2} \quad (\text{Eq.2-99})$$

When plotting σ vs. E , the plot can show no peaks (as with ion diffusion) or can show a minima at a redox couple if electron diffusion control is present. The minima can be skewed from the $E^{0'}$ of a couple if a disparity exists between the chemical activities coefficients of the reduced (a_{red}) and oxidised couple (a_{ox}). This relationship follows the Eq.2-100.

$$E_{min} - E^{0'} = \left(\frac{RT}{2nF} \right) \ln \left(\frac{a_{ox}}{a_{red}} \right) \quad (\text{Eq.2-100})$$

Warburg impedance arises when diffusion of a substrate to, or diffusion of a product from an electrode becomes rate limiting. When no significant faradic reaction happens, charge transfer takes the form of ion desorption and diffusion to maintain electro-neutrality. Warburg diffusion can take several forms;

- 1) Semi-infinite Warburg diffusion, where the bulk concentration is unchanged and a linear concentration gradient exists between flat electrode surface and the reaction site impedance.
- 2) Reflective finite transmissive diffusion, where e^- transfer from a redox active polymer into the solution occurs, via buffer or mediator, resulting in a highly charged double layer. Layers that respond this way are characterised by a finite amount of electro-active material, producing near infinite impedance when consumed.
- 3) Open ended or transmissive finite diffusion, where the diffusion boundaries are not set and no ions in solution can accept charge. In this situation charge transfer from the electrode to the polymer has become rate limiting.

Gerischer impedance manifests itself in the complex plane plot as a reflective transmissive Warburg impedance with a depressed semi-circle. It is frequently applied to porous electrodes but also situations where reactions occur in the bulk electrolyte [86].

In responses with well distributed time constants the response of a single parallel capacitor-resistor time constant (τ) can be given by Eq.2-101. As pure capacitance has infinite impedance at 0Hz and zero impedance at ∞ Hz the standard admittance is used for a constant phase element, Y^0 . Only in the case of a CPE and resistor in parallel can the true capacitance be found from the frequency at the peak of the arc in Eq.2-103. The relation between capacitance and resistance follows Eq.2-102.

$$\tau = R_0 C \quad (\text{Eq.2-101})$$

$$\tilde{\omega}_p = 1 / R_0 C \quad (\text{Eq.2-102})$$

$$C = Y^0 (\tilde{\omega}_p)^{N-1} \quad (\text{Eq.2-103})$$

Where R_0 is the Z' value of the arc when extrapolated to 0Hz ($-Z''=0$). $\tilde{\omega}_p$ is the frequency at the peak of the arc, also known as the ‘hopping frequency’ (rad s^{-1}).

If a multi-component equivalent circuit is limited (the vast majority of current loss and phase discrepancy) by a single one of these components under given conditions, the entire equivalent circuit may be approximated by the equations that describe that single component. The frequency range where a single component dominates can also be examined and linear regression used on the modified frequency term to obtain (σ) in diffusion control (Z vs. $\tilde{\omega}^{-0.5}$ plot [87, 88]).

The rather complex term for finite Warburg impedance simplifies towards the higher frequency end of the region of mass diffusion control, approximated by $Z_W = 2\sigma * \tilde{\omega}^{-1/2}$ in a narrow frequency region, analogous to infinite diffusion. If plotting the real component only to avoid noise from adsorption capacitance, the plot Z' vs. $\tilde{\omega}^{-0.5}$ produces a gradient where Eq.2-98 can be applied, providing the $\sqrt{2}$ term is removed.

2.7.3 Faradic reactions in EIS

In the instances where the resistance to charge transfer (R_{ct}) of a faradaic reaction has been successfully separated from other impedance effects, the R_{ct} at $E=OCP$ is related to exchange current by Eq.2-104 and charge transfer kinetics by Eq.2-105. In a narrow potential range around OCP the dI/dE response is nearly linear, provided $|b_c|=b_a$. Charge transfer resistance is measured as the width of the semi-circle or arc in the nyquist plot. The arc is easily identified by its significant potential dependence, with R_{ct} reaching a parabola maxima at OCP .

$$R_{ct} = RT / nF i_0 \quad [89] \quad (\text{Eq.2-104})$$

$$i_0 = nFAk^0 C_{0,Ox}^{(1-\alpha)} C_{0,Red}^{\alpha} \quad (\text{Eq.2-105})$$

$$k^0 = \frac{RT}{n^2 F^2 A C_{0,Ox}^{(1-\alpha)} C_{0,Red}^{\alpha}} \frac{1}{R_{ct}} \quad [90] \quad (\text{Eq.2-106})$$

At open circuit potential these equations combine to produce is transformed in using Eq.2-106 to yield k^0 from R_{ct} [91]. This analysis is valid for Randles plots, where $R_{ct}W[C]$ circuits occur. The relative diffusion co-efficients of the oxidised and reduced couple cannot be applied to irreversible reactions such as ORR.

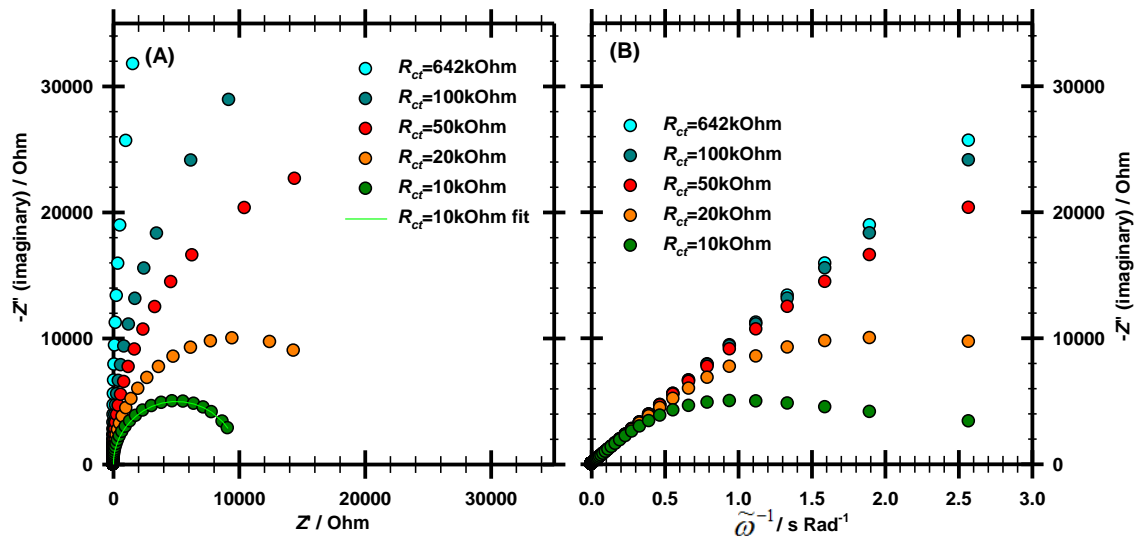


Figure 2-20. Model of $R_{ct}[C]$ circuit as a function of potential No substrate diffusion limitation. $C=10^{-4}$ F, $C_{0,Red}=10^{-10}$ Moles cm^{-3} , $C_{0,Ox}=10^{-6}$ Moles cm^{-3} , $\alpha=0.5$, $A=1\text{cm}^2$, $i_0=1 \times 10^{-8}$ Amps, $T=298.15^\circ\text{K}$.

In Figure 2-20(B) it can be seen that when the contribution from the resistor is relatively high the gradient of the $-Z''$ vs ω^{-1} plot is linear, it's inverse yielding the low frequency capacitance. In this example $k^0=2.6 \times 10^{-6} \text{ cm s}^{-1}$ is obtained from a semi-circle fit as seen in Figure 2-20(A) using the previous formulae.

If the faradic reaction contains a substrate adsorption step that may become the RDS of the reaction, then a time constant may need to be included [92]. R_{ads} and C_{ads} of this process are expressed as...

$$R_{ads} = RT / n^2 F^2 C_{cl,Ox} kA \quad (\text{Eq.2-107})$$

$$C_{ads} = n^2 F^2 A C_{cl,Ox} / RT \quad (\text{Eq.2-108})$$

Where $C_{cl,Ox}$ is the surface concentration of the oxidised couple (in the case of a reduction reaction). The rate constant (s^{-1}) of this process is given by...

$$k_{ads} = 1/R_{ads}C_{ads} \quad (\text{Eq.2-109})$$

This can be transformed into a heterogeneous rate constant by multiplication by the film thickness (δ_{film}). In many processes reactant adsorption is strong and this feature may not be visible on the nyquist plot.

2.7.4 Analysis of intersecting time constants in EIS

The difference in $Z''=0$ intercept values of the HF arc and $Z''=0$ intercept from linear regression of Warburg response in the low frequency diffusive arc in the Nyquist plot (Z'' vs. Z'). This process is only accurate with poorly defined diffusive and faradic process, time constants of 1-2 orders of magnitude. If time constants are well separated error increases. (e.g. Figure A-18). The formula depends on the other components present in the time constant and the nature of the diffusive species, for a $C_{dl}[R_{ct}W]$ time constant where a neutrally charged substrate (i.e. O_2) is diffusing, σ ($\Omega \text{ cm}^2 \text{ s}^{-0.5}$) is given by Eq.2-110. In the instance where ion charge diffusion through a medium is limiting Eq.2-111 is applied [93]. This relationship can be analysed for a relation to binder.

$$R_w - R_0 = 2\sigma * C_{dl} \quad (\text{Eq.2-110})$$

$$R_w - R_0 = 2\sigma^2 * C_{dl} \quad (\text{Eq.2-111})$$

R_w ($\Omega \text{ cm}^2$) is the resistance obtained from extrapolating the Warburg gradient ($m=1$) back to the Z' axis to $\omega=\infty \text{ Rad s}^{-1}$.

2.7 Analysis of ion exchange materials and redox polymers with EIS

There are many instances where e^- or ion diffusion through polymeric film determines catalytic turnover [91, 94-100] and overall electrode impedance. This diffusion can occur via three main ways [100]; 1) electron hopping, 2) Physical migration of the redox centre in the film (not applicable to irreversibly adsorbed FePc, or 3) anion or

cation migration to maintain electro-neutrality. Broadly speaking, a Warburg response transforms to that of capacitive response, as seen in the model for finite reflective diffusion in Figure 2-21. The physical explanation being that $(2D/\tilde{\omega})^{0.5}$ becomes comparable to the penetration depth δ_{film} of the AC signal at a certain low frequency. The descriptor B terms the limit of diffusion in Eq.2-112.

$$B = \delta_{film} / \sqrt{D} \quad (\text{Eq.2-112})$$

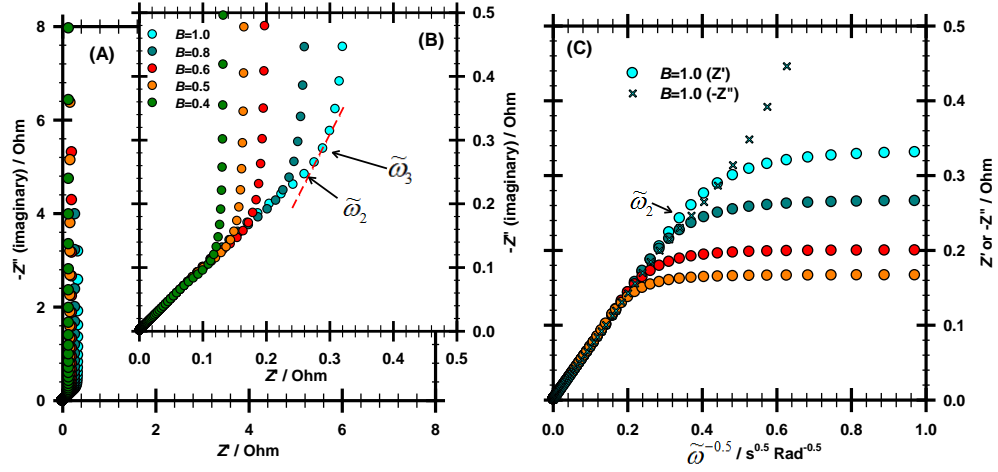


Figure 2-21. Model of finite reflective diffusion as (A)(B) Nyquist plot, or (C) Randles plot showing Z' vs $\tilde{\omega}^{-0.5}$ for $1.0 > B > 0.4$ and $-Z''$ vs $\tilde{\omega}^{-0.5}$ plot for $B=1$. $Y^0=1\text{Mho}$, red line on (A) reflects $\tilde{\omega}_2$ at $-dZ''/dZ'=2$. $\tilde{\omega}_2$ labelled for $B=1$

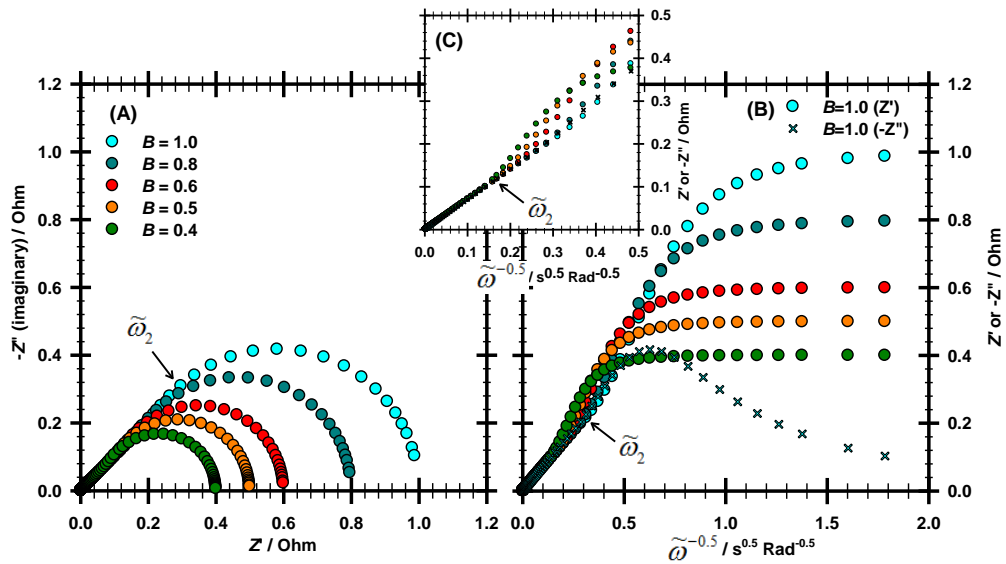


Figure 2-22. Model of finite open-ended diffusion (A) Nyquist plot, (B)(C) Randles plot showing Z' vs $\tilde{\omega}^{-0.5}$ for $1.0 > B > 0.4$ and $-Z''$ vs $\tilde{\omega}^{-0.5}$ plot for $B=1$. $Y^0=1\text{Mho}$. $\tilde{\omega}_2$ labelled for $B=1$

Figure 2-21 depicts the response for a perfect conducting polymer. The HF intercept is at value $R_{W,\infty}$. When no reaction occurs the LF response is capacitive, extrapolating this LF nyquist response to the real axis produces R_{low} (Figure A-19). Eq.2-113 is valid for both types of diffusion, the response being identical up to $\tilde{\omega}=B^2$.

$$\tilde{\omega}_2 = 2/B^2 \quad (\text{Eq.2-113})$$

A series of equations governing the situation of mixed ion resistance and electron diffusion resistance is provided by Armstrong et al [94], Mathias et al [101] and Cameron [102]. Provided the entire film is oxidised/reduced, the diffusion of electrons, D_E (cm s⁻¹) can be related to film thickness, δ_{film} (cm) by Eq.2-114. The other variable can be obtained from slope extrapolation (see appendix).

$$D_E = \delta_{film}^2 \tilde{\omega}_3 / 5.12 \quad (\text{Electron diffusion}) \quad [103] \quad (\text{Eq.2-114})$$

$$D_E = \delta_{film}^2 / R_E C_{diff} \quad (\text{Electron diffusion}) \quad [102] \quad (\text{Eq.2-115})$$

$$R_E = 3(R_{low} - R_{W,\infty}) \quad (\text{Electron diffusion}) \quad [102] \quad (\text{Eq.2-116})$$

$$R_W = R_s + [1/(1/R_{ion})(1/R_E)] \quad (\text{Mixed e}^-/\text{ion diffusion control}) \quad [102] \quad (\text{Eq.2-117})$$

$$R_{low} = R_s + (R_{ion} + R_E)/3 \quad (\text{Mixed e}^-/\text{ion diffusion control}) \quad [102] \quad (\text{Eq.2-118})$$

$$R_{low} = \delta_{film}^2 / 3D_{ion} C_{low} \quad (\text{Ion diffusion}) \quad [87] \quad (\text{Eq.2-119})$$

Where R_E is the resistance (Ω) from electron diffusion or Fe(II)Pc towards the active site, R_{ion} is the resistance to ionic movement in the film (Ω) stern layer to GC, C_{diff} is the capacitance of the immediate boundary response (F) after Warburg control, $\tilde{\omega}_3$ is the radial frequency prior during a switch from Warburg to capacitive behaviour, where the gradient $d|Z'|/dZ'=2$ [94]. R_{low} is the resistance (Ω), obtained from extrapolating the semi-bounded response back to the Z' axis. In the some instances of bounded diffusion within the film a term d (cm) can be used. This may also describe the mean diffusion distance in the high frequency portion.

The overall capacitance of an electrode without a significant faradic reaction can be obtained at the lowest frequency gradient in Eq.2-120 [104].

$$C_{\Sigma} = -1/2\pi f Z'' \quad [105] \quad (\text{Eq.2-120})$$

Two low frequency capacitances were termed due to the non-ideal response of the system, in some instances the linear capacitance after warburg control (see appendix Figure A-19) produced a different response to the lowest frequency $-Z''$ vs. $\tilde{\omega}^{-1}$ behaviour. In electro-catalytic systems a differential capacitance (C_{diff}) arises in redox polymers in oxidising/reducing the film and should form a perfect distribution around $E^{0'}$ of the diffusion couple, this should provide mechanism confirmation [100]. This quantity is calculable for reflective finite diffusion from the $-Z''$ vs. $\tilde{\omega}^{-1}$ plot with the gradient equalling $1/C_{\Sigma}$ comprising almost exclusively of the pseudo capacitance (C_{diff}) [102]. If the double layer capacitance can be removed (typically negligible) then Eq.2-122 can be used to confirm (n), or film thickness (δ_f) or diffusion length (d).

$$C_{\Sigma} = C_{diff} + C_{dl} + C_{ads} \quad (\text{Eq.2-121})$$

$$C_{low} = \left(\delta_f n^2 F^2 / RT \right) ([O]^* [R] / [X]) \quad (\text{Eq.2-122})$$

$$C_{low} \sigma = 0.5 \left(\delta_f / \sqrt{D_{app}} \right) \quad (\text{Eq.2-123})$$

$$\sigma = \delta_f / \sqrt{2D}^{0.5} C_{diff} \quad (\text{Eq.2-124})$$

Various cases can be tested by inputting likely values of δ_f and n the value for $[O]^* [R] / [X]$ can be obtained. This can then be compared to Eq.2-98, the Warburg coefficient in an amalgamated condition ($1/[X]^* \sqrt{D_{app}}$), and as individual rate constants ($1/[O]^* \sqrt{D_o}$) + ($1/[R]^* \sqrt{D_R}$) to find a case that fits all values and confirms the mechanism of charge transfer.

Chapter

3

Chapter 3. Literature Review of Electrocatalysis of O₂, Ion exchange polymers, Bioelectrochemical systems and their materials

3.1 Summary of Electron Acceptor Performances in MFCs

Table 3-1 summarises the performance of electron acceptors and their associated catalysts in MFC systems. The Power density (P) of each system (W m^{-2}) is quoted based on a geometric cathode area. In some instances reactor geometry is not been provided and volumetric power density (W m^{-3}) is used. P is reported for the electron acceptor relative to a control setup, such as ORR on a Platinum catalyst benchmark. The ratio of P in experiment: control is reported by an improvement factor, ' F ' (unit less). Improvements ($F > 1.0$) and some studies with $F < 1.0$ are included if representing a major cost saving.

Table 3-1. Electron acceptor and associated catalysts previously studied in MFCs. All potentials quoted vs Ag|AgCl (3M NaCl)

Electron Acceptor / Catalyst	Cell Design (#Chambers/Anode /Membrane)	Catholyte	Control Setup	Increase P_{max} mW m^{-2}	F	OCV or $E^{\circ'}$ / mV Ag AgCl	
Biocathode							
O_2 / <i>Consortia Fe²⁺ and Mn³⁺ oxidisers</i>	2Ch/G-Granules/Nafion/C-Granules-MnOx-FeO cat.	Acetate PBS AWW=anolyte	MnOx-FeO C-Granule anode	28 W m^{-3}	168	242	[106]
O_2 / <i>Consortia-Xanthomonas Sp.</i>	2 Ch/Carbon/Nafion/Pt Cathode	PBS and minerals	Biofilm removed	570	2.85	-	[107]
NO_3^- NO_2^- / <i>Consortia</i>	2 Ch /Carbon/CM17000	Spent Anolyte- PBS, NO_3^-	Cat. biofilm fed O_2 instead of NO_3^-	6.1 W m^{-3}	0.37	21 (NO_2) 8 (NO_3)	[108]
NO_3^- / <i>Consortia-grown in O₂</i>	2Ch/Carbon/Carbon separator	N_2 sat. Glucose PBS AWW-trace NO_3^-	Re-aerated catholyte	42	0.5	-	[109]
MnO_2 / generated by <i>Leptothrix Discophera</i> #	2Ch/G-Rod /2x J-Cloth+CEM	ATTC Medium, pH 7.2	$\text{O}_2(\text{aq})$ red. on abiotic carbon	126.7	32.5	418.5	[110]
ClO_4^- / <i>Dechloromonas Sp.</i>	2 Ch /Carbon/CEM	PBS+Growth Media, ClO_4^- and NO_3^- - no O_2	No ClO_4^- , only NO_3^-	0.0746 W m^{-3}	n/a	c.a. -350	[111]
Fe(III) / <i>Acidithiobacillus Ferrooxidans</i> #	2Ch/C-Felt/Bi-polar membrane	Biocatalyst, FeSO_4 , Nutrients, pH2 Air sat.	No control	1200	n/a	c.a. 580	[112]
Macrocycles							
O_2 / <i>FePc-C pyr. (0.5% wt. Fe) AC</i>	1Ch/C-Felt/J-Cloth	Acetate PBS AWW	0.5 mg_{Pt} cm^{-2}	720	0.88	c.a. 187	[113]
O_2 / <i>FeAc - NH₃ pyr. AC</i>	1Ch/C-Felt/J-Cloth	Acetate PBS AWW	0.5 mg_{Pt} cm^{-2}	300	0.37	c.a. 207	
O_2 / <i>FeTMPP-Cl -C pyr. AC</i>	1Ch/C-Felt/J-Cloth	Acetate PBS AWW	0.5 mg_{Pt} cm^{-2}	660	0.8	c.a. 240	
O_2 / <i>CoTMPP-Carbon pyr. - AC</i>	2Ch/C-Cloth/ Nafion117	High Saline (250mM) Acetate PBS AWW	0.5 mg_{Pt} cm^{-2}	1062	1.3	c.a. 200	[114]
O_2 / <i>FeEDTA - Carbon pyr. AC</i>	1Ch/G-Brush/ Membrane-less	Acetate PBS AWW	0.5 mg_{Pt} cm^{-2}	1122	0.96	814 ^g	[115]
Transition Metal Oxides							
O_2 / <i>Octahedral Sieve Co-MnO₂ - AC</i>	1Ch/GG/ Membrane-less	High[Acetate]AWW Continuous	0.5 mg_{Pt} cm^{-2}	897	3	124 ^g	[116]
O_2 / <i>Octahedral Sieve Co-MnO₂ - AC</i>	1Ch/GG/ Membrane-less	Acetate+ Wastewater Batch	0.5 mg_{Pt} cm^{-2}	180	0.91	147 ^g	[117]
O_2 / <i>Sputtered CoO_x on carbon - AC</i>	1Ch/Carbon/ Nafion layer	Acetate PBS AWW	0.5 mg_{Pt} cm^{-2}	28	0.34	-	[118]
O_2 / <i>MnO_x-C</i>	2Ch/Carbon/Nafion 117	250mM PBS, pH7 - open to air	0.82 mg_{Pt} cm^{-2}	161	0.83	506	[119]
O_2 / β phase-MnO ₂ -C - AC	1Ch/G-Granules/Nafion	Glucose-trace PBS	0.5 mg_{Pt} cm^{-2}	172	0.64	-	[120]

Carbon modification							
O₂ / <i>HNO₃ treat. Vulcan - AC</i>	1Ch/C-felt/CEM	Acetate PBS AWW	Vulcan-XC72R	170	3.3	-	[121]
O₂ / <i>Carbon Nanotube – AC</i>	1Ch/G-Brush/PTFE	Acetate PBS AWW	Carbon Black	329	2.2	-	[122]
O₂ / <i>(PPy-AQDS)-Carbon</i>	2Ch/ADQS-Carbon/CEM	PBS	No cat. AQDS mod.	823	1.3	314	[123]
O₂ / <i>1000m² g⁻¹ Activated Carbon Felt</i>	2Ch/C-Felt/100µm pore separator	Aerated Glucose PBS AWW	C-Paper-0.2mg _{pt} cm ⁻²	52.5	2.5	397	[124]
O₂ / <i>Polypyrrole-Carbon - AC</i>	1Ch/C-Felt/Membrane-less	Glucose PBS AWW	Nafion-Carbon	401.8	4.3	-	[125]
O₂ / <i>Crumpled Graphene on Carbon Cloth</i>	2Ch/Crumpled Graphene/CEM	100mM PBS, pH7 - Air sparged	Planar Graphene on C-Cloth	440	1.32	-	[126]
Chemical Acceptor (finite)							
MnO₄⁻ / <i>Carbon</i>	2Ch/Carbon/Nafion	PBS-10mM KMnO ₄	PBS-O ₂ sat. +Pt-C	4.35 Wm ⁻³	3.2	935	[127]
ClO⁻ / <i>Graphite Rod</i>	2Ch/G-Rod/NaCl Bridge	20g/L (Ca(OCl) ₂)	N/A	12.2	-	1482* (pH7)	[128]
S₂O₈⁴⁻ / <i>Carbon Paper</i>	2Ch/C-paper/Nafion	10mM K ₂ S ₂ O ₈	10mM [Fe(CN) ₆] ³⁻	211.9	1.3	1284 (pH7)	[129]
[Fe(CN)₆]³⁻(aq) / <i>C-Felt</i>	2Ch/Carbon Felt/Nafion-115	PBS+100mM [Fe(CN) ₆] ³⁻ - No O ₂	Pt/C Air Cathode	6130	6.3	228(pH7)	[130]
	2Ch/C-Felt/Gore-tex	2% NaCl at pH3	Carbon Felt	341	6.6	<u>≈+1280</u>	[131]
V(V) (VO₂⁺) and Cr(IV) (Cr₂O₇²⁻) / <i>Carbon</i>	2 Ch /C-Felt/Nafion 117	Simulated mine WW, pH2 continuous -no O ₂	Cathode Aeration (Carbon Felt)	970	1.7	<u>≈+776</u> (pH2)	[132]
V(V) (VO₃⁻) / <i>Carbon</i>	2 Ch /C-Felt/Nafion 117	“ “	Fe(CN) ₆ catholyte (E ^o =400mV)	572	-	<u>≈+810</u> (pH2)	[133]
PbO₂/C	2Ch/Carbon Cloth /KCl-Agar Bridge	PBS, pH7	Pt/C using O ₂ aqueous	77	1.7	-	[134]
Cu²⁺ / <i>Carbon-Copper</i>	2 Ch /Graphite plate /Bi-polar membrane	CuCl ₂ , pH3	Aerated pH3 media, no CuCl ₂	800	30	<u>≈+100</u> (pH3)	[135]
Fe₄[Fe(CN)₆]_(s) / <i>PANI</i>	2 Ch /Granular graphite/Nafion 117	K ₂ /H ₂ SO ₄	No control	1.4 x10 ⁻⁶	-	0.606	[136]
Cr_x[Fe(CN)₆]_(s) / <i>Carbon</i>	2Ch/G-felt, <i>Hansuela Anomina</i> / Nafion	KCl (pH6), KCl(pH2) or PBS (pH7)	No Control	<u>0.45</u> Wm ⁻³	-	0.701	[137]

Key; Ch(Chambers), G-Rod(Graphite Rod), C-Felt(Carbon Felt), G-Granules (Graphite Granules), G-Brush (Graphite brush), Cat.(Cathode), AC(air cathode), PPy-AQDS(Polypyrrole-anthraquinone-2,6-disulfonate), PANI(Polyaniline.), ^oSuspected reference electrode drift, *OCV = 1.56V, ^oNo cathode control study

Electron acceptors with lower or similar formal potential ($E^{o'}$) to anode biofilms such as H⁺ (Microbial Electrolysis Cell), CO₂ and SO₄²⁻ require external electrical energy input and are omitted from Table 3-1. To the best of the author's knowledge, environmentally relevant electron acceptors such as SrO₂, S₂O₃²⁻, BO₃⁻ and CrO₄²⁻ have not been assessed in MFCs. If reference electrodes are not used cathode $E^{o'}$ is formulated from OCV and $E^{o'}$ of Geobacter type outer membrane cytochromes when fed with acetate (Eq.1-2).

From the formal potentials of Table 3-1 it is apparent that the electron acceptor with the highest $E^{0'}$ which requires no electrochemical regeneration is O_2 . Other electron acceptors are rare in nature (ie. $V(V)_{(aq)}$, $S_2O_8^{4-}_{(aq)}$). Whether electron acceptor Ox is confined to the electrode to loading, Γ_{Ox} (mole) or solvated in the catholyte, C_{Ox} (mol cm^{-3}) the maximum theoretical charge that could be passed Q , associated with its reduction obeys Eq.3-1. The symbol 'e' is the elementary charge 1.6022×10^{-19} C $mole^{-1}$ and n the number of electrons used to reduce one molecule of Ox.

$$Q = n(\Gamma_{Ox} + VOL_{cat}C_{Ox})e \quad (Eq.3-1)$$

Notable exceptions are Fe(III) and MnO_2 , (c.a. $\Delta G=76kJ\ mol^{-1}$ and $\Delta G=242kJ\ mol^{-1}$ for $1e^-$ and $4e^-$ reduction with Eq.1-1) which can be produced via certain strains of microbes at the cathode and electrochemically reduced extracellularly on the biocathode surface. Maintaining an isolate at the cathode complicates cell design. The catalysis of oxygen reduction at pH7 is the focus herein.

3.2 Oxygen reduction catalysts

Literature on ORR catalysis is extensive with at least 45 papers being released per annum [138]. Discussion is limited to those applied to pH7 Bioelectrochemical Systems (BES) and Half-Cell studies with catalysts such as metal chalcogenides receiving no attention.

3.2.1 Pure metals

Un-alloyed transition metals are rarely implemented in electrochemical devices unless as an electron donor (ie. Zn) or as a noble metal (ie. Au, Pt, Pd). For an electro-catalyst the surface oxide phase of pure metals (other than Au) is required to be ORR active.

Tang et al have implemented carbon supported Ag nanoparticles as a cathode for acetate fed membrane-less single chambered microbial fuel cell (SCMFC) [139]. They demonstrate some inhibition of oxygen respiring heterotrophic bacteria that would otherwise form a parasitic biofilm on the cathode. Prietto et al applied a highly active Au(100) bead that catalysed an ORR wave at $E=0.21V$ (Ag|AgCl) in Na_2SO_4 (pH6)

[140], producing H_2O_2 when phosphate buffer was added highlighting the importance of the anion.

An evaluation of the formal potentials of ORR and competitive adsorption on Platinum in Phosphate can be found in section 10.5.3. In an MFC system Platinum remains the benchmark cathode catalyst [113, 141].

3.2.2 Alloys

The catalytic activity of a metal surface is a function of the binding energy of O_2 and the subsequent intermediates (O , OH , O_2H and H_2O_2) [142]. This forms the basis of an approach to understanding catalytic activity called Density Functional Theory (DFT).

Microbial Fuel Cell anodes and cathodes and current collectors [143, 144] frequently use passive Stainless Steel. On the atomic level, the surface possesses a distribution of O_2 binding energies and ORR activity. As such it is widely used as a current collector for cathodes of a large area. It is also used as a hydrogen evolution electrode in the microbial electrolysis cell [145]. The wide variety in activity comes from surface forms owing from differing interactions between the Mn, Cr, Mo, Ni and Fe. The specific activity (A cm^{-2}) of active surface area is low but can be compensated for by high surface areas. Alloys with non-metal components cover a wide variety of materials such as chalcogenides. Isolated metal nitrides and metal carbides have not previously been implemented in MFC cathodes.

3.2.3 MeOx with and without graphite support

The surface oxide phase possesses low conductivity, oxide layer thickness determines whether the metal is a suitable current collector. Metals that are reactive in their elemental state possess thick oxide layers such as Titanium are seldom used as electro-catalyst supports unless they possess desirable photocatalytic properties [146]. In MFC Titanium is widely used as current collector [147], being electrochemically inert electro catalytically inactive and un-corrodible [148] in pH7 PBS [149].

The catalytic activity of MeO_x is documented primarily for its reactivity with H_2O_2 [146] a quality that has seen it used as a co-catalyst with another $2e^-$ ORR catalyst [150-

156] but has also been employed in an MFC cathode as PbO_2 [134] and MnO_x [119]. The crystal phase may also determine activity [120, 157].

3.2.4 Graphite with and without chemical or thermal treatments

Carbon forms available as commercial electrodes are shown in Figure 3-1;

- Highly Ordered Pyrolytic Graphite (HOPG)-inter-sheet π -bonds overlap at regular intervals presenting a basal plane to the electrolyte. This aligned carbon has few pores or defects. [158]
- Edge Plane Pyrolytic Graphite (EPPG). Graphite sheets are perpendicular to the electrolyte. Electrons flow unimpeded along planes and do not traverse non-conductive ordered sheets. EPPG catalytic activity for ORR is altered by electrochemical or chemical modification.
- Carbon Nanotubes (CNT). Deposited in end-on configuration are highly conductive with smallest peak potential (E_p) Ferricyanide redox probe voltammetry [158]. CNT basal planes are low temp chemically modifiable unlike HOPG.
- Glassy Carbon (GC). A highly compressed and temperature annealed ribbon like matrix of non-graphitic carbon (produced from heated resins of phenolic aldehyde, furfuraldehyde and hexamethylenetetramine). No nitrogen or pores are contained in the Sp^2 bonding matrix which is resistant to chemical attack [159].

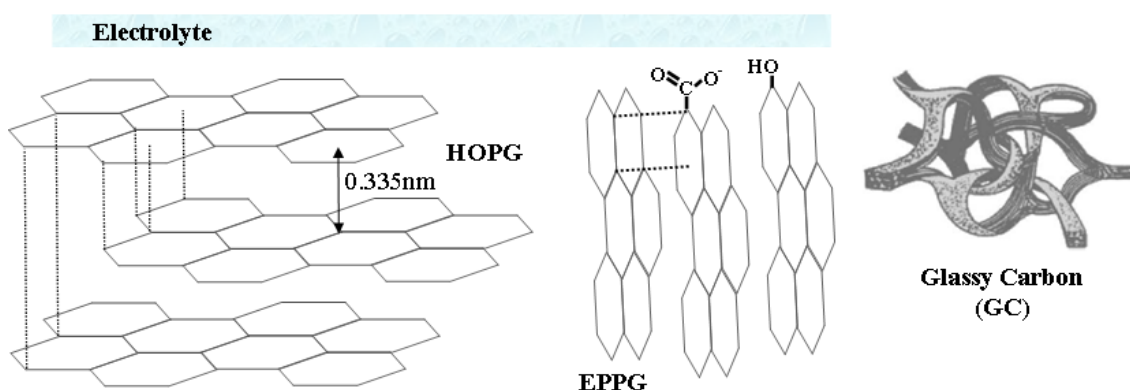


Figure 3-1. Forms of commercial carbon electrode. EPPG – graphite edge plane is oxidised. Ribbon like structure of Glassy Carbon liquid and gas impermeable

Graphitic carbons are also used in a porous matrix for increasing the relative area in contact with an electrolyte. As such they can greatly increase the relative rate of

reaction in circumstances where linear substrate diffusion is not a limiting factor. Interaction between graphite sheets due <0.335nm from strong π - π influence the electron density and may influence ORR activity. While graphite electrodes are widely used, Graphene electrodes have not been widely studied at pH 7.0 [160] but would omit plane-plane interaction effects.

No commercial activated carbon is devoid of small concentrations of metal, the only way to completely remove metal being aqua regia [161]. ORR activity of carbon materials can be attributed to edge plane impurities (non C or H elements). Zheng et al examined three methods of metal impurity removal from carbon [162]. Carbon nanofibres were; 1) Chemically cleaned—4M NaOH wash at 80°C, 4hrs then 2M HCl 60°C, 2hrs, or 2) Thermally cleaned—de-aerated to vacuum then thermally treated in Argon to 1700°C for 12hrs, or 3) Electrochemically cleaned—in de-aerated 0.5M HClO₄ (0V to 0.6V vs. SCE) by repeated CV. Electrochemical cleaning in de-aerated media (no H₂O₂) was performed until CV responses were purely capacitive (dI/dE=constant). The cleaned catalyst displayed mild ORR activity, $E < 0.28\text{V}$ vs SCE (0.32V Ag|AgCl). Thermally and chemically cleaned carbons produced an ORR wave at low potentials, $E < 0.1\text{V}$ for chemical cleaning and $E < 0\text{V}$ after heat-treatment.⁴

The ratio between two carbon signals in raman spectroscopy (1345 cm⁻¹ and 1585 cm⁻¹) was used to show relative prevalence of edge plane atoms, halving after the thermal treatment. This demonstrates that pyrolysis causes edge planes to coalesce into larger graphite sheets. The value was unaltered by electrochemical cleaning, showing it to be a non-destructive process to the graphite.

3.2.5 Chemical treatment/pyrolysis of graphite

Quinones are among the most ORR active edge plane groups produced from non-metal based oxidative chemical treatments. This activity is attributed to the quinone/•quinone⁻ redox potential, the anionic quinone radical then binds O₂ via the scheme [163].



⁴ Chemical or thermal treatment may produce materials that are inactive to ORR at $E = -0.45\text{V}$ in pH7 PBS making them an ideal inactive support for testing dispersed catalysts.



Valarselvan et al deposited quinones on a Polypyrrole support to ascertain the ORR activity of each type. It is feasible the author's choice resulted in unique active sites from strong π - π bonds producing active sites between Pyrrolic Nitrogen and quinone which is not raised by the author. The general structured of quinone comprises aldehyde groups on benzene, shown in the 1,4 position (anthraquinone) as seen in Figure 3-2. It is feasible the authors choice to deposit quinones All quinones produced H_2O_2 from ORR. An oxygen reduction wave was catalysed by 2,6-dihydroxyanthra-9,10-quinone (c.a. $E=+0.38V$ Ag|AgCl in pH6) [164].

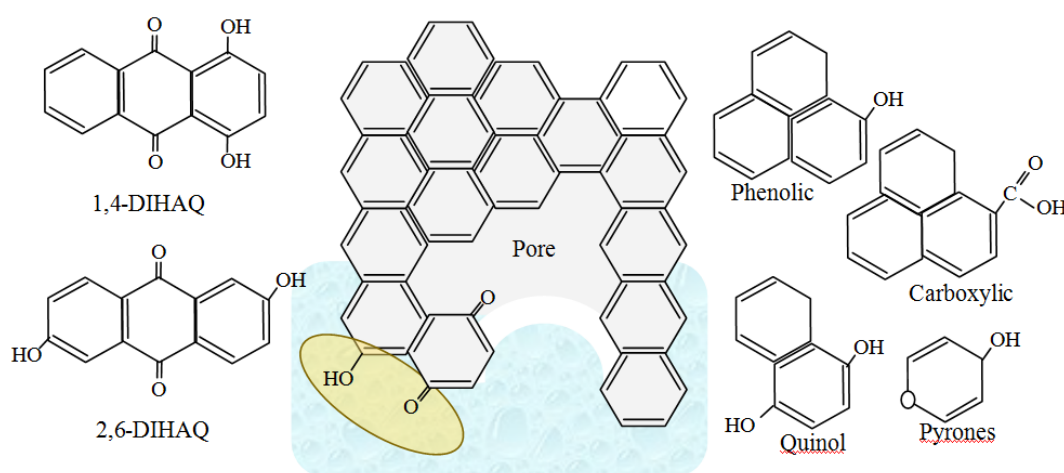


Figure 3-2. Illustration of edge plane active quinone groups on edge plane graphite [164] (left). Quinolic sites in hydrophobic activated carbon (centre) with active site area highlighted (brown). Oxidised edge-place groups (right)

Larsen et al showed that selective OH or COOH functionalization of nanotubes causes H_2O_2 production to increase $\approx 72\%$ H_2O_2 and $\approx 38\%$ H_2O_2 respectively [165] in comparison to unmodified CNT. In addition this group linked higher pyrolysis temperatures to lower the ORR activity.

Wet chemistry approaches for modification include conc. HNO_3 or $ClO^-_{(aq)}$, $O_{3(aq)}$ or H_2O_2 . Edge plane groups that are quinolic, carboxylic or phenolic structures (Figure 3-2) can be produced. Erable et al, improved ORR activity of graphite granules as an MFC catholyte filler using concentrated HNO_3 [166]. Duteanu et al compared HNO_3 treatment of activated carbon (Vulcan XC-72R) to treatment with strong KOH, H_2O_2 ,

H₃PO₄ solutions [121]. ORR current increased with HNO₃ treatment from 1 to 2 A m⁻² at $E=-0.3\text{V}$ (vs. Ag|AgCl). The E_{ORR} was largely un-affected by the oxidative treatment of HNO₃.

In pyrolysis the carrier gas, maximum temperature (T_{max}) and duration affect edge plane chemistry and morphology of re-graphitisation. Pirjamali et al outline a matrix of treatment methods of Ketjen Black carbon [167] that involve (a) HF/HCOOH acid treatment, (b) heat-treatment; $T_{\text{max}}=600/900^{\circ}\text{C}$ in H₂/N₂/CO₂. All treatments produced uniform ORR performance ($E=294\text{-}206\text{mV}$ at 50mA cm^{-2}), with highest temperatures in non-reducing carrier gases creating greatest ORR current. Significant increases in surface area are obtained with $T_{\text{max}}>900^{\circ}\text{C}$ in all carrier gases (753 to $913\text{ m}^2\text{ g}^{-1}$ in N₂). Symański et al compiled information on degradation temperatures of carbon structures. They report on Pyrones and some quinol (Figure 3-2) groups are the only original C-O_x species to survive $T_{\text{max}}=900^{\circ}\text{C}$ pyrolysis.

Metal can be incorporated into the graphite sheet itself using 1) pyrolysis in a carrier gas (such as NH₃) that will produce chelating sites 2) adsorption of readily chelated metals (N₄, N₂S₂ or S₄) on basal planes and pyrolysing [168, 169] or plasma-treating [170, 171] the resulting carbon. This is discussed in more detail in 2.2.8.

3.2.6 Enzymes

Enzymes are the most active ORR catalysts available, typically harvested purified from fast growing gram negative aerobic organisms such as the fungi *Myrothecium Verrucaria*. The active site is a multi-copper oxidase consisting of three copper atoms each co-ordinated by 2-3 imidazole's [172]. Gupta et al incorporate this enzyme into an air cathode [173], the response to polarisation is impressive, from $OCP=0.65\text{V}$ (Ag|AgCl) and $J_0=2\times 10^{-5}\text{ A cm}^{-2}$ an ORR wave of $b_c=-26.6\text{mV dec}^{-1}$ is seen, offering a significant improvement over Platinum. The authors offer a kinetic explanation of $2e^-$ transfer with $\alpha=0.5$ or $4e^-$ transfer with α being far from 0.5. In the view of the author of this thesis, migration of the adsorbed oxo-species between multiple sites complicates this issue. Establishing the RDS and $E^{0'}$ of each sequential activated complex will provide an answer.

Some organisms prioritise enzyme stability over activity, the Fe-heme/Cu oxidase possesses an active site potential of $E=0.142\text{V}$ vs Ag|AgCl at pH7, (roughly analogous to *OCP*) [18]. The opposing copper site scavenges toxic peroxo species, even so enzyme lifetimes are only days [18] for mammalian mitochondria. Such a stability limitation makes utilisation of enzymes in cathodes for wastewater treatment impossible even with ion selective membranes.

3.2.7 Biocathodes

Biocathodes may operate over a wide pH range, many organisms acidify (*Leptothrix* Discophera [110]) or alkalify (catalase +ve organisms) as a result of their metabolism. They are typically employed in MFC for removal of electron acceptors that are viewed as pollutants, such as NO_3^- , ClO_4^- , Cr(IV) azo dyes or even O_2 [174]. Examples can be found in Table 3-1. You et al [175] attained ORR at $E<0.525\text{V}$ (Ag|AgCl) from an biofilm grown from activated sludge. The conditions required to cultivate such a biofilm from wastewater may not apply to an air cathode with chemical electrocatalyst, fouling is not anticipated to be beneficial.

3.3 Transition metal macrocycles for ORR

Transition metal macrocycles are inspired by enzymes found in cell membranes, blood and cytoplasm [18]. All chlorophyll and bacteriochlorophyll comprise of a porphyrin type macrocycle ligand with a magnesium nucleus. Cobalt nucleus macrocycles can perform isomerisation's, demethylation or dehalogenation in the body (Vitamin B₁₂). Iron nucleus macrocycles react with oxygen species such as O_2 (catalase, haemoglobin) or H_2O_2 (cytochrome-C). All consist of a transition metal co-ordinated by four pyrrole nitrogen atoms [18]. They are capable of adsorption of oxygen providing O_2 can substitute the existing ligand (such as H_2O or X^-). In nature, planar Iron N₄-macrocycles may possess aliphatic tails or electronegative groups, altering the $E^{0'}$ of the heme. These “periphery groups” are attached to the outer pyrrole. Synthetic Phthalocyanine ligands contain periphery benzene making them insoluble (MePc). The similarity between the O_2 binding site in haemoglobin (Haem B) and Iron Phthalocyanine (FePc) can be seen in Figure 3-3.

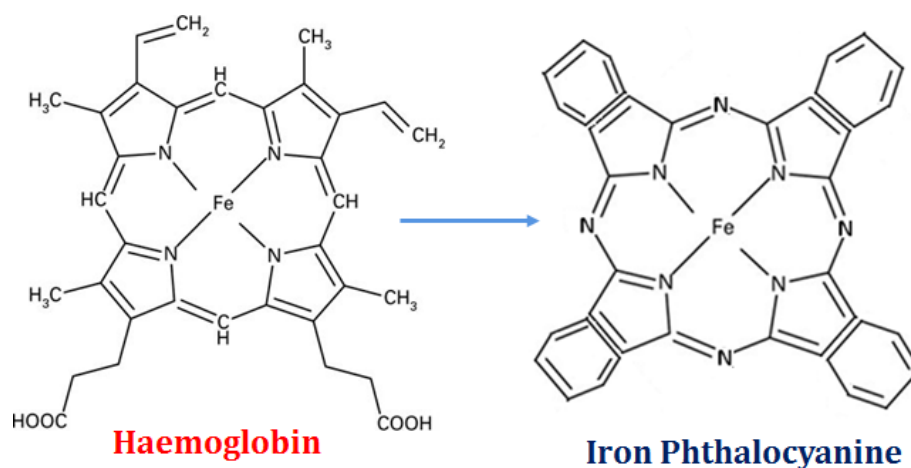


Figure 3-3. Similarities between Haemoglobin and Iron Phthalocyanine

After co-ordination by a tetra dentate N₄-macrocyclic ligand such as porphyrin or phthalocyanine, the iron possesses two remaining vacant ligand spaces for mono dentate ligands [176, 177]. Typically in aqueous solution each one of these spaces can be occupied by “axial ligands” that can be; 1) H₂O 2) a reactive oxygen species; O₂, •OH, H₂O₂, OOH₂ or elementary •O• 3) a solvated anion; Cl⁻, HPO₄²⁻, NO₃⁻, SO₄²⁻, CN⁻ etc. 4) a nucleophilic compound; imidazole, pyridine, ammonia etc [177]. The response to polarisation from an Iron-N₄ macrocycle varies with the axial ligand. Stronger ligands substitute weaker ones as seen in the spectrochemical series [178]. Previous studies attribute the total electro negativity of all ligands to the redox potential of the metal ion [179-181].

Metal phthalocyanine's have been studied for ORR in neutral media. Firstly by Savy et al [182] (Me=Co, Cu, Fe and Ni), who assessed monomer and polymer phthalocyanine's for oxygen reduction in pH 6.7 PBS. This study demonstrated an important aspect for the most active Phthalocyanine forms; ordered polymeric deposition improved ($-b_c$) tafel slopes.

Heat treated versions of various metal macrocycles on carbon support supports were assessed in a gas diffusion half-cell (GDC) by HaoYu, et al [169]. Pyrolysis alters the active site. This study performed the first neutral pH comparison of different chelated metals when embedded into graphite by pyrolysis [183]. A Platinum air cathode was used as a performance bench-mark. Macrocycles of Manganese, Cobalt, Iron and mixtures of Iron-Copper and Iron-Cobalt were precipitated on carbon supports from concentrated H₂SO₄ solutions then washed then pyrolysed at 800°C. Composite

macrocycle mixtures of copper and cobalt did not improve intrinsic activity, Cobalt and Iron Phthalocyanine's (Ketjen Black support) produced the best result. In an MFC the FePc on Ketjen Black produced the highest power output (634mW m^{-2}) with a biofilm on a NH_3 activated carbon cloth in 50mM PBS and Glucose.

Following this result the pyrolysed FePc catalyst was studied with electrochemical impedance spectroscopy (EIS) and Galvanostatic polarisation [184]. Air cathodes were subjected to potentiostatic EIS, the resistance associated with electron insertion into O_2 , the resistance to charge transfer (R_{ct}) was 131.8Ω at *OCP* and reduced to 40Ω at an applied potential of 0V (Ag|AgCl). A separate term associated with resistance from O_2 adsorption rate onto the iron site produced a less significant resistance (0.1Ω) at -0.2V but increased between 0V and -0.2V, reaching 3.16Ω at *OCP*. At *OCP* this value is 1/40 the R_{ct} value, demonstrating that O_2 adsorption is not a limiting step below *OCP*. ORR proceeded by a -62mV dec^{-1} tafel slope in PBS.

The nature of the active site after pyrolysis was explored by Lalande et al using time of flight secondary ion mass spectrometry [183]. Pyrolysis at 500-600°C (of FePc on carbon black) yielded the most active catalyst in acid media but reasonable stability was only observed at 700-800°C. This active form was correlated to surface evolution of Iron and Nitrogen indicating the nature of chelation has drastically changed. The FePc molecule suffered complete deterioration between 500-600°C, though partial deterioration initiated at lower temperature.

The catalytic activity is linked to the Fe(II)/Fe(III) redox potential [32, 169]. Due to large variation in produced sites resulting from pyrolysis it is easier to draw conclusions about ORR mechanisms catalysed by FePc without pyrolysis. Li et al use the density functional theory approach, asserting that the sequence of oxygen reduction starts with the Fe(II) state, in FePc. The basis being the low binding energy of Fe(II)- $\text{H}_2\text{O}=0.10\text{eV}$ [185] making H_2O substitution by O_2 favour the forward reaction, compared to the generated intermediary state; Fe(II)- $\text{O}_2=0.12\text{eV}$.

The rate constant of the next step ($k_{\delta C}$) is thought to vary drastically according to pH [186]. The rate constant is very high and instantaneous in all but low pH, favouring the forward reaction.



Baker et al show irreversible FePc attachment to basal plane graphite when immersed upside-down in a FePc solution of Isopropanol, a solvent that forms a weak ligand [179]. The known geometry of molecular Iron Phthalocyanine on a basal plane ($1.5 \times 10^{-14} \text{ cm}^2$). They establish that this method produced an average deposition equating to 2.1 monolayers, suggesting primarily flat adsorption (see Figure 3-4). ‘Edge on’ adsorption of FePc Benzene groups perpendicular the graphite plane was the explanation for the value being larger than anticipated. Coulometric analysis on the thin FePc layers show linear correlation between Fe(II)→Fe(III) peak height (J_p) and the scan rate (v). As such, they demonstrate that the removal/insertion of electrons from the monolayer requires no diffusive element.

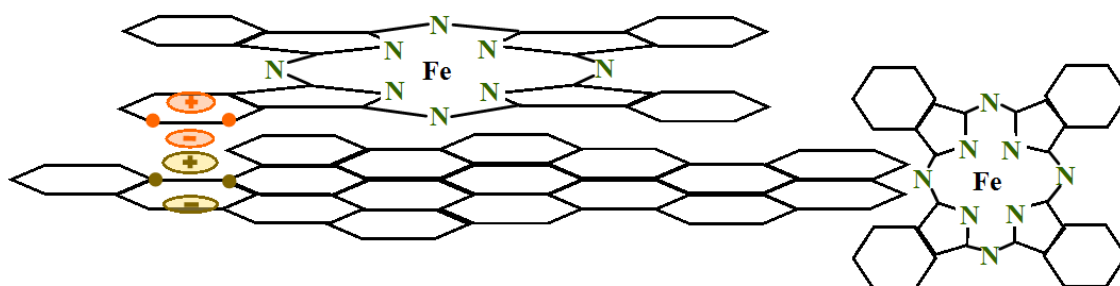


Figure 3-4. A schematic representation of the types of FePc deposition on graphite planes, basal – arising from π -bond overlap (brown and orange), and edge plane.

In neutral media, Kozawa et al provide a series of i - E responses for FePc and elementary metals in Phosphate Buffered Saline [187, 188]. Cl^- and $H_2PO_4^-$ adsorption are accounted for in FePc activity. They investigate potential catalysts supports for intended blood medium applications. FePc layers catalysed ORR waves more efficiently than metallic Au, Ag, Ni, Mo, Ti, Nb, Ta, Zr and TiB₂ alloy, only Pt and Pd outperformed FePc-Graphite electrodes.

CH_3COO^- (acetate) Me^{2+} adsorption onto FePc are evaluated by RRDE [176]. The information can be adapted to FePc use in an artificial and real wastewater medium (Table 1-1). Adsorption of Mg^{2+} and Pb^{2+} cations to Pyrrolic nitrogen in FePc increased the potential of the oxygen reduction wave while Ca^{2+} had no effect. FePc catalysed ORR waves at E =c.a. 0.18V in PBS and E =c.a. 0V in CH_3COONa , though H_2O_2 reduction was identical in either anion at equivalent pH. Acetate and PBS adsorption to the FePc was used to account for the difference, though pH change in the un-buffered

CH_3COO^- may also have occurred in the view of this thesis author. CN^- caused FePc de-activation. This was reversible with washing in neutral sodium acetate solution and the *i-E* response of ORR was restored. This suggests that if strong X-type axial ligand adsorption is reversible other substances could reversibly adsorb.

Chen and co-workers also observed reversible $\bullet\text{OH}$ adsorption [70]. DFT calculations on (H_2O , OH , HOOH , O_2H and H_2OO) intermediary oxygen species adsorbed on FePc [70]. They demonstrate that the binding energy of FePc-OH (-3.41eV) is significantly stronger than Pt(111)-OH (-2.39eV) as such desorption without further reduction is unlikely. The orientation of all adsorbed peroxide forms (-0.99eV, -1.01eV) is slightly less stable than adsorbed water (-1.05eV), suggesting H_2O substitution of H_2O_2 and peroxide release is possible if H_2O_2 is formed, enhancing rate k_{6f} . FePc passivation as the FePc(OH)₂ moiety with a DFT value of -1.05eV may result from H_2O_2 homolysis. This was suggested as the de-activating ROS species for FePc. The implications being that inert FePc will regain activity by washing with aerated or de-aerated alkali. OH-FePc-OH would be gradually substituted by two H_2O ligands or O_2 .

Scherson et al draw attention to the HO_2 and OH^- intermediary/product, with O_2 adsorption being blocked and FePc de-activated. Another de-activation mechanism arising from H_2O_2 was highlighted by Nilekar et al who detected cleavage of the nitrogen atoms connecting the pyrrole ring as the likeliest point of chemical/thermal disintegration [189]. The product of reaction between FePc and strong H_2O_2 would be phthalic anhydrides, detectable by Mößbauer spectroscopy.

Van der Brink, et al present an important study where they isolate the individual reaction rate constants k_1 , k_{2f} and k_{3f} (Figure 2-8) in alkali media [67]. In the unsupported thick FePc film direct $4e^-$ route dominated by two orders of magnitude at low overpotential ($k_1=10^{-4} \text{ m s}^{-1}$ at +0.7V vs RHE). As such, peroxide release by FePc films should be below 1% at low η in alkali. Secondary H_2O_2 reduction (k_3) increases in unison with peroxide production (k_{2f}) in this region. At high η the rate constant of peroxide production (k_{2f}) increases to be larger than direct $4e^-$ reduction (k_1) at $E=+0.18\text{V}$ vs RHE. It has been demonstrated that in porous carbon supported FePc electrodes the actual rate of H_2O_2 reduction ($[\text{FePc-H}_2\text{O}_2]*k_3$) and disproportionation ($[\text{H}_2\text{O}_{2(\text{aq})}]*k_{4ii}$) cannot keep pace with H_2O_2 production [190].

Savy et al studied α and β FePc forms deposited on Au [191] or carbon [182, 192]. These films are crystalline and stacked along the molecular plane with 0.373nm Fe-Fe separation (α -FePc). The most pertinent aspect is the use of Phosphate of various pH, allowing direct comparison to this thesis. A linear relationship was uncovered between ΔG of the RDS and solution pH of approximately 19kcal mole⁻¹ in pH6.7 PBS, increasing by 2.7kcal mole⁻¹ per pH unit [192].⁵ A Langmuir adsorption isotherm was established [192]. In their last study they show that the reduction of Fe(III)Pc-O₂⁻ form sets the electrode *OCP* [191] and polymeric (multilayer) FePc deposited on carbon black reduces activation energy, with $|b_c|=37\text{mV dec}^{-1}$, in comparison to monomeric (monolayer) FePc on Au, $|b_c|=82\text{mV dec}^{-1}$ [182]. Substrate plays a large effect at monolayer coverage [191], GC supported monolayers may yield a different result. The effect of multilayer or monolayer FePc coverage on J_0 was not reported, but extrapolating the graph to the *OCP* produced $\sim 1.1 \times 10^{-8} \text{ A cm}^{-2}$ for FePc on Acetylene Black carbon. The importance of co-facial ‘polymer’ for FePc is noted in some of the literature [191] and could feasibly be destroyed by pyrolysis.

3.3.1 Approaches to enhancing ORR through macrocycle modification

Functional groups on the periphery of the macrocycle ring can be used to change the electron withdrawing/donating characteristics of the macrocycle ligand [191, 193]. This in turn affects the redox potential of the metal [32]. As described by Coowar et al..

“the effect of ligand substitution introducing electron donation to the central ion would be to shift the associated redox potential to more positive values.” [194]

⁵ Based on this value, the author of this thesis calculates $\eta=0$ of the RDS adsorbed reactant and product to occur at 0.619V (Ag|AgCl).

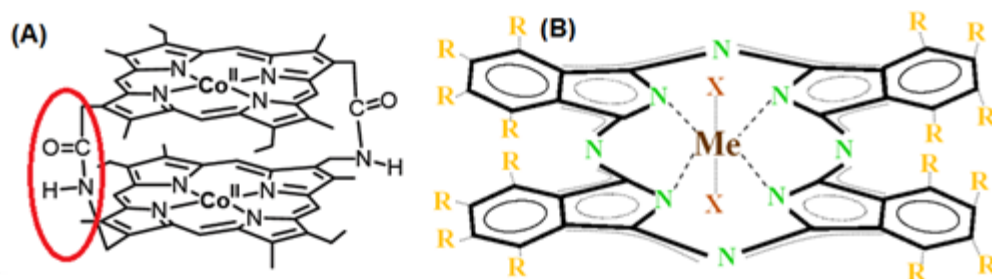


Figure 3-5. Approaches to modifying Me Phthalocyanine activity for ORR; (A) A co-facial oligomer [195] and [196]. (B) Axial ligand X, or periphery groups R, for Fe metal.

In unmodified FePc position R contains Hydrogen (Figure 3-5). Substitution with Cl, F, NO₂, SO₃, OCH₃, NH₂ or COOH and replacing benzene molecules with pyridines and methyl pyridines have been studied [32]. A near perfect correlation was found between the electron withdrawing strength of the new macrocycle ligand (Hammett Parameter) and the redox potential $E^{0'}$ of the metal ion it co-ordinates [197]. In FePc, the Hammett parameter value, $-\Sigma\sigma=0$ for the Pc ligand [198], negative $-\Sigma\sigma$ values increase the $E^{0'}$ of Fe(II)/Fe(III) and the overall rate constant, k_{app} . The maxima for the Fe(II)/Fe(III) has not been found for planar ring modified FePc [199]. The drawback of this approach is increased solubility and that $E^{0'}$ can only be 'tuned' within a certain range.

Zagal et al show a plot of E at $J_k=30\mu\text{A cm}^{-2}$ vs Me(II)/Me(III) $E^{0'}$ of O₂ reduction creates a linear relationship with Fe, Mn or Cr for periphery modified Phthalocyanine's. The gradient was 0.8 (dimensionless) and the $E^{0'}$ ranged across 0.25V for each metal [199]. Multilayer deposition on carbon blacks may be affected by periphery ligands, disrupting the π -bond lattice (Figure 3-4).

Co-facial oligomers with molecular spacers can be formed with periphery group modification Figure 3-5(A) to alter Me-Me separation. For FePc this results in two faces being available for ligand addition from the electrolyte. The co-facial oligomer is better suited for 5-valent metals such as CoPc (one ligand vacant). Frémond et al [195] demonstrated this turning a 2e⁻ ORR CoPc catalyst into a 4e⁻ catalyst.

Axial ligands may be added by treatment of FePc treatment or adsorb from the electrolyte. This produces an adduct (AB) or bis adduct (AB₂), which can be defined as a combination of two distinct molecules (A and B) with no loss of electrons or protons and the formation of two bonds with a net reduction in bond multiplicity present in at

least one of the reactants (Eq.3-6). The resultant species may have unique electrochemical properties not present in A or B.



In FePc, the adsorption of the 5th and 6th mono dentate or a single bi dentate ligand form adducts with a significant shift in E^0 [67]. Ponce and Zagal improved FePc monomers (low activity) by tethering them to the Au support by a thiol presenting a phenyl amine or pyridine axial ligand to FePc. This produced an increase in the potential of the ORR wave of 0.1V and 0.2V respectively (pH4). In pH4 de-metallation will have a strong impact, the author of this thesis expects this approach to stabilise the FePc from demetallation (Eq.3-8) but the effect on stability was not reported.

Contamin et al state that Phosphate adsorption from the electrolyte (position X on Figure 3-5[181]) displaces H₂O adsorption on FePc [84]. As with O₂, Phosphate may adsorb as a mono dentate or bi dentate ligand [200, 201]. Simultaneous ligands of mono dentate O₂ (end on) and mono dentate Phosphate are feasible, as such the activity in PBS may be unique amongst anionic salts. They state that electrocatalytic activity to O₂ binding and reduction on the remaining ligand position will be affected.

Table 3-2 lists kinetic parameters of electrochemical studies on Iron Phthalocyanine with different deposition methods and electrolytes. In alkali media slopes of $30 < |b_c| < 40 \text{ mV dec}^{-1}$ are generally reported. However, there is generally discord as to the reason why. Appleby et al, suggest that the low tafel gradient (30 mV dec^{-1}) is due to a chemical reaction RDS between H₂O and adsorbed HO₂⁻ [202] to produce two •OH radicals. The •OH radical could be reduced in the inner Helmholtz plane meaning a N_{ORR} of almost 4. In two studies by Zagal et al, large tafel slopes dominate ($|b_c| = 150 \text{ mV dec}^{-1}$) [186, 199], the author observed higher surface loading decreases $|b_c|$. The ‘dipping’ in FePc solution method of surface attachment may have resulted in monolayer or sub-monolayer coverage. Table 3-2 aims to link the RDS to deposition method and media.

Table 3-2; Summary of ORR kinetic studies on Iron Phthalocyanine. Influence of deposition method and electrolyte. Plotted from earliest to latest to assess evolution of theory.

Deposition Method	Electrode supp./Binder	Electrolyte	Tafel Gradient (/b _c /)	4e ⁻ / 2e ⁻ or <i>N_{ORR}</i>	Rate Determining Step (RDS)	
Monomer FePc film vacuum deposition on Au (1000Å)	Au / no binder	pH6.7 PO ₄	55mV dec ⁻¹	-	-	[182]
10% wt. FePc on Acetylene Black – Polymer film 30Å	Au / no binder	pH1.3 PO ₄	82mV dec ⁻¹	-	-	
		pH6.7 PO ₄	38mV dec ⁻¹	-	-	
		pH 1.3 PO ₄	45mV dec ⁻¹	-	-	
10% wt. FePc on Acetylene Black (30Å film)	Au / no binder	pH12 PO ₄	29mV dec ⁻¹	-	O ₂ ⁻ (ads)+2H ₂ O+3e ⁻	[192]
		pH6.7 PO ₄	37mV dec ⁻¹	-	→ 4OH ⁻	
		pH1.3 PO ₄	45mV dec ⁻¹	-	HO ₂ ⁻ (ads)+3H ⁺ +3e ⁻ →H ₂ O	
Monomer FePc films vacuum deposition on Au (4100Å) /(1300Å FePc film)	Au / no binder	pH12 PO ₄	62mV dec ⁻¹	2e ⁻ or 2e ⁻ +2e ⁻	-	[191]
		pH6.7 PO ₄	60mV dec ⁻¹	-	-	
		pH1.3 PO ₄	55mV dec ⁻¹	-	HO ₂ (ads)+H ⁺ +e ⁻ → H ₂ O ₂	
Vacuum deposited film	Au / no binder	6N KOH	30 mV dec ⁻¹	4e ⁻ > 0.6V	HO ₂ ⁻ (ads)+H ₂ O→ 2•OH +OH ⁻	[202]
Ferrocene/TCB on Acetylene black	Thin PTFE on Al mesh/PTFE	6N KOH	40 mV dec ⁻¹	-	“	[203]
H ₂ SO ₄ prec. on acetylene black		6N KOH	55-65 mV dec ⁻¹	-	-	
Gas phase dep. FePc; on Cl ₂ treat Carbon at 2000°C on Ar treat Carbon at 2700°C	Thin PTFE on Al mesh/PTFE	6N KOH	30 mV dec ⁻¹ 1 50 mV dec ⁻¹ 1 90 mV dec ⁻¹ 1	- - -	Polymer; HO ₂ ⁻ (ads)+H ₂ O → 2•OH+OH ⁻ Monomer; Fe ^(III) Pc+O ₂ → Fe ^(III) Pc-O ₂ ⁻	[204]
FePc-Pyridine equilibrium ads. on carbon ¶	Au screen / PTFE	8N H ₂ SO ₄	85mV dec ⁻¹	-	1 st e ⁻ transfer	[205]
FePc-H ₂ SO ₄ prec. (20% wt. FePc on carbon)	Au screen / PTFE	6N KOH	35 mV dec ⁻¹	-	2 nd e ⁻ transfer	
		8N H ₂ SO ₄	85mV dec ⁻¹	-	1 st e ⁻ transfer	
		6N KOH	35 mV dec ⁻¹	-	2 nd e ⁻ transfer	
Non-supp. – Deposited from H ₂ SO ₄ (polymer FePc) ¶	PG / Binder less	1M KOH	60mV dec ⁻¹	4e ⁻ to η=100mV	1 st e ⁻ transfer RDS.	[206]
Non-supp. – Deposited from Pyridine (monomer FePc)¶	PG / Binder less	1M KOH	120mV dec ⁻¹	<4e ⁻ η>100mV	OH ⁻ desorption not limiting at pH13	
H ₂ SO ₄ prec. Or Pyridine equilibrium ads. on BRX ¶	Au / Binder less	6N KOH	50 mV dec ⁻¹	<4e ⁻ , same at all E	-	[207]
Vacuum deposit (450°C) on Gold	Au / binder less	1M KOH	120 mV dec ⁻¹ at low η	4e ⁻ then <4e ⁻ at E<0.75V	Fe(III)Pc-O ₂ ⁻ +e ⁻ →Products (low η)	[67] [208]
Non-supported – Equilibrium ads. from Pyridine solution ¶	PG / Binder less	1M KOH	-	-	-	[209]
		0.5M H ₂ SO ₄	-	2e ⁻	-	
BRX Carbon – FePc from DMSO equilibrium ads. or H ₂ SO ₄ prec.	Au / PTFE	8N H ₂ SO ₄	~72mV dec ⁻¹ ~72mV dec ⁻¹	-	-	[210]
Non-supported – Equilibrium ads. from FePc-DMSO on PG	PG / binder less	0.1M NaOH	40mVdec ⁻¹ (η=0-50mV)	-	Fe(III)Pc-O ₂ ⁻ →intermediates	[186]
Non-supported – Equilibrium ads. from FePc-DMSO on PG	PG / Binder less	0.1M NaOH	150 mV dec ⁻¹	4e ⁻	1 st e ⁻ RDS; 1e ⁻ + Fe(III)Pc(O ₂ ⁻)→products	[199]
Equilibrium ads. FePc-Ethanol to Vulcan (α-phase)	GC / Binder less	0.5M H ₂ SO ₄	α-65mV dec ⁻¹ for E>0.7V _{RHE} 121mV dec ⁻¹ for E<0.7V _{RHE} β-FePc; 65mV dec ⁻¹	α-phase; 0% H ₂ O ₂ >0.7V _{RHE} , 4% H ₂ O ₂ <0.7V _{RHE}	1 st e ⁻ transfer step; Fe(III)Pc-O ₂ ⁻ +H ⁺ +e ⁻ →Fe(II)Pc-O ₂ H at E<0.7V _{RHE}	[211] [212]
α-phase Heat treatment 450°C produces (β-phase)				-	“ “	
Non-supported- Equilibrium ads. IPA/H ₂ O sol. Monolayer	GC / Binder less	0.1M H ₂ SO ₄	92 mV dec ⁻¹	3	O ₂ -Fe(II)Pc+e ⁻ +H ⁺ →HO ₂ Fe(III)Pc	[213]
H ₂ SO ₄ prec. on Vulcan XC-72R carbon	GC / Nafion	0.1M NaOH	42mV dec ⁻¹ (1 st) 120 dec ⁻¹ (2 nd)	3.8	FePc/C and Pt/C similar RDS of O ₂ adsorption	[70]

Key

Poly=Polymer, Mono=Monomer, CNT=Carbon Nanotubes, THF=Tetrahydrofuran, ads.=adsorption, GC=Glassy Carbon, PG=Pyrolytic Graphite, BRX=Norit BRX carbon black brand, TCB=Tetracyanobenzene, prec.=precipitation, pyr.=pyrolysed, “““=as

above, ¶=remaining Pyridine adduct, no thermal removal ($T>245^{\circ}\text{C}$), 9. Results for highest BET area carbon. Low BET carbon resulted high $|b_c|$. Additional studies on FePc kinetic information; [176, 183, 187, 188, 214-221]. Studies were plotted earliest to most recent to assess theory evolution.

Some key observations on kinetic studies;

- Van de Brink suggests that the back-binding step with oxygen is not the RDS [67].
- Van de Brink [67] and Zagal [222] show discord on the nature of the RDS in alkali. Van der Brink et al argues that the Fe(III)Pc-O_2^- oxidation state would not be stable and that a single e^- accepting RDS would result in $|b_c|=120\text{mV dec}^{-1}$.
- Zagal et al [32] state the onset of ORR should be strongly controlled by electro-reduction of Fe(III)Pc-O_2^- or $\text{Fe(III)N}_x\text{-O}_2^-$ adduct.

An unusual characteristic of FePc is H_2O_2 production at high potential, as seen from N_{ORR} values in Table 3-2. Metals and alloys release H_2O_2 at higher overpotential. The $E^{0'}$ of H_2O_2 release from Pt in pH7 depends on the C_{0,O_2} and anion activity co-efficient. The $E^{0'}$ of H_2O_2 is between 0.075V ($p[\text{O}_2]=1$, 1M H_2O_2 , 1M SO_4^{2-}) [223] or 0.12V for a more realistic conditions ($C_{0,\text{O}_2}=0.2$, 5mM H_2O_2 , 1M SO_4^{2-} [17]). It is likely that $C_{0,\text{H}_2\text{O}_2}$ is not a consistent concentration and significantly smaller than 5mM, causing a larger $E^{0'}$.

3.3.2 Approaches to enhancing stability through macrocycle modification

Baranton et al showed deactivation from de-metallation (Eq.3-8) is significant in FePc [211]. A 65% reduction in ORR current occurred from polarisation of unpyrolysed FePc for 3hrs ($E=0.5\text{V}$ vs RHE).



The reaction occurs from certain formation of non-redox active adducts. Stefan et al showed that $\bullet\text{OH}$ and H_2O adducts cause Fe^{2+} heme to ‘pop’ out of the macrocycles plane changing the Fe-N distance from 1.95 to 1.98Å [224]. With O_2 adsorption this distance increases even further, and iron is then susceptible to demetallation.

Demetallation of FePc has been studied in K_3PO_4 electrolyte [176], Tang et al found that stability occurred \sim pH9 but rapid deterioration at pH5-7.

Heat-treatment increases performance in acidic media with pyrolysis [183, 209, 225]. Pyrolysis of FePc in inert atmospheres (argon, N_2) completely disintegrates the macrocycle at $T > 400^\circ C$. This has been confirmed by ToF-SIMS data and XRD [183], and thermo-gravimetric analysis [226]. FePc catalysts may retain a small peak after pyrolysis at high temperatures [227, 228], but surface concentration of viable catalyst is higher at $T \leq 500^\circ C$ [183], though less stable.

In PBS-artificial wastewater medium pyrolysed FePc on Ketjen Black ($T = 700^\circ C$) retained a redox peak [113]. After pyrolysis at 1000 or 800 $^\circ C$ no increase in $E^{0'}$ of Fe(II)/Fe(III) is seen [183, 229]. In alkali media, the stability improvement of FeN₄ chelate pyrolysis is relatively unstudied. Savy et al report that air cathodes of FePc perform better at 300mA cm⁻² without pyrolysis ($E = -0.49V$ vs Hg|HgO) than with ($E = -0.6V$ vs Hg|HgO). They reported galvanostatic potentials to be higher for FePc than pyrolysed FeTPP [230], requiring 500hrs of operation at 150mA cm⁻² before significant de-activation.

The model of Fe-N_x intercalation into the graphite sheet with pyrolysis is proposed by Lalande et al [183]. If accurate, the prevalence of co-facial mechanism sites could be greatly reduced and the O₂ binding in Figure 2-10(D) would be less prevalent. The Fe-Fe separation in α -FePc is 3.73Å [191], graphite sheets are separated by 3.35Å. The former distance allows for Fe-Fe sites to form staggered di-oxygen fixation across the Van der Waals planes between graphite sheets. It is plausible that the number of sites with an Fe-Fe distance of $3.6 < \text{\AA} < 3.9\text{\AA}$ is negligible in number.

In conclusion the methods employed to enhance FePc activity can be broadly split in to two groups 1) axial ligand modification (Me-N distance), and 2) controlling Me-Me distance, and 3) periphery ligand modification. As noted by leading authors [32], the effect of the Phosphate ligand is largely unstudied for FePc, though a PO_4^{3-} ligand should impede charge donation to O₂ [231].

3.4 Anion Exchange Materials

3.4.1 Anion exchange material implemented in MFC

Saito et al, put forward [232] a study on Polyphenylsulfone of various degrees of sulfonation, which affect the cation exchange capacity in MFC cathodes. The most hydrophobic binder with 0% sulfonation produced the highest current in half-cell LSV and single chamber MFCs. The decrease in performance with increased sulfonation was attributed to charge transfer resistance (R_{ct}) rather than O_2 mass transfer resistance. R_{ct} ranged from 8Ω (no sulfonation) to 23Ω with an ion exchange capacity of 2.34 meq/g. They propose an uneven dispersion of non-ionic binder is beneficial, exposing some Pt surface[232], making uncovered Pt highly active which was evident from the decreased J_0 but increased α value suggesting that sulfonate ionomer covered Pt to be a different active site. Though α values (<0.1) are low when compared to literature values in the presence of Phosphate [233]. In the view of the author of this thesis the high ionomer loading (400 μ l of 5%wt. ionomer per cathode) will cover a large portion of the Pt surface, $\frac{1}{4}$ this binder loading being a typical amount.

3.4.2 Anion exchange groups

A small number of cationic groups have been assessed in alkali media and one in neutral media (quaternary ammonium). The list of eligible anion exchange groups is extensive and can be based on Phosphorous or Nitrogen cations [234].

3.4.3 Dabco chemistry

Dabco is an organic chemical that functions as a quencher of singlet oxygen in both air and liquid media [235]. It is also capable of metal chelation, iodide fixation and catalyses a variety of organic synthesis reactions [236]. Several patents have implemented supported Dabco as an anion exchange material [237-239]. A polyepochlorohydrine supported Dabco [237] focused on chloride exchange and found to be suitable for exchange of large anions (eg. boric acid sugar esters) which would otherwise block the pores.

The study by Ogryzlo and Tang [240] suggests that Dabco quenches O_2 by a partial transfer of charge to upon contact, the O_2 then being adsorbed. This occurs at a potential

closely linked to the ionisation potential (*IP*) of such O₂ quenching compounds [235]. The *IP* of methyl-Dabco and O₂ fixated methyl-Dabco are not known.

Titration of Dabco reveals two buffering regions; Dabco(H⁺)₂/Dabco(H⁺) $pK_a=2.97$ and DabcoH⁺/Dabco $pK_a=8.82$ [241]. Dabco is also a weak base exchanger $pK_b=5.18$ [242]. Methyl-Dabco is usually represented in the ionic state [243]. The pK_a of ethyl-Dabco or QDPSU is anticipated to shift relative to Dabco. In addition, chelation of oxygen, metal or a counter-ion may alter the base equilibrium. Protonated Dabco on an Ag|AgCl electrode in de-oxygenated Chloride [241] has previously shown adsorption on AgCl as a function of potential, indicating amine-Cl bond formation. A similar effect has been observed with Phosphate [244]. In acid media Phosphate binding to Dabco produces doubly protonated Dabco and one bound phosphate Dabco:HPO₄²⁻ of 1:1.2 [244].

The Dabco ring opening nucleophilic substitution reaction was outlined by Maras [245], usually requiring high temperature and catalyst. Methyl-dabco is thought to be impervious to this kind of degradation [245] it could plausibly be facilitated by localised environments in the catalyst layer, graphite edge planes or H₂O₂. This would result in soluble Dabco or polymerised two-trimethylated nitrogen sites, possibly redox active.

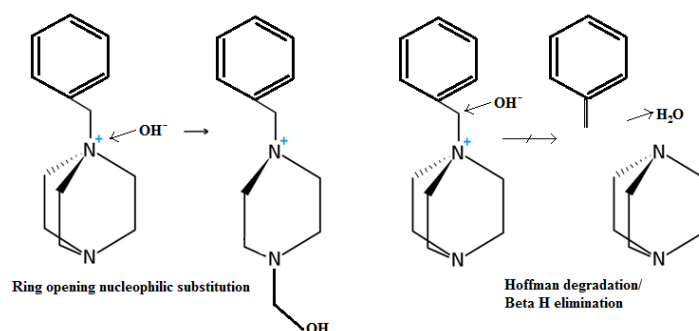


Figure 3-6. Types of nucleophilic degradation recorded in literature.

As in Dabco-Polyepichlorohydrin, the substitution of β -Hydrogen on the Polysulfone backbone (Hoffman degradation) may cause Dabco ejection [246]. This would result in a soluble Dabco moiety. The Dabco moiety itself is not susceptible to beta-hydrogen substitution [246], but an accumulation of H₂O₂ in the catalyst layer could plausibly facilitate other moiety decomposition reactions.

3.5 Anion exchange membranes in bioelectrochemical systems

An improved performance in single chamber Microbial Electrolysis Cells (MEC) with anion exchange materials is also documented by Rozendal et al [247]. The pH gradient was reduced from 6.4 pH units (cation) to 4.4 pH units (anion), thus demonstrating the improved pH balancing (Phosphate) performance of AEM's. An MFC configuration was also used by Rozendal et al [248]. The total amount of charge transferred externally was largest for AEM indicating columbic efficiency benefits. The AEM (Fumasep-FAB) showed a preference for exchange of OH^- over H_2PO_4^- despite the molarity presence of the former being significantly smaller than the later. When viewed as H^+/OH^- exchange as a portion of the total charge exchanged, in other words the selectivity to avoid pH splitting, the highest performance was Bi-polar>Anion>Cation Exchange Membrane.

Van Sleutels et al [249] demonstrate the relative amount of exchanged anions and cations over a batch performance MEC. The clearly demonstrate that H^+ / OH^- exchange is increased with an AEM. The CEM shows a proclivity for exchange of K^+ with an initial concentration change of -0.6 M in the anode compared to a practically unchanged K^+ concentration in the MEC using AEM. Critically, they report that charge transfer resistance in PBS ($80\Omega \text{ cm}^2$) is significantly larger than membrane resistance ($2\Omega \text{ cm}^2$) [249]. They also compared cationic charge transport facilitated by HPO_4^{2-} to that performed by H^+ and OH^- (membrane dependent). Compared to the sum of electrical charge transferred approximately 37% of this value was $\text{H}^+ \text{ OH}^-$ ionic charge transport for the CEM compared to 77% by the AEM. In comparison implementation of the AEM increased transfer by HPO_4^{2-} to only 4% from 1.5% in the MEC utilising a CEM. This would seem to conflict the model put forward by Fan et al [250], who study non-ion selective separators (J-cloth) and identify a carbonate or phosphate cycle as the main mechanism for proton delivery and pH stabilisation in the catalyst layer, ie. $\text{HCO}_3^- \leftrightarrow \text{CO}_3^{2-} + \text{H}^+$ or $\text{H}_2\text{PO}_4^- \leftrightarrow \text{HPO}_4^{2-} + \text{H}^+$. Instead, the study by Van Sleutels et al of ion selective membranes demonstrates the selectivity of the OH^- transit through the membrane followed by neutralisation from a higher pH on the anode side. For PEM membranes, Harnisch et al note that with Nafion 117 trans-membrane diffusion constants are relatively similar for most anions [251].

Ji et al clearly define the interface region of a dual chamber MFC for microbial fuel cell scientists, based on the work on dialysis membranes by Długolecki et al [252]. They break charge transport resistances down into (i) electrical double layer (R_{dl}) at the membrane-electrolyte interface, (ii) diffusion boundary (R_{dbl}), and (iii) membrane polymer phase ionic resistance (R_m) [253]. The double layer (100-300 Ω) and diffusion layer resistances (>700 Ω) become more dominant at the low solute concentrations (10mM PBS) seen in typical microbial fuel cell applications. The resistance of the membrane and electrolyte (R_u) cannot be separated in Nyquist plots. This study also offers typical maximum O₂ flux rates for anion exchange membranes 140-180 μ m thick in contact with a gas diffusion electrode open to the air, the values range from 1.6-3x10⁻⁸ mmol s⁻¹ cm⁻². This provides a guideline for balancing O₂ utilisation against target O₂ diffusion into the cell from a dissolved O₂ source in order to avoid aerobic conditions.

The typical method of ascertaining membrane ionic resistance is the four electrode setup [252, 254, 255]. Fixating a membrane in a two electrolyte chambers between two Platinum foil plates and sensing the potential drop with two Pt wires [256] or two reference electrodes [252, 254]. Gu et al, state that AC impedance analysis with EIS at a frequency range of 1Hz to 100kHz produces a semi-circle on the $-Z''$ vs. Z' plot, the right side of which (R_0) corresponds to the membrane resistance. The frequency range employed in this thesis has produced a di-electric relaxation response in some studies of membranes in aqueous electrolyte [257], though the authors seldom state the nature of the desorbing species.

Nguyen et al provided an equivalent circuit model for a porous electrode with a membrane and current collector [258]. Dielectric relaxation spectroscopy of membranes typically utilises a higher frequency range and is not anticipated to be a problem with this investigation [259]. In Długolecki et al the equivalent circuit for a DC flow of ions is an $R_s + R_m(R_{dl}[C_{dl}])(R_{dbl}[Q_{dbl}])$ in standard notation. In contrast Nikonenko et al [255] observe open ended Warburg diffusion behaviour in place for $R_{dbl}[Q_{dbl}]$ (see Figure 2-22) to explain a linear region in the nyquist plot.

3.6 Analysis of ion exchange materials and redox polymers with EIS

The nature of ion exchange polymer is expected to play a critical role. As stated by Cameron ‘it is important to establish whether electron or ion diffusion limits the performance [102].’

Contamin et al demonstrate that High Frequency (HF) capacitance is associated with Phosphate adsorption on FePc [84], but a linear HF response in the domain of impedance versus square inverse of frequency (Z vs. $f^{-0.5}$) signifies limitation from diffusion of minority carriers that control performance, namely Fe(II) centres in the case of a binder-less vacuum deposited crystalline film. This process could be applied to air cathodes for assessment of binders which facilitate or hinder this process. The intercept of the Z vs. $f^{-0.5}$ linear region extrapolates to the total resistance value of all resistors in series with the Warburg element.

A H₂Pc film [95] was vacuum deposited on a gold electrode and immersed in strong KOH solutions. Charge diffusion accounted for the majority of the resistance. H₂Pc is a p-type semi-conductor as is FePc but O₂ adsorption is reversible (Eq.3-5). Contamin and co-workers evaluate the movement of electrons through this film utilising Eq.2-114, and establish diffusion through the entire film thickness and reaction at the electrolyte/film interface. In their study on FePc films [84], σ vs. E plots and effect of O₂ were not reported, but the idea of competitive adsorption between Phosphate, Oxygen and Glutathione was investigated, using FePc as an analogue of cellular cytochromes.

To the author’s knowledge the approach has not been used to evaluate ionomers in catalyst layer for neutral media, the Koutecký-Levich approach being favoured instead. A study on a Nafion ionomer film in NaCl [99] by Komura et al, focused on the σ vs. E and σ vs. pH behaviour of the film with and without immobilised redox mediator. It was found that electron hopping accompanied by H⁺ migration in the opposite direction controlled the overall diffusion constant, present at $D=1.1 \times 10^{-11} \text{ cm}^2 \text{ s}^{-1}$ in 0.4M HCl, with an abrupt decrease at higher pH.

3.7 MFC systems – Architecture and Substrate Treatment

3.7.1 *Anode biofilm dispersion and models*

Piciooreanu et al performed computer modelling of anodic biofilms on flat and porous electrodes [260]. They input physical constants and initial estimates for parameters, considering charge balance, electromigration, convection (cross-flow) in a porous layer. The models generated concentration gradient maps of localised pH and soluble electron shuttles generated by the bacteria and current production and biomass as a function of time. They mixed fermentive, methanogenic and exoelectrogenic biofilm was fed with mixed organics in wastewater under carbonate buffering. Overall maximum current was expected to decrease in the case of a consortia $J=0.3 \text{ A/m}^2$ vs $J=0.9 \text{ A/m}^2$ for single species as exoelectrogens are reliant on the rate of hydrolysis and fermentation and must compete with fermentive bacteria for acetate. Surprisingly the planar electrode (0 roughness factor) produced more current $J=0.9 \text{ A/m}^2$ ($5 \text{ g}_{\text{biomass}}/\text{m}^2$) than the porous electrode for a single species utilising a mediator. Forced convection, artificial buffering or electrogenesis via nanowires could improve this further. Carbon felt is therefore anticipated to produce a similar power output to that of roughened carbon cloth, with the majority of biofilm being distributed on the felt surface.

Logan et al circumvented this problem by a graphite brush, possessing distinct bristles. Organic diffusion limitation is overcome and extra current collector is required [261]. In this seminal study for lab scale reactor design, maximum biomass and power density was increase with a brush (2.4 Wm^{-2}) designed to fit a cube reactor with a geometrically flat carbon felt (1.07 Wm^{-2}). Such a design would not increase the volumetric power density (W m^{-3}) if the felt were placed closer to the membrane in a compact design.

3.7.2 *Wastewater and coulombic efficiencies*

Velasquez-Orta has obtained high coulombic efficiencies (ϵ_c) from real wastewater. Paper, dairy, bakery or brewery industry wastewater produced $\epsilon_c = \text{c.a. } 80\%$ in single chamber MFC [262]. Autoclaving the wastewater did not drastically alter the result and de-aeration was used prior to insertion. A seven fold increase in conductivity to 7.1 mS cm^{-1} resulted double power output. Fornero et al compile tabulated lists of maximum power densities from various substrates and coulombic efficiencies in batch operation [263]. They cite studies with acetate fed reactors producing $\epsilon_c=99\%$.

Although high COD removal rates for single chamber cubed cell systems up to $167\text{kg}_{\text{COD}} \text{m}^{-3} \text{day}^{-1}$ are obtained [23], the ε_C should be quoted with COD removal rates to avoid consideration of non-electrogenic degradation of organic matter. In this study fermentive and non-electrogenic metabolism caused only $\varepsilon_C=0.7\%$ making exogenous COD removal $1.169 \text{ kg}_{\text{COD}} \text{m}^{-3} \text{day}^{-1}$. Increasing residence time to 4hrs (loading $1.75\text{kg}_{\text{COD}} \text{m}^{-3} \text{day}^{-1}$) increased COD removal to 33% and $\varepsilon_C=26\%$ making exogenous removal $0.150\text{kg}_{\text{COD}} \text{m}^{-3} \text{day}^{-1}$.

3.7.3 Cathodic limitation

In an important study on the limitation of charge transfer observed for the cathode, Fan et al mathematically correlated cathode limitation to electrode area by reducing the size of the anode. They reported R_{ct} and P_{max} (anode based) in single chambered membrane-less MFCs when anode area was altered relative to a fixed Pt air cathode. An infinitely large cathode could be extrapolated from the experimental results. With this approach the theoretical P_{max} obtainable with no solution resistance or cathode polarisation was calculated to be $19,369 \text{ mW cm}^{-2}$ (based on anode area planar diffusion).

By contrast, Table 3-3 highlights cathode design improvements to MFCs using O_2 as an electron acceptor. Not all are mutually implementable (ie. Flow through cathode and PTFE diffusion layers), some could be combined.

Table 3-3. Studies on cathode design improvements effect on P_{max} and OCP.

Design Improvement / Purpose or effect	Cell Design (#Chambers/Anode /Membrane)	Catholyte	Control Setup	Increase P_{max} mW m ⁻²	F	OCP or E^0 / mV vs Ag/AgCl
Sandwich Design (Pt-C, AC.) / + Volumetric Power Density	1Ch/C-Paper /Nafion 115	PBS, Acetate, pH7-Agitated	Anode spaced from cathode MEA-4cm	1180	3.33	≈+400 [264]
Nafion binder (35% wt.) for Pt-C, AC / Improved proton conductivity	1Ch/C-paper /membrane-less	PBS, Glucose, pH7	35% wt. PTFE binder for Pt-C, AC	480	1.33	≈+304 [265]
Low pH (2) Catholyte – FePc-C, pyr. - AC / Higher E^0	2Ch/G-Granules, C-Felt/Gore-Tex	1% NaCl/HCl, pH2. Circulated	pH7 NaCl catholyte	256	1.13	≈+568 [131]
4xPTFE layers air side of Pt-C, AC / reduce O_2 crossover	1Ch/C-Cloth, an-cat= 4cm /membrane-less	PBS, Glucose, pH7	No PTFE diffusion layers	766	1.4	302 [266]
Growth of N-doped nanofibres on SS mesh / reduce cat. resistance	2Ch/Graphite Plate/CEM	50mM PBS, pH7	Platinised SS Mesh	1900	1	- [144]
Flow through cathode / Improve oxygenation and pH balance	Catholyte flow through cathode to anolyte/G- plate/Membrane-less	Glucose AWW	Up flow without De-oxygenation	30	2.1	- [267]
30 Mesh size SS Current Collector and PDMS for Pt-C, AC / balance conductivity and O_2 diff.	1Ch/G-Brush/ Membrane-less	Acetate 50mM PBS AWW	SS-90 Mesh	1616	3.1	177 [268]
Increase specific area of Pt-C, AC (24cm²) / reduce R_{ct}	1Ch/G-Brush/ Membrane	Acetate PBS AWW	7cm ² cathode area	2031	1.3	- [269]
PDMS + SS current collector diffusion layer / Improve O_2 diff.	1Ch/C-Brush/ Membrane-less	Acetate PBS AWW	C-Cloth Current Collector	1610	1.03	585 [143]
Mix CO₂/Air sparged catholyte for Pt-C / use flue gas sparge, replace PBS	2Ch/C-Cloth /AEM- AMI 7001	CO ₂ contact H ₂ O HCO ₃ ⁻ /CO ₃ ²⁻ ions	CO ₂ sparge + 0.1M PBS Catholyte	83	0.74	≈+310 [270]
AC fed moist gas; 21% CO₂, 79% Air mix for Pt-C / Catholyte pH balance	2Ch/C-Cloth /AEM-AMI 7001	Moist AC –some HCO ₃ ⁻	Moist air, no CO ₂ (few solvated ions)	50	2.5	-
Nickel based paint for MnO₂-C, AC. on cloth / Conductive diffusion layer	1Ch/C-felt /CEM	Brewery WW– NaCl, pH8	Graphite based Paint MnO ₂ -C, AC	86	3.5	≈+130 [271]
Glass Fibre 1 Separator for MEA (Pt-C, AC) / non-biodegradable separator and higher CE, 2 biofilms	1Ch/C-Cloth, 2cm from cathode/GF-Separator	Acetate PBS AWW	CEM membrane (CMI-7000)	791	4.47	- [272]
AC cleaned of bio fouling (Aged Pt-C) / ORR selectivity by facile Pt	1Ch/C-Cloth, 2cm from cathode/Membrane- less	Acetate PBS AWW	Before biofilm removal	425	1.05	-
Glass Fibre 1 Separator for sandwich MFC / stop short-circuit - reduce Ω and O_2 crossover	1Ch/Carbon Cloth /GF-Separator	Acetate PBS AWW	2x J-Cloths, Sandwich configuration	1195	1.09	-

Additional Symbols and abbreviations; AC-Air Cathode, Ch-Chambers, PDMS-Polydimethylsiloxane, MEA-Membrane Electrode Assembly, AWW-Artificial Wastewater, SS-Stainless Steel, diff.-Diffusion, GF-Glass Fibre, CEM-Cation Exchange Membrane, CMI-7000-Type of CEM, pyr-Pyrolised, cat.-Cathode, C-Felt-Carbon Felt, G-Carbon (Graphite carbon type=Rod, Granules, Brush, Plate).

3.7.4 MFC lab scale designs

In Figure 3-7 the main MFC lab scale designs are depicted. The single chambered model (A) is the simplest to assemble.

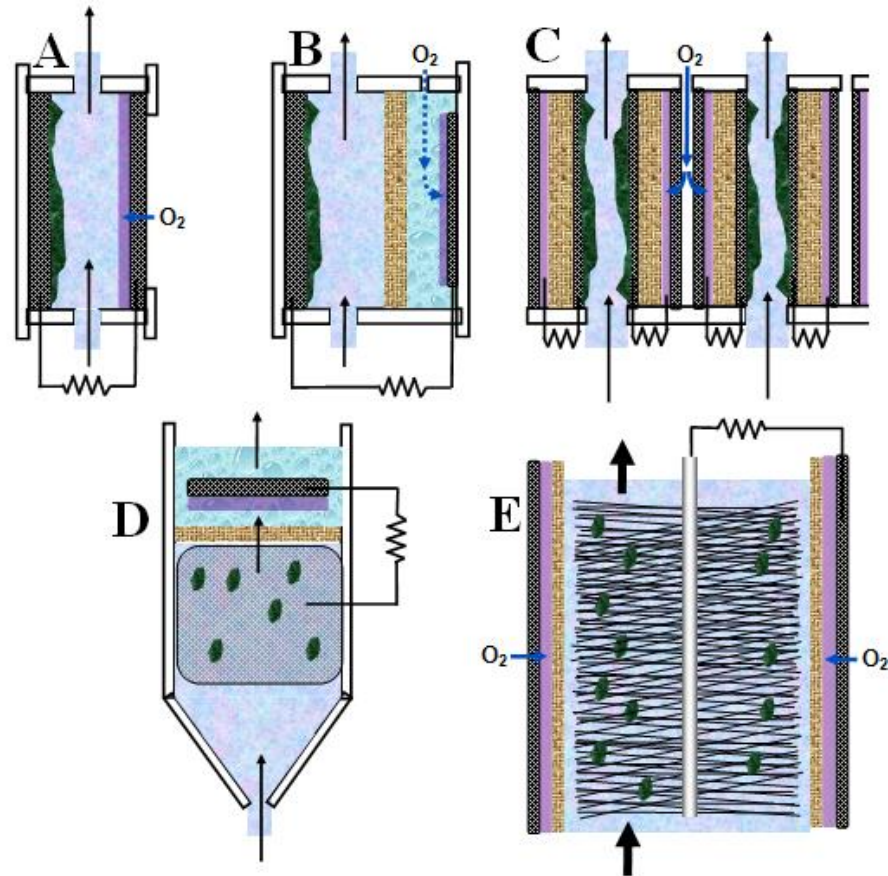


Figure 3-7. Lab-scale MFC designs of continuous flow configuration.

A) Single Chamber air cathode. B) Two chamber design with membrane. C) Sandwich design of anode-membrane-cathode assemblies. D) Dual Chamber Up flow MFC flow-through membrane. E) Single Chamber Tube-MFC, graphite brush anode wrap-around membrane-air-cathode. Green-Biofilm, Purple-Cathode catalyst layer, Black-Carbon, Blue/Purple-Brackish water, Blue-Abiotic electrolyte.

Zhang et al [272] demonstrate that the highest volumetric current density (and therefore COD removal rate) is obtained with a sandwich type MFC, Figure 3-7(C). This improvement is attributed to a decrease in ionic resistance (Table 3-3). Design choice for anode-anode electrode spacing are constrained by clogging of the anolyte channels. This design has been used to produce the largest volumetric power density and COD removal rate by Fan et al [25] and Shimoyama et al [273] respectively, 1.01 kW m^{-3} (0.4cm anode spacing) and $5.8 \text{ kg}_{\text{COD}} \text{ m}^{-3} \text{ day}^{-1}$. Methanogenesis is suppressed due to trace oxygen cross-over through the membrane. The COD removal rate is equivalent to state of the art up flow anaerobic sludge blanket (UASB) technology ($\approx 1.5\text{-}5.3 \text{ kg}_{\text{COD}} \text{ m}^{-3} \text{ day}^{-1}$) [274].

Chapter

4

Chapter 4. Experimental methodologies

4.1 Chapter 5 and 6 Experimental

4.1.1 Catalyst Preparation

Iron Phthalocyanine +95% wt. purity (Alfa Aesar) was deposited using concentrated H_2SO_4 (98% wt. Alfa) or Di-Methyl Formamide (99.7% wt. Alfa). Carbon supports; Carbon Monarch 1000 (Cabot) and Ketjen Black EC300J (Akzo Nobel) are referred to as MON and KJB here-after. Synthetic Graphite, <20 μm particle size (sigma), was used to assess the effect of treatments during carbon black production on the activity in PBS. A 20% wt. Pt/C benchmark (Alfa Aesar) and the Iron Phthalocyanine were used as received. Stepwise preparation method and abbreviated names are shown in appendix Table A-1. Millipore water with 18 $\text{M}\Omega\text{ cm}^{-1}$ resistivity was used to prepare solutions. All chemicals were analytical grade unless otherwise stated. Pyrolysis was performed by placing the catalyst in a ceramic boat (Alfa Aesar) inside an air tight tube (snoop tested). The pyrolysis was preceded by N_2 flushing of the chamber for 2hrs (0.5L min^{-1}) followed by heating at the target temperature of 800°C for 2 hours, at a heating and cooling ramp rate of 300°C hr^{-1} in a dark room [210]. A preparation chart of all catalysts used in this study is contained within the appendix (Table A-1).

4.1.2 Unsupported iron phthalocyanine films

A fully solvated 1.76 mM solution of FePc in DMF was ultrasonicated in an ice bath and a 10 μl aliquot ($\Gamma_{\text{FePc}}=6.77\times 10^{-8}$ Moles cm^{-2}) was applied to a clean RRDE disc. It was allowed to evaporate slowly (40°C) over 1hr. As FePc deposition from a DMF solution onto graphite is instantaneous [70, 275] and yields similar results to deposition from H_2SO_4 [70] in an anticipated α -FePc crystalline form [220]. The resulting electrode was immersed in air saturated PBS, then N_2 sparging under electrode rotation, followed by several polarisations to remove adsorbed O_2 then the data presented in Figure 5-2 was collected.

For potentiostatic scan analysis (Figure 5-10) an RRDE tip with $\tilde{\Gamma}=4\times 10^{-9}$ Moles cm^{-2} of FePc was prepared as above, from a 0.105mM FePc DMF solution. In this instance, no prior polarisation was applied before the presented results.

4.1.3 Binder materials

Binding agents used; PTFE, pH7 Na⁺-Nafion, protonated H⁺-Nafion and a Dabco-Polysulfone based ionomer (QDPSU) were prepared in-house [276]. PTFE (60% wt. emulsion) was purchased from Sigma Aldrich and was diluted (x10) in de-ionised water before use. Neutralised Nafion was prepared from (5% wt.) ionomer (Sigma) received with a H⁺ exchange cation; 15mg of NaOH crystals (Merck) was incrementally added to 10ml of the resin under temperature control (<40°C), the resulting Ionomer had a pH of 6.5 and was fully solvated (Na⁺ exchange cation). This was done to remove problems of catalyst damage or micro-acidic environments which have previously been reported as a problem [113]. A novel in-house anion exchange material consisting of a Dabco based anion exchange material (Cl⁻ exchange anion) side chain grafted onto a Polysulfone backbone was prepared [277], referred to hereafter as QDPSU unless referring to the functional group. Preparation procedure in this study [276] resulted in a loading of 12-15% wt. of ionomer in Di-methyl acetamide. Polymerisation and extrusion of this material successfully produced a membrane in this study.

4.1.4 Ink preparation for thin films

Catalyst inks with high binder contents were prepared. Unless otherwise mentioned, catalyst inks consisted of 10mg of catalyst powder, two drops of DIW, then 340μL of protonated Nafion (Sigma) and 3mL of absolute ethanol. This resulted in binder:catalyst powder wt. of 1.565:1. Inks were ultrasonicated with ZrO₂ balls in a sealed vial in an ice bath until a colloid was formed. An aliquot of 6μl was pipetted onto the clean RRDE GC disk ($A=0.2475\text{ cm}^{-2}$), completely covering it. The loading was $71\mu\text{g cm}^{-2}$ for all catalyst powders. Inks were used within 30 minutes of preparation (exception in section 10.4) to prevent catalyst dissolution, side reactions and irreversible O₂ adducts forming.

For chapter 6 different binder materials were used. A volume (X)μl of unmodified binding agent was added to the 10mg of catalyst powder followed by 3ml of absolute Ethanol (VWR). Volumes of unmodified binding agents (2.1.) were 340μl of H⁺-Nafion (Sigma) or 85μl of QDPSU solvated by DMAC. This resulted in binder to catalyst powder weight ratios of binder:powder=124.5% for QDPSU and 156.5% for Nafion. Inks were ultrasonicated with ZrO₂ balls in a sealed vial placed in an ice bath until a colloid was formed. Resulting inks of pH2 (Nafion) and pH7 (QDPSU).

4.1.5 Deposition of thin films on glassy carbon disc electrode

Surface cleaning of RRDE electrode tip (Pine research instrumentation, model E7R9) was performed prior to each modification of the GC disc. This consisted of abrading the GC and Pt ring surface with 1 μ m and 15 μ m diamond micro-crystal emulsion (BASi). After ethanol rinsing the disc was polarised in 1M H₂SO₄ electrolyte (-0.2<E<+1.0V vs Ag|AgCl) and the ring (-0.2<E<+1.2V vs Ag|AgCl), using a separate reference electrode for H₂SO₄. CV was performed until stable *i*-E response then rinsed with DIW. This electrode is hereafter referred to as the ‘clean RRDE GC disc.’

For the RRDE analysis in chapter 6, $\Gamma_{QDPSU}=88.4\mu\text{g cm}^{-2}$ should be present on the disc (assuming even distribution on carbon black), the molecular weight of the repeating unit is 703 $\mu\text{g }\mu\text{mol}^{-1}$, each repeating unit contains 2 Dabco molecules. The resulting density was calculated at 1.12g cm⁻³. [Dabco]=0.251 $\mu\text{mol cm}^{-2}$ is expected to be present on the disc.

4.1.6 Air cathode preparation for Gas Diffusion Cell

The Gas Diffusion Cell (GDC) is designed to model an air cathode in the intended electrolyte without overall performance being subject to biofilm variation at the anode. Performance constraints relevant to thicker catalyst layers that cannot be modelled effectively in thin films, such as three-phase contact region and ion/electron diffusion can be quantified in GDC. The air cathode (working electrode–WE) in Figure 4-1 is prepared as follows;

Some of the air cathodes prepared in section 4.3.1 were cut with a circular hole punch (diameter 1cm) for the Gas Diffusion Half Cell. Working electrodes were fixed into the Gas Diffusion cell with silicon gaskets reducing the area in contact with the electrolyte to $A_{WE}=0.2826\text{cm}^2$ which was the basis for all calculations. Upon removal of the air cathode only this area is wetted. The approximate catalyst thickness was calculated at 0.01cm (see appendix), irrespective of binder.

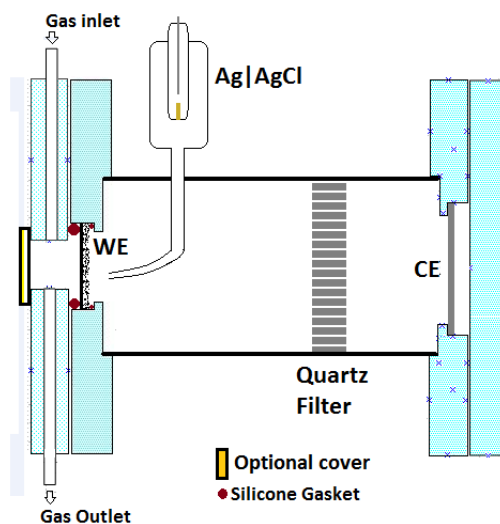


Figure 4-1. Gas Diffusion Cell (GDC) used in assessment of air cathodes in isolation of biofilm variance. Pyrex glass body, acrylic ends.

The distance between the luggin tip and the catalyst layer is 2mm. The counter electrode is titanium foil boiled in oxalic acid and platinised with chloroplatinic acid to produce a Pt foil which is then further galvanostatically platinised at higher current density to produce a Pt black surface.

4.1.7 Electrochemical experiments

The RRDE apparatus can be seen in the appendix (Figure A-6) and the basic principle illustrated in figure 2-3. Electrocatalytic activity was evaluated by CV, potentiostatic polarisation and LSV. All electrochemical measurements were taken using an Autolab PGSTAT303 bipotentiostat controlled with GPES software produced by EcoChemie.

RRDE experiments used a custom made single compartment 3-electrode cell with a reference electrode in a luggin capillary with a tip 0.8cm from the disc. The Pt ring potential was maintained at $E=+0.6V$ (see appendix discussion). The counter electrode was a Pt wire spiral, 0.5mm diameter by 200mm (Pine). An electrolyte of 50mM PBS pH7 ($5.5 < \kappa < 6.2 \text{ mS cm}^{-1}$) was used for all experiments unless otherwise stated. A BASi (RE-5B) Ag|AgCl 3M NaCl reference electrode (+0.208V vs. NHE) was used. All potentials are reported relative to this electrode unless otherwise stated. The reference electrode potential was checked regularly against new electrodes for drift (section 10.8).

Most experiments used potential operating range of $-0.4 < E < 0.5\text{V}$, exceptions are noted (eg. Figure 5-3). This potential window includes typical MFC cathode potentials but avoids the onset of O_2 and H_2 evolution by Pt in PBS and aryl-aryl formation in FePc catalysts and Fe(I)Pc formation.

For CV and LSV experiments, electrodes were H_2O wetted to prevent gas bubbles then inserted in air saturated electrolyte and *OCP* recorded. N_2 sparging (BOC Gases) for 20 minutes was accompanied by electrode rotation to de-aerate the electrolyte and catalyst layer, then a low flow rate blanket N_2 gas stream over the electrolyte to maintain anoxic conditions. The first polarisation detected redox soluble species ($\omega=800\text{rpm}$ $v=5\text{mV/s}$ LSV). The following de-oxygenated experiments LSV and CV experiments were performed in quiescent electrolyte at varying scan rate.

O_2 sparging (BOC gases) for 20 minutes and electrode rotation fully saturated the solution and catalyst layer with O_2 . ORR activity was assessed with electrode rotation or in quiescent solution (blanket O_2) at $v=5\text{mV/s}$ then $v=1\text{mV/s}$ (tafel analyses). Higher scan rates assessed redox peak characteristics in N_2 or O_2 . RRDE experiments were then carried out at $v=5\text{mV/s}$ at $100 < \omega < 3200\text{rpm}$. The electrolyte was then resparged with O_2 with electrode rotation for 15 minutes before recording stabilised *OCP* of the aged film.

In all cases mentioned above, 30s of potentiostatic polarisation ($E=0.35\text{V}$) was applied to provide a consistent starting transient response from the step from $E=0.35\text{V}$ to $E=0.5\text{V}$. Scans then proceeded in a cathodic direction to $E=-0.4\text{V}$ unless otherwise stated. Ring polarisation was only used with electrode rotation.

For the potentiostatic scan experiments, no polarisation was used prior to data recording. The disc was subject to single potentiostatic potential for 3 minutes and J recorded. The last five J values were averaged for the stable current at that potential. This was performed at 10mV intervals from high to low applied potential.

In the electrochemical stability assessment, the RRDE tip was immersed and N_2 sparged as in method 1). Then the disc was subjected to 100 consecutive CV at $v=50\text{mV/s}$ in quiescent solution. The electrolyte then O_2 sparged (as in method 1) and the procedure repeated in quiescent oxygen saturated electrolyte.

Trumpet plots and Randles-Ševčík analysis, were performed in quiescent solution. The modified electrodes were electrochemically cleaned for 20CV at 100mV/s, data was gathered on the cleaned electrode at $v=0.001, 0.005, 0.01, 0.02, 0.03, 0.05, 0.08, 0.1, 0.15, 0.2, 0.3, 0.5, 0.8, 1, 1.5, 2, 3$ and 5Vs^{-1} . In the case of Randles-Ševčík, after the experiment in air saturated solution the solution was de-aerated and the charging current obtained for each of the scan-rates above to produce i_p .

4.1.8 Air cathode half-cell

Phosphate diffusion and wetted surface area were analysed by potentiostatic EIS at $E=0.28\text{V}$. Gas diffusion electrodes were inserted and the EIS polarisation started after 2hrs of catalyst layer wetting at *OCP*. A frequency range $100,000\text{Hz} \rightarrow 0.01\text{Hz}$ was used at 10mV sinusoidal potential. A potentiostatic scan (section 4.1.7) was then performed. A Titanium wire current collector was abraded and immersed in acetone between use. The resistance of the oxide layer of Ti was sporadically recorded to check for over-oxidation. The Ti wire was pressed against the catalyst layer.

4.1.9 Determination of kinetic current

Kinetic current was determined at high overpotential by the intercept j^{-1} over $\omega^{-1/2}$ Koutecký-Levich (K-L) plot. At low overpotential O_2 concentration polarisation was removed from $v=1\text{mV/s}$ LSV data using Eq.2-52 [278]. O_2 reduction wave kinetics are reported using Eq.2-52 (see appendix, Figure A-2 for description).

4.1.10 QDPSU redox peak analysis

Dabco redox peaks were treated with the baseline subtraction e.g. Figure 2-18 with Eq.2-86, Eq.2-88 and charge integration being used to evaluate surface coverage. Linear least squares fits were applied in excel.

4.1.11 Koutecký-Levich analysis of film with different binder

Reliance on binder is assessed by K-L examination at high over-potential [279]. The linear fit is applied to the four lowest rotation speeds, 100rpm, 200rpm, 400rpm, and 800rpm to minimise the effect of small kinetic currents as $\omega \rightarrow 3600\text{rpm}$. The slope,

intercept and ‘goodness of fit’ of linear K-L regions are reported by the R^2 value obtained using Microsoft Excel 2010 default settings of the functions “slope” “intercept” and “RSQ.”

4.1.12 RRDE methodology

Broadly outlined in section 10.5.3, continual polarisation of the disc was not used to attain steady state [61] as this situation is affected by H_2O_2 accumulation in the bulk electrolyte, yielding non-linear $I_{D,L}/(I_{D,L}-I_D)$ vs $\tilde{\omega}^{-0.5}$ plots. The RRDE tip was centred in the glass cell prior to experimentation.

4.3 Chapter 7 Experimental

4.3.1 Air cathode preparation for MFC

Binding agents were prepared as in section 4.1.3. Catalyst inks of different binding agents were prepared from mixing 40mg of FePc/C, a volume (X) μ l of prepared binding agent (volume adjusted for loading) and 6ml of Iso-propanol. Volumes (X) of prepared binding agents (2.1.) were 38.2 μ l of x10 diluted PTFE, 86.9 μ l of neutralised Na^+ Nafion, 86.9 μ l of untreated protonated H^+ Nafion, and 27.3 μ l of QDPSU. Inks were manually stirred to reduce FePc/C agglomeration then ultrasonicated with ZrO_2 balls in a sealed vial placed in an ice bath until a colloid was formed. The entire contents of each vial were pipetted onto a circular (19.6cm²) air cathode (Hesen). The commercial carbon paper contains a Gas Diffusion Layer, catalyst was deposited and evaporated in layers (in 1ml portions) on the anterior side to the GDL to produce the best results [266]. The binder to catalyst weight ratios of all cathodes were binder:FePc=20% and binder:FePc+Carbon=10%. Platinum air cathodes were prepared for the MFC using this methodology but Iso-propanol was substituted for Ethanol and omitting the Nafion neutralisation step (used as received). Pt metal loading was 0.5mg cm⁻² (Alfa Aesar 20% wt. Pt). Nafion neutralisation was used in air cathode preparation for GDC as the process electrolyte was smaller and recording *OCP* was an experimental factor.

4.3.2 MFC polarisations and batch cycle

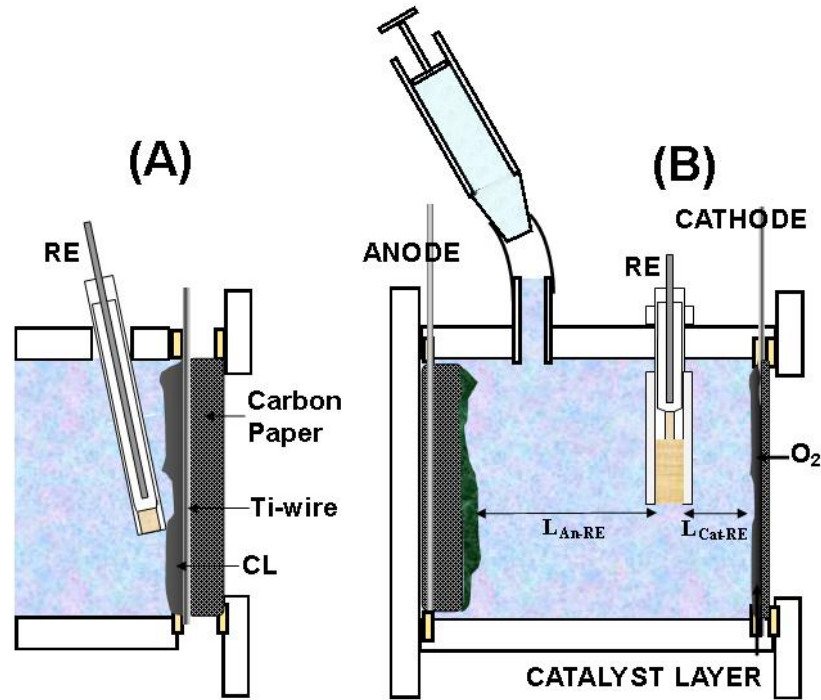


Figure 4-2. Diagram of (A) Half Cell used in EIS or (B) MFC used in batch or polarisation curve evaluation of air cathodes. RE–Reference Electrode. CL–Catalyst layer. Ti – Titanium. $L_{cat-RE}=1.68$ cm and $L_{An-RE}=1.3$ cm.

Anode and cathode potentials were determined using Eq.4-1, as used by Cheng and Logan [41]. This method is highly accurate at open circuit but includes iR -loss. Therefore reference electrode position can be accounted for to produce the actual driving force over the double layer for individual electrode potentials. The iR -loss subtracted electrode potentials are referred to in the text.

$$E_{an} = E_{cat} - V_{cell} \quad (\text{Eq.4-1})$$

The relationship between solution resistance (R_s) and the separation of the anode to the RE-frit (true E_a) and cathode to the RE-frit (true E_{cat}) is outlined in Eq.4-2. L_{An-Cat} represents the distance of anode and cathode electrode spacing, for illustration of distances L_{An-RE} and L_{Cat-RE} see Figure 4-2.

$$E_{An} = E_a - R_s \left(L_{An-RE} / L_{An-Cat} \right) I_{cell} \quad (\text{Eq.4-2})$$

$$E_{Cat} = E_c - R_s \left(L_{Cat-RE} / L_{An-Cat} \right) I_{cell} \quad (\text{Eq.4-3})$$

The distance from the RE-tip to the surface of the Ag wire can be ignored in these equations as negligible current flows in this direction. This modification of electrode potentials has only been done for comparison of air cathodes during MFC polarisation and the Half-cell tests.

Silicone rubber, 1.5mm thick (Cole Palmer) was used to place the air cathodes and Ti wires under compression. The Ti wire was compressed along the diameter of the air cathode. The resulting separation between biofilm and WE surface is 31.75mm. The RE (diameter 5.7mm) was fixed perpendicular to the cell wall using washers. The resulting separations in the direction of current are described in the caption of Figure 4-2.

Electrode potentials were corrected by measuring the RE after every cycle vs. a new electrode in 3M NaCl. The result was a consistent anode potential, $OCP = -0.482V \pm 0.007V$ for all polarisation curves in PBS and PBS amended wastewater.

The electrolyte for all MFC tests was one of 1) artificial wastewater, consisting of 500-5000mg/L CH_3COONa + 50mM PBS + trace nutrient (see appendix Table A-7), 2) 50mM Phosphate buffered primary clarifier influent wastewater, or 3) un-supplemented primary clarifier influent wastewater. COD tests were carried out using the Hg and Chromate oxidant method previously described [280, 281].

Steady state polarisation curves are carried out by;

- 1) Injection of fresh electrolyte (N_2 sparged) into the cell.
- 2) Setting the cell at open circuit and covering the air cathode with parafilm to prevent electrolyte oxygenation, leaving the MFC for a period of 16hrs.
- 3) Removing parafilm until a maximum plateau in V_{cell} is obtained (typically 5-10minutes) then fixing a $1M\Omega$ external resistor.
- 4) Allow cell to stabilise for 20 minutes and record V_{cell} and E_{cat} , decrease external resistance with resistor box and allow 20 minutes stabilisation again before recording.
- 5) Repeat step 4 with external resistance 600k Ω , 300k Ω , 100k Ω , 60k Ω , 30k Ω , 10k Ω , 6k Ω , 3k Ω , 1k Ω , 600 Ω , 300 Ω , 100 Ω .

4.3.3 EIS analysis on thin films

The Frequency Response Analyser programme from Autolab® was utilised. Electrode preparation and solution de-aeration (as in method 1) was used before EIS analysis in quiescent solution. A potentiostatic signal with a 10mV square wave sinusoidal amplitude was applied with perturbation frequencies from 100kHz to 0.1Hz at 90 readings over a logarithmic frequency distribution. The impedance response was measured for several applied potentials, starting at high potential to low potential. This procedure was then repeated in fully O₂ saturated electrolyte.

4.3.4 EIS analysis of Air cathodes

Electrode preparation for GDC half cells were carried out according to the methodology outlined in 4.3.1 and 3.3.3. Experiments on MFC air cathodes were conducted in the cube cells (see appendix) with the biofilm being substituted by a high surface area platinised mesh [282]. The reference electrode (RE-5B, BASi) was placed with the tip c.a. 1mm from the catalyst layer surface. No temperature control was used to avoid convection arising from temperature gradients; convection may impact low frequency measurement. Cells were left un-polarised for 2hrs (GDC) or 40minutes (MFC air cathode) following electrolyte insertion. This approach ensured layer wetting. Both MFC air cathodes and GDC air cathodes were polarised and a 10mV square wave perturbation was applied to obtain an impedance spectra. GDC air cathodes were polarised at $E=0.28\text{V}$ ($0.01\text{Hz} < f < 100,000\text{Hz}$), and MFC air cathodes were polarised at a range of potentials in the order OCP , 0.4V, 0.2V, 0.15, 0.1, 0.05, 0, -0.05, -0.1, -0.15, -0.2 and -0.3V.

4.3.5 Data analysis

Where a linear trend in $-Z''$ vs. $\tilde{\omega}^{-1}$ plots was found capacitance was extracted. Where a linear trend in Z vs. $\tilde{\omega}^{-0.5}$ plots was found Eq.2-98 was applied. Wherever possible, the oxidised and reduced couple were amalgamated into a single diffusion co-efficient and molarity presence. This approach was selected to determine this parameter, as opposed the iteration of values in an entire equivalent circuit. The reason being that a minimum number of frequency dependent components should be selected for the equivalent

circuit is advised [283], this leads to large inaccuracies at high frequency as fitting at low frequency produces a larger improvement in χ^2 values.

The diffusion factor (σ) was obtained from least squares fit of the linear regions of a) the Z vs. $\tilde{\omega}^{-0.5}$ plot, b) the Z' vs. $\tilde{\omega}^{-0.5}$ plot [284] or c) Eq.2-110 or Eq.2-111. Double layer capacity was calculated according to Y^0 and N [285] with Nova software, but can be calculated by Eq.2-102 and Eq.2-103. For air cathodes and MEA the manual arc fitting, R_∞ and R_0 values are obtained by fitting three points from at f_p and at the LF and HF limits of the arc response using Nova software (ie. Figure A-18).

4.4 Experimental – Chapter 8

4.4.1 *Physical parameters of membranes*

To extrapolate the resistance from the conductivity of the membranes tested, some literature had to be consulted. AMI-7001 in de-ionised H_2O after treating with OH^- and rinsing with DIW was $1.72 \times 10^{-2} S cm^{-1}$. QPSU (Quaternized Polysulfone) was $0.72 \times 10^{-2} S cm^{-1}$ [286]. The QDPSU membrane produced an OH^- conductivity of $26 mS cm^{-1}$ at room temperature [276]. A similar calculation was performed on FAA reported by Gu et al [256], a value of $0.017 S cm^{-1}$ in 1M KOH equates to $2.38 \times 10^{-4} \Omega$ for a membrane of unknown area. In the review by Xu et al [287], the ADP membrane is described as having a high demineralisation activity, while the FAA and FAD membranes are described as base stable and acid dialysis membranes respectively.

Table 4-1. Physical and chemical properties of commercial membranes used.

Membrane / Manufacturer	Functional X- change group / Solvated ion	Backbone	Thickness (wet) / (μm)	Reported κ (Ω cm ²) / in electrolyte		Working pH	Price / (m ²)	Pore Size / (nm)
CEM								
F-930 / Fumatech	PerFluo-SO ₃ ²⁻ / H ⁺	PTFE-Co- polymer	30	<0.2 / 0.5M NaCl		N/A	€833	-
CMI-7000 / Membranes International	SO ₃ ²⁻ / Na ⁺	Gel Polystyrene/ divinyl benzene	450	<30 / 0.5M NaCl		(1-10)	\$97	-
AEM								
FTAM-A (PA) / Fumatech	Q-Ammonium / Cl ⁻	Polyamide (Nylon)	500-600	<8 / 0.5M NaCl		(5-13)	€333	-
FAA (PEEK) / Fumatech	Q-Ammonium / Cl ⁻	PEEK	130-150	<2 / 0.5M NaCl		(1-14)	€583	-
AMI-7001 / Membranes International	Q-Ammonium / Cl ⁻	Gel Polystyrene/ divinyl benzene	450	<40 / 0.5M NaCl		(1-10)	\$97	-
Morgane ADP® / Solvay	Q-Ammonium / Cl ⁻	PTFE - Xlink	150	1.5-4.5 / 0.6M NaCl	0.5 / 1M NaOH	(0-10)	-	-
QDPSU-PTFE x- link / made in house	Methyl-DABCO ⁺ / Cl ⁻	Polysulfone + PTFE - Xlink	30	N/A		N/A	-	-
Separator								
Rhinohide / Entek	None / Oil content	High Mol.W. Polyethylene	250 ^a	N/A		N/A	-	26°

4.4.2 Method for membrane fixation

Membranes were assessed in three electrolytes (a) 50mM PBS, pH 7.0 (b) 50mM NaHCO_3 (Sigma Aldrich #401676), pH 7.91 (c) 50mM NaCl (VWR #27788.297), pH 7.0. Membranes were rinsed in de-ionised water then soaked in target solutions for at least 12hours with electrolyte replacement until the pH of the spent electrolyte and new electrolyte matched (3-8 washes). Catalyst layers were wetted with target solution prior to fixation of wet membranes to maintain osmolarity. A rigid stainless steel mesh was introduced to prevent bulging and air pockets forming. The SS-mesh produced a non-uniform surface for EIS but aided catalyst layer contact and abated pockets of electrolyte.⁶ The MEA half-cell setup is shown in Figure 4-2(B). The air cathode was 5.5cm in diameter and the membrane 5.7cm. The preparation procedure is as follows.

- 1) Cut and rinse membrane with de-ionised water then place in 50mM PBS solution for 1hr.
- 2) Pipette 50mM PBS solution onto catalyst layer to allow pore ion saturation.
- 3) Assemble cell with a fresh FePc air cathode. A slightly wider membrane is placed on top of gas diffusion layer and then bound with 304 stainless steel mesh. Holes at top remain unplugged.

⁶ There is no foreseeable reason thermosetting biofoul resistant plastics cannot be used for this application, provided embrittlement was no problem.

- 4) Fill cell with air Saturated 50mM PBS 2 hours before start of experiment to allow for Phosphate Diffusion through membrane into wetted pores.
- 5) Rinse and insert RE-5B reference electrode (BASi) into cell at an angle until contact is made with the steel mesh (separation of Ag wire and mesh will mean no short circuit).

4.4.3 Batch performance and polarisation of MFCs with MEA.

Batch performance tests with MEA utilise the same methodology described in section 4.3.4. The cell configuration was Figure 4-2(C) but utilising the cathode MEA assembly of Figure 4-2(B). All batch tests and polarisation curves used artificial wastewater.

4.4.4 EIS evaluation of membrane electrode assembly

- 1) Record open circuit potential (should range from 0.25 to 0.32V).
- 2) Start EIS run programme of various applied potentials (*OCP*, 0.4, 0.2, 0.15, 0.1, 0.05, 0, -0.05, -0.1, -0.15, -0.2, -0.3V). This should use a range of frequencies from 100,000 Hz to 0.01Hz on a logarithmic distribution scale of 103 readings. Sinusoidal amplitude 10mV in either direction [288].

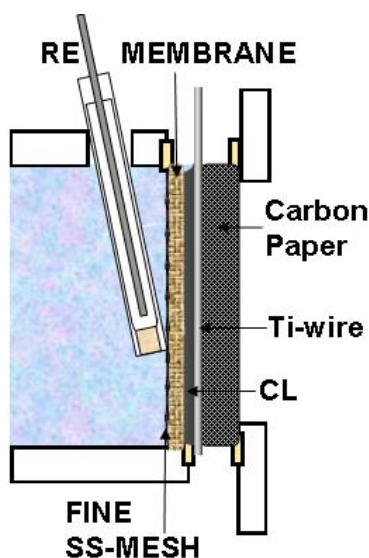


Figure 4-3. Diagram of Half Cell assembly used to assess membrane performance with EIS. RE – Reference Electrode. SS-304 Stainless Steel. CL – Catalyst layer. Ti – Titanium.

Chapter

5

Chapter 5. Results - oxygen reduction catalysed by carbon supported iron phthalocyanine at neutral pH

5.1 Introduction

Research with the aim to augment the kinetics of the oxygen reduction reaction in neutral media is quite limited. The majority of MFC cathode work focuses on architecture, and periphery equipment as opposed to catalyst design. In this chapter a first principles electrochemistry study has been applied to a heme-like catalyst. The large reaction overpotential incurred by base-metal or Carbon materials at pH7 [188] and the possibility of medical applications may justify the fundamental research. Precious metal catalysts are believed to constitute 40-50% of complete MFC unit cost [289] and cannot be used.

Iron phthalocyanine (FePc) has been employed in MFCs as a low cost ORR catalyst and showed promising performance [125, 216]. At pH 7 the ORR mechanism is not well studied, particularly for non-Pt catalyst. This chapter attempts to draw parallels from acid and alkali media studies where kinetic analysis in neutral is not present. Two terms have been defined to allow clarity in expression of catalyst activity.

5.2 Catalyst activity

5.2.1 *Carbon supports in phosphate buffer*

In Figure 5-1, thin films of carbon materials are deposited onto a GC tip to a consistent loading. Relative charging currents are evaluated with CV (C) and (D) whilst steady state conditions (A) and (B) evaluate parameters of ORR.

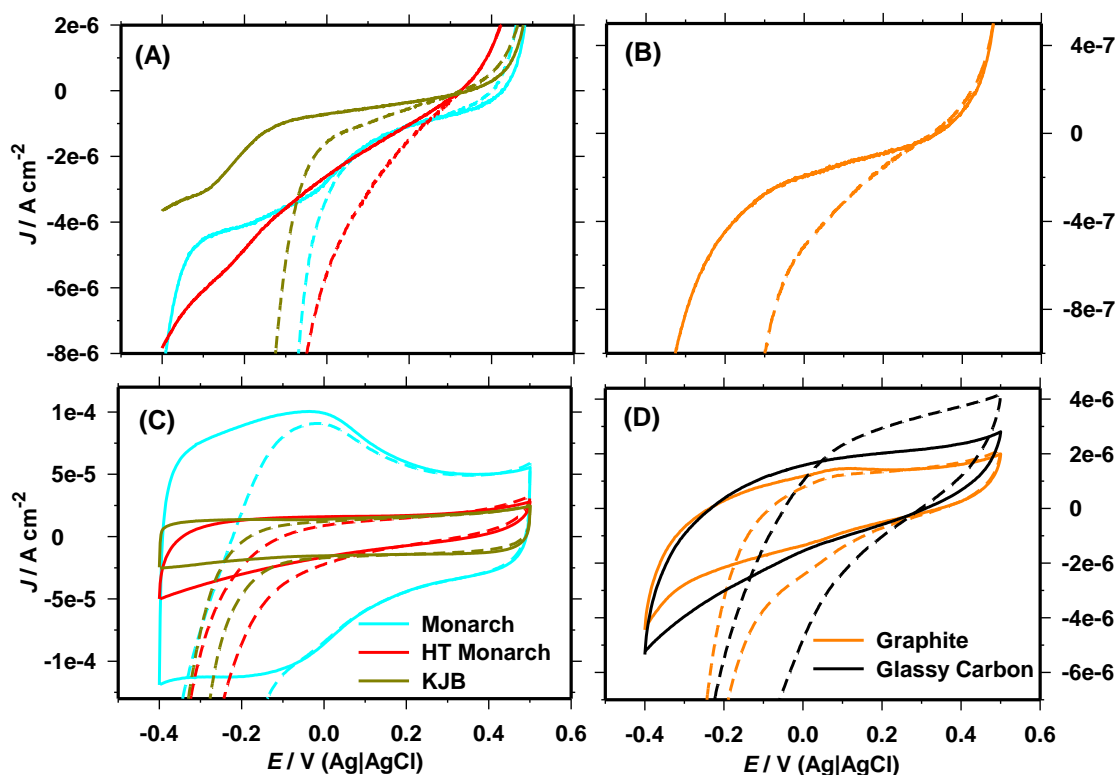


Figure 5-1. (A)(B) Steady state i - E curve ($\nu=1\text{mV/s}$) or (B)(C) stable CV ($\nu=20\text{mV/s}$) of carbon materials used in this thesis. GC disc (D)+thin films ($71\mu\text{g cm}^{-2}$) of Nafion binder with (B)(D) Graphite, or (A)(C) Monarch, pyrolysed Monarch or KJB. Electrolyte; N_2 saturated (line) or O_2 saturated (dash line) 50mM PBS, pH 7.0.

Modifying GC with synthetic graphite and Nafion produces a similar i - E profile to the unmodified electrode, Figure 5-1(D). A reduction in total capacitance (C_{Σ}) of 16-25% (Eq.2-16) from unmodified GC shows Nafion to be inert to accumulation of Phosphate anion charge. When modified with carbon black, the GC electrode acts as a electrochemical double-layer capacitor in de-aerated media, with C_{Σ} increasing in the trend Monarch>KJB>HT Monarch. Electrocatalysis of water splitting is not observed and overpotentials of di-oxygen reduction are $\eta>0.4\text{V}$ ($E^{0'}=0.605\text{V}$).

All carbon materials in Figure 5-1(A) and (B) perform ORR at low potential ($E<-0.05\text{V}$) attaining O_2 diffusion limitation at c.a. $E=-0.4\text{V}$. Divergence in i - E response in O_2 and N_2 electrolytes at high potential ($0.3>E>0\text{V}$) is not of a diffusion limitation or kinetic type as a $\log_{10}(i)$ vs E relationship is not present and could be attributed to chemisorbed O_2 enhancing charging current. At $\nu=1\text{mV/s}$ current in N_2 and O_2 diverge at; Monarch ($E=0.05\text{V}$), HT Monarch ($E=0.28\text{V}$), KJB ($E=0.28\text{V}$) and Synthetic Graphite ($E=0.28\text{V}$).

Monarch 1000 was pyrolysed ($T=800^{\circ}\text{C}$) to assess thermal stability of groups that may possess electrocatalytic properties in carbons. This effect must be separated from pyrolysis of carbon supported catalyst in section 5.4.1-5.4.3. Redox activity occurring in Monarch ($E<0.1\text{V}$) is attributed to edge plane oxygen [163, 290] and is removed by pyrolysis resulting in C_{Σ} decreases of 70-90%. Szymanski et al report inert atmosphere thermal decomposition of quinone structures at $T=600-980^{\circ}\text{C}$ [291], which would account for a loss of redox activity. Oxidative decomposition of electrocatalysts adsorbed onto these sites may occur with pyrolysis.

5.2.2 Unsupported FePc films in phosphate buffer – electron transfer activity

Unsupported FePc was studied to avoid the influence of binder or reactions such as k_5 or H_2O_2 production from a carbon substrate. FePc typically forms co-facial polymer (π - π stacking) when deposited from DMF [70] (section 10.5.1), Figure 5-2 shows the i - E response in de-aerated PBS.

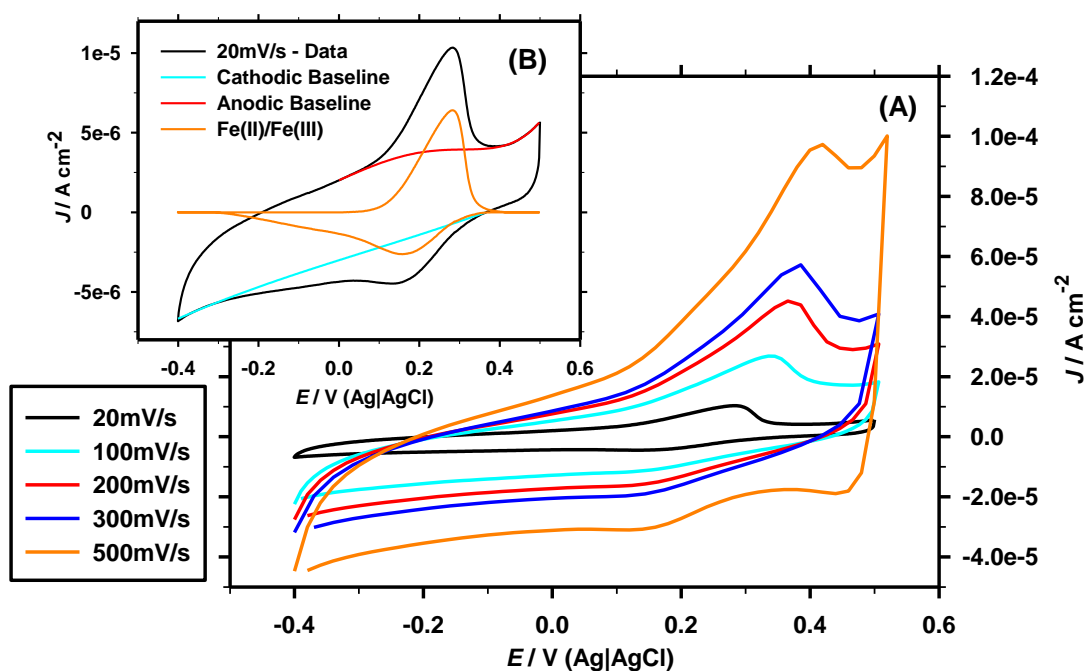


Figure 5-2. (A) Scan rate effect on $\text{Fe(II)} \rightarrow \text{Fe(III)}$ peak of FePc adsorbed onto Glassy carbon from FePc-DMF solution to c.a. $\Gamma_{\text{FePc}} = 6.77 \times 10^{-8} \text{ Moles cm}^{-2}$. (B) Subtracted charging current ($\nu = 20 \text{ mV s}^{-1}$). Electrolyte; N_2 sat. 50mM PBS, pH 7.0; $\nu = 20-500 \text{ mV s}^{-1}$

A thin but visible dark purple layer was produced from DMF-FePc solution. In Figure 5-2(B) a non-Gaussian distribution of the Fe(II)→Fe(III) peak is seen in contrast to that predicted from the Gaussian response from the theory of unhindered redox polymers in conductive films [82]. The baseline was applied with the same *i-E* profile as from Glassy Carbon in Figure 5-1(D), equating the magnitude of anodic and cathodic for each peak; $Q_{an}=|Q_{cat}|=4.08\times10^{-5}\text{C cm}^{-2}$. Without solvated O₂ significant ‘tailing’ in the Fe(III)→Fe(II) reaction are apparent [292, 293] and no clear peak is seen from slow electron transfer through multi-layers. At higher scan rates, the Fe(III) was not fully reduced at $E=-0.4\text{V}$. From Q_{an} the redox active FePc is $4.23\times10^{-10}\text{mol cm}^{-2}$, similar to that from Eq.2-86 ($3.3\times10^{-10}\text{mol cm}^{-2}$), the slight irregularity caused from the lag in peak symmetry. The value from Q_{an} is a fraction (0.6%) of the overall loading calculated from solution aliquot, showing electronically insulated regions are formed. For Fe(II)↔Fe(III) charge conservation the cathodic redox charge must equal that of the anodic redox charge.

It was shown that reversibility of Fe(II)/Fe(III) redox is low in thick FePc films. The behaviour is analogous to a ‘gated’ periplasmic enzyme [294] in the absence of substrate, where the reduced product insulates electron transfer in one direction, only oxidation is facile.

5.2.3 Unsupported FePc films in phosphate buffer – activity in O₂

Figure 5-3 displays the *i-E* response from the FePc film in Figure 5-2 when aerated and subjected to CV until a stable response is obtained (3 scans).

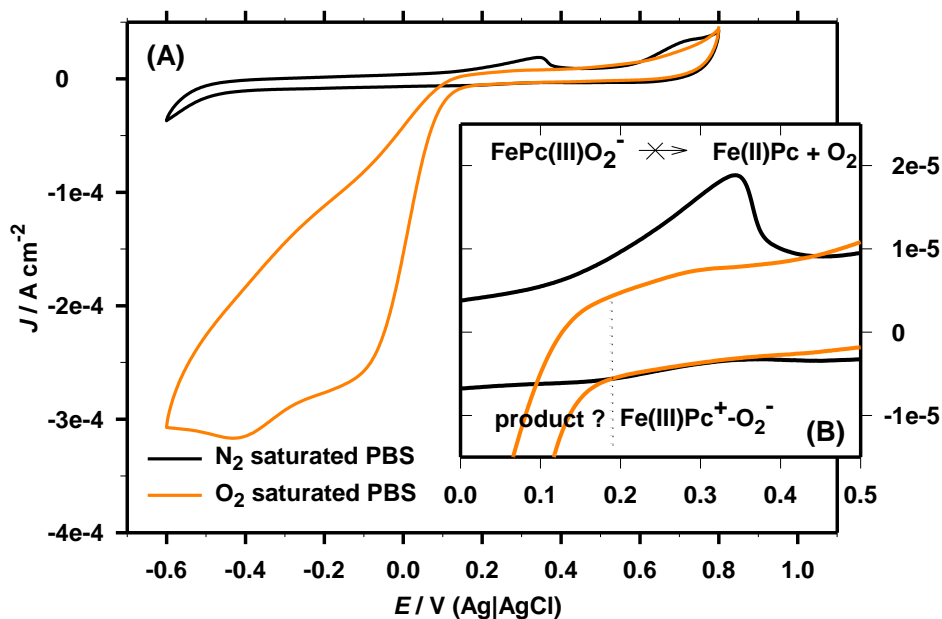


Figure 5-3. CV of unsupported FePc film in N₂ or O₂ saturated electrolyte(see Figure 5-2). (B) enlarged 0<E<0.5V region of (A). Electrolyte; 50mM PBS, pH 7.0. $\omega=0$ rpm. $\nu=20$ mV/s.

In Figure 5-3(B) the aerated FePc film no longer displays an Fe(II)→Fe(III) peak indicating partial O₂ coverage of the electrocatalyst in contact with the solution tends towards 1.0. The process is reversible with de-aeration and cathodic polarisation indicating a strong bond between FePc and O₂ displacing a ligand of H₂O or Phosphate. Zagal states that the E_{ORR} potential is set from the reduction of the Fe(III)Pc-O₂⁻ adduct [32]. As the reaction between FePc and O₂ has occurred at $E>0.19$ V, this step is not the RDS. Fe(II)Pc must be regenerated prior to O₂ adduct formation, a reaction such as Eq.5-1 (anaerobic), or Eq.5-2 (aerobic)[186] occurs with cathodic polarisation.



5.2.4 Confocal microscopy of carbon supported FePc films

In Figure 5-4 an Olympus BX-41 confocal microscope was used to view FePc/KJB catalyst (A) and a thin film of FePc/KJB catalyst with binder on a GC tip, prepared as per section 4.1.3-4.1.5.

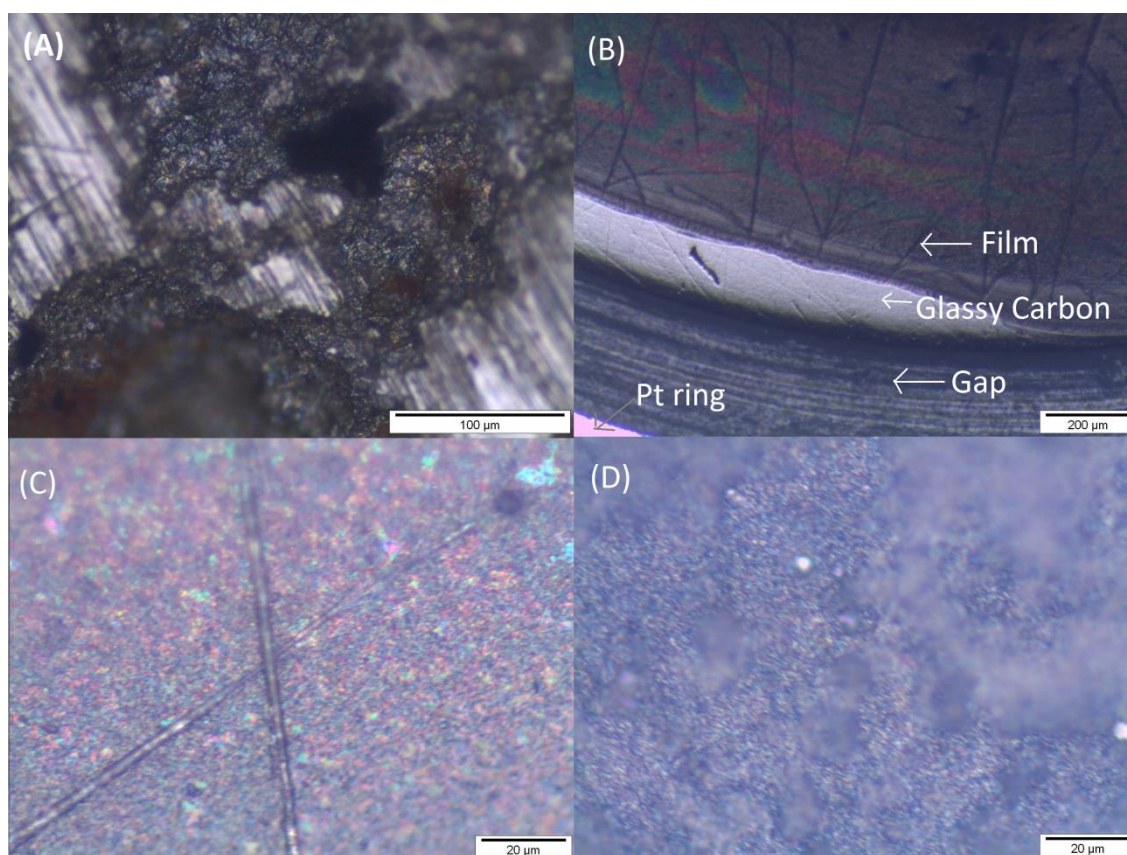


Figure 5-4. Confocal microscope image of (A) FePcKJB powder and (B)(C)(D) FePcKJB film on GC disc. Binder of (B)(C) Nafion or (D) QDPSU at magnifications of (A) 20x (B) 5x or (C)(D)50x.

The 320μm insulating gap between disc and ring can be seen in Figure 5-4(C). Typically no bare GC was left when applying the film, for the purposes of confocal microscopy the film was not applied all the way to the edge in this instance only. When depositing from colloids (no sedimentation) the film appeared evenly dispersed with a reflective surface from the ionomer applied to excess. Though the GC surface was scarred from repeated polishing the thickness could be seen from confocal microscopy between the edge of the film and the GC support, eg. Figure 5-4(B). The difference between the focal length was 1.5μm. An example is found in Figure A-23 in the appendix.

5.2.5 O_2 diffusion limitation in carbon supported FePc films

The influence of forced convection on the FePc/KJB Nafion thin film is seen in Figure 5-5. An attempt to determine C_x in the presence of ORR is made through the treatment

described in Figure 2-6. iR -drop and concentration over-potential correction (Eq.2-52) are applied.

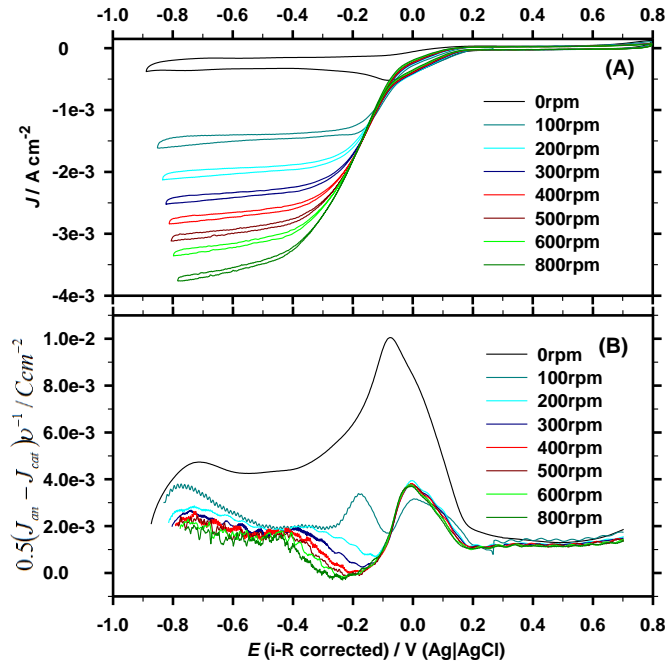


Figure 5-5. Influence of electrode rotation on CV for FePc/KJB film with Nafion binder.

(A) J vs. E response and (B) $(0.5(J_{an} - J_{cat})/v)$ vs. E . iR correction=125 Ω (Figure 7-1).

Electrolyte; 50mM PBS, pH7. v =20mV/s

Observing Figure 5-5(A) a definite change in i - E response could be seen c.a. E =-0.05V with the current increasing. It is clear that the lack of reversibility in the ORR produces negative $(0.5(J_{an} - J_{cat})/v)$ values which mean that Eq.2-16 does not hold at potentials which ORR is occurring ($E < 0.22$ V). At higher potentials $C_s = 1.18 \times 10^{-3}$ C cm⁻² can be concluded and is not a function of potential, indicating surface state capacitance only.

At high electrode rotation the limiting current does not form a definitive plateau. If “ n ” is consistent (e.g. 3.95) the continual rise in J_L indicates increased prevalence of surface sites at the electrolyte interface, ie. at E =-0.4V, $\theta_{FePc-X} > 0$, where X hinders O₂ adsorption. The $\log|J_k|$ vs. E plot (not shown) of the data in Figure 5-5(A) produced two tafel regions; $0.17 > E > 0.09$ V and $-0.08 > E > -0.18$ V with the high overpotential tafel region possessing a $-b_c$ value x1.46 larger than the $0.17 > E > 0.09$ V region. The high scan-rate (v =20mV/s) means Eq.2-18 or Eq.2-10 cannot be applied. After i -R correction two linear J_k vs. E regions ($0.12 > E > -0.02$ V and $-0.08 > E > -0.22$ V) are still present showing resistance in the catalyst layer.

At $\omega=100\text{rpm}$ Figure 5-5(B) is similar to the result obtained by Van der Brink in KOH medium [208] for FePc, with C_z maxima at 0.82V and 0.38V vs RHE (0.2V and -0.24V Ag|AgCl). In Figure 5-5 maxima in $(0.5(J_{an}-J_{cat})/v)$ at obtained at $E=0.02\text{V}$ and $E=-0.22\text{V}$. Their explanation was a p-type semiconductor covering the electrode surface. If this is the case it is striking that coverage of an ORR intermediary rather than process anion causes an accumulation of surface capacitance.

5.2.6 PBS effect of pH buffering and adsorption for FePc activity

Thin films of FePcKJB Nafion are immersed in mono anionic solutions with solvated O_2 . Figure 5-6(A) depicts the first cathodic polarisation from $E=0.5\text{V}$, the second CV is shown in Figure 5-6(B).

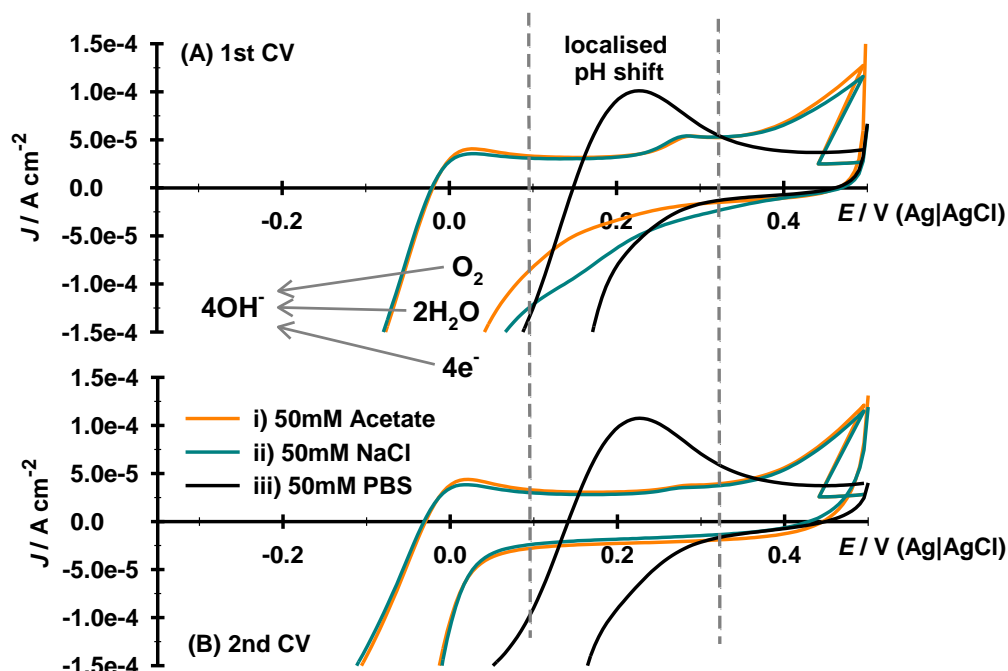


Figure 5-6. Localised pH shift in catalyst layer from ORR in (A) 1st and (B) 2nd consecutive CV. Grey lines= E_{ORR} shift without buffering. Electrolyte; O_2 saturated, 50mM CH_3COONa , pH 8.9 (orange). 50mM NaCl, pH 7.0 (blue) or 50mM PBS (black). $\omega=0\text{rpm}$. $v=50\text{mV/s}$

FePc is a strong ionophore [295], yet O_2 adsorption is feasible in the presence of Cl^- , $\text{H}_2\text{PO}_4^-/\text{HPO}_4^{2-}$, and CH_3COO^- ions in Figure 5-6(A). Without prior cathodic polarisation, $E_{ORR}=0.25\text{-}0.32\text{V}$ for all three electrolytes. The catalyst layer alkalifies and $\log_{10}(J)$ vs E plots of the data in Figure 5-6(A) are non-linear until pH stabilisation

occurs. The i - E response of scan#2, Figure 5-6(B), is similar to scan# 100 (not shown) indicating local pH stability within the catalyst layer. A cathodic shift in E_{ORR} of 0.22V has occurred in the non-buffering electrolytes. No change in E_{ORR} is seen in Phosphate. This concurs with findings of Kozawa et al [187], who also noted increased reversibility of CV with Phosphate but did not offer an explanation.

5.2.7 Peroxide generation of FePc

Facile H_2O_2 oxidation can occur at potentials higher than the Fe(II)/Fe(III) redox ($E > E^{0'}$) [67]. The production of H_2O_2 was evaluated with RRDE, disc modifications of carbon supported and unsupported FePc in Figure 5-7.

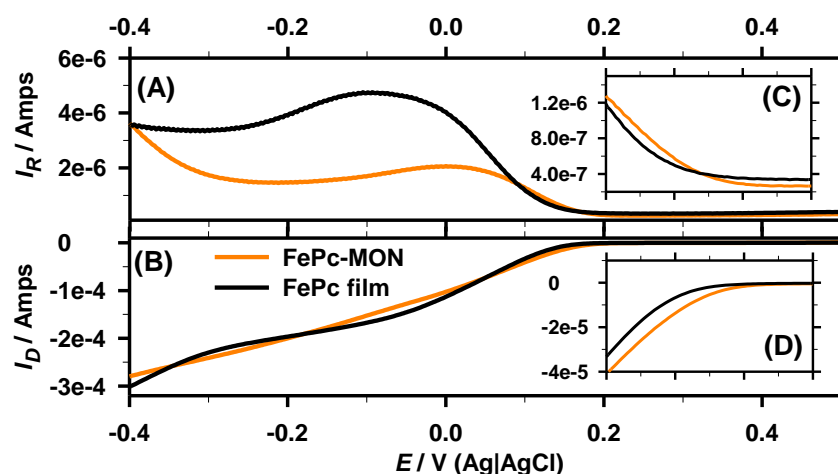


Figure 5-7. RRDE study of disc modifications of FePc/MON or FePc film from DMF. (A)(C) i_R vs. E and (B)(D) i_D vs. E . (C)(D) show $0.1 < E < 0.25$ V enlarged x-axis. O_2 saturated 50mM PBS, pH 7.0. $\omega=200$ rpm. $\nu=5$ mV s^{-1}

Figure 5-7 shows the i_R vs. E and i_D vs. E plot for 1) FePc/MON (Nafion) 2) FePc film (from DMF). The ring is poised at $E=0.6$ V and oxidises H_2O_2 released from the disc;

- i_D vs. E produces a similar profile for both films yet H_2O_2 release is significantly decreased with Nafion and carbon support.
- H_2O_2 is detected at potentials as high as $E=0.22$ V in this study (see Figure 5-7).

In the unsupported film, only a few layers of FePc are active (Figure 5-2), yet H_2O_2 lifetime in the unsupported film is larger than in FePc/MON. Either disproportionation/reduction (k_4) accounts for the difference or the reaction on the unsupported film occurs at the electrolyte/film interface. The data was modified with Eq.2-56 to with the treatment described in the text accompanying Figure A-9. In Figure

5-8 the ratio of H_2O_2 leaving the layer to the ratio of O_2 reduced as a function of potential.

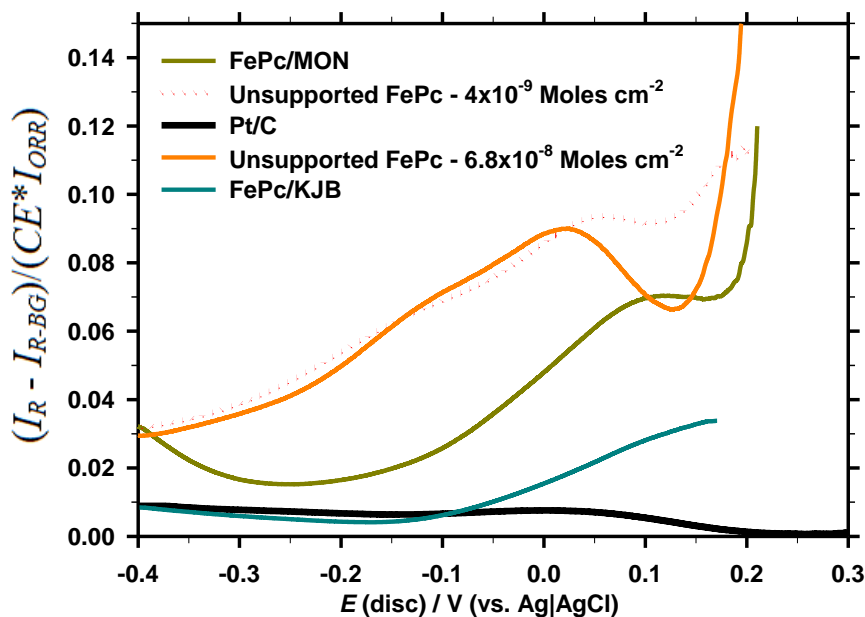


Figure 5-8. % H_2O_2 vs. E profile from RRDE study on FePc films and Pt benchmark. Data manipulated with (Eq.2-56) from LSV. Electrolyte; 50mM PBS, pH 7.0. $\nu=5\text{mV s}^{-1}$. $\omega=200\text{rpm}$.

With FePc/MON and FePc/KJB films the % H_2O_2 increased at $E < -0.25$ V, a feature not present in unsupported FePc films. The result indicates that ORR occurs on the carbon surface at high overpotential, a process that releases H_2O_2 [296]. All FePc film produce less than 10% H_2O_2 , with and without carbon support. Accuracy decreases with overpotential, as amounts of H_2O_2 become small. A linear decrease in % H_2O_2 is seen in unsupported FePc films $E < 0\text{V}$, a process invariant of film thickness. A process that confers linear dependence between H_2O_2 creation/decomposition kinetics and applied potential is sought. It is plausible the influence of Phosphate surface coverage $\theta_{\text{FePc-X}}$ [84] or mode of O_2 adsorption may inhibit $4e^-$ active sites at high potential. Further studies in mono anionic electrolyte evaluate the former possibility.

The parabolic decrease in % H_2O_2 attains a minima at $E=0.125\text{V}$ and is present in the $[i_R - i_{R-BG}]/[i_D \cdot CE]$ vs E plot (not shown) as with the $[i_R - i_{R-BG}]/[i_{ORR} \cdot CE]$ vs E plot (Figure 5-8), indicating a change in the product of electrocatalysis as opposed to the influence of a redox of the type in Figure 5-2. The influence of film thickness is negligible at $E < 0\text{V}$ and significant at $E > 0\text{V}$. As $k_3 > 0$ with FePc catalysed ORR [67], movement of

the reaction site from electrode/film interface ($E > 0V$) to film/electrolyte interface ($E < 0V$) is present, in agreement with the observation of van der Brink et al [208] of a decrease in i_k with increasing film thickness. An analysis capable of discriminating the successive $k_2 \rightarrow k_3$ from the direct k_1 mechanism is required following the detection of significant H_2O_2 .

5.3 Catalyst kinetics

5.3.1 Kinetic rate of ORR quinone activity in the support

Thin films of HT Monarch and Monarch (as received) were subjected to potentiostatic steps applied at 10mV intervals (3min) in a cathodic direction, Figure 5-9. At the end of the 3 min transient decay a stable current is produced. The aim is to create steady state condition for measuring small ORR current at low η .

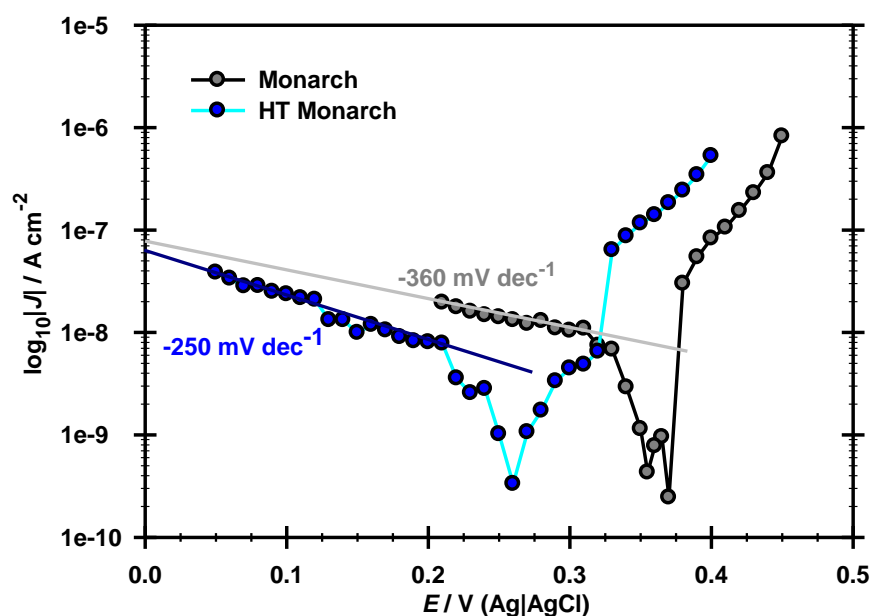


Figure 5-9. Potentiostatic sweep of Monarch 1000, used as received or with pyrolysis prior to thin film modification of GC tip. Catalyst loading $71\mu g\ cm^{-2}$, Nafion loading $111\mu g\ cm^{-2}$. Electrolyte; O_2 sat. 50mM PBS, pH 7.0

The oxygen reduction current obeys the tafel equation when measured at steady state in Figure 5-9. Large values, $b_c = -360\text{mV dec}^{-1}$ for Monarch and $b_c = -250\text{mV dec}^{-1}$ for HT-Monarch indicate a complex reaction mechanism and sluggish kinetics. The high values are consistent with low overall values for ' n ' and an early limiting step in the reaction.

The b_c values for oxygen reduction on carbon at low potential ($E < -0.05\text{V}$) are common to all graphitic materials [297] and are not depicted in Figure 5-9. This study highlights the need to separate multi-component exchange currents [298] from carbon supported catalysts to that of pristine carbon. For the thesis duration, J_0 is reported by extrapolating the ORR wave catalysed by the supported catalyst.

5.3.2 Unsupported FePc

Thin films of unsupported FePc or Pt/C Nafion are subjected to the same potentiostatic step experiment applied as in Figure 5-9. The result is shown in Figure 5-10.

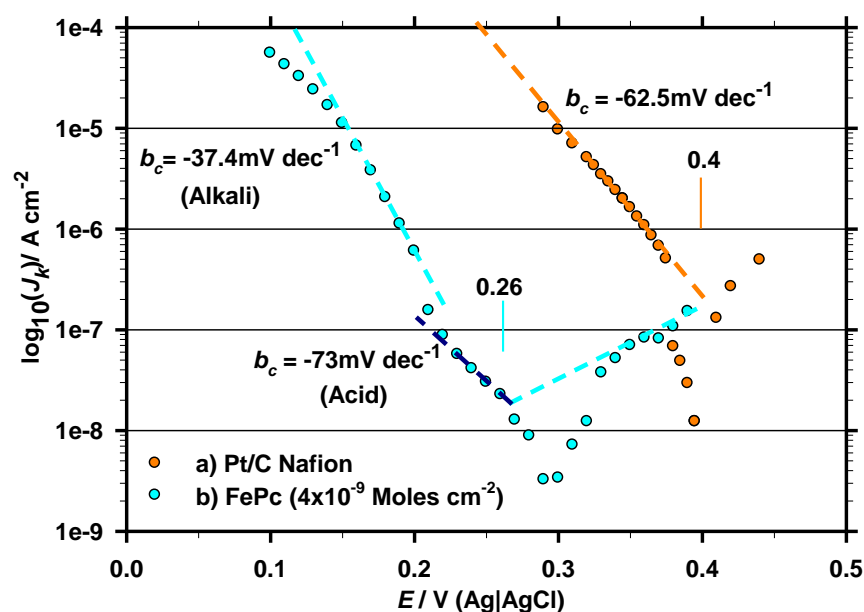


Figure 5-10. Potentiostatic scan of a) 20% wt. Pt/C (Nafion) or b) unsupported FePc. Loading of a) $14.2\mu\text{g}_{\text{Pt}}\text{ cm}^{-2}$ or b) $\Gamma=4\times 10^{-9}\text{ Moles cm}^{-2}$ FePc. iR-correction. Acid or alkali mechanism tafel slope (b_c) and OCP are marked. Electrolyte; O_2 saturated 50mM PBS, pH 7.0.

The Pt/C benchmark was used to verify the validity of this method. $\text{Log}_{10}|J_k|$ vs. E plots produced consistent Pt/C tafel slopes ($b_c=-62.5\text{mV dec}^{-1}$) to that recorded at $v=1\text{mV/s}$ ($b_c=-63.2\text{mV dec}^{-1}$) in Table 5-1, verifying steady state in both experiments and consistent with literature [169] (PBS, pH7).

The result from FePc was obtained prior to previous polarisation to observe film re-ordering if present [208]. Protons as a substrate may be used low η ; the $|b_c|=73\text{mV dec}^{-1}$ at $0.26 > E > 0.22\text{V}$ is more typical of FePc O_2 catalysis in acid media [205, 210] and was

not observed after the first cathodic polarisation, indicating re-ordering may occur. The remaining tafel region at $E < 0.2\text{V}$ ($|b_c| = 37.4\text{mV dec}^{-1}$) produces the majority of current. Extrapolation to $OCP = 0.25\text{V}$ yields $J_0 = 1.5 \times 10^{-8} \text{ A cm}^{-2}$. The comparability with carbon deposited or vacuum deposited films in pH 6.7 PBS [182, 191, 192]; $|b_c| = 37\text{--}38\text{mV dec}^{-1}$, is in good accord with Figure 5-10. The results differ from the result for monomeric FePc [191] ($|b_c| = 60\text{mV dec}^{-1}$).

Savy et al noted OH^- product from ORR in Phosphate media [192], predicting local pH swings, this relevance of this aspect to engineering is addressed in further sections of this thesis. Reviewing Table 3-2, the alkali mechanism pathway is prevalent in highly buffered neutral media, and is studied in detail herein, predicting rapid catholyte alkalination.

Eq.2-19 predicts $|b_c| = 38.8\text{mV dec}^{-1}$ if $\beta_c = 0.5$ [299] with the RDS occurring on the 2nd electron transfer ($n_c = 1$). In Figure 5-10, $(n_c + \beta_c n_j) = 1.55$ shows a close fit and requires α to be determined independently. This scenario was postulated by Zagal et al [193].

A film identical to that in Figure 5-3 was applied examined by CV in air saturated electrolyte to apply the Randles-Ševčík criteria in Eq.2-36. The raw data is plotted in Figure 5-11(A) whilst (B) contains the I_p vs $v^{0.5}$ data.

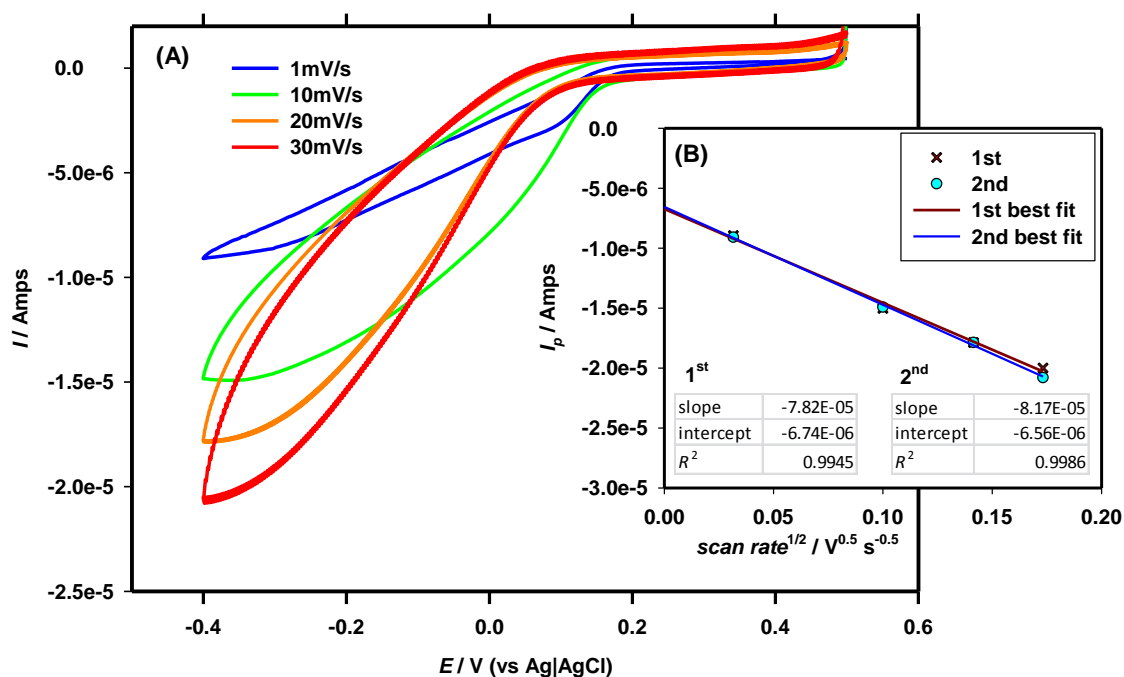


Figure 5-11. (A) i - E data of ORR on unsupported FePc films as a function of scan rate. (B) Randles-Ševčík plot of peak current (i_p) vs $v^{0.5}$ with two identical films from FePc-DMF solution. Electrolyte; Air saturated 50mM PBS, pH 7.0.

Cathodic limit extension would permit a scan rate range to be evaluated but generates Fe(I)Pc [186] with unknown effect on reversibility and unfeasible in MFC operation. The slope of $-7.99 \times 10^{-5} \text{ A s}^{0.5} \text{ V}^{-0.5}$ is relatively low for ORR in this media [300]. Treating with physical data in Table A-2 and C_{O_2} measurements from Table A-3 in Eq.2-36, yields $n_c + \alpha_n$ is 0.048, an unfeasibly low response ($0.2 < \alpha < 0.8$). Reviewing the terms of Eq.2-36 it would appear that an additional film resistance from O_2 diffusion to the active site is present, as the use of Eq.2-39 produces $n_c + \alpha_n = 1.51$. If the reaction site is located at the disc/film interface this discrepancy could be accounted for provided O_2 percolation through the film is slow. Without the presence of O_2 , electron percolation was slow (Figure 5-2) and no cathodic peak is seen rendering trumpet plot analysis on the TFE unfeasible. A plot of E_{pc} vs $\log_{10}(v)$ of a similar film in air (Figure A-5) produced a gradient of $-0.03629 \text{ V}/\log_{10}(\text{Vs}^{-1})$ generating a more plausible $\alpha = 0.413$, more consistent with the $n_c = 1$, $\alpha_n = 0.51$ of the tafel plot. Evaluation in thinner or carbon supported films is required.

5.3.3 Kinetic performance of carbon supported FePc/Nafion films

A plot of E_{pc} vs $\log_{10}(v)$ of the Fe(II)/(III) reaction in an FePc/KJB Nafion film is shown in Figure 5-12.

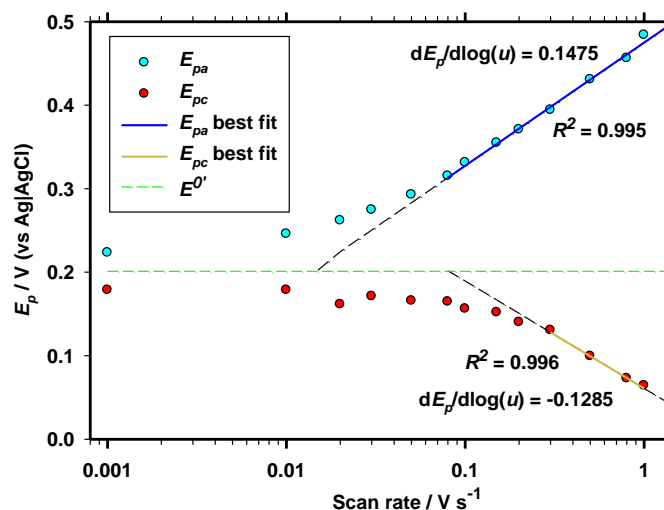


Figure 5-12. Trumpet plot of Fe(II)↔Fe(III) redox of FePcKJB Na-Nafion thin film

In de-aerated PBS the peak potentials produced a linear E_p vs $\log_{10}(v)$ response in the 0.1-1 $V s^{-1}$ range. Using Eq.2-89 the anodic slope and cathodic responses produce $2.3RT/(1-\alpha)nF$ and $2.3RT/\alpha nF$ respectively, resolving to $\alpha=0.44\pm0.03$ for the de-aerated electron transfer. A low error margin is attached as the value α and $(1-\alpha)$ summate to 1.053. Where the extrapolated line meets $E_p-E^{0'}=0V$, Eq.2-89⁷ can be resolved at the corresponding scan rates, $v_{an}=0.013857 V s^{-1}$ and $v_{ca}=0.0811 V s^{-1}$ to produce an electron exchange value k_E at $E^{0'}$,⁸ the average of the oxidation and reduction scan is $k_E=0.9s^{-1}$ with and error margin ±0.55 . Using Eq.2-90 and $\delta_{film}=1.5\mu m$ the heterogeneous rate of electron exchange is $k_{E,h}=0.000135cm s^{-1}$, a non-limiting process compared to typical k_{app} [67]. This illustrates the importance of the carbon support. With the introduction of O_2 , two cathodic peaks are present (Figure 5-13), one associated with ORR visible at low v . In porous films the surface coverage of O_2 does not appear to be complete (eg. Figure 5-6), the Fe(II)/Fe(III) process is still present at high v (ie. Eq.5-1 or with phosphate ligand). Comparison of Eq.2-36 and Eq.2-86 predict $I_p \propto \sqrt{v}$ and $I_p \propto v$ for aerated faradic and de-aerated surface reactions respectively. Hence the ORR reaction is obscured by the Fe(II)/Fe(III) surface reaction at high scan-rate.

⁷ Valid for $E_{pa}-E_{pc}>0.2V$.

⁸ $E^{0'}$ estimated from $E_{pa}-E_{pc}$ at $0.001V s^{-1}$, near as possible to steady state.

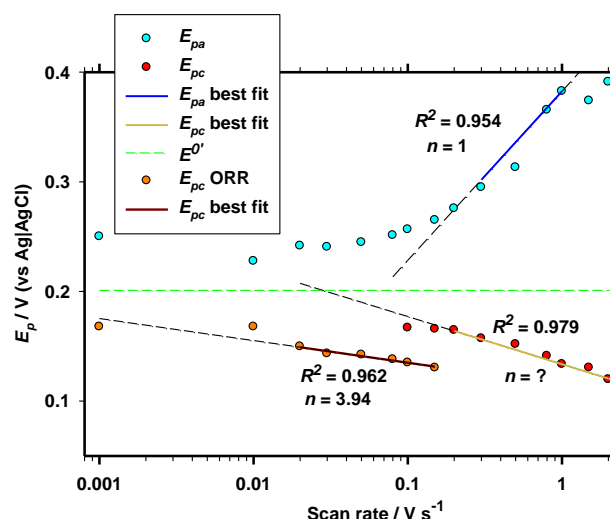


Figure 5-13. Trumpet plot same FePcKJB Nafion electrode in the presence of O₂. Two E_{pc} are present; ORR (orange) and Fe(III)→Fe(II) (red).

Figure 5-13 shows that the gradient of the anodic peak (no bound O₂) has possibly decreased, though $\alpha=0.366\pm0.1$ (from $\alpha=0.44$ in N₂). This value is obtained from $(1-\alpha)$ in the anodic slope. In air, the R^2 co-efficients are lower for all peaks compared to N₂, a larger error margin is attached. E_p is discernable from nearly amalgamated peaks from points of inflexion in the i - E response at $v=0.15\text{ V s}^{-1}$, the linear trend in the E_p vs $\log_{10}(v)$ is maintained with this method. The cathodic ORR peak in Figure 5-13 produces a gradient of $-0.02016\text{ V}/\log_{10}(v)$, Eq.2-30 is non-applicable unless the 1st ET is rate determining [35]. With the addition of O₂, a complex situation occurs on the Fe(III)→Fe(II) peak. The gradient decreases relative to the N₂ data (Figure 5-12), though for conservation of the anodic charge the reaction is predicted to be the same. Applying the predicted $n=1$ variable produces an unfeasibly high transfer co-efficient. Analysis on the anodic slope with Eq.2-89 produces $k_E=1.7\text{ s}^{-1}$ ($0.000425\text{ cm s}^{-1}$), a minor source of rate constriction.

Using the LSV method outlined for method 1, a tabulated summary of all catalysts applied to a GC as thin films with nafion binder thin film electrode catalysts was compiled in Table 5-1. Catalyst preparation and names, Table A-1.

Table 5-1. Various catalyst ORR activity in thin films-Nafion binder.Total powder loading; 71 $\mu\text{g cm}^{-2}$, Nafion ionomer; 111 $\mu\text{g cm}^{-2}$ on GC discs. Tafel and J_0 reported from $\nu=1\text{mV/s}$ LSV data, $\omega=0\text{rpm}$. Electrolyte; 50mM PBS, pH7.

Catalyst	Tafel Slope (η_{O_2} corrected)		J_0	E_{Onset}	RAS	J_{ORR}	$E@$	Initial	OCF
	Process	mV dec^{-1}	A cm^{-2}	mV	10^{13} site cm^{-2}	@-0.1V A cm^{-2}	0.4A m^{-2} mV	OCF mV	O_2 mV
<i>Composites</i>									
FePcMnO_x/MON	MnO _x red.(N ₂)	-163	-						
	ORR(Mn-FePc)	-35.9	1.1E-07	419	27.0	-7.89E-05	165	430	270
FePcMnO_x/KJB (Mn²⁺+KMnO₄)	MnO _x red.(N ₂)	-	-	414	38.8	-1.41E-04	106	460	260
	ORR(Mn-FePc)	-58.2	2.0E-07						
FePcMnO_x/KJB (KMnO₄)	MnO _x red.(N ₂)	-	-	386	4.4	-1.56E-04	156	460	260
	ORR(Mn-FePc)	-39.0	2.7E-07						
TiO_xFePc/MON	ORR(Ti-FePc)	-38.7	4.1E-08	405	21.0	-1.64E-04	150	310	290
<i>Supported FePc</i>									
FePc/MON	ORR(FePc)	-33.4	5.1E-08	407	38.8	-1.60E-04	173	320	280
FePc/KJB	ORR(FePc)	-35.7	2.0E-07	353	223.0	-1.88E-04	201	230	280
<i>Pyrolised FePc</i>									
FePc/MON pyr	ORR(FeNx)	-81.6	2.4E-07	426	-	-1.51E-04	164	320	360
FePc/KJB pyr	ORR(FeNx)	-39.9	3.7E-07	402	3.7	-1.55E-04	169	300	260
<i>Supported MeOx</i>									
MnO_x/MON	MnO _x red.(N ₂)	-125	-	400	-	-8.57E-06	-172	450	50
	ORR(Mn-C)	-87.1	2.3E-07						
TiO₂/MON	ORR(C-TiO ₂)	-89.8	-	379	-	-6.45E-06	-186	190	-
TiO₂/MON pyr	ORR(C-TiO ₂)	-97.5	5.1E-08	352	-	-7.86E-06	-199	160	120
<i>Carbon Supports</i>									
Synthetic Graphite	2e ⁻ ORR	-170.2	3.8E-08-	323	-	-7.33E-07	-348	160	140
KJB	2e ⁻ ORR	-118.9	n/a	329	-	-4.26E-06	-230	160	-
Monarch	2e ⁻ ORR	-79.4	2.3E-07-	400	-	-1.25E-05	-145	260	50
Monarch HT	2e ⁻ ORR	-141.7	1.3E-07	326	-	-1.00E-05	-197	300	190
Pt/C	First Tafel	-63.2	2.2E-06						
	Second Tafel	-110.4	8.7E-06	414	-	-2.31E-04	307	390	400

An example of tafel slopes determination is seen in Figure 5-14. Tafel slopes for carbon materials occurred in the potential range ($-0.1 < E < 0.05\text{V}$). Redox active site (RAS) for Fe(II)Pc/Fe(III)Pc is obtained as Figure 2-18 ($\nu=20\text{mV/s}$). " $J_{\text{ORR}}@E=-0.1\text{V}$ " represents current obtained in $\nu=1\text{mV/s}$ LSV in N₂ subtracted from the $\nu=1\text{mV/s}$ LSV in O₂ at a potential of $E=-0.1\text{V}$. " $E@0.4\text{A m}^{-2}$ " represents the potential at $J=0.4\text{A m}^{-2}$. J_0 is obtained by extrapolating the tafel slope to OCF as in Figure 5-14.

Data obtained under N₂ is shown in green, ORR tafel response in blue for carbon and black for FePc/KJB. The dash black line is OCF for the FePc/KJB electrode.

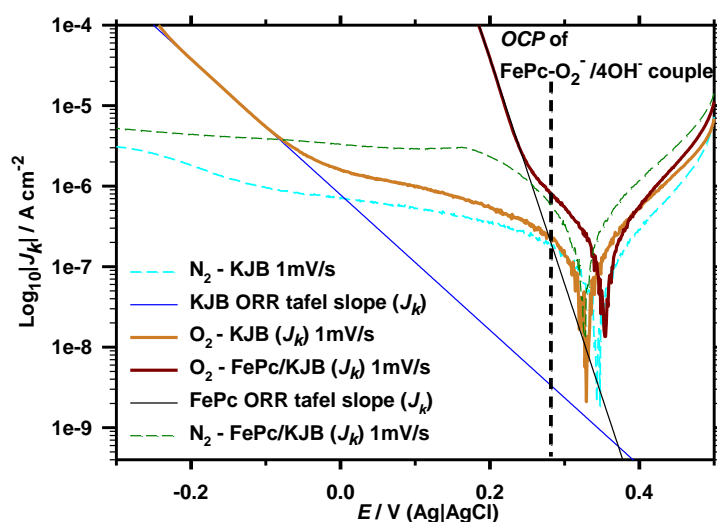


Figure 5-14. Tafel slope of KJB and FePc/KJB films on GC. Example of extrapolating J_0 . Vertical dash black line = OCP of FePc/KJB films in O_2 . Electrolyte; O_2 saturated 50mM PBS, pH 7.0; $\omega=0$ rpm, $\nu=1$ mV s⁻¹

The OCP of iron porphyrin based catalysts is controlled by the $FePc-O_2^-/4OH^-$ couple [192]. If this premise holds for carbon supported FePc films, extrapolating the tafel slope of ORR to OCP produces J_0 of the RDS. Comparing Figure 5-10 to Figure 5-14 shows a 13 fold increase in geometric exchange current related to this mechanism, the average electroactive FePc, $\bar{\Gamma}_{FePc} = 3.9 \times 10^{-9}$ Moles cm⁻² (Table A-8) resulting in the increase in J_0 over the unsupported film. The tafel slope is present at $E < 0.22$ V and shows improved kinetics, $|b_c| = 33.4$ to 35.7 mV dec⁻¹, over the unsupported film with a small influence of type of carbon support.

The KJB film produced tafel behaviour at $E > -0.05$ V. A comparison between E_{onset} (KJB; 0.329 V. Monarch; 0.4 V) and OCP (0.05 to 0.019 V of all carbon materials) indicates E_{onset} is a poor method of validating ORR activity in porous films. Small discrepancies between N_2 and O_2 for KJB may be due to additional surface charges nucleating around chemisorbed O_2 increasing C_2 .

Key observations on other carbon and FePc/C catalysts in Table 5-1;

- Tafel slopes of FePc materials in Table 5-1 are among the best recorded when compared to literature values (Table 3-2).⁹
- For carbon black, tafel behaviour $120 > |b_c| > 90$ mV dec⁻¹ is within value range reported in literature [214], the increase consistent with HNO_3 treatment [301].

⁹ It should be stated that use of O_2 concentration and iR correction in cited studies is unknown.

- Combining exchange current from the high and low potential mechanism [298] on Pt produced $J_0=1.1 \times 10^{-5} \text{ A cm}^{-2}$.

5.3.4 FePc – influence of rotation on kinetic current

Electrode rotation was used to examine the influence of substrate diffusion limitation on catalytic turnover. The result for thin films of FePc deposited from DMF (a) and FePc/KJB films with Nafion binder (b) are depicted in Figure 5-15.

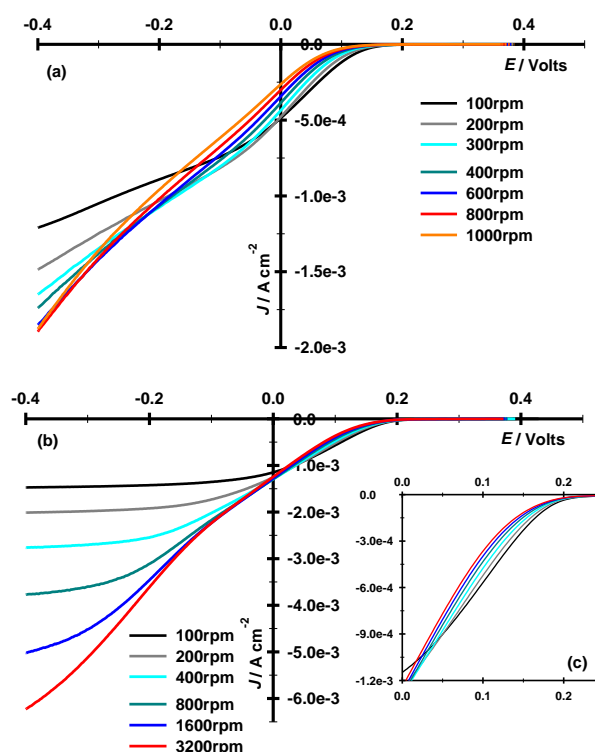


Figure 5-15. Influence of ω on kinetic control region of J vs E plot in thin films; (a) unsupported FePc ($\Gamma=4 \times 10^{-9} \text{ Moles cm}^{-2}$) or (b) FePc/KJB Nafion, inset (c) enlarging the $0 < E < 0.25 \text{ V}$ region of (b). $\nu=5 \text{ mV/s}$. Electrolyte; 50mM PBS, pH7.

Electrode rotation inhibited current at potentials of kinetic control ($E > 0.05 \text{ V}$) in FePc films in Figure 5-15(A) and (B). The simultaneous occurrence of catalyst de-activation made application of limiting current scenarios [33, 59, 60, 77] unfeasible. In $1e^-$ ET kinetic control situations a $J \neq f(\omega)$ could be expected [35]. The Koutecký-Levich (K-L) plot for Carbon and Pt/C layers indicated a 1st order reaction with O_2 over the majority of the potential range. The plot could not be made for FePc indicating a significant chemical step in PBS media. Homolysis of adsorbed peroxide could feasibly be cleaved

by $\text{OH}^-_{(\text{aq})}$ as opposed to further electroreduction. Rapid agitation may neutralise alkalination and explain the rotation dependent chemical step in Figure 5-15(A), further evidence is required. This response is briefly observed by Mamuru et al for FePc-Multiwalled Carbon Nanotubes [89] and immobilised Iron Porphyrins and cytochrome C in PBS [302].

The data in Figure 5-15(A) and (B) produced linear tafel slopes at all rotation (not shown). Inhibition of $|b_c|$ was greater for FePc than FePc/Nafion. Reduction in $|b_c|$ would exclude the possibility of active site blocking [70], this blocking phenomenon causes tafel plots to shift down the current axis, maintaining a constant gradient. A more detailed mass balance is required to test the hypothesis of an important chemical step.

5.3.5 Wroblowa analysis of intermediates and heterogeneous rate constants

This analysis aims to differentiate between direct $4e^-$ reduction to H_2O (k_1) and sequential $2e^-$ reduction to H_2O_2 (k_2) followed by $2e^-$ reduction to H_2O (k_3). Mechanism evaluation at $E \approx 0.2\text{V}$ is the primary aim. Unsupported FePc film was used as k_5 is negligible; no other species than FePc are present in the film. In a carbon supported film k_5 and k_3 occurring simultaneously.

In Figure A-11 the slope of the $I_{D,L}/(I_{D,L}-I_D)$ data can be converted to $\text{m}^2 \text{s}^{-1}$ (k_{app}) using Eq.2-84, multiplying the slope (Figure 5-16) by $Z=8.68 \times 10^{-6}$. The linearity of this graph indicates H_2O_2 flux back from the solution ($k_{D,\text{H}_2\text{O}_2,b}$) is negligibly small over the experiment timescale [74] and k_4 is small [44]. Unfortunately the intercept $\neq 1$ in all cases, so no simple assumptions about k_1+k_2 can be made [61, 72, 303].

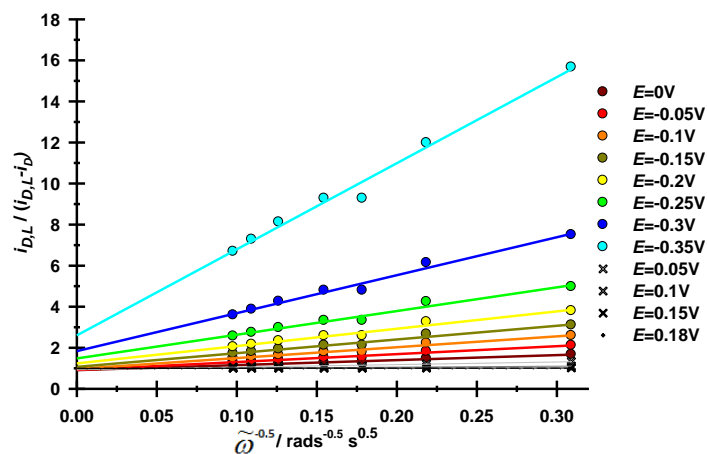


Figure 5-16. $i_{D,L}/(i_{D,L}-i_D)$ vs $\tilde{\omega}^{-1/2}$ plot for unsupported FePc film
($\Gamma=4 \times 10^{-9}$ Moles cm^{-2}), $v=5\text{mV/s}$.

The $CE \cdot i_D/i_R$ vs. $\tilde{\omega}^{-1/2}$ plot for unsupported FePc is presented in Figure 5-17 ($\Gamma_{FePc}=4 \times 10^{-9}$ Moles cm^{-2}). The goodness of fit of the $200 < \omega < 1000\text{rpm}$ data is plotted in Figure 5-17 as a function of potential in Figure 5-18. The data was modified to $CE \cdot i_D/i_R$ vs. $k_{D,H_2O_2}^{-1}$ plot using Eq.2-72 and the corresponding slope vs. intercept (S vs J) is represented in Figure 5-17. Each approach or correction for CE and the effect on the general shape of the S vs. J plot is located in the appendix.

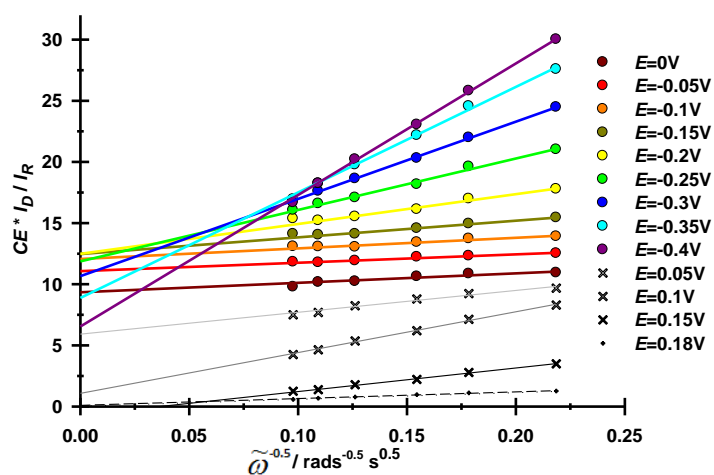


Figure 5-17. $CE \cdot i_D/i_R$ vs $\tilde{\omega}^{-0.5}$ plot for unsupported FePc film ($\Gamma=4 \times 10^{-9}$ Moles cm^{-2}). Split into several graphs of similar Y-axis range, least squares best fit lines applied, $CE=0.37\%$ for all ω . $v=5\text{mV/s}$. Electrolyte; 50mM PBS, pH7.

The plots of $CE \cdot i_D/i_R$ vs $\tilde{\omega}^{-0.5}$ are linear in all instances. This indicates a) all disc reactions are first order [74], and b) the only reaction occurring on the ring is H_2O_2 oxidation [74].

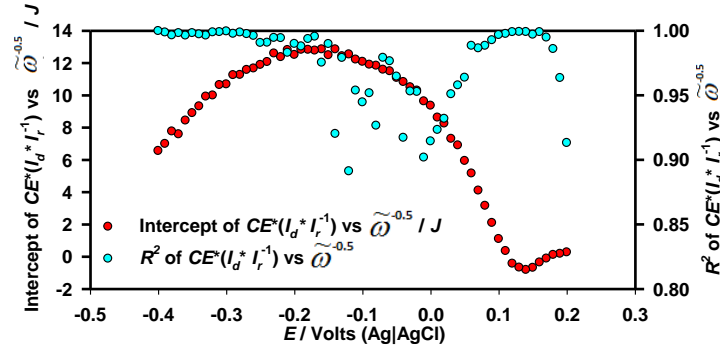


Figure 5-18. Intercept and R^2 fit of data from the CE^*i_D/i_R over $\omega^{-1/2}$ plot of the film in Figure 5-17.

The R^2 value of the fit displayed two regions of high correlation; $0.05 < E < 0.18\text{V}$ and $-0.4 < E < -0.18\text{V}$. According to the derivation these regions correspond to kinetic control and diffusion control respectively. The highest R^2 values were obtained using CE vs ω correction from Glassy Carbon for the unsupported Iron Phthalocyanine. For catalysts films such as FePc/MON the CE vs ω correction from a film of synthetic graphite (Figure A-8) produced linear trends. The reason could be interpreted as physical unevenness of carbon film surfaces and Nafion coatings affecting distribution of H_2O_2 to the ring.

Figure 5-18, the FePc film;

- The intercept value is potential dependent, increasing above unity with increasing potential, passing through unity at $E=0.19\text{V}$.
- The intercept J is relatively constant from $0.2 > E > 0.14\text{V}$, implying a constant k_1/k_2 ratio.

In Figure 5-19 the CE^*i_D/i_R vs $\tilde{\omega}^{-0.5}$ slope values are modified from $\text{rad}^{0.5} \text{s}^{-0.5}$ to m s^{-1} using Eq.2-62 or the analogous Eq.2-72 and data presented as an S vs C plot for the unsupported film.

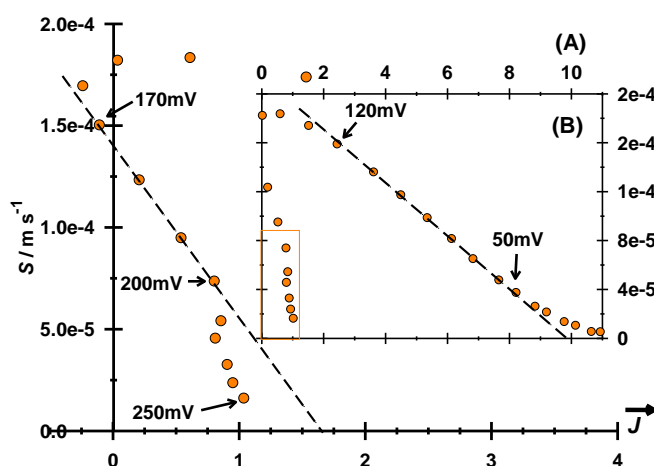


Figure 5-19. S vs J plot of unsupported FePc film. Film $\Gamma=4 \times 10^{-9}$ Moles cm^{-2} . Dash black line extrapolates to J axis at $J=J'$. (A) low η region (B) $0.24 > E > -0.03\text{V}$ region.

Linear regions in this plot are seldom acquired [44], when they are k_1 , k_2 , k_6 and k_3/k_5 are usually acquirable [44]. A minimum C value of unity should be observed [42], the intercept approaches <1 for regions of high correlation ($R^2 > 0.99$) at $0.18 > E > 0.12$. Regardless of whether the Appleby or Wroblowa criteria is applied, Eq.2-71 is applicable for linear S vs J regions. Though negative rate constants can sometimes be obtained [44], the scenario where $k_1 = \text{c.a.} -0.3k_2$ at low overpotential is an unlikely scenario considering H_2O_2 oxidation is not possible $E < E_{\text{Fe(II)/Fe(III)}}^{0'}$ for Iron Phthalocyanine. With ring current background subtraction (Figure A-9) an intercept value $J'=1$ was obtained, hence this result is treated as $k_1 < k_2$. This interpretation is consistent with Figure 5-8 where H_2O_2 release is highest in this potential region.

Two linear regions at high potential were observed and one at low potential. The high potential regions are 1) $0.21 > E > 0.18\text{V}$ and 2) $0.09 > E > 0.04\text{V}$. Interestingly, the gradient of S vs. J (m s^{-1}) for these regions are $-1.54 \times 10^{-4} \text{ m s}^{-1}$ ($0.18 > E > 0.15\text{V}$) and $-1.542 \times 10^{-5} \text{ m s}^{-1}$ ($0.1 > E > 0.06\text{V}$), one order of magnitude lower. The negative gradient cannot be explained. It did not occur in any other carbon catalysts, only Pt.

Potentials where gradient $S \rightarrow 0$ such as $E=0\text{V}$ show that k_3+k_4 is insignificant in relation to k_{5f} . If it can be shown that k_{5f} is negligible (ie. $k_1 \gg k_2$) then it can also be proved disproportionation is negligible. As ($S \neq 0$) it must be concluded H_2O_2 is capable of adsorption onto FePc as anticipated and an adsorption equilibrium described by

Wroblowa must be considered. This conclusion supports the body of work in H_2O_2 electrolyte described by many authors [187, 208].

The high overpotential J' intercept is 9.8 ($0.09 > E > 0.04\text{V}$), producing $k_1 = +4.4k_2$. The second linear region ($0.04 < E < 0.9\text{V}$) is associated with the direct $3e^-$ electrochemical reduction of FePc-O_2^- to OH^- as postulated by Savy [192]. Behret et al [206] studied Iron Naphthalocyanine films in 1M KOH, producing $k_1/k_2=75$ for polymeric Fe(III) and $k_1/k_2=8$ for polymeric Fe(II) at similar η to this study. Suggesting the thin fully reduced underlayers catalyse an electron “conveyor belt” that would be blocked with Fe(III)Pc and facilitates k_2 .

Figure 5-20 displays $\log_{10}(S J^{-1})$ vs E plot to obtain H_2O_2 oxidation/reduction data. Depending on whether the Appleby or Wroblowa criteria reflect the system, Eq.2-81 or 2-68 reflects the linear (tafel) regions of the residual plot. Numerous solutions are applied depending on which method of CE vs ω correction is used (see appendix 10.5.3.), the method producing the highest R^2 fit (Figure 5-18) is shown with orange dots.

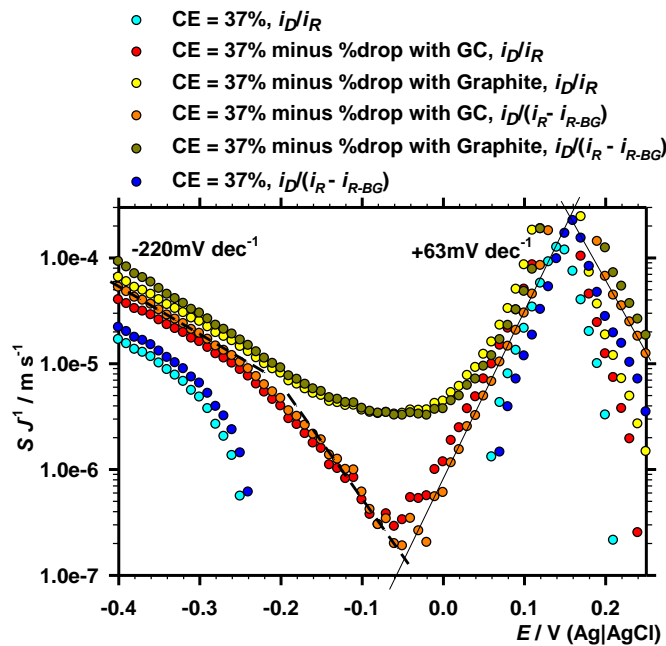


Figure 5-20. S/J vs. E plot of the data from Figure 5-19. $CE \cdot i_D/i_R$ vs. $k_{D,\text{H}_2\text{O}_2}^{-1}$ data treated with different means (see key). Kinetic rate of intermediary reactions separated from ORR tafel plot. Tafel regions indicate dominance of one term in the Eq.2-81.

The S/J vs. E plot in Figure 5-20 reaches a minima at $E = -0.05\text{V}$. The complex behaviour could not be described by Eq.2-70, as $k_I \neq 0$. The tafel like behaviour describes

the fate of H_2O_2 on the FePc surface, becoming apparent when one of the rate constants in Eq.2-81 dominates. Conversely this process reaches a rate maxima at $E=0.16\text{V}$. Reconciling the fact that $k_4 \neq f(E)$ this would suggest that k_4 is negligible at all potentials, otherwise the tafel behaviour in Figure 5-19 would not be seen.

The S/J vs E plot is potential dependent at all potentials, inputting the reasoning k_4 is negligible. In which case, the S/J value is equal to k_3+k_{5f}/k_3k_{5b} in Appleby's method. Clearly, k_3 increases with cathodic $|\eta|$, resulting in a plot inverse to Figure 5-20. Another tafel dependent rate constant is missing from the balance. $k_{E,h}$ from Figure 5-13 could not be determined for unsupported films but neither Wroblowa or Appleby's theorem account for the effect of polarisation on electron propagation in the film. k_3 shows that this term dominates the equation and k_{5b} and k_{5f} relatively consistent in the $E>0\text{V}$ region. The assumption $2k_1/k_2=0$ cannot be used to reduce Eq.2-68 or Eq.2-81.

Other Materials..

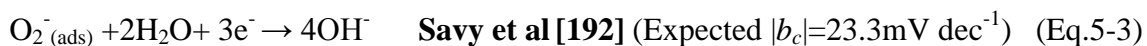
- The S/J maxima at $E=0.16\text{V}$ is also seen in FePc/MON (not shown), though the lower minima is convoluted from disproportionation.
- For FePc/MON two linear S vs C regions 1) ($0.2>E>0.17\text{V}$) at $J'=1.2$ ($k_1=0.1k_2$) and 2) ($0.1>E>0.04\text{V}$) producing $J'=15.7$ ($k_1=7.35k_2$).
- For Pt/C, the S vs. J intercept (J') produced a large linear range of $-0.15>E>-0.4\text{V}$ with $J'=69.8$ ($k_1=34.4k_2$). This suggests ~3% of ORR on Pt/C proceeds through k_2 , cross-referencing with Figure 5-8 shows 0.9% H_2O_2 is detected at the ring, suggesting the majority is further reduced to H_2O .

In terms of k_1 and k_2 the reaction regime is essentially the same on supported and unsupported carbon. For the low overpotential ORR wave the release of H_2O_2 is controlled by adsorption strength and duration. As H_2O_2 is degenerative to the catalyst, potentials greater than $E=+0.1\text{V}$ should be avoided for MFC operation of FePc and FeN_x cathodes.

5.3.6 The rate limiting step

Each scheme is dependent on FePc preparation method. Anticipated tafel slopes are reported for cases of $4e^-$ reduction for a value of $-\beta_c=0.5$ using Eq.2-19. The scheme

proposed by Zagal and Savy both depend on electroreduction of Fe(III)Pc-O₂⁻. The scheme by Savy represents the direct 4e⁻ route (*k*₁).



A small range in FePc tafel slope values (-37.4 to -25.4 mV dec⁻¹) shows dependence on support and binder (chapter 6). Improved tafel slopes with the hydrophilic anion exchange binder is accompanied by a larger %H₂O₂ in supported catalyst. It is known that the symmetry factor is indirectly affected by binder [304]. Appleby et al propose a chemical step where electron insertion is not the RDS so symmetry factor is irrelevant, meaning a fixed tafel gradient.

In the scheme proposed by Appleby, •OH is produced, an extremely strong oxidising agent (*E*^{0'} = 2.19V), catalyst damage would be extensive as the ring may be susceptible to oxidation, and free Fe detected. Deactivation would increase with *k*₃. Electro-reduction of •OH would not require adsorption (outer sphere).

From the K-L study, the non-linearity two potential explanations remained; 1) An chemical step consisting, accompanying or following the RDS, or, 2) severe electron propagation limitation with a reaction located at the electrode-film interface and not occurring at the film-electrolyte interface [305]. If this model is applicable non-linearity may disappear in thinner films with monolayers and low loading of FePc. In the authors opinion this is an implausible reason; electron conductance and propagation through the film would not be impeded by high rotation and it appears that the K-L non-linearity 'doubled back' on itself as opposed to reaching a plateau. In other words, the film should not be less e⁻ conductive at high *ω*. Electron propagation limit appears unlikely.

This suggests a chemical step following electron transfer [306]. No chemical step would follow electron transfer in the scheme proposed by Appleby. The non-linearity occurs over a wide range and is present in the region dominated by the 27.7 < |*b*_c| < 37.4 mV dec⁻¹ and the |*b*_c| < 60 mV dec⁻¹ regions suggesting both perform a significant chemical step.

For supported FePc;

Low η ; $(0.2 > E > 0.17\text{V}) k_2 \text{ (RDS)} \rightarrow k_3 \text{ electro-reduction and chemical step (Eq.5-5)}$

Medium η ; $(0.1 > E > 0.04\text{V}) k_1 \text{ (RDS) electro-reduction and chemical step (Eq.5-6)}$

5.4 Iron Phthalocyanine stability

5.4.1 De-activation of FePc - Consecutive cyclic voltammetry in O_2

A mechanism of de-metallation was identified in the catalyst ink in appendix section 10.4. This study demonstrates FePc de-metallation does not require polarisation. The timescale is relatively long and included the presence of ethanol. To establish what co-factors and conditions are required for Eq.3-8 to occur, the stability of the main Fe(II)/Fe(III) peak was evaluated with consecutive cyclic voltammetry (Potentiostatic scan in section 4.1.7) and depicted in Figure 5-21.

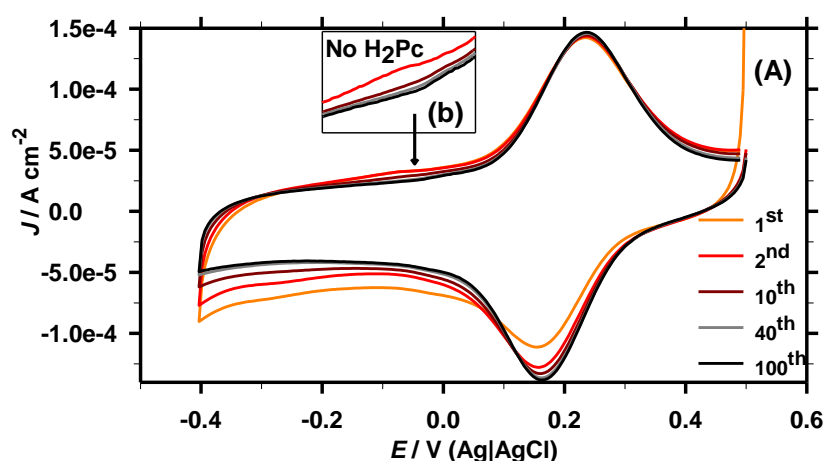


Figure 5-21. FePc stability in de-aerated PBS.(A) Consecutive CV of FePc/KJB (Nafion) films. (b) Enlarged $-0.2 < E < 0.05$ region showing no H_2Pc redox. Electrolyte; N_2 saturated 50mM PBS, pH 7.0. $\omega=0\text{rpm}$. $\nu=50\text{mV/s}$

In de-aerated PBS the surface active FePc increases with electrochemical surface cleaning. No H_2Pc redox was detected. The adsorption of Phosphate does not cause the Fe to dislocate from the macrocycles plane [211], a process making Fe susceptible to proton cleavage from the macrocycle plane when O_2 is the ligand .

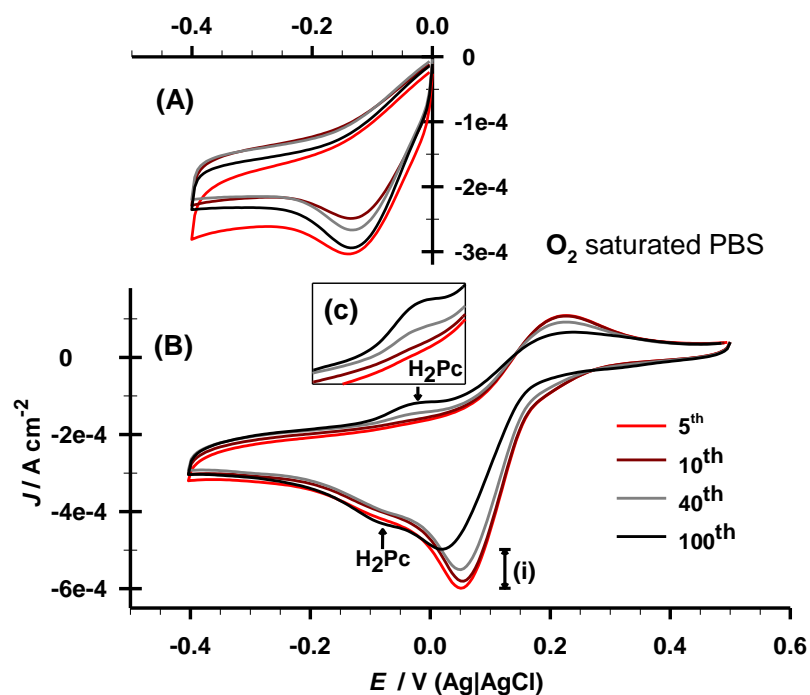


Figure 5-22. FePc stability from ROS production in FePc/KJB Nafion thin films
Consecutive CV (100 scans) over (A) $-0.4 < E < 0\text{V}$ or (B) $-0.4 < E < 0.5\text{V}$ with (c) showing H_2Pc redox ($-0.2 < E < 0.05$) in (B). Electrolyte; O_2 saturated 50 mM PBS, pH 7.0. $\omega=0\text{rpm}$.
 $\nu=50\text{mV/s}$

Following polarisation in N_2 -PBS (Figure 5-21) the solvent was sparged with O_2 the procedure repeated for the same potential range, Figure 5-22(B). A fresh FePc/KJB Nafion film was subjected to CV in the range of ($-0.4 < E < 0\text{V}$) in Figure 5-22(A).

The H_2Pc peak observed after creation in the catalyst ink is also generated electrochemically from O_2 turnover. From the ink the anodic peak occurs at a similar potential $E_{pa}=-0.076\text{V}$ as from electrochemical degradation $E_{pa}=-0.032\text{V}$ in Figure 5-22(B), but the corresponding cathodic peak shows an anodic shift, pointing to interaction between ethanol and oxidised Phthalocyanine in the ink. The produced moiety increases with repeated CV to 13.2% the charge of the de-aerated Fe(II)/Fe(III) redox by scan# 100. When the anodic range is cropped to $E=0\text{V}$ the H_2Pc is not created in significant quantity, as the peak ($E_p=-0.134$) did not grow with consecutive scans. The explanation being avoidance of the O_2 free Fe(III) state. The explanation of H_2O_2 production chemically oxidising the aza-nitrogen [142] of the macrocycle causing ring opening has been offered by some authors. However, the produced Pyrrole-2-amine type moiety is not anticipated to yield the redox activity in Figure 5-22(C).

To omit the possibility of residual protons in acidified Nafion binder exacerbating demetallation, the test was repeated with Na⁺Nafion, using a higher rotation speed to remove produced soluble material and increase O₂ turnover. In Figure 5-23 the *i*-*E* plot was obtained in N₂ (A) prior to extensive ORR (B) in air saturated PBS, then the solution de-aerated again and the effect of ORR on the redox properties of residual FePc was shown (B).

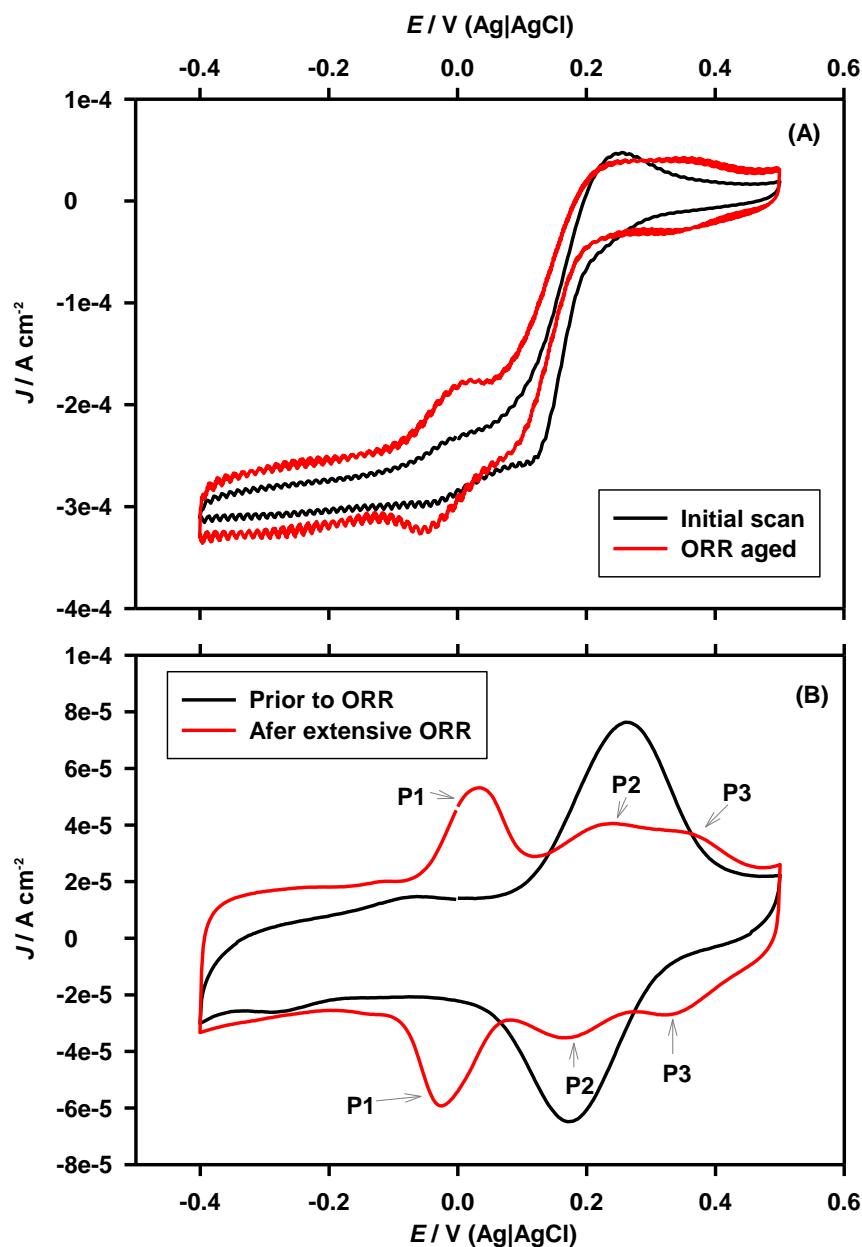


Figure 5-23. Redox properties of moieties generated from ORR induced FePc deactivation CV of FePc/KJB films with Na⁺Nafion binder in 50mM PBS pH 7.0 Electrolyte; (A) Air saturated, $\omega=100\text{rpm}$ followed by (B) N₂ saturated, $\omega=0\text{rpm}$. $v=20\text{mV/s}$

The result indicates that the single Fe(II)/Fe(III) redox was split into 3 redox couples with peaks, P1, P2 and P3. Forward and reverse peak potentials of Fe(II)Pc/Fe(III)Pc

(P2) was consistent after electrochemical aging. Only the moiety P1 produces an oxygen reduction wave in plot (A). Moreover, the redox feature P2 is approximately the same size (Q) and peak potential E_p in aerated media and de-aerated media, indicating minimal interaction between an O_2 ligand to the P2 moiety. This is in keeping with studies on H_2Pc , which describe no ORR activity of this molecule, and the conclusions in Figure 5-22. The creation of this moiety under rapid turnover conditions (high rotation) meant that quiescent solutions frequently had to be used.

5.4.2 Pyrolysis effect on active site

The reduction in Fe(II)/Fe(III) redox charge in the $-0.4V < E < 0.5V$ range after pyrolysis of FePc/KJB is seen in Figure 5-24 and the peak characteristics described in Table 5-2.

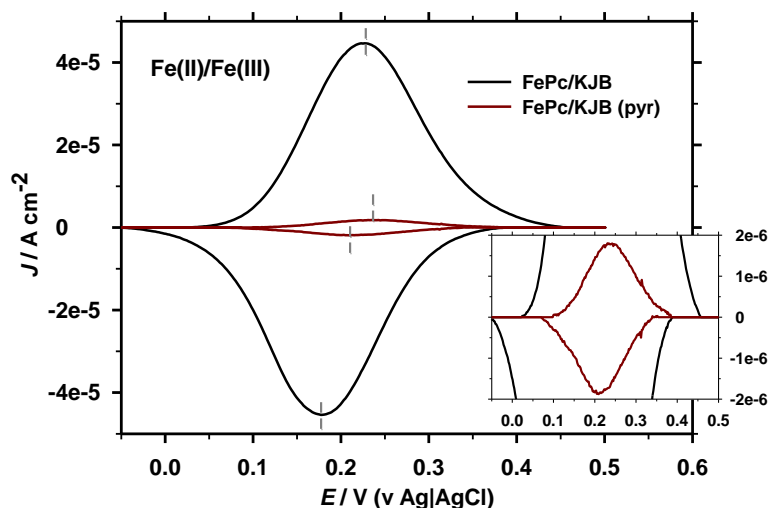


Figure 5-24. Redox potential of Fe chelate. The effect of pyrolysis on the Fe(II)/Fe(III) redox potential of FePc/KJB, Capacitive current subtracted. Inset shows FePc/KJB pyr. Electrolyte; N_2 saturated 50mM PBS, pH 7.0. $\nu=20\text{mV/s}$

Table 5-2. Peak characteristics of Figure 5-24.

	FePc/KJB		FePc/KJB (pyr)	
	Fe(II) \Rightarrow Fe(III)	Fe(III) \Rightarrow Fe(II)	Fe(II) \Rightarrow Fe(III)	Fe(III) \Rightarrow Fe(II)
$\nu=20\text{mV/s}$				
Charge / $C\text{ cm}^{-2}$	3.57E-04	-3.58E-04	1.24E-05	-1.25E-05
$W_{1/2} / V$	0.149	0.145	0.143	0.127
Distribution	Gaussian	Gaussian	Gaussian	Gaussian
$J_p / A\text{ cm}^{-2}$	4.47E-05	-4.54E-05	1.80E-06	-1.88E-06
$E_p / V\text{ (Ag AgCl)}$	0.2229	0.1773	0.2309	0.209

At this pyrolysis temperature no intact Phthalocyanine chelate remains [183]. The peak is reduced from 357 to 12.4 $\mu\text{C cm}^{-2}$ after pyrolysis, while the peak remains Gaussian, indicating sites are still accessible to electrolyte and are not electrically insulated. The remaining Iron was detected as a ring current in the original polarisation of the film in de-aerated media. Re-organisational energy is lost during Fe(II)/Fe(III) redox as the ideal $W_{1/2}=0.089\text{V}$ (Eq.2-88) is not seen, with $W_{1/2}$ being 0.149 and 0.143 prior and after pyrolysis. A slight anodic shift in $E^{0'}$ is attained from 0.2V to 0.231V which results in a shift in E_{ORR} provided the produced moiety can bind O_2 .

5.4.3 Pyrolysis effect on potential of the ORR wave

In Figure 5-25 the value of E_{ORR} is obtained from subtracting current in N_2 from that in O_2 during $v=1\text{mV/s}$ LSV. No peak was observable for pyrolysed FePc/KJB at $v=1\text{mV/s}$, becoming visible at $v=5\text{mV/s}$.

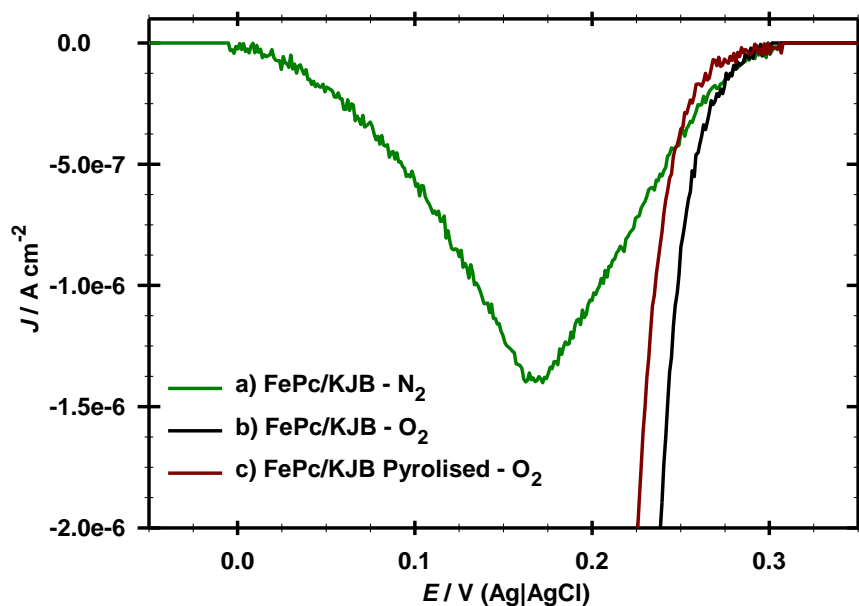


Figure 5-25. Components of current (J_{ORR} and Fe(II)/Fe(III)) in thin FePc/KJB films with Nafion binder, data from $v=1\text{mV/s}$ LSV of a) FePc/KJB in N_2 , b) J_{ORR} of FePc/KJB in O_2 , or c) Pyrolysed FePc/KJB in O_2 . $\omega=0\text{rpm}$. Electrolyte; 50mM PBS, pH7.

E_{ORR} remained constant (0.3-0.31V) before and after pyrolysis despite $E^{0'}$ FeII/III shifting anodically. This result indicates the $\text{Fe(III)N}_x\text{-O}_2^-$ adduct reduction potential [32] is influenced by the electron donating strength of the new iron chelate site. The

decrease in tafel slope is marginal (Table 5-1) indicating reaction mechanism remains unchanged.

5.4.4 Peroxide generation of pyrolysed FePc

With use of Eq.2-56 the ratio of ring H_2O_2 oxidation ORR current at the disc is presented for FePc/C materials before and after pyrolysis ($T=800^\circ\text{C}$) in Figure 5-26.

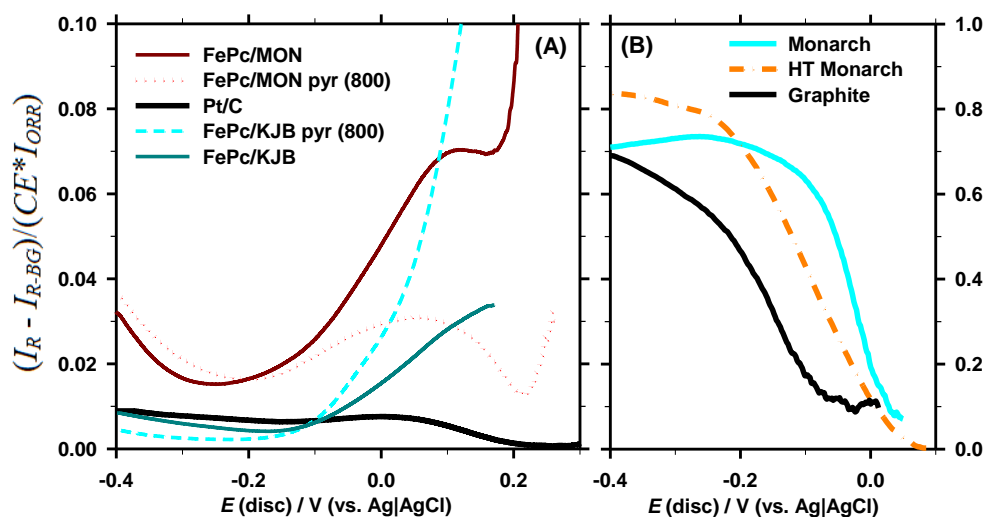


Figure 5-26. Effect of pyrolysis on $\%\text{H}_2\text{O}_2$ vs. E profile of thin films applied to $71\mu\text{g cm}^{-2}$.

(A) supported FePc materials (B) carbon supports with and without pyrolysis.

Electrolyte; 50mM PBS, pH 7.0. $\omega=200\text{rpm}$. $\nu=5\text{mV s}^{-1}$

For pyrolysed Iron chelates Figure 5-26(A) the proportion of H_2O_2 released drops with potential until $E < -0.1\text{V}$ where $\%\text{H}_2\text{O}_2$ becomes relatively constant. The $\%\text{H}_2\text{O}_2$ vs. E profile generally shows comparability with alkali media [208, 215]. The environment of FePc deposition appears to be differ between the two carbons, with pyrolysis decreasing $\%\text{H}_2\text{O}_2$ in Monarch and increasing $\%\text{H}_2\text{O}_2$ with KJB. The basic, high surface area carbon (KJB) supports the catalyst in a surface environment that efficiently decomposes H_2O_2 .

Up to 23% H_2O_2 could be detected from FeNx/KJB warranting significant investigation as to whether k_3 is inhibited by pyrolysis. Peroxide ring current was detected at disc potential 0.03V before and 0.06V after HT treatment of Monarch. Despite a significant quantity of edge plane oxygen susceptible to thermal decomposition the $\%\text{H}_2\text{O}_2$ vs E for

Monarch following appears similar before and after pyrolysis, indicating minimal influence of re-graphitization on k_4 .

5.5 Conclusions

Activity;

Unpyrolysed FePc produces superior tafel slopes to carbon and platinum, the MFC cathode materials of choice. They release less than 10% peroxide showing good energy efficiency, and supporting FePc on carbon black reduces this amount to a minimum 0.6%, recorded for FePc/KJB thin films at a realistic MFC cathode operating potential. The primary product of the ORR reaction was OH^- when catalysed by FePc, this has design ramifications for air cathodes, explaining why alkali crystals occur in catalyst layers after extended operation in chapter 6.

The Phosphate anion affects the activity of FePc, future work on anion effect on FePc catalysis is recommended as it should influence membrane and ionomer selectivity. This may be accomplished with buffered mediums with weak complexing ligands, such as NaCl–PIPES buffered electrolyte.

The nature of ORR on carbon materials was advanced by pH7 study, allowing potential carbon treatments to be assessed and capacitive effects omitted from reporting. A recommendation for carbon supports for FePc would be for high surface area inactive materials with a purely capacitive response to voltammetry.

Mechanism;

ORR is strongly linked to surface concentration of Fe(II)Pc (Figure 5-25). No rate limitation is associated with the O_2 adsorption step, unlike in acid media [307]. Large tafel gradients associated with H^+ utilisation were insignificant in comparison to the $|b_c| < 60 \text{ mV dec}^{-1}$ associated with alkali media ORR. An electron transfer limiting step must be at-least the 2nd e^- transfer. The RDS is not thought to be exclusively of a chemical nature due a small variation in tafel slopes for FePc, as if influenced by symmetry factor in inner sphere electron transfer. A scheme was presented with an RDS that varied with potential. Increased H_2O_2 release at high potential suggests a peroxo intermediary in a strong adsorption at equilibrium. It is almost certain the last step in the reaction is electron insertion into an $\text{Fe(III)Pc-PO}_4^{x-}$ or $\text{Fe(III)Pc-H}_2\text{O}$ moiety devoid of

oxygen. The decrease or absence of the $\text{Fe(III)} \leftrightarrow \text{Fe(II)}$ peak in O_2 suggests that O_2 cannot bind to Fe(III)Pc by replacing a H_2O ligand. Unlike Haemoglobin, O_2 desorption from FePc appears slow and low in reversibility, unless substituted by a stronger ligand.

Stability;

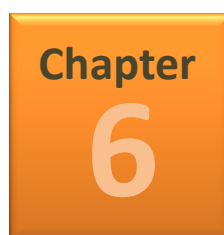
New techniques for quantifying iron macrocycle de-activation are outlined and should be valid for measurements in solutions of Phosphate/Phosphoric acid. The reduction in $\text{Fe(II)Pc} \rightarrow \text{Fe(III)Pc}$ peak and rise of H_2Pc redox can be used to quantify demetallation rate and separate from reactive oxygen species deactivation. De-activation requires the presence of oxygen and cannot occur with Phosphate alone. The de-activation rate is greatly increased by polarisation, though de-metallation is higher than ROS deactivation when an acidified binder is used. De-metallation increases significantly with polarisation at high potentials and was not negligible at pH7.

Pyrolysis may not be required for neutral media application unless significant stability improvements can be demonstrated.

Pyrolisation;

For neutral media, pyrolisation may result in a small number of sites with an increase in thermodynamic performance (lower E_a), as with CoN_4 moieties in acid media [301]. However, the kinetic performance (k_{app}) is greatly impeded, resulting in inferior tafel slopes, unlike acid media studies [225, 301]. Pyrolysis of two carbon supported FePc catalysts was repeatedly inferior to the unpyrolysed version.

Post pyrolisation performance and chemical treatment of the carbon support may be strongly related. The carbon support with fewer quinolic structures (FePc/KJB) resulted in a higher pyrolysed FePc performance, due to large amounts of wasted chelated precursor. Some solid $\text{Fe(III)O}_x/\text{Fe(IV)O}_x$ was produced. The best tafel slope of pyrolysed FePc was $|b_c|=39.9\text{mV dec}^{-1}$. Though pyrolysis caused a decrease in $\%\text{H}_2\text{O}_2$ release at low potential, the overall life of the catalyst was short. On balance, the author would not recommend pyrolisation of FePc for MFC cathodes.



**Chapter 6. Results - Improved kinetic performance of Iron
Phthalocyanine from a novel anion exchange ionomer**

6.1 Background - inspiration from alkali membrane fuel cells

It has been demonstrated that the low selectivity of protons in Cation Exchange Membranes (CEM) creates a large performance barrier to MFC performance [308]. In CEM's the low molarity presence of protons (10^{-7} M) is dwarfed by the abundant presence of cations such as Na^+ , K^+ , NH_4^+ , Ca^{2+} , Mg^{2+} , representing a portion of the overall ion transport 4-5 orders of magnitude higher than H^+ transport [308]. The conductivity of sulfone based ion exchange materials decreases rapidly with increasing pH [254]. H^+ transport can be partially balanced in Anion Exchange Membranes (AEM) by the $\text{HCO}_3^-/\text{CO}_3^{2-}$ and $\text{H}_2\text{PO}_4^-/\text{HPO}_4^{2-}$ couples [250] in systems where the concentration of these anions greatly exceeds that of OH^- .

In chapter 5 it was demonstrated that the alkaline pathway is responsible for the majority of ORR in FePc cathodes. The lessons on AEM could be applied to pH balancing and ion transport in a catalyst layer containing anion exchange ionomer (AEI). The ionomer comprises of exchange group and polymer backbone.

Several qualities are sought for the AEI, resistance to irreversible adsorption or nucleophilic attack from anionic pollutants in wastewater capable of membrane permeation. Ion selectivity to the OH^- or pH balancing anions present in the process wastewater are desirable according to the influence Eq.1-10 possesses over pH dependent faradic reactions. Novel AEM and AEI synthesised in academia are applied to alkali fuel cells or water treatment, this study [309] being the first exception. Exchange group stability is rarely reported other than OH^- [310] or carbonate [311] nucleophilic substitution. The chemical stability of exchange groups in real wastewater has not been reported from an electrochemical perspective to the best of the author's knowledge.

In this study a new AEI, Quaternary-1,4-Diazabicyclo-[2.2.2]-octane Polysulfone (QDPSU) has been trialled with catalyst layers of FePc/KJB, KJB or Pt/C in neutral pH conditions. This material was originally produced for alkali media and is based on Polysulfone and Diazabicyclo-[2.2.2]-octane (Dabco) [276, 277], an oxygen scavenging molecule widely used in organic catalysis [236]. Methylated side chains have been added to Polysulfone and serve as a site for grafting Dabco producing the polymer displayed in Figure 6-1. The polysulfone backbone possesses broad spectrum chemical

resistance (organic solvents, mineral acids, OH^- and H_2O_2 produced by the cathode) and a broad window of electrochemical stability [246]. This makes it a viable candidate for an MFC binder.

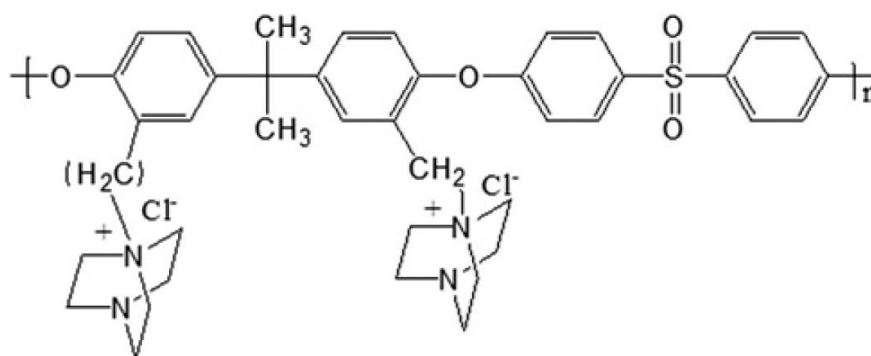


Figure 6-1. Structure of QDPSU repeating unit [276, 277].

6.2 QDPSU binder in thin carbon black films

6.2.1 An O_2 related redox peak in QDPSU electrodes

Thin films of KJB with Nafion or QDPSU binder were prepared and the i - E response assessed in Figure 6-2. Evidence was sought for the redox activity or ion interaction of the Dabco moiety.

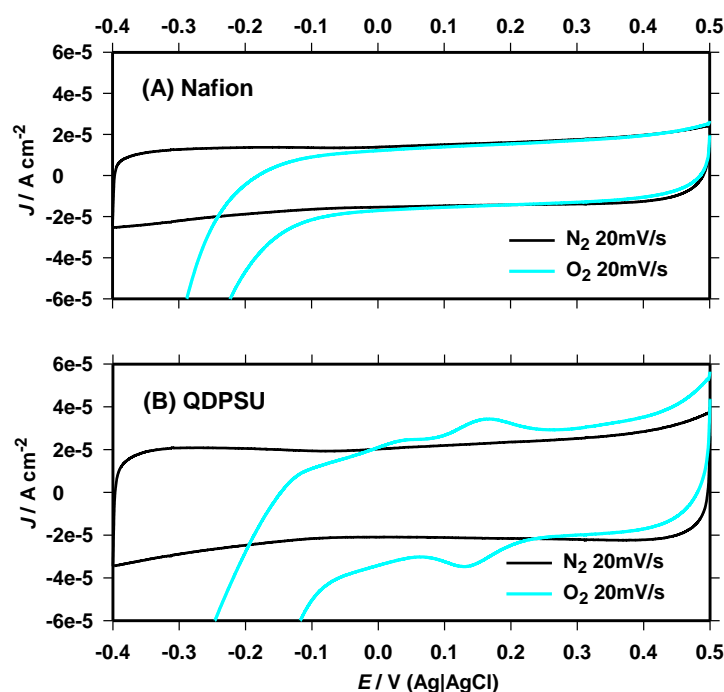


Figure 6-2. Redox active Dabco/ O_2 moiety. CV of KJB carbon with (A) Nafion or (B) QDPSU binder on GC disc in Electrolyte; 50mM PBS, pH 7.0. $\omega=0\text{rpm}$, $\nu=20\text{mV s}^{-1}$

The most notable observation in Figure 6-2 is the redox peak present in oxygenated electrolyte which occurs only when QDPSU is used. To the authors knowledge this has not been isolated in electrochemical studies based on Dabco oxygen scavenger at the date of publication [234, 240, 243, 312-318]. The Polysulfone is redox inactive [319], when coated on carbon. Several possible explanations are examined;

- 1) Redox active Dabco fixated O_2 in all Dabco ionomer in electrolytic contact.
- 2) Redox active Dabco interacting with graphitic edge planes that contain chemisorbed O_2 . A portion of all Dabco in electrolytic contact.
- 3) Redox active Dabco inert to O_2 chelation by phosphate in equilibrium adsorption to the triethyl Nitrogen.
- 4) Hoffman degradation or nucleophilic substitution (see Figure 3-6). This might plausibly be mediated by phosphate.
- 5) Trace metal chelation by Dabco resulting in a redox active moiety with dispersion of formal potentials.

The high ionisation potential of Dabco [320] may explain why no redox is seen without O_2 . The redox seen in Figure 6-2 is approximate to the second photo-excitation IP [313, 316]. Partial charge transfer to O_2 may produce a cationic hole on the nitrogen [321] and reverse this process during oxidation. In RRDE experiments, no increase in i_R accompanied the redox on the disc suggesting no released intermediary from partial ORR. The possibility of nucleophilic degradation must be eliminated for QDPSU to be a viable candidate for air cathode implementation; accordingly effort was made to determine the nature of this feature.

6.2.2 Redox peak geometry

The KJB QDPSU thin film was subjected to CV of various scan rate. The corresponding effect on peak potential (E_p) and shown in Figure 6-3.

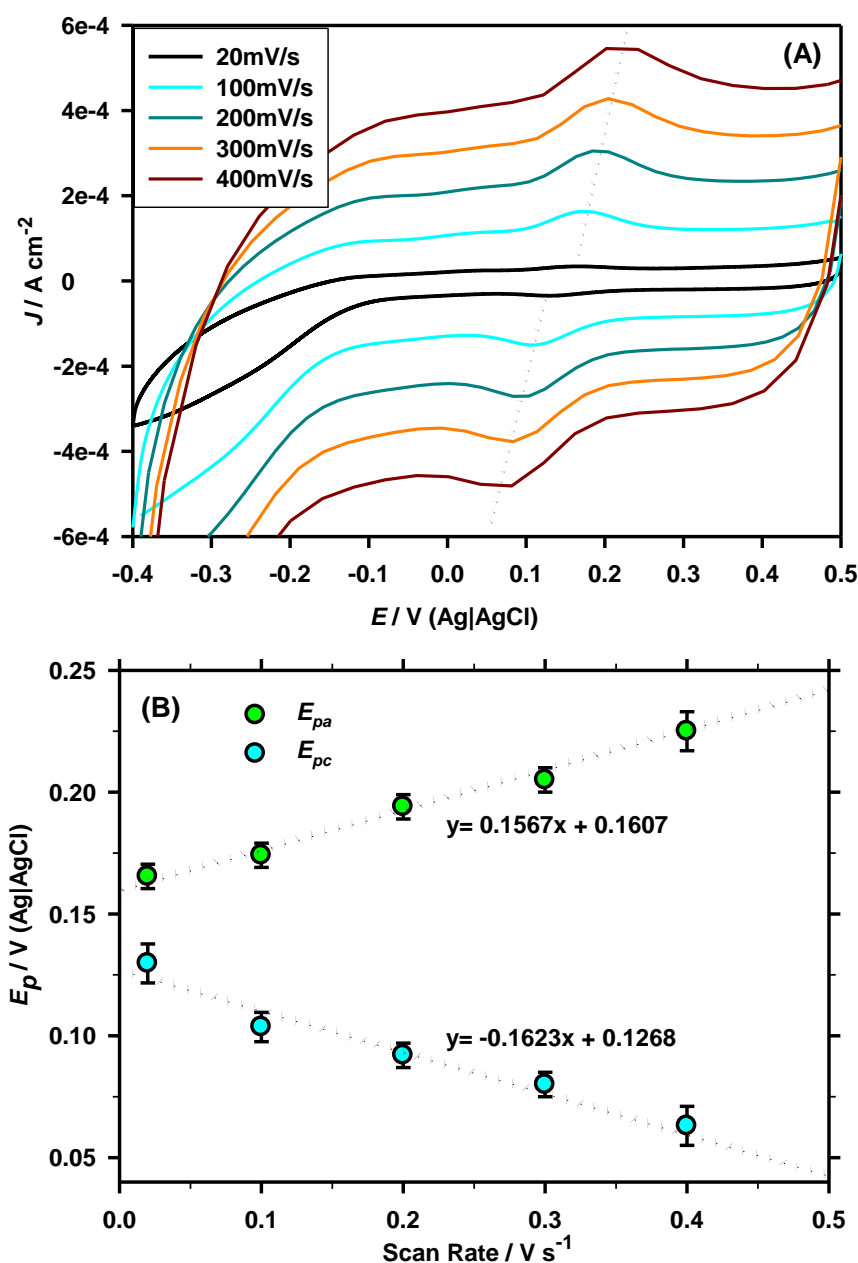


Figure 6-3. Redox active Dabco/O₂ moiety – influence of scan rate.

(A) CV data and (B) E_p vs. ν plot using least squares fit. A thin film of KJB carbon with QDPSU ionomer on a GC disc Electrolyte; 50mM PBS, pH 7.0. $\omega=0$ rpm. $\nu=20$ -400 mV s⁻¹

When $\nu \rightarrow 0$ mV/s a surface constrained redox should show symmetrical peaks [82]. $W_{1/2}$ is predicted to obtain a $W_{1/2}=89/n$ mV minimum when reversibility is high and thermodynamic lag (bond re-organisation) is negligible [82, 293, 322]. The QDPSU ionomer the scan rate affects $W_{1/2}$; 0.094V ($\nu=20$ mV/s), 0.101V ($\nu=100$ mV/s), 0.11V ($\nu=200$ mV/s), 0.118V ($\nu=300$ mV/s) and 0.129V ($\nu=400$ mV/s), a linear relationship between $W_{1/2}$ vs ν ($R^2<0.9974$) with slope $d(W_{1/2})/d\nu=0.0907$ s. Eq.2-88 anticipates $W_{1/2}=89/n$ mV at low scan rate (20°C). Peak broadening can be due to interactions between redox active sites [323] or steric hindrance of adsorption [324].

E_p vs. v produces a linear plot in Figure 6-3(B), though scan rate was not increased high enough for E_p vs $\log_{10}(v)$ region to be observed. The gradient for $E_{pa}/v=0.1567\text{s}$ and $E_{pc}/v=-0.1623\text{s}$ are nearly identical indicating $\alpha \approx 0.5$ [82].

In cases where no diffuse element or thermodynamic lag is present, as $v \rightarrow 0\text{V s}^{-1}$ the term $E_{pa}-E_{pc} \rightarrow 0\text{V}$ [293]. In cases with a diffuse element an extrapolation to $59/n$ for 25°C should be seen (100% reversible). Therefore the redox is quasi-reversible. In addition, a comparison of $E^{0'}$ from peak extrapolation (0.14V) and the $OCP = 0.16\text{V}$ demonstrates that the oxidised state is thermodynamically favourable. Figure 6-4 shows that a linear relationship between J_p and $v^{1/2}$ occurs.

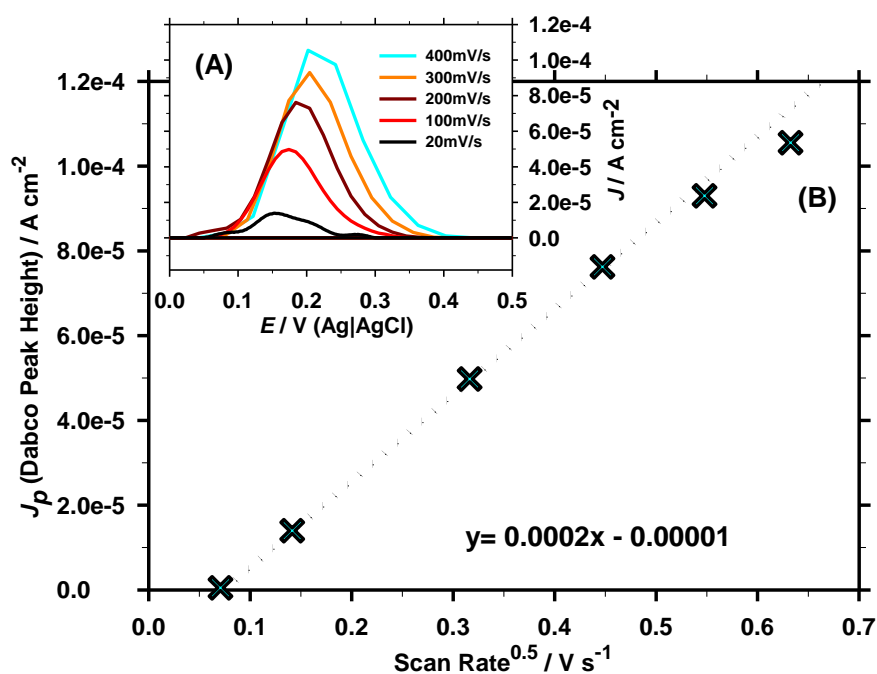


Figure 6-4. J_p vs. $v^{1/2}$ plot for redox peak of O_2 insertion in Dabco (A). Thin-film of KJB and QDPSU binder. Inset (B) shows peak profile after baseline subtraction. Electrolyte; 50mM PBS, pH 7.0. $\omega=0\text{rpm}$. $v=20\text{-}400\text{mV s}^{-1}$

This is usually indicative of a diffusion controlled process [325]. The physical dispersion of ion exchange sites along the binder backbone means the Laviron's multilayer model [293] cannot apply to Methyl-Dabco sites. The QDPSU ionomer acts more like a conducting polymer film. This can mean either 1) slow ion ($\text{H}^+/\text{Na}^+/\text{OH}^-$ or PO_4^{x-}) transfer from solution to redox active site [98], 2) slow transfer from site to graphite. A least squares linear fit produces a relationship of $J_p = 0.0002v^{1/2} - 0.00001$. The $v=5\text{mV/s}$ scan produces $J_p = 4.8 \times 10^{-7} \text{A cm}^{-2}$ confirming that the axis does not bisect

the origin but at $J_P = -1 \times 10^{-5} \text{ A cm}^{-2}$, as previously seen for the Fe(II)→Fe(III) oxidation of FeNPc with a variety of anions [194]. This can be due to;

- 1) The redox species possesses no uniform $E^{0'}$ but is distributed according to local environment on the graphite surface, causing peak splitting at low ν and peak amalgamation into one peak at high ν .
- 2) The ad/desorption of counter-ions which show increased adsorption the potential of J_P ($E_p = 0.1607 \text{ V}$, Figure 6-3).

6.2.3 Electrolyte effect on QDPSU

The presence of a diffusive element (Figure 6-4) may suggest desorption and diffusive movement of Phosphate or OH^- to maintain electro-neutrality as electrons move throughout the film [77], if this process were slow. To discount this possibility fresh KJB QDPSU films were applied and subjected to consecutive polarisation (method 3- chapter 4). The peak size was recorded with consecutive scan number in order to ascertain whether the process is irreversible and electrode constrained.

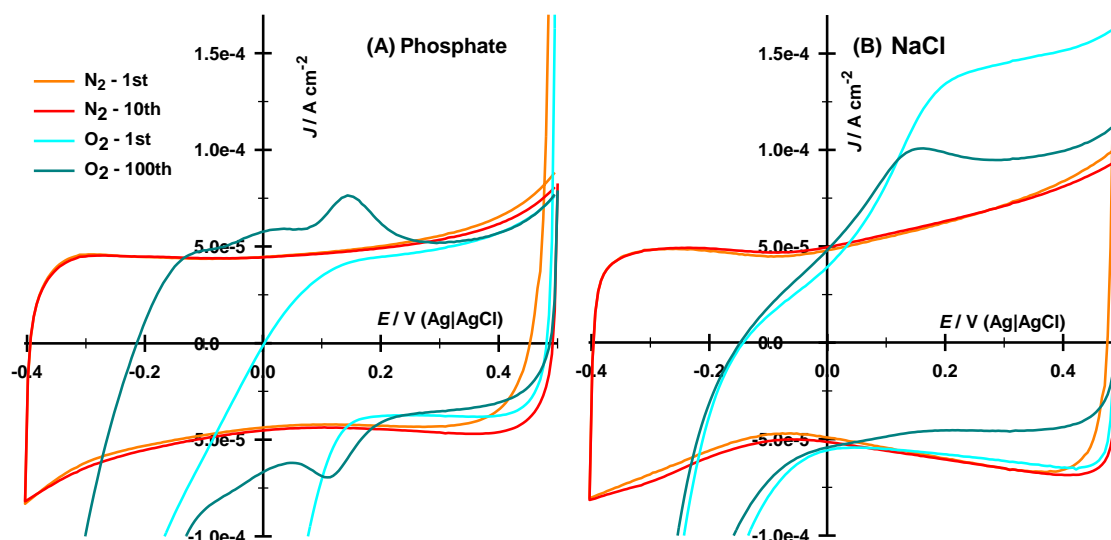


Figure 6-5. Redox activity of Dabco/ O_2 moiety – role of Cl^- and PO_4^{X-} anion. Thin film of KJB carbon with QDPSU binder. Consecutive CV in N_2 sat. followed by O_2 sat. electrolyte (scan# shown in key). Electrolyte; (A) 50mM PBS, pH 7.0 or (B) 50mM NaCl, pH 7.0 (right). $\omega = 0 \text{ rpm}$. $\nu = 50 \text{ mV s}^{-1}$

In Figure 6-5, scan #1 and #100 are shown for PBS and NaCl electrolyte. During scan# 1 the Dabco/ O_2 redox peak did not exist in PBS, the Dabco is initially ORR active but

the site de-activated within one CV. The peak was reported in a previous communication [309], increasing in size (Q_{an}), becoming visible by scan #10, reaching the maximum size by scan #40, gradually decreasing thereafter. The relative charge passed by ORR wave in scan#1 and the redox in scan#100 shows that de-activation required more than a single turnover. The behaviour indicates de-activation by ORR intermediary, though the Dabco moiety is rendered ORR active initially by interaction with Phosphate. In NaCl, Figure 6-5(B), the largest forward peak is seen at scan #5 and the reverse peak has cathodically shifted (pH dependent) to be obscured by the carbon catalysed ORR wave, indicating a possible OH^- ligand to amine. Peak characteristics were examined to determine which explanation applies;

- 100th anodic scan; $E_p=0.163\text{V}$ (NaCl), $E_p=0.144\text{V}$ (PBS)
- Peak area (Q_{an}) on scan #100; $9.5 \times 10^{-5} \text{ C cm}^{-2}$ (NaCl) and $6.3 \times 10^{-5} \text{ cm}^{-2}$ (PBS).
- In O_2 sat. PBS in the anodic scan, the peak remained Gaussian throughout as in Figure 6-3 and $W_{1/2}=\text{c.a. } 94\text{mV}$ at all scan#>10.
- In O_2 sat. NaCl, at scan #5 $E_p=0.163\text{V}$, $W_{1/2}=0.135\text{V}$ (Lorentzian) but shifted cathodically to a more Gaussian distribution by scan #100 to $E_p=0.134\text{V}$, $W_{1/2}=0.153\text{V}$.

The rapid alkalination of the film in NaCl appears not to have influenced E_{pa} while E_{pc} is cathodically shifted in unbuffered NaCl. The anodic peak is not influenced by catalyst layer pH or adsorbed solution anion. The reverse peak is a function of one of these aspects. The comparable size in the peak (Cl^- is x1.5 than PO_4^{x-} after 100 CV scans) demonstrates the counter anion is not crucial to formation. The result suggests that in PBS Phosphate binds to an amine, while in NaCl OH^- is bound to the amine.

In PBS the symmetrical nature of the peak proves charge is not transferred to a soluble phase. The peak size between Cl^- and PO_4 is identical, whereas OH^- concentration is expected to be larger in un-buffered NaCl catalyst layers. These factors make nucleophilic substitution by the solution anion or OH^- an unfeasible explanation. This shows consensus with the study of Iojoy et al [246] who demonstrate this process to not be feasible.

6.2.4 Redox mechanism of QDPSU O₂ fixation

The QDPSU content predicts a Dabco loading $\Gamma = 2.51 \times 10^{-7} \text{ mol cm}^{-2}$ (Eq.2-87). Using Eq.2-86 this would correspond to $2.4 \times 10^{-2} \text{ A cm}^{-2}$ ($v = 100 \text{ mV/s}$) if all QDPSU is redox active. Instead only 0.208% ($J_p = 4.98 \times 10^{-5} \text{ A cm}^{-2}$) of the predicted loading is active. Therefore the redox may be particular to interaction with a certain graphitic edge plane group and O₂. Peak splitting at low v would support this assertion. O₂ is clearly required, meaning an interaction between Dabco-O₂ and Phosphate/OH⁻ or a carbon group.

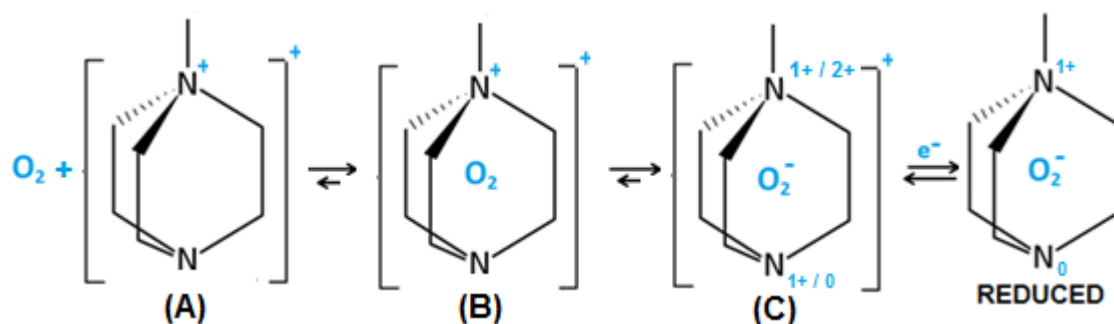


Figure 6-6. Quasi-reversible O₂ insertion into Dabco group in QDPSU. Oxidised methyl-Dabco groups at higher potentials (B) and (C) are postulated. Two charge distribution scenarios NC₄⁺-NC₃⁺ or NC₄²⁺-NC₃ are shown in (C).

Considering that O₂ is required for this redox to occur the first step of the reaction is not the electro-reduction of the oxygen-less dabco. Several factors should be considered;

- e⁻ transfer from the Dabco amine to fixated O₂ isn't detected by the potentiostat unless immediately followed by insertion of an externally sourced electron.
- The electrode is initially inserted into air saturated PBS giving ample time for O₂ fixation. Following N₂ sparging no redox peak is detected during scan #1. Therefore the O₂ fixation reaction must be reversible.

6.2.5 QDPSU interaction with ORR active carbon sites

The possibility of QDPSU interaction with carbon edge planes of known ORR activity was evaluated with LSV experiments performed at steady state in Figure 6-7.

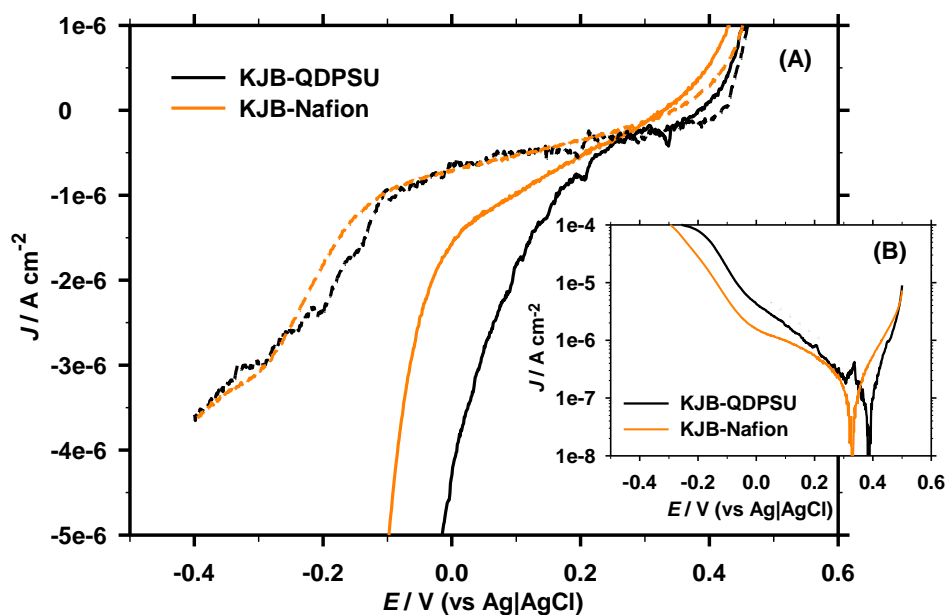


Figure 6-7. (A) i - E response showing interaction between Dabco in QDPSU with KJB. (B) Corresponding Tafel plot. Electrolyte; O₂ saturated (solid) or N₂ saturated (dash) 50mM PBS, pH 7.0. $\omega=0$ rpm. $\nu=1$ mV s⁻¹

Figure 6-7(A) shows that an oxygen reduction wave is enhanced with the use of QDPSU binder. Figure 6-7(B) shows a new faradic reaction occurring at $E=0.2$ V, for which region the $\log_{10}(J)$ vs E response is curved when Nafion is used. This indicates creation of a new site rather than increased exchange current of an existing site. K-L analysis of KJB films with binders of Nafion and QDPSU at $E=-0.4$ V is presented in Figure 6-8.

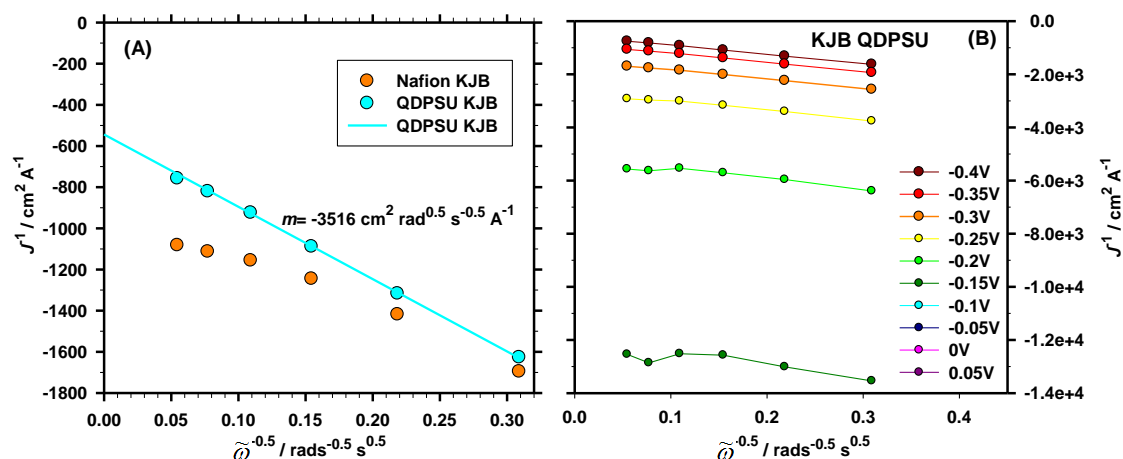


Figure 6-8. K-L plots of current obtained with thin films of KJB with binders of (A) Nafion or (A)(B) QDPSU at (A) $E=-0.4$ or (B) various E . Least squares fit applied to $100 < \omega < 800$ rpm. Electrolyte; 50mM PBS, pH 7.0. $\nu=5$ mV/s.

In Figure 6-8(A) the transition from O₂ limiting current to kinetic limitation is seen with Nafion binder, and absent with QDPSU. A linear fit applied to lower electrode rotation rates ($100 < \omega < 800 \text{ rpm}$) to the QDPSU electrode produced an $R^2=0.9998$, corresponding to $k_{app}=0.034 \text{ cm s}^{-1}$ using Eq.2-51. In this instance, the difference in the number of electrons exchanged is significant, any error due to collection efficiency loss is causes a significant effect on calculated D_{O_2} from Eq.2-51, nevertheless $D_{O_2}=6.05 \times 10^{-5} \text{ cm}^2 \text{ s}^{-1}$ is calculated when the corresponding value of n is determined from RRDE work in section 6.3.1. With QDPSU the ORR was 1st order w.r.t [O₂] at all potentials cathodic enough for mass transport limitation.

6.3 QDPSU binder in thin films of FePc/KJB and Pt/C

Using the same electrochemical methods described for Table 5-1, Table 6-1 is produced for catalysts using PTFE or QDPSU binder.

Table 6-1. Various catalyst ORR activity in thin films–QDPSU or PTFE binder. Total catalyst powder; $71 \mu\text{g cm}^{-2}$, Binder content; QDPSU; $88.4 \mu\text{g cm}^{-2}$, PTFE; $28.4 \mu\text{g cm}^{-2}$.

Catalyst	Tafel Slope (η_{O_2} corrected) Process	mV dec^{-1}	J_0 A cm^{-2}	E_{Onset} mV	RAS $10^{13} \text{ site cm}^{-2}$	J_{ORR} @ -100mV mA cm^{-2}	$E@$ 0.4 Am^{-2} mV	OCP Air→N ₂ mV	OCP O ₂ mV
QDPSU									
FePc/KJB	ORR (FePc)	-27.7	$5.1\text{E-}08$	396	205	-1.92E-04	216	0.24	0.28
FePc/KJB pyr	ORR (FeNx)	-35.2	$1.0\text{E-}07$	353	-	-1.88E-04	201	0.26	0.29
KJB	(i_{dl})+ trace ORR								
	2e ⁻ ORR Wave	-97.8	$4.5\text{E-}08$	388	-	-1.71E-05	-145	0.09	0.16
Pt/C	First Tafel	-63.6	$1.8\text{E-}06$	407	-	-1.50E-04	304	0.25	0.4
	Second Tafel	N/R	N/R						
PTFE									
FePc/KJB	ORR (FePc)	-32.9	-	385	422	-1.29E-04	217	0.3	-

The films are predicted to be identical in carbon/catalyst compared to the Nafion films when applied from a colloid. Table A-8 shows that electro-active availability may differ within less than a fifth of an order of magnitude.

6.3.1 Binder influence on kinetics in thin films

Slow scan rate ($v=1\text{mV/s}$) LSV in aerated quiescent PBS highlights the effect of binder on $E_{1/2}$ and kinetics in Figure 6-9.

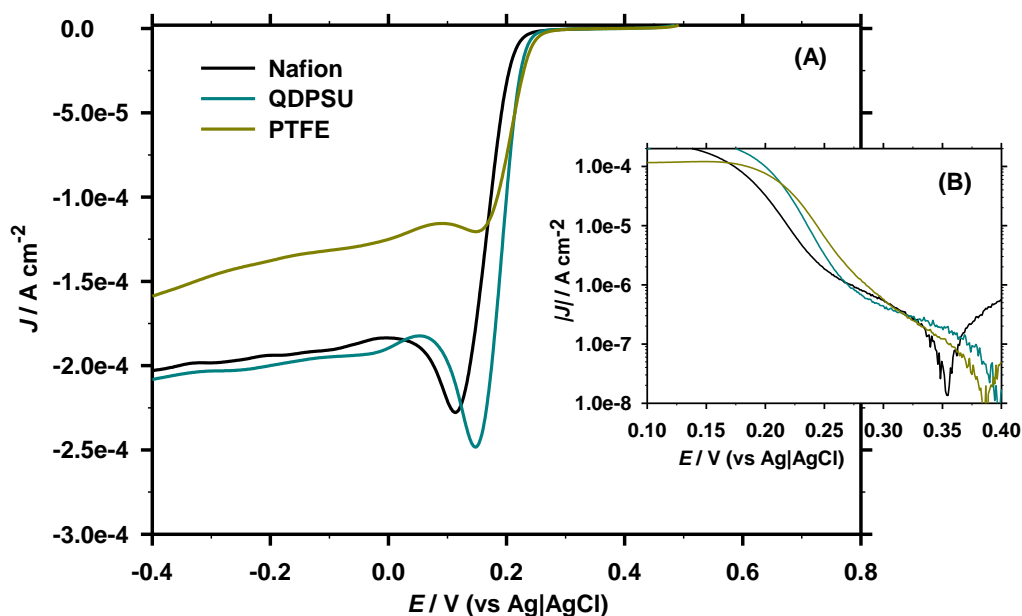


Figure 6-9. (A) LSV of FePc/KJB with QDPSU, PTFE or Nafion binders - quiescent solution. (B) Tafel plot of (A). Electrolyte; 50mM PBS, pH 7.0. $\nu = 1\text{mV/s}$

In Figure 6-9 a cathodic shift in $E_{1/2}$ is present when PTFE or QDPSU binder is used. Although agitation is not used, cathodic of the minima in current (at $0 < E < 0.5\text{V}$) the current increases after δ obtains a stable size. Phosphate desorption is observed with all binders indicating it to be an FePc, and is a reversible process on the FePc heme [176]. The data obtained under forced convection also shows this feature. The i - E response for a cathodic LSV scan at low rotation speed is shown in Figure 6-10.

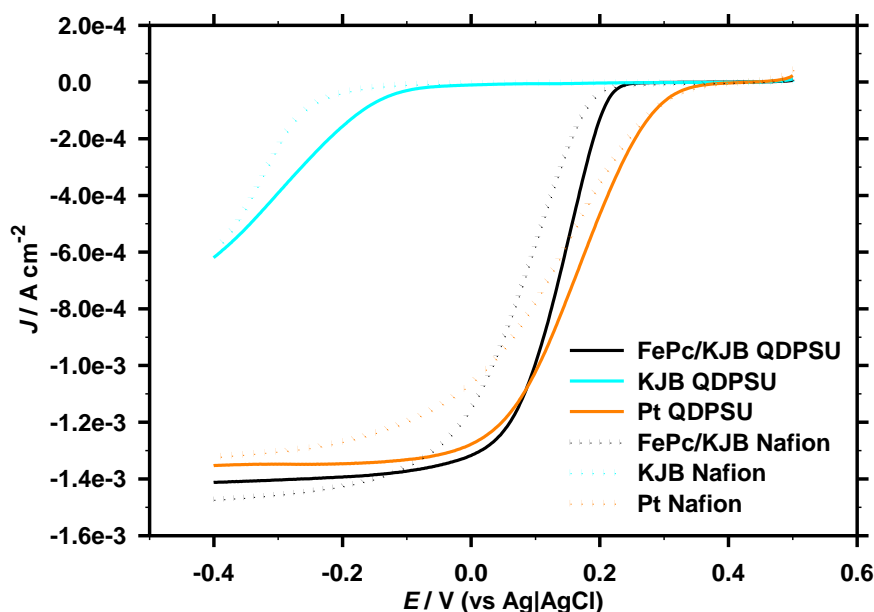


Figure 6-10. Thin RRDE films on a GC disk using a binder of H^+ -Nafion (dotted), or QDPSU (solid line) for main MFC catalyst materials; Pt/C, FePc/KJB and KJB. Electrolyte; O_2 saturated 50mM PBS, pH 7.0. $\omega=100\text{rpm}$. $\nu=5\text{mV/s}$

In Figure 6-10, the dI/dE gradient at $E < -0.2\text{V}$ is larger for FePc than Pt, though figure 5-26 predicts an increase in the portion of H_2O_2/OH^- product with $E \rightarrow -0.4\text{V}$, thus showing proportional increases in i_D , with the same reaction product.

Electrocatalysis on Pt was examined to discern the influence of binder on O_2 diffusion and counter ion charge compensation, at low η gradients of $\log_{10}(J_k)$ vs E are consistent with Nafion and QDPSU (Table 6-1 vs Table 5-1). Two tafel slopes are observed for both catalysts, a c.a. $|b_c| = \text{c.a. } 60\text{mV dec}^{-1}$ and $|b_c| = \text{c.a. } 120\text{mV dec}^{-1}$, as usual [278]. The cathodic limit of the facile tafel slope is extended from $E=0.3\text{V}$ $|J_k|=6 \times 10^{-5}\text{ A cm}^{-2}$ to $E=0.28\text{V}$ $|J_k|=2.5 \times 10^{-4}\text{ A cm}^{-2}$. No considerable difference was found in the CV of de-aerated Pt/C samples (Figure A-16) indicating the Pt/PtO couple was not affected by QDPSU surface coverage, though more reliable result are obtained with monocrystalline Pt. For Nafion ($J_L=1.32\text{mA cm}^{-2}$) is similar to QDPSU ($J_L=1.35\text{mA cm}^{-2}$) indicating a consistent reaction product and surface mechanism with QDPSU covering the Pt surface. At this cathodic potential O_2 diffusion through the film is not required. As Dabco is a known O_2 chelator, the QDPSU electrodes are assessed with K-L analysis.

In FePc as J_0 and $\tilde{\Gamma}_{FePc}$ are only marginally lower with QDPSU, ionomer dispersion is reasonable.

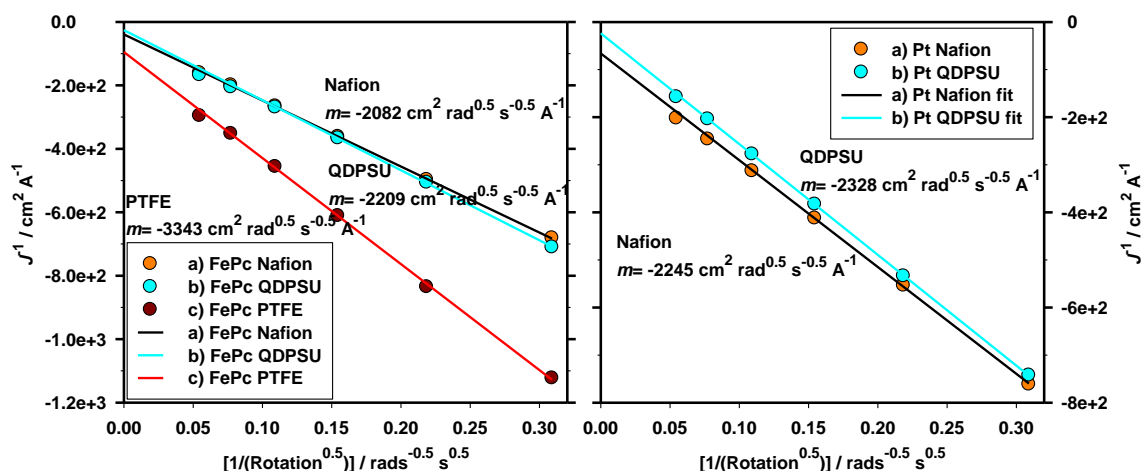


Figure 6-11. K-L plots of limiting current obtained with FePc/KJB (left) or Pt/C (right)

thin films with binders of a) Nafion b) QDPSU and c) PTFE at $E=-0.4\text{V}$.

Least squares fit of $100 < \omega < 800 \text{rpm}$. Electrolyte; 50mM pH 7.0. $\nu=5\text{mV/s}$.

The K-L plot is linear at low potential indicating the film is fully reduced. In Figure 6-11 the least squares fit for electrode rotation speeds $100 < \omega < 800 \text{rpm}$ was highly linear; R^2 was above 0.9994 for both Pt and FePc electrodes with all binder.

When applying Eq.2-51 to the K-L gradient one assumes several criteria are either identical or have a negligible effect, such as ν and $[\text{O}_2]$ in the hydrated ionomer phase. Using N , obtained from Figure 6-13 and adjusting these values for % H_2O_2 of 0.6% (QDPSU) and 0.8% (Nafion) and 1% (PTFE). Though the reaction occurs at the sol/film interface the catalyst particles are covered in an ionomer film of Nafion/QDPSU (Figure 5-4) through which O_2 must diffuse. From Eq.2-51 $D_{\text{film}}=6.76 \times 10^{-5} \text{cm}^2 \text{s}^{-1}$ (Nafion), $D_{\text{film}}=6.17 \times 10^{-5} \text{cm}^2 \text{s}^{-1}$ (QDPSU) and $D_{\text{film}}=3.32 \times 10^{-5} \text{cm}^2 \text{s}^{-1}$ (PTFE). Adjusting for $\tilde{\Gamma}_{FePc}$ from Table A-8 with Eq.2-54, produces K_{app} values; $5.17 \times 10^9 \text{cm}^3 \text{M}^{-1} \text{s}^{-1}$ (QDPSU), $3.13 \times 10^9 \text{cm}^3 \text{M}^{-1} \text{s}^{-1}$ (Nafion), $0.686 \times 10^9 \text{cm}^3 \text{M}^{-1} \text{s}^{-1}$ (PTFE). The K-L gradients that can be reliably obtained ($R^2 > 0.999$) are displayed in Figure 6-12 for a number of films.

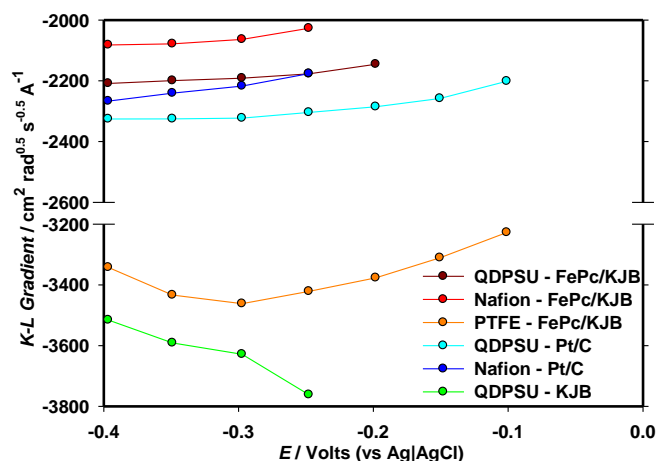


Figure 6-12. K-L plot gradient for thin films. Least squares fit of $100 < \omega < 800$ rpm data.

Electrolyte; 50mM PBS, pH 7.0. $\nu = 5$ mV/s.

In Figure 6-12, K-L gradients of QDPSU and Nafion films show relative consistency with potential at that at high overpotential. In the case of Pt, the Levich currents ($E = -0.375$ V) obtained matched $D_{film} = 5.994 \times 10^{-5} \text{ cm}^2 \text{ s}^{-1}$ with Nafion and $D_{film} = 5.68 \times 10^{-5} \text{ cm}^2 \text{ s}^{-1}$ with QDPSU. With QDPSU ionomer, the D_{film} value for KJB (Figure 6-8) was marginally lower than FePc/KJB. With both films poised at $E = -0.4$ V, the diffusion path length to the site of reaction is larger in the KJB film. The approach of mixing KJB with FePc/KJB to enhance conductivity may not enhance O_2 diffusion.

D_{film} for PTFE binder is x1.946 higher than D_{O_2} in PBS electrolyte (Table A-2). This is frequently observed, as oxygen diffuses through gaseous phases arising from hydrophobic domains, in-between graphite sheets or small pores. This Knudsen diffusion constant can be as high as $0.12939 \text{ cm}^2 \text{ s}^{-1}$ [326], approximately x43,130 faster than through pure hydrated Nafion ionomer ($0.3 \times 10^{-5} \text{ cm}^2 \text{ s}^{-1}$) [327].

The J^1 intercept values for FePc correspond to $J_k = 38.5 \text{ mA cm}^{-2}$ (QDPSU), $J_k = 10.5 \text{ mA cm}^{-2}$ (PTFE), $J_k = 25.3 \text{ mA cm}^{-2}$ (Nafion), orders of magnitude higher than air cathodes. Using Eq.2-51 at $E = -0.4$ V, $k_{app} = 0.0435 \text{ cm s}^{-1}$ (QDPSU), $k_{app} = 0.0286 \text{ cm s}^{-1}$ (Nafion), $k_{app} = 0.01187 \text{ cm s}^{-1}$ (PTFE), the value for OH^- exchanging QDPSU being similar to that obtained by Van den brink [67] in KOH.

The implication of this study being that K-L plots cannot be used to determine $\% \text{H}_2\text{O}_2$. As anticipated by models [60, 77], other factors influence J_L in neutral pH redox catalyst. The RRDE investigation is shown in Figure 6-13.

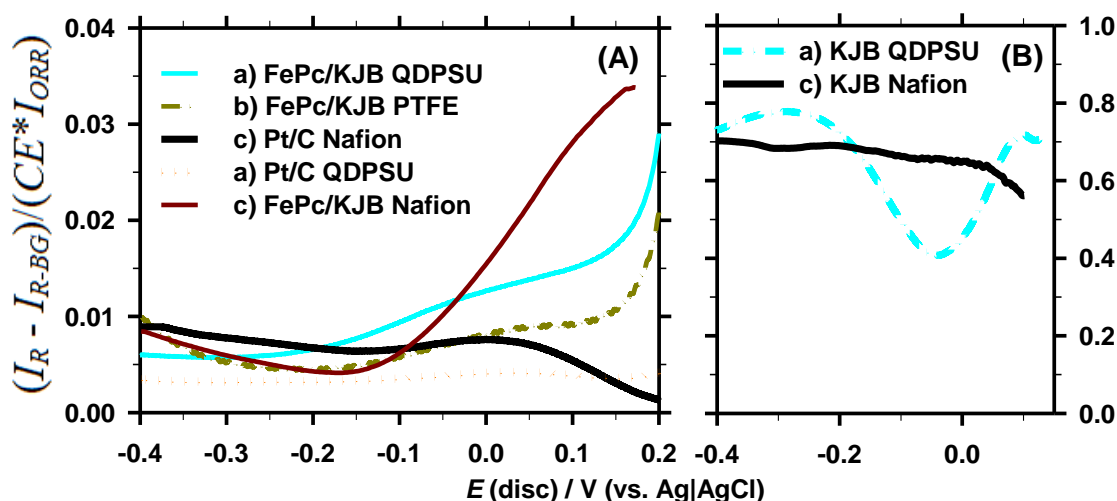


Figure 6-13. Effect of binder on %H₂O₂ released from ORR thin films of (A) Pt or FePc or (B) KJB. Relative binder: powder weight of a) QDPSU (124.5% wt.), b) PTFE (40% wt.) or c) H⁺-Nafion binder (156.5% wt.). Electrolyte; 50mM PBS, pH7.0. $\omega=200\text{rpm}$. $\nu=5\text{mV s}^{-1}$

The method aims to assess relative contributions FePc de-activation from H₂O₂, and H₂O₂ decomposition by QDPSU. With QDPSU a dip in %H₂O₂ exiting a KJB film was seen with a minima at $E=-0.05\text{V}$ and not present with Nafion. No corresponding decrease in %H₂O₂ vs. E occurred in Pt/C or FePc/KJB films, signifying QDPSU scavenging of H₂O_{2(aq)} is not present and QDPSU had a negligible impact on k_4 , ie. $k_4 \neq f(E)$. The result indicates QDPSU and graphitic edge plane interaction, yield small loadings of 4e⁻ ORR active sites.

For FePc/KJB, proportionally more H₂O₂ is released at $-0.04\text{V} < E < 0.15\text{V}$ with Nafion. Relatively nafion impedes k_3 . As also seen in Pt/C, where QDPSU caused a 50% decrease in %H₂O₂ compared to Nafion at $E < 0.05\text{V}$.

With FePc/KJB the profile of %H₂O₂ vs. E was similar for PTFE and QDPSU, significantly more H₂O₂ is detected with Nafion. A working theory can be generated; H₂O₂ is in equilibria with FePc catalysts and it's release is a function of adsorption residence time prior to reduction (k_3), which requires an initial chemical step. With QDPSU, residence time is shorter than with Nafion or PTFE, indicating k_3 may require an anion in a chemical step, following a C_iEE mechanism, by classic nomenclature, an irreversible chemical reaction followed by two electron transfer steps. If this theory is valid, rate determining k_1/k_2 should remain un-affected with binder change, whilst k_3

increases. A K-L plot of FePc/KJB QDPSU is depicted in Figure 6-14 to evaluate changes in k_{app} .

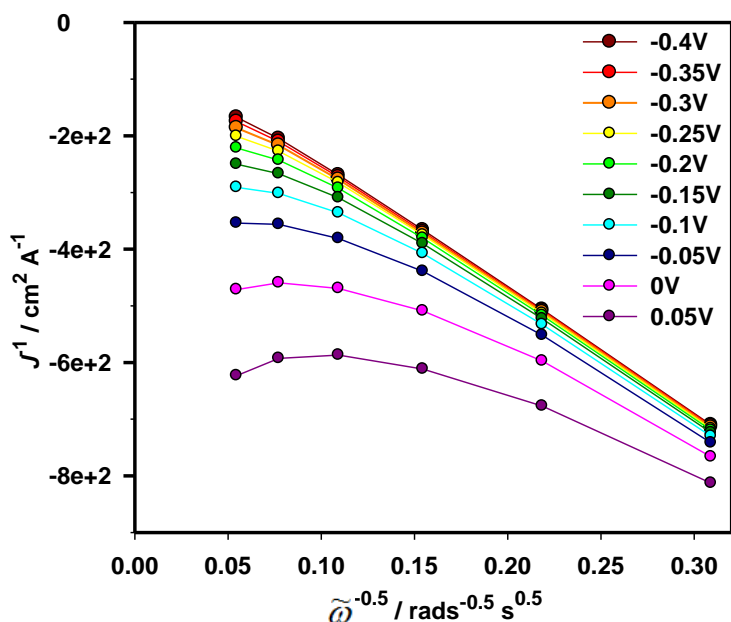


Figure 6-14. K-L plot of FePc/KJB QDPSU thin film.

Electrolyte; 50mM pH 7.0. $\nu=5\text{mV/s}$.

In Figure 6-11, the K-L plot is linear at low potential with no significant shift up the axis, indicating k_{app} is consistent at low potential. The slope is in the range 2180-2209 $\text{cm}^2 \text{rad}^{0.5} \text{s}^{-0.5} \text{A}^{-1}$ for at all potentials $-0.4 < E < -0.25$ with $R^2 > 0.9997$. From 3-26, n is consistent in this range. At high potential the results are difficult to interpret, and J_k cannot be extrapolated. At fixed potential, oxidation of the film would be more rapid if the local pH were alkali, as is the case at low ω . In order to establish whether the reaction at low overpotential occurs at constant k_1/k_2 ratio the situation lends itself to the criteria specified in section 2.4.5. The raw data and goodness of fit are located in Figure A-12 and Figure A-13 respectively. The S vs C plot is from CE^*I_D/I_R vs $k_{D,H_2O_2}^{-1}$ plot using conversion from CE^*I_D/I_R vs $\omega^{-0.5}$ data of the utilised conversion using Eq.2-72 for FePc/KJB QDPSU is presented in Figure 6-15.

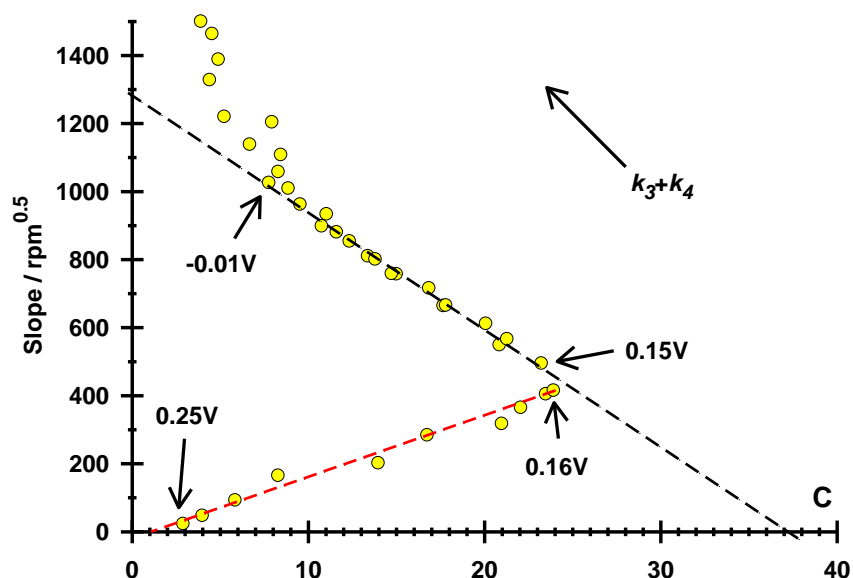


Figure 6-15. S-C Wroblowa plot from N^*i_D/i_R over $\omega^{-1/2}$ data recorded for FePc/KJB (QDPSU) of thin films. Black lines represent linear region. Electrolyte; 50mM PBS, pH 7.0. $\nu=5\text{mV/s}$.

In comparison to the unsupported film Figure 5-19 the region $E \geq 0.2\text{V}$ is more visible than in FePc/KJB. Two linear regions were observed, corresponding to two ORR mechanisms.

$0.25\text{V} > E > 0.16\text{V}$;

- A least squares fit ($R^2=0.981$) produced a gradient $17.34 \text{ rpm}^{0.5}$ with a C axis intercept of $C'=0.992$.

$0.15\text{V} > E > -0.01\text{V}$;

- A least squares fit ($R^2=0.991$) produced a gradient $-34.24 \text{ rpm}^{0.5}$ with a C axis intercept of $C'=37.38$.

The $0.25\text{V} > E > 0.16\text{V}$ region is c.a. $C=1$ and corresponds to a region where k_1/k_2 is a consistent value, showing $k_2 \gg k_1$ (see Figure 5-19). The high potential mechanism is the same as on unsupported FePc, namely a strongly adsorbed peroxo intermediary. As the intercept $C=1$, the k_{D,H_2O_2} is significantly larger than k_3+k_4 . In other words, in this potential region all the peroxide that is released from FePc ends up at the ring. In Figure 6-13 the i_R/i_D value for the film is 1.7% at $E=0.16\text{V}$. Therefore 96.6% of H_2O_2 is undergoes disproportionation. The k_2 domination region occurs over a wider potential range with QDPSU ($0.25\text{V} > E > 0.16\text{V}$) than Nafion ($0.18 > E > 0.15\text{V}$).

The $0.15\text{V} > E > -0.01\text{V}$ region is also observed for carbon supported FePc with Nafion binder ($0.12 > E > 0.04\text{V}$). In chapter 5 it was established as direct $4e^-$ reduction. The value $k_1 = 18.9k_2$ (Eq.2-71) was consistent in this large potential bracket, both pathways appear to have a similar dependence on potential, growing in unison. The corresponding S/C vs E values (not shown) produce a maxima at $E = -0.05\text{V}$ as opposed to the minima observed with unsupported films and the Nafion FePc/KJB electrode. All S/C values possess a flat baseline 10^{-3} to 10^{-5} m s^{-1} , generally faster than k_{app} , recorded as $4.35 \times 10^{-4} \text{ m s}^{-1}$ at $E = -0.4\text{V}$ from Figure 6-14 and Eq.2-51.

6.3.2 Binder influence on kinetics in air cathodes

In Figure 6-16 air cathodes with different binders were subjected to potentiostatic sweep (LSV method, section 4.1.7). This method removes charging current of the large FePc surface.

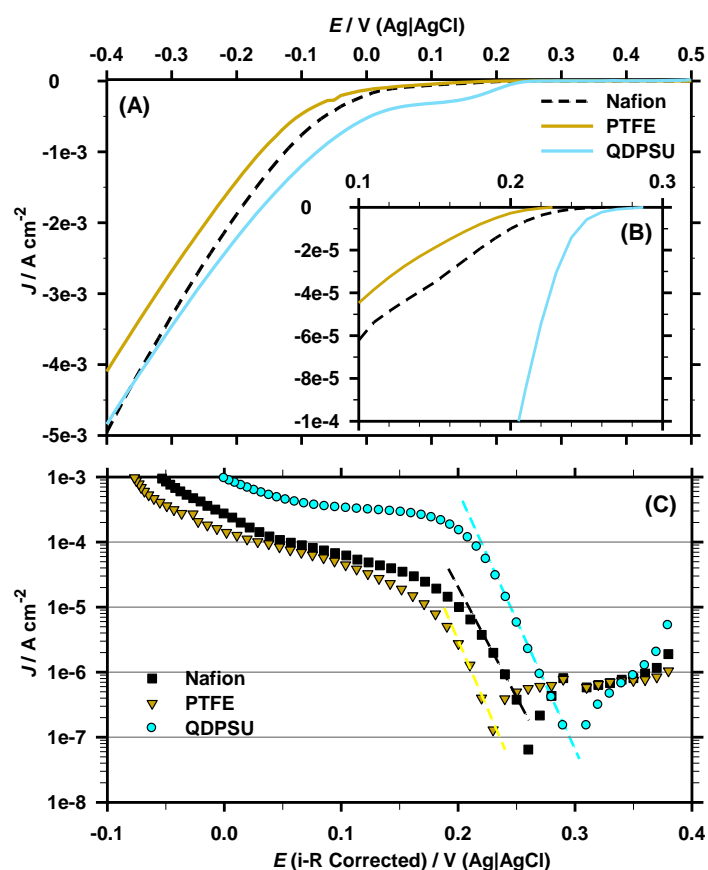


Figure 6-16. Potentiostatic scan of FePc/KJB air cathodes using Na⁺-Nafion, PTFE or QDPSU binder. Plotted as (A) LSV with (B) low overpotential region or (C) $\log_{10}(J)$ vs E . Electrolyte; air-saturated 50mM PBS, pH 7.0.

OCP was recorded (2hrs) prior to recording the data in Figure 6-16. Comparison to the data in Figure 6-16;

- After 2hrs $OCP=0.271V$ (QDPSU), $OCP=0.232V$ (PTFE) and $OCP=0.259V$ with Nafion, though Nafion had not produced a stable result indicating continual alkalination, This follows the same trend in E_{onset} in Figure 6-16(C).
- At $0.14 > E > 0.08V$ an $i-E$ plateau is seen with QDPSU. The cause for limitation warrants evaluation with EIS.
- $J_0=8 \times 10^{-7} A\ cm^{-2}$ (QDPSU), $J_0=9 \times 10^{-8} A\ cm^{-2}$ (PTFE) and $J_0=4.5 \times 10^{-8} A\ cm^{-2}$ (Na-Nafion).
- Linear tafel behaviour occurs over a large potential range for QDPSU ($0.29 > E > 0.22V$) relative to PTFE ($0.23 > E > 0.21V$) or Nafion ($0.25 > E > 0.23V$).
- For QDPSU air cathodes $|b_c|=25.4 mV\ dec^{-1}$ and Nafion air cathodes $|b_c|=29.9 mV\ dec^{-1}$.

To the authors knowledge the tafel slope recorded for FePc/KJB QDPSU is the highest recorded for ORR in any electrolyte, comparable to air cathodes of Bilirubin Oxidase ($|b_c|=26.6 mV\ dec^{-1}$) [173]. However, the intermediate complexes possess a higher $E^{0'}$ with BOX, as is the exchange current.

6.3.3 Anion influence on QDPSU and FePc in de-aerated medium

Consecutive CV was carried out on thin films of QDPSU or Nafion binder with FePc/KJB in several electrolytes. The aim was 1) establish unselectivity of QDPSU Dabco moiety towards oxidation/reduction of a variety of anions present in real wastewater, 2) establish stability of QDPSU in the presence nucleophilic anions, 3) establish a spectrochemical series for FePc.

Prior to polarisation in O_2 , localised pH is similar to bulk electrolyte pH. Thus, changes in $E^{0'}$ of reversible Fe(II)/Fe(III) peaks in N_2 are due to ligand influence on the electrocatalyst as opposed to pH. The mean amount of electro-active FePc in both layers is discussed in Table A-8 and is found to be slightly lower QDPSU ($\bar{\Gamma}=3.4 \times 10^{-9}$ mole cm^{-2}) than Nafion ($\bar{\Gamma}=3.9 \times 10^{-9}$ mole cm^{-2}), though this is within a standard deviation. This may be due uneven ionomer dispersions from QDPSU following precipitation from DMF solution upon dilution with ethanol. Q_{an} is anticipated to be similar for each

anion. Common anions of CH_3COO^- and Cl^- are supporting electrolytes for CV experiments depicted in Figure 6-17.

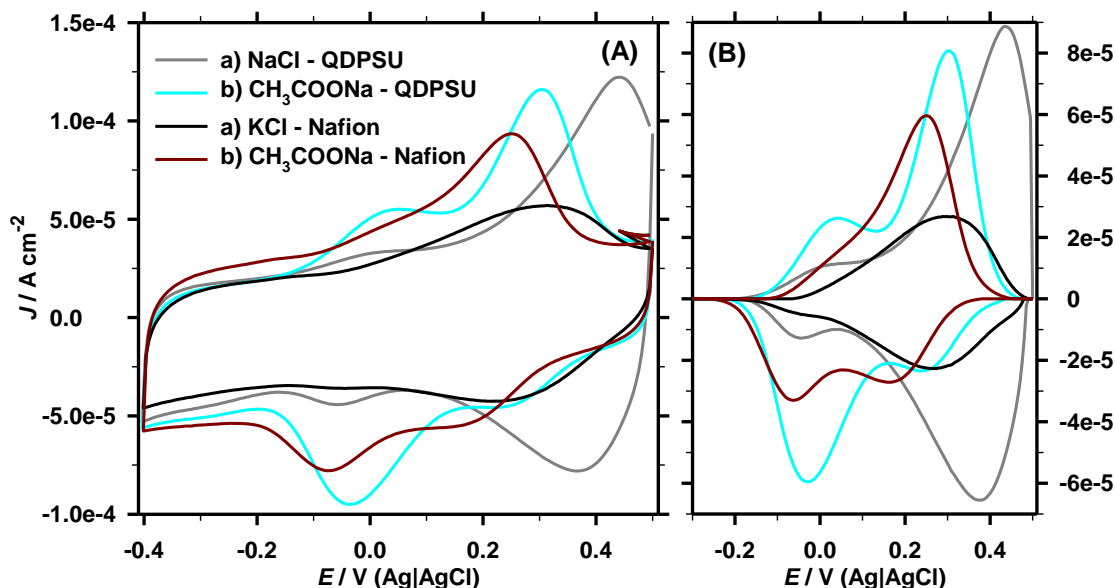


Figure 6-17. CH_3COO^- and Cl^- anion binding to FePc with QDPSU or Nafion binder. FePc/KJB film. (A) Stabilised i - E response, and (B) with charging current subtraction. Electrolyte; N_2 saturated a) 50mM NaCl/KCl, pH 7.0. or b) 50mM CH_3COONa , pH 8.9. $\omega=0\text{rpm}$, $\nu=50\text{mV/s}$

In CH_3COONa electrolyte peak splitting was observed. Dissociated CH_3COOH binds weakly in comparison to CH_3COO^- [176, 328] producing competitive forms of heme/ligand adsorption [176], meaning electrode blocking occurs over time. No detectable redox reaction or wave was associated with QDPSU, neither oxidative chemisorption nor electrooxidation of acetate. Two redox couple peaks were seen with Nafion and QDPSU binder, suggesting reorientation of adsorbed acetate with polarisation. With QDPSU binder Fe(II)/Fe(III) $E^{0'}$ potential shifted positive.

A peak in Cl^- ($E_{pc}=-0.06\text{V}$) is observably larger with QDPSU than Nafion. The redox activity is not attributed to QDPSU due to absence in KJB-QDPSU films (Figure 6-5). This peak increased with consecutive scan# and is present in other non-buffering electrolytes with a consistent reduction potential (Figure 6-18). It is established [329] that AEM fouling with anionic pollutants increases electrode capacitance (C_x). With acetate, the 11% increase in C_x with QDPSU vs Nafion is negligible (Eq.2-16, $E=-0.3\text{V}$). The interpretation being that exchange capacity is not lost from the action of the Cl^- or CH_3COO^- ion with polarisation.

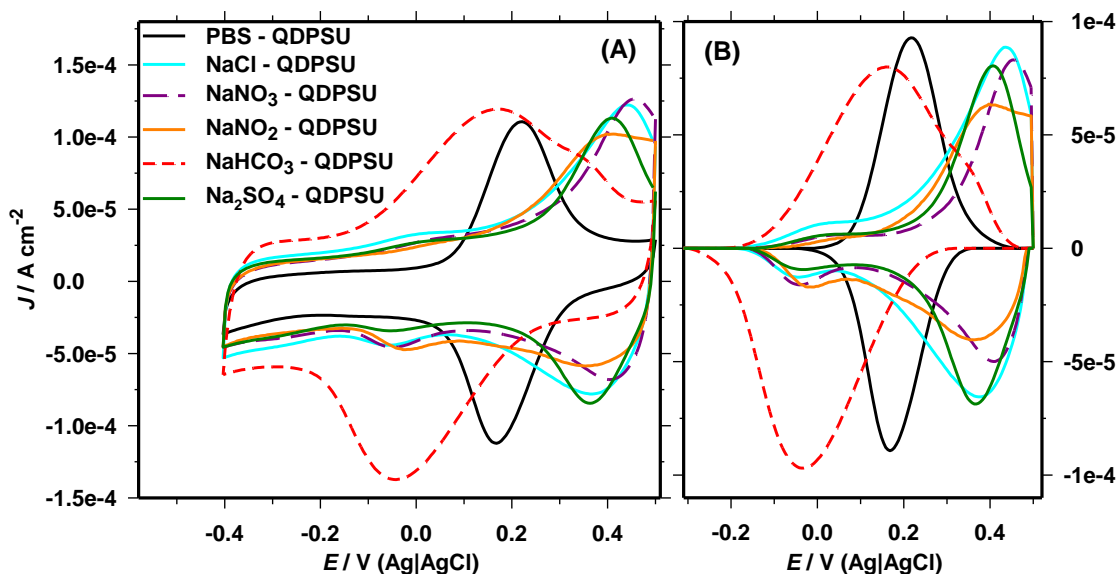


Figure 6-18. (A) Anion adsorption in the CV response of FePc/KJB (QDPSU) thin films.(B) Subtraction of charging current. N_2 saturated electrolytes; 50mM PBS pH 7.0 (black), 50mM NaCl pH 7.0 (cyan), 50mM $NaNO_3$ pH 5.5 (purple), 50mM $NaHCO_3$ pH 8.5 (red), 50mM Na_2SO_4 pH 6.5 (green). $\omega=0$ rpm, $\nu=50$ mV/s

In Figure 6-18(A), a similar stabilised response from Cl^- , NO_3^- and SO_4^{2-} was seen (Figure 6-18), despite being anions predicted to be strong ligands [181, 295, 330] of FePc and Iron in general. In $NaHCO_3$ the Q_{an} for $Fe(II) \rightarrow Fe(III)$ increased, a larger portion of the FePc surface had become electrochemically active, a phenomenon hitherto only observed in KOH [67]. The $NaHCO_3$ produced a broader single peak ($W_{1/2} = 0.256V$) than with other electrolytes, ie. PBS ($W_{1/2} = 0.150V$). Peak broadening indicates H^+ release from adsorbed HCO_3^- upon $Fe(III)Pc$ reduction. In air cathodes, limitation from electron diffusion is expected to be more severe in $NaHCO_3$ media than PBS. Partial splitting of the forward $Fe(II)/Fe(III)$ peak with FePc/KJB QDPSU air cathodes has been observed in $NaHCO_3$ [331], in tandem with x1.5-2.5 fold C_x increase ($E=-0.3V$) with $NaHCO_3$ vs any other electrolyte, this indicates strong interaction between QDPSU and HCO_3^- . No significant redox active interactions with QDPSU can be isolated from fast scan voltammetry, nor did QDPSU catalyse any anion electrooxidation/reduction in de-aerated environments. The results are summarised in Table 6-2.

Table 6-2. Influence of anion and binder on features of Fe(II)/Fe(III) redox. Electrolyte; as Figure 6-17. †Charge integration for all oxidation peaks, ‡for a single corresponding redox couple, * largest reduction peak, ° reduction peak where ORR occurs, ND – non-distinguishable. $\omega=0\text{rpm}$, $\nu=50\text{mV/s}$

Air			N ₂ – Scan #100							
OCP /			E_{pa} (Ox)	E_{pc} (Red)	Ox-Red	$E^{0'}$ ‡	$W_{1/2}$ (Red)	Fe(II)/Fe(III)		
Electrolyte	Binder	V	/ V	/ V	/ V	/ V	/ V	ΔQ vs. Scan#	Moles cm ⁻² †	
PBS	Nafion	0.27	0.236	0.168	0.068	0.202	0.144	Grow	3.74E-09	
PBS	QDPSU	0.27	0.217	0.168	0.049	0.192	0.137	Grow	3.13E-09	
KCl	Nafion	0.34	0.246	0.280	0.018	0.263	0.299 *	Shrink	1.61E-09	
			ND	c.a. -0.03	N/A	N/A		Shrink		
NaCl	QDPSU	0.22	0.441	0.368	0.073	0.405	0.242 *	Grow	4.19E-09	
			0.057	0.000	0.057	0.028		Shrink		
CH ₃ COONa	Nafion	N/A	0.253	0.168	0.086	0.210	0.385¶	Grow	2.65E-09	
			0.050	-0.064	0.114	-0.007		Shrink		
CH ₃ COONa	QDPSU	0.25	0.305	0.236	0.068	0.271		Grow	3.76E-09	
			0.090	-0.027	0.117	0.031	0.2 °	Shrink		
Na ₂ SO ₄	QDPSU	0.17	0.407	0.368	0.039	0.388	0.168 *	Grow	3.10E-09	
			0.046	-0.037	0.083	0.004		Shrink		
NaHCO ₃	QDPSU	0.18	0.168	-0.042	0.210	0.063	0.256	Grow	5.41E-09	
NaNO ₂	QDPSU	0.18	0.398	0.354	0.044	0.376	0.295 *	Grow	3.11E-09	
			0.090	-0.013	0.103	0.039		Shrink		
NaNO ₃	QDPSU	0.24	0.456	0.407	0.049	0.432	0.191 *	Grow	2.87E-09	
			0.09	-0.037	0.127	0.026		Shrink		

The range $1.6\text{--}5.4 \times 10^{-9}$ Moles cm⁻² the values of Q_{an} for $\tilde{\Gamma}_{FePc}$ in all anions are in the same range as Table A-8 where all binders are tested in Phosphate. This indicates no anion totally blocks electron transfer in FePc. The general trend in non-buffering electrolytes was a redox couple at high potential, increasing in Q_{an} with consecutive scan#, whilst a peak that produced ORR active catalyst at low potential decreased with consecutive scan#.

Redox activity of FePc in PBS appears to be unique. This is supported by the observation of Contamin et al [84], that Phosphate will replace a water ligand, making $E^{0'}$ of the Fe(II)/Fe(III) redox unique to PBS. From the split peak response of HCO₃²⁻ and CH₃COO⁻ these ligands preferentially bind to FePc ahead of H₂O.

All anions examined (bar Cl⁻) are capable of forming a mono dentate (ORR active) or bi dentate (inactive) ligands of metals. As such the spectroscopic series can only be

accurately determined by repetition of this experiment with a non-complexing, non-ionic buffer. With QDPSU FePc/KJB electrodes the redox couple linked to ORR has the peak separation series;

$$E_{pa}-E_{pc} ; \text{PO}_4^{x-} < \text{Cl}^- < \text{SO}_4^{2-} < \text{NO}_2^- < \text{CH}_3\text{COO}^- < \text{NO}_3^-$$

6.3.4 Anion influence on QDPSU and FePc in oxygenated medium

As established in chapter 5, the 2nd consecutive CV produces near stabilised response in terms of E_{ORR} and the low overpotential region is similar in the 2nd and 100th CV in O₂.

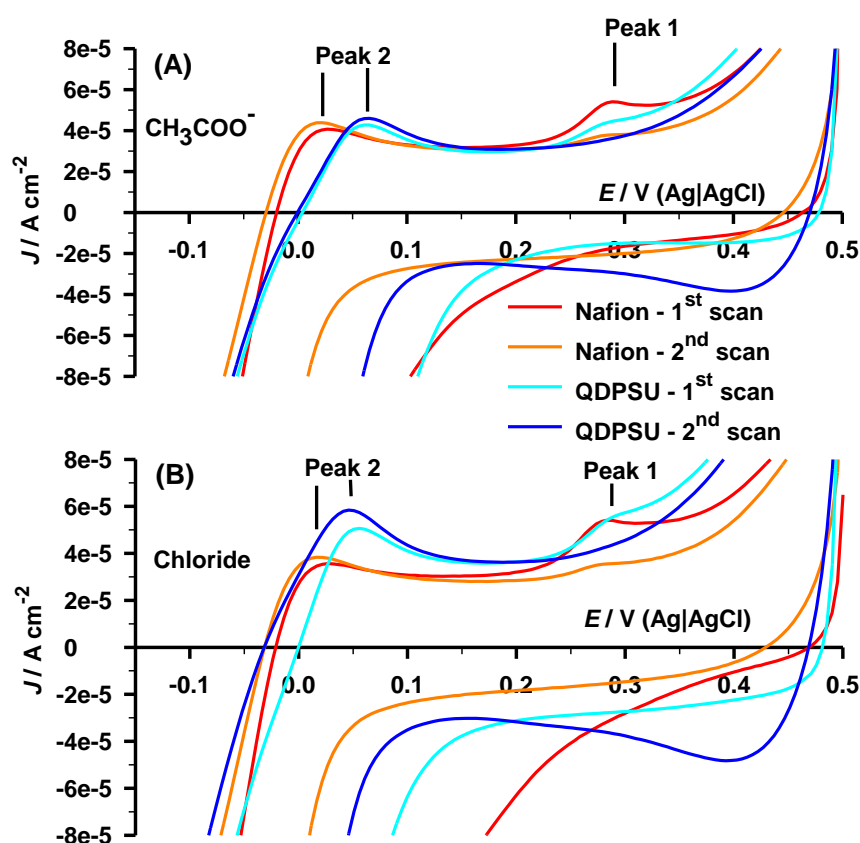


Figure 6-19. Effect of binder on pH swing from ORR in non-buffered electrolytes. FePc/KJB with a) Nafion or b) QDPSU binder on GC disk. 1st and 2nd CV. O₂ saturated electrolytes; (A) 50mM CH₃COONa pH 8.9 or (B) 50mM NaCl pH 7.0. $\omega=0$ rpm, $\nu=50$ mV/s

On scan#1 the reduction peak c.a. $E=0.4$ V was absent in all electrolytes, consecutive CV created this feature in SO_4^{2-} , NO_3^- , Cl^- and CH_3COO^- but remained largely absent in HCO_3^- and NaNO_2 . This is also present in de-aerated media, Figure 6-18(B). This result

can be interpreted as the rate of anion ligand substitution of O₂, a competitive adsorption.

Peak 1 ($E_{pa}=0.285\pm0.01V$) occurs after O₂ sparge with both binders in SO₄²⁻, NO₃⁻, Cl⁻ and CH₃COO⁻, disappearing after several scans, completely absent from scan#1 for HCO₃⁻ and NO₂⁻. Two interpretations are possible; (1) incomplete anion surface coverage of FePc (Eq.5-1), or (2) FePc with a weakly adsorbed orientation of O₂, lower than NO₂⁻ and HCO₃⁻ in the spectrochemical series. Comparison with Figure 6-18 suggest the series occurs in the order HCO₃⁻/CO₃²⁻, H₂PO₄⁻/HPO₄²⁻, NO₂⁻ > SO₄²⁻, NO₃⁻, Cl⁻, CH₃COO⁻.

Peak 2 varies E_{pa} with binder but not solution anion, CH₃COONa; QDPSU ($E_{pa}=0.06\pm0.005V$), Nafion ($E_{pa}=0.022\pm0.005V$). NaCl; QDPSU ($E_{pa}=0.051\pm0.005V$), Nafion ($E_p = 0.022\pm0.015V$). For peak 2 the E_{pa} difference between Nafion and QDPSU shows agreement with the relative improvement of OH⁻ diffusion with QDPSU [309], of significant importance in unbuffered electrolytes.

The slope and potential range of a linear log₁₀(J_k) vs E response is a function of solution anion, the results are summarised in Table 6-3.

Table 6-3. ORR influence by anion for FePc/KJB QDPSU thin films. Non-steady state response over high and low potential ORR limit, lowest linear $|b_c|$ value. $\nu=50mV/s$, $\omega=0rpm$.

Electrolyte	Binder	$ J_k $ vs. E linear region - Non-steady state		
		E (high) / V	E (low) / V	$ b_c $ / V dec ⁻¹
PBS	Nafion	0.144	0.105	119
PBS	QDPSU	0.173	0.129	51
KCl	Nafion	0.012	-0.018	81
NaCl	QDPSU	0.017	-0.018	66
CH ₃ COONa	Nafion	0.017	-0.008	80
CH ₃ COONa	QDPSU	0.022	-0.042	71
Na ₂ SO ₄	QDPSU	0.041	-0.042	59
NaHCO ₃	QDPSU	0.041	-0.042	100
NaNO ₂	QDPSU	0.002	-0.047	62
NaNO ₃	QDPSU	0.007	-0.032	56

Variance in $|b_c|$ proves anion adsorption influences ORR in some cases. This may take the form of adjacent sites or mono dentate ligands, allowing mono dentate O₂

adsorption. At $v=50\text{mV/s}$ the amount of viable Fe(II)Pc is limited in a partially reduced film, $|b_c|=f(k_E)$, thus mechanism conclusions and comparison with $v=1\text{mV/s}$ data cannot be made. The lag in FePc activity with Nafion ($|b_c|=119\text{mV dec}^{-1}$) compared to QDPSU ($|b_c|=51\text{mV dec}^{-1}$) establishes limitation from k_E . The series for $|b_c|$ is $\text{PO}_4^{x-} \ll \text{NO}_3^- < \text{SO}_4^{2-} < \text{NO}_2^- < \text{Cl}^- < \text{CH}_3\text{COO}^- \ll \text{HCO}_3^-$. The linearity of the tafel gradient suggests that electrostatic repulsion of CH_3COO^- explanation [176] is not applicable.

QDPSU cannot produce H_2O_2 (Figure 6-13). Evidence of H_2O_2 scavenging by QDPSU was sought with thin film RRDE technique in several electrolytes. The data in Figure 6-20 was obtained following electrochemical aging in the $-0.4 < E < 0.5\text{V}$ range. The initial current IR current at $E=0.5\text{V}$ follows a transient decay until H_2O_2 oxidation is detected at $E=0.2\text{V}$.

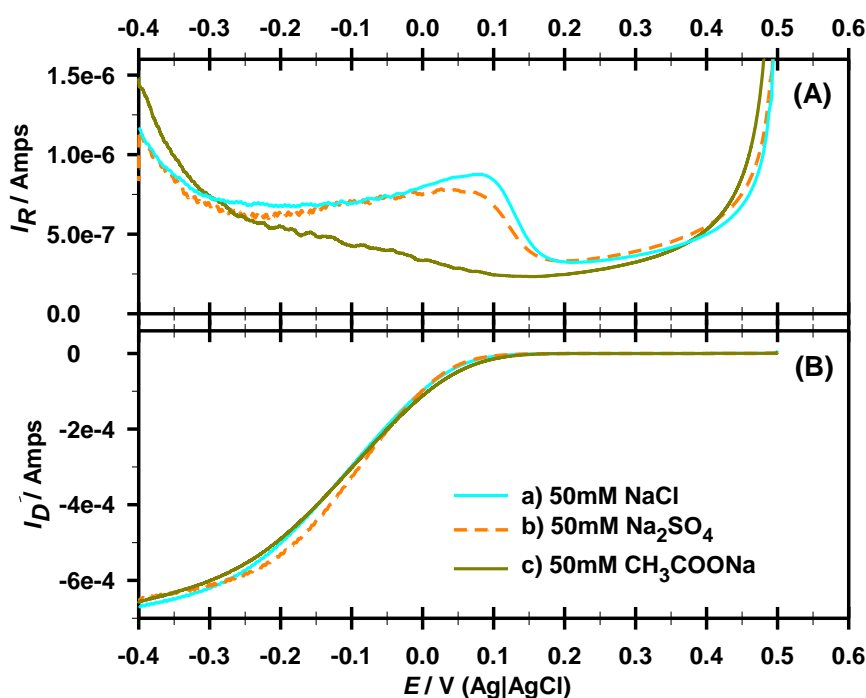


Figure 6-20. Solution anion effect on (A) i_D vs. E and (B) i_R vs. E plots during ORR catalysed by FePc/KJB QDPSU thin films. Electrolyte; O_2 saturated with initial pH of (a) 50mM NaCl pH 7.0, (b) 50mM Na_2SO_4 pH 6.5, (c) 50mM Sodium Acetate pH 8.9.

$\omega=800\text{rpm}$, $v=1\text{mV/s}$

In Figure 6-20(B) the results of i_D vs E at high over-potential are comparable, making quantitative analysis of i_R vs E simple. At low overpotential ($-0.15 < E < 0.15\text{V}$), FePc produces H_2O_2 in Cl^- and SO_4^{2-} , as in PBS, but H_2O_2 is less significant at E_{ORR} in CH_3COO^- . Literature on H_2O_2 release in alkali at low overpotential [176, 208] suggests

a different working pH in CH_3COO^- is not the explanation. Release of H_2O_2 from FePc shows a similar dependence on potential between CH_3COO^- and PBS with the results of Kozawa et al [176].

Viewed in conjunction with Figure 6-19 it appears either k_3 or k_4 may be enhanced by acetate adsorption. No Wroblowa analysis is performed on this data, so k_1/k_2 is not known, thus meaning k_1 domination (at low E) and inhibition of k_2 with acetate cannot be determined. Potential H_2O_2 scavenging to form peroxyacetic acid can be excluded due to a) low conversion rate [332] and b) a similar proportion being released at low potential as in NaCl.

Electrode blocking from CH_3COO^- coverage accounts for J_L reduction in quiescent acetate solutions [176]. MFC tests on Iron macrocycles with acetate based artificial wastewater are anticipated to produce lower power outputs than predicted by phosphate electrolyte due to acetate adsorption identified here. This work has ramifications for proposed design of dissolved oxygen probes [333] and sensors that detect neurologically and pharmaceutically important molecules in PBS medium [334, 335] and use of cyclic voltammetry for assessment of selectivity and stability.

6.4 Stability

6.4.1 FePc/KJB QDPSU stability in PBS

The large Γ_{FePc} in air cathodes increases the timescale of deactivation. The effect of QDPSU on FePc de-activation is assessed by thin films, in identical method to Figure 5-22.

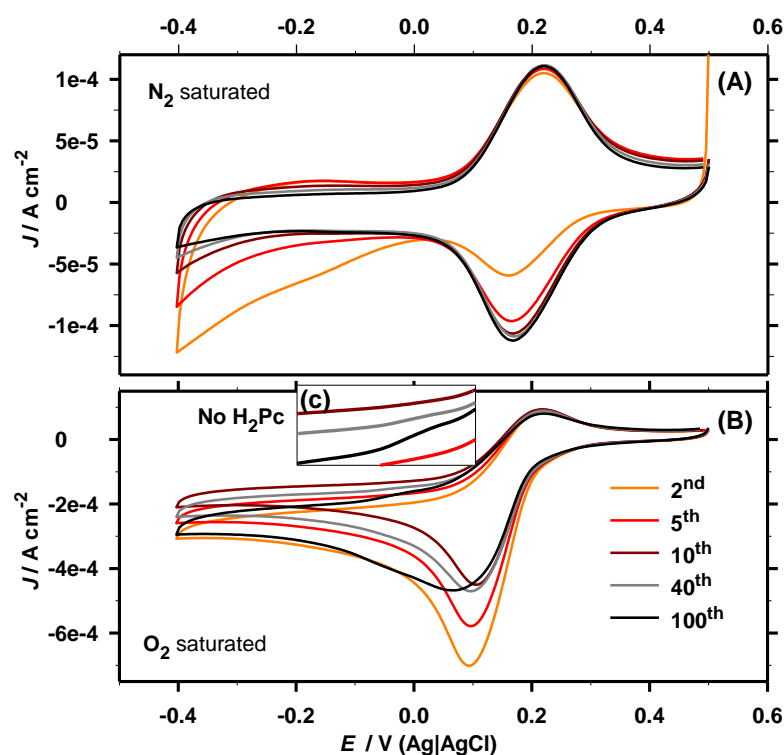


Figure 6-21. FePc stability in FePc/QDPSU thin film from (A) polarisation in N_2 or (B) ROS production. Consecutive CV (100scans). (c) Inset is magnification of $-0.2 < E < 0.05V$ region in O_2 . Electrolyte; 50mM PBS, pH 7.0. $\omega=0rpm$, $\nu=50mV/s$

In de-aerated media no FePc deactivation occurs as is the case with Nafion. The $\tilde{\Gamma}_{FePc}$ increased with consecutive CV, consistent with electrochemical surface cleaning. With O_2 the H_2Pc formation in Figure 6-21(C) was negligible, unlike with H^+ -Nafion binder. E_{pc} is consistent up to scan#40 as with Nafion, as would be seen for a decrease in viable $\tilde{\Gamma}_{FePc}$ on the surface. This is confirmed in Figure 6-22, where the tafel slope is plotted for scan#2 and scan#100, as predicted by Eq.2-53.

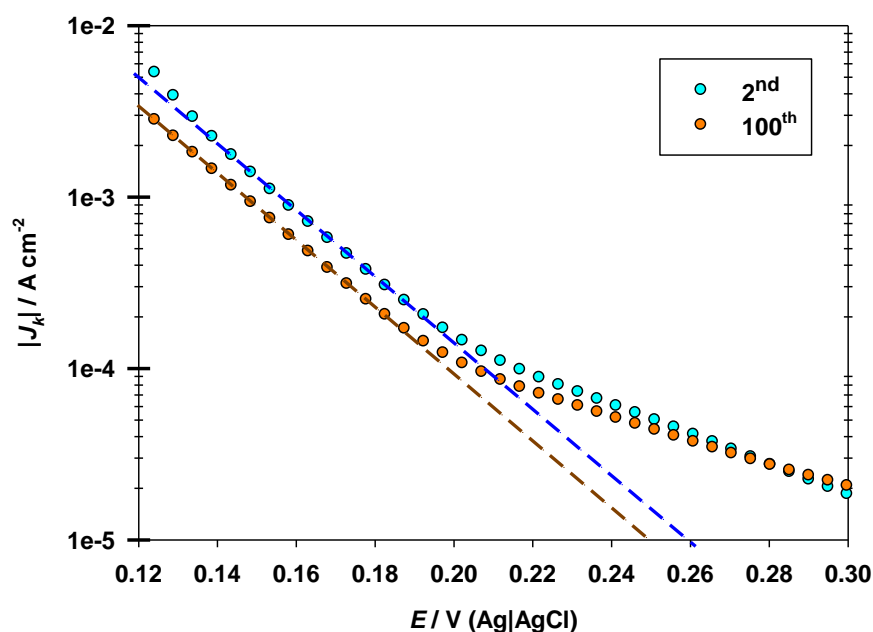


Figure 6-22. Tafel plot of 2nd and 100th CV scan from data in Figure 6-21. O₂ overpotential corrected, Non-steady state.

In Figure 6-22 the lines of the tafel plot are linear and parallel (decreased geometric J_0 , consistent $|b_c|$). The line shifted down the axis with consecutive polarisation. This is indicative of increasing partial coverage of a blocking ligand or permanent de-activation to the active site [84], rather than a shift in reaction mechanism. From scan#2 to scan#100 $|J_k|$ decreased 49.2% with Nafion and 32.5% with QDPSU at $E=0.16\text{V}$. The work by Chen et al [70] suggests FePc passivation with $\bullet\text{OH}$ from H_2O_2 . The fact that blocking appeared more extreme with Nafion than QDPSU pointed to a mobile species.

6.4.2 FePc/KJB QDPSU stability in other electrolytes

To establish whether deactivation occurred by anion site blocking, ROS or demetallation, current density at a potential c.a. $i_p/2$ was selected ($J=0.3\text{mA cm}^{-2}$) and plotted vs consecutive scan# in Figure 6-23.

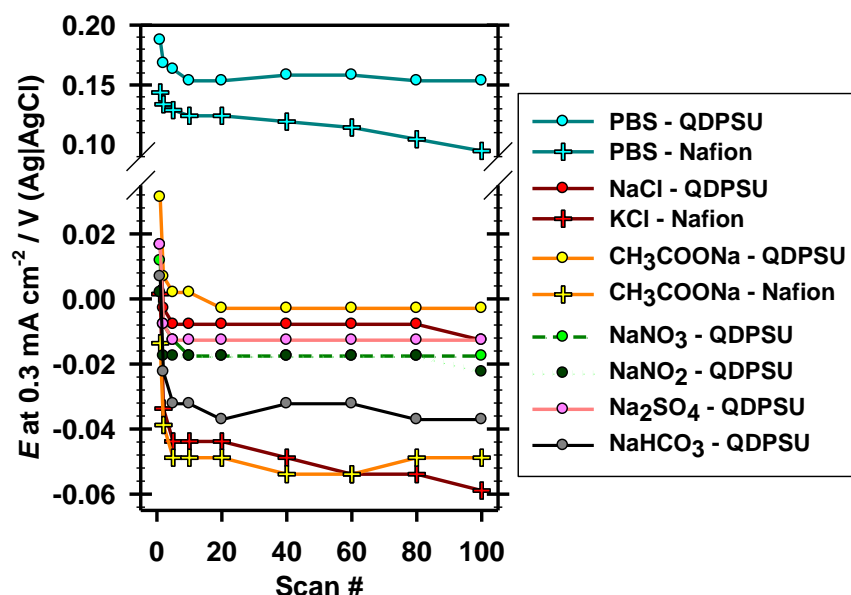


Figure 6-23. Anion and Binder influence on FePc deactivation in O_2 saturated electrolytes described in Figure 6-18. Potential recorded at $J = -300 \text{ mA cm}^{-2}$ during consecutive CV (100 scans). $\omega = 0 \text{ rpm}$, $\nu = 50 \text{ mV/s}$

QDPSU produced higher catalytic activity in PBS, NaCl and CH_3COONa than Nafion. After stable responses were obtained from catalyst layer consumption of O_2 , the QDPSU electrode produced a plateau in activity c.a. $E = 0.16\text{--}0.15 \text{ V}$ from scan#10 to scan#100 in PBS, with no deterioration in this potential in NaCl, CH_3COONa , NaNO_3 , NaNO_2 , Na_2SO_4 or NaHCO_3 . With Nafion binder sustained deterioration is seen, from scan#10 to scan #100 the decrease is 15.2mV (NaCl) and 29.3mV (PBS) with no sustained deterioration in CH_3COONa .

In conclusion, the de-activation of FePc showed no correlation with aqueous phase H_2O_2 (Figure 6-13). Reconciling the results in Figure 6-22 with Figure 6-23 was possible by demonstrating de-activation with QDPSU appeared finite. A situation which occurs if de-activation is from an equilibrium adsorbed ROS species, FePc-OH or FePc-(OH)₂, as postulate by Chen [70]. With Nafion de-metallation was not separated from this reaction but de-activation was irreversible.

6.5 Conclusions

QDPSU was shown to have a similar O_2 permittivity to Nafion. In PBS, the QDPSU enhanced the catalytic activity of unmodified carbon, originally a $4e^-$ ORR active site is produced which becomes redox active and non-catalytic on initial polarisation. The

chelation ability of Dabco may be instrumental in lowering O_2 binding energy by weakening the dioxygen pi-bond, indicating the use of F-tiR investigation to establish splitting of the O_2 bond strength is warranted for electrodes at various potentials.

The FePc catalyst layers demonstrated greater stability when using QDPSU in place of Nafion, though this improvement was not linked to decreased H_2O_2 release. The change in tafel plot with consecutive scan showed the number of viable sites remained higher with QDPSU, as if the process described by Chen et al [70] were partially mitigated with a covering of the anion exchange material. De-metallation of the FePc was also reduced with implementation of QDPSU relative to Nafion.

Chapter

7

Chapter 7. Results - Performance and stability of cation and anion exchange binder in wastewater half cells and Microbial Fuel Cells

7.1 Introduction

7.1.1 *EIS analysis of cathodes*

Impedance spectroscopy was used to quantify sources of impedance by resolving them in the time domain. Once established, the influence of catalyst binder in the air cathode was used to separate the changes in the types of impedance in PBS, NaCl and Phosphate Buffered Wastewater. Some of these techniques and equations are used in chapter 8 for membranes. Relating these observations to performances in MFC's, conclusions on the role of binder in cell operation were made.

7.2 Results and Discussion

7.2.1 *Impedance response of thin film electrodes in N_2 and O_2*

EIS has not been applied to unpyrolysed FePc/C material in phosphate buffer [84, 184], background impedance spectra were obtained for thin films to build up the theory. The thin film technique accurately establishes features relating to O_2 electrocatalysis by providing a totally anoxic FePc film, requiring a glove box to obtain with air cathodes. Focus was temporarily reverted to Nafion, in order to discount the QDPSU/ O_2 redox activity observed in chapter 6. This permitted charge and ion percolation through the FePc/KJB film to be resolved in the time domain, in the absence of faradic reaction. The thin film technique (chapter 4) was applied to FePc/KJB Nafion film.

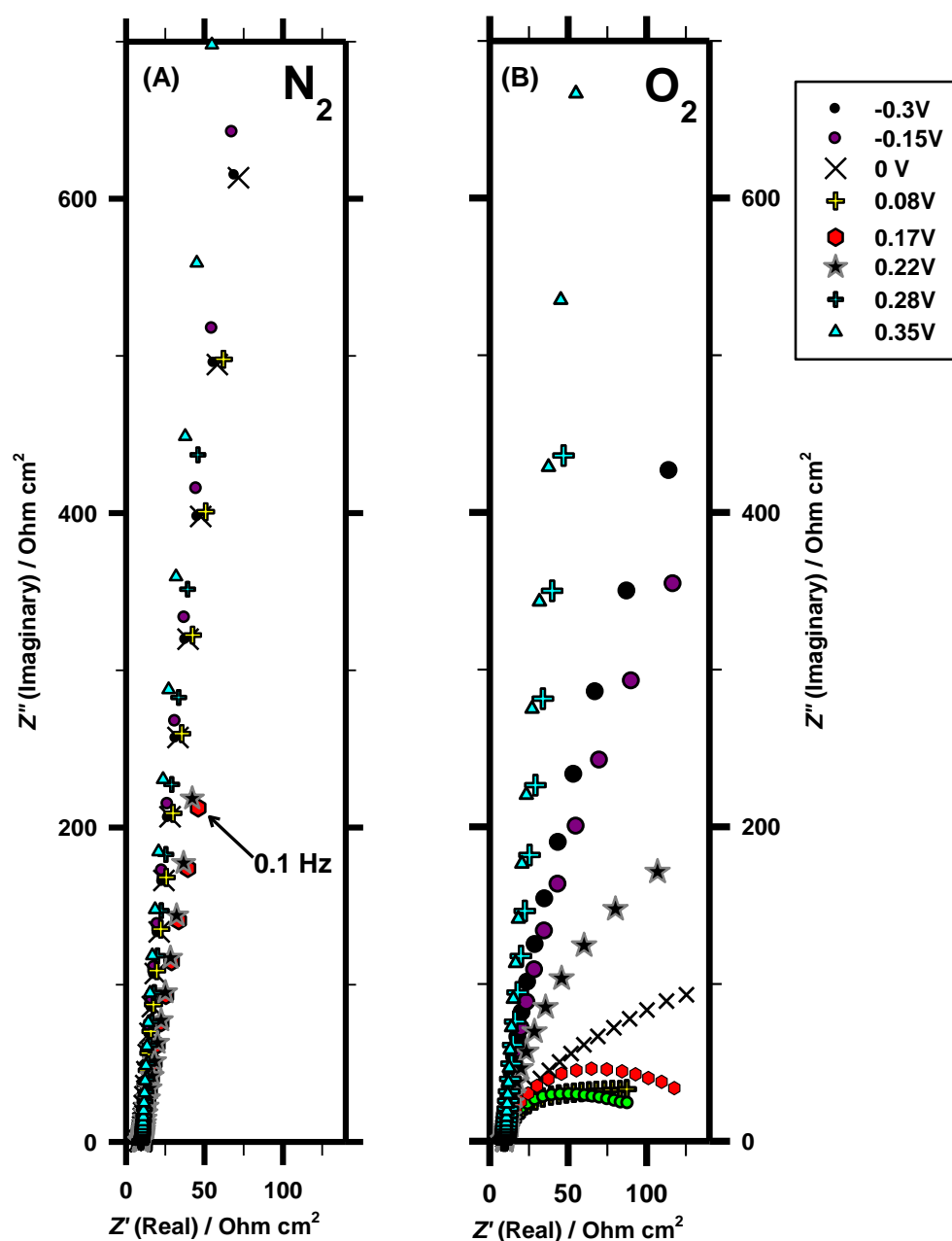


Figure 7-1. LF Impedance spectra of thin FePc/KJB Nafion film in (A) de-aerated (B) or aerated PBS media. Applied frequency, $f=10,000\text{Hz}\rightarrow 0.1\text{Hz}$.

The LF portion of the impedance spectra for FePc/KJB films is shown in Figure 7-1 in O₂ and N₂ saturated PBS. The main aspects of the complex plane plot are;

- A single arc is observed relating to ORR charge transfer (R_{ct}). It starts to become prevalent at $E \leq 0.22\text{V}$, starting at $f=316\text{Hz}$.
- At $E=0.28\text{V}$ the complex plane plot is identical in O₂ and N₂ at all frequencies, bar a +ve shift in Z' of 1Ω in N₂.
- Deviation from the R_{ct} semi-circle at $E=0.17\text{V}$ is seen clearly at $f < 0.4\text{Hz}$. The gradient of the deviation from an RC time constant is dependent on potential. At

0.28 $\geq E \geq 0V$ the arc is skewed with $-dZ''/dZ' < 1.0$. At $E < 0V$ the gradient increases higher than warburg behaviour ($m > 1$) indicating an approach to reflective finite transmissive behaviour [336] with a CPE as opposed to a purely capacitive boundary.

- At 0.08 $> E > 0V$, R_{ct} starts to increase (Table 7-1).
- Resistance of adsorption (R_{ads}) [184] could not be isolated in thin films within the 10kHz $> f > 0.1Hz$ range.
- Eq.2-110 or 4-26 could not be applied in the case of thin films with this frequency range, as no overlap between time constants of Warburg diffusion and R_{ct} is seen.

Table 7-1. Influence of applied potential on C_Σ and R_{ct} for FePc/KJB Nafion thin film in O_2 and N_2 . Determined from least squares fit and manual arc fit respectively.

E / V	0.35	0.28	0.22	0.17	0.12	0.07	0	-0.15	-0.3
In O_2									
$R_{ct} / \Omega cm^2$			1782	374	230	213	400		
$C_\Sigma / F cm^{-2}$	6.89E-04	1.09E-03	2.42E-03				7.84E-03	7.16E-04	1.09E-03
In N_2									
$C_\Sigma / F cm^{-2}$	6.58E-04	1.06E-03	2.15E-03	2.20E-03	N/A	9.27E-04	7.51E-04	7.16E-04	7.48E-04

Eq.2-120 was applied to the thin film at the LF limit to generate the capacitance reported in Table 7-1. The plateau of $C_\Sigma = 1.2mF cm^{-2}$ seen at $E > 0.2V$ in CV (0rpm) is different to that observed in Table 7-1 with capacitance increasing with decreasing potential. With EIS in O_2 , the total capacitance was not accurately determined due to convolution from ORR. This is due in part to the fast scan rate ($v = 20mV/s$). As there is little difference in C_Σ between O_2 and N_2 saturated electrolyte it can be deduced that adsorbed O_2 at high potential, $Fe(III)Pc-O_2^-$, does not drastically alter surface state capacitance (C_{ads}).

Table 7-1 shows the R_{ct} value in O_2 , the value in N_2 being immeasurably high. R_{ct} becomes significantly higher near to OCP and drops to a measured minimum of 213 Ωcm^2 at $E = 0.07V$. The R_{ct} increases again between $E > 0.08V$, showing consistency with the transition range between two mechanisms described in Figure 5-5.

An equivalent circuit fit had to be used to generate an R_{ct} value at OCP ($E=0.28V$) for the FePc/KJB Nafion film as manual fitting of a large arc is arbitrary with a large degree of error. In thin films Warburg limitation of oxygen diffusion was present at $E \leq 0.22V$, above this potential and in N_2 another diffusion component had to be placed in the circuit (O_2 diffusion could be removed). This Warburg diffusion was placed in series with a constant phase element (see Figure 7-10). The resulting value of $R_{ct}=8.94 \text{ k}\Omega \text{ cm}^2$ equated to $J_0=8.3 \times 10^{-7} \text{ A cm}^{-2}$, a value x4.2 higher than that observed in Table 7-1 from extrapolating the tafel slope of the alkali mechanism.

7.2.2 High frequency ion diffusion through thin films

Figure 7-2 depicts the response of 2-3 μm thick FePc/KJB films with aged in bottle (1.5 year) QDPSU binder in de-aerated media. Two distinct features occur, an ultra-high frequency arc (discussed section 7.2.6) and a high frequency electrode resistance was shown to be diffusive by linear regions in the (Z') vs. $\tilde{\omega}^{-0.5}$ plot at high frequency only, in Figure 7-2 [96, 337, 338]. An example with Nafion binder is shown in with FePc/KJB thin films (Figure 7-4), present in aerated and de-aerated media. The markers f_1 and f_2 represent the high and low frequency limits of the linear Z' vs. $\tilde{\omega}^{-0.5}$ plot. In all cases the marker f_2 increased when plotting the real component only; Z' vs $\tilde{\omega}^{-0.5}$ as opposed to Z vs $\tilde{\omega}^{-0.5}$ [87]. The gradient of the Z' vs $\tilde{\omega}^{-0.5}$ plot decreased slightly compared to Z vs $\tilde{\omega}^{-0.5}$ (though not by a factor of $\sqrt{2}$ as mathematically predicted [87]). To extract kinetic information, Eq.2-96 has been used to convert the slopes in Z vs. $\tilde{\omega}^{-0.5}$ plots to Z' vs. $\tilde{\omega}^{-0.5}$ in order to report σ values using radial frequency [96]. $\tilde{\omega}_1$ and $\tilde{\omega}_2$ correspond to f_1 and f_2 when the plot is expressed in radians s^{-1} . As there is no solvated O_2 for a faradic reaction into which electrons can be sunk, the thin film saturates with charge and the warburg regime displays reflective finite diffusion at the high frequency limit as the plot tends towards charge accumulation ($dZ''/dZ' \gg 1$).

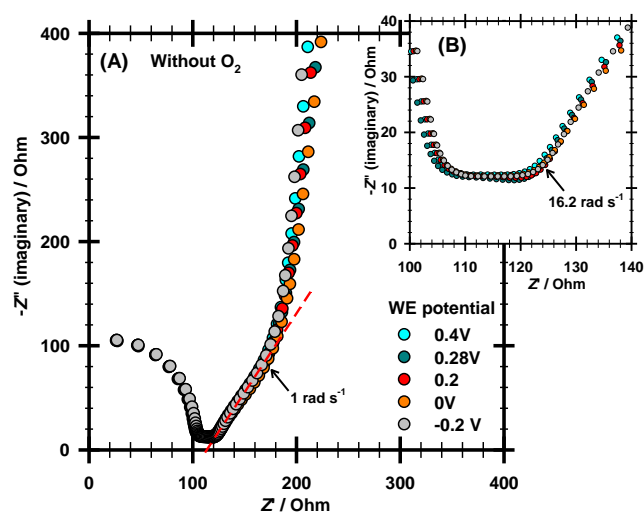


Figure 7-2. (A) High and (B) Mid frequency complex plane response, invariant of applied potential in FePc/KJB-QDPSU thin film in de-aerated media. Frequency range $1\text{MHz} > f > 0.1\text{Hz}$. $E=0.35\text{V}$. Electrolyte; 50mM PBS, pH 7.0.

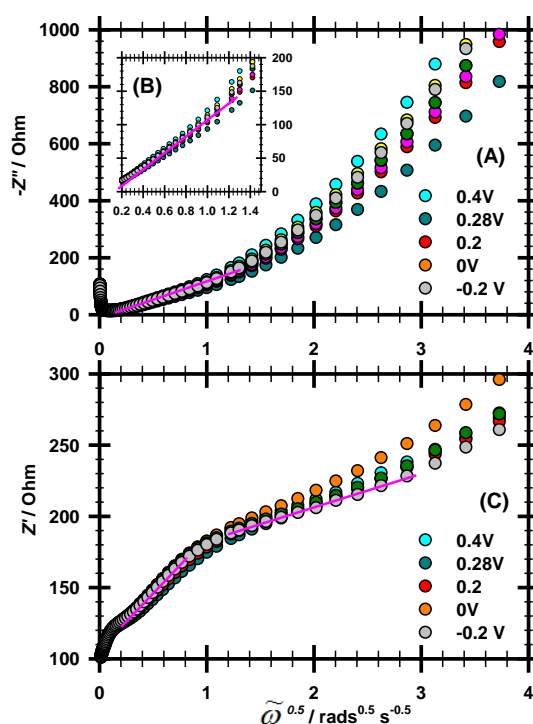


Figure 7-3. Corresponding warburg plot to data in Figure 7-2. Data of (A)(B) imaginary and (C) real impedance as a function of the root inverse of radial frequency.

With both Nafion and QDPSU, two linear Z' vs. $\tilde{\omega}^{-0.5}$ regions were identified at mid-high frequency. In FePc/KJB thin films with Nafion binder regions occurred at; 1) $8260 > f > 2500\text{Hz}$, $R^2 > 0.9991$ and 2) $204 > f > 40\text{Hz}$, $R^2 > 0.9993$. Though these ohmic contributions are relatively small in the thin film (2-3 Ohm cm^2 each), their importance

becomes apparent in thick air cathodes and wastewater electrolyte. In the $-Z''$ vs $\tilde{\omega}^{-0.5}$ plot, Figure 7-4(A), this region is not linear as with QDPSU, Figure 7-3(A). The presence in both electrodes allows both singlet oxygen diffusion and O₂ chelation to be discounted as an explanation and suggests a capacitive element occurs in series with the Warburg element within the same time constant.

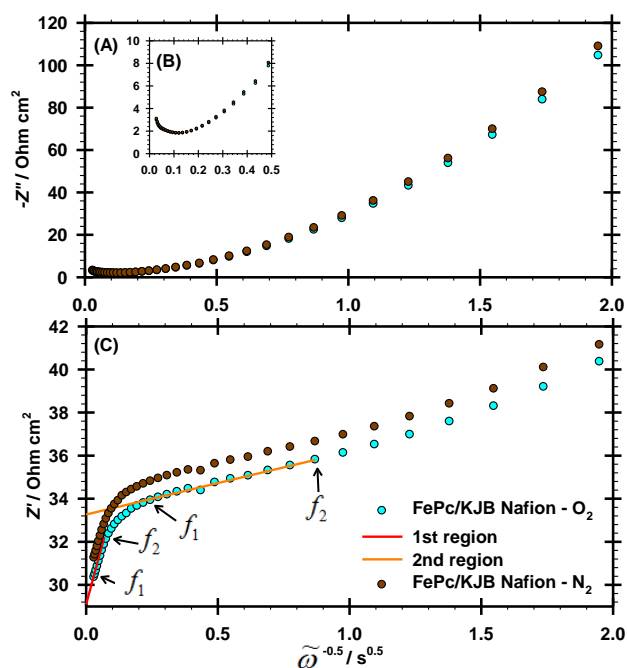


Figure 7-4. (A) Z' vs. $\tilde{\omega}^{-0.5}$ and (B) $-Z''$ vs. $\tilde{\omega}^{-0.5}$ plot to illustrate diffusive control in thin FePc/KJB Nafion film. $E=0.35\text{V}$. Electrolyte; 50mM PBS, pH 7.0.

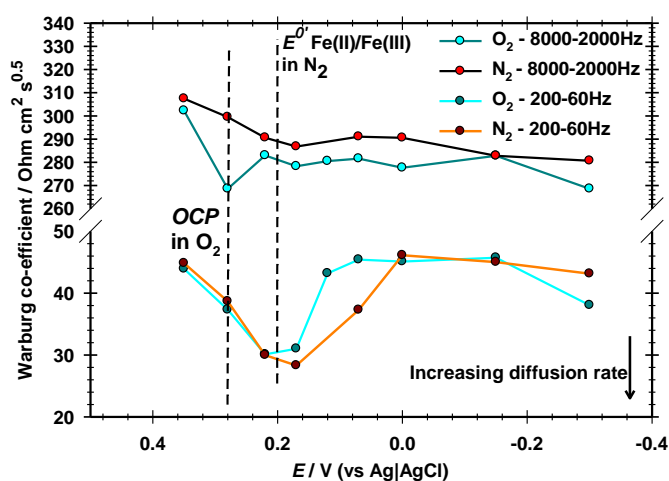


Figure 7-5. HF linear regions of Z vs. $\tilde{\omega}^{-0.5}$ plot in thin FePc/KJB Nafion film. Expressed as σ vs E for diffusion controlled behaviour in frequency ranges i) $8\text{kHz} > f > 2\text{kHz}$, or ii) $200\text{Hz} > f > 60\text{Hz}$. Quiescent electrolyte of N₂ sat. or O₂ sat. 50mM PBS, pH 7.0.

In Figure 7-4 the Warburg diffusion parameter for the Nafion electrode is plotted as a function of potential. Similar gradients were observed at all potentials (Figure 4-4 bottom) in O₂ and N₂. The main features of this plot are;

For the highest frequency range ($8\text{kHz} > f > 2\text{kHz}$);

- The Z' value and Z value form a plateau at $f > f_2$, this indicates that in this high frequency no capacitance is in series with this diffusive element.
- The dip in σ at c.a. $E = OCP$ in O₂ indicates a charge migration process [98, 99] with FePc, the speed of which is marginally increased with adsorbed O₂.
- Diffusion appears faster in the presence of O₂ suggesting the minority charge carrier utilises O₂. I.e. the ion interacts with FePc-O₂⁻ as anticipated by [339].

For the 2nd frequency range ($200\text{Hz} > f > 60\text{Hz}$);

- The Z' value and Z value increases at $f > f_2$, this indicates a capacitance is in series with this diffusive element or f_2 occurs at a higher frequency still.
- The dip in σ presents an anticipated minima c.a. 0.2V in O₂ and 0.16V in N₂, this potential is somewhat more negative than OCP (0.28V) and is discussed below.
- The difference in σ between O₂ and N₂ is negligible at potentials above 0.22V and below 0V, indicating O₂ does not affect transport of this limiting species.

It was established by Alberly and co-workers that a characteristic of the Warburg coefficient for limiting ion diffusion is a limited dependence of potential [340]. The Warburg coefficient shows a minima c.a. $E^{0'}$ of a redox, this can be associated with limiting electron diffusion [103] or limiting ion diffusion [98, 99] when the ion interacts with a redox centre. The minima is due to the fact that the product of $[O] \cdot [R]$ is smallest when $[O] = [R]$, referring to the entire complex [98].

It is possible that the low frequency response could be the same redox Fe(II)/Fe(III) couple; it is predicted that the minima is skewed from the formal potential when the log ratio of the chemical activity coefficients $\ln([a_{ox}/a_{red}])$, is large or very negative [98]. Using Eq.2-100 a negative shift in Warburg minima of 0.08V in O₂ and 0.12V in N₂ would equate to an a_{ox}/a_{red} ratio of 565 in O₂ and 13446 in N₂. Alternatively it corresponds to another redox couple other than that which controls OCP . Two potential explanations; 1) a mixed case of resistance from both ion diffusion and accompanying electron diffusion, or 2) a secondary effect of ion diffusion, being enhanced when able to utilise free FePc sites.

Eq.2-98, Eq.2-112, Eq.2-113 are utilised with several assumed concentrations, ie. $[\text{OH}^-] = 10^{-10} \text{ Mole cm}^{-3}$, $[\text{O}_2] = 5.67 \times 10^{-10} \text{ Mole cm}^{-3}$ and $[\text{Na}^+] = 7.88 \times 10^{-5} \text{ Mole cm}^{-3}$ and maximum δ_{film} measurements of $2.5 \times 10^{-4} \text{ cm} \pm 20\%$ (see section 10.7.2). The obtained diffusion constants (1.24×10^{-11} , 9×10^{-4} and $7.8 \text{ cm}^2 \text{ s}^{-1}$ respectively) are not in the same order of magnitude as the anticipated 10^{-6} - $10^{-8} \text{ cm}^2 \text{ s}^{-1}$ for ions in solution. Thus OH^- , O_2 and Na^+ may be discounted as either rate limiting diffusive species or limiting charge carriers in Figure 4-4.

An attempt to model the scenario of exclusive electron diffusion control was made with Eq.2-115 and Eq.2-116 by the treatment shown in appendix Figure A-19 using C_{diff} , the capacitance extrapolated from the steepest portion of the $-Z''/Z'$ plot in Figure 7-1. This method avoids the requirement for known concentrations of the exact diffusing species. By assuming the thin film thickness (0.00038cm) the electron diffusivity of $D_E = 2.3$ - $2.5 \times 10^{-4} \text{ cm}^2 \text{ s}^{-1}$ is obtained, clearly D_E from electron hopping is not the limiting factor in thin Nafion films. The possibility of electron hopping along diffusion distances less than the entire length of the film is excluded, as the diffusion boundary frequency was related to film thickness. To see which Warburg co-efficient the C_{diff} capacitance is related to, Eq.2-123 is applied to the σ values in Figure 4-4 and $\delta_f = 0.00038 \text{ cm}$ assumed. For the $E = 0.35 \text{ V}$ data the c.a $45 \Omega \text{ cm}^2 \text{ s}^{0.5}$ produces $D = 5.4 \times 10^{-6} \text{ cm}^2 \text{ s}^{-1}$, an entirely plausible link, whilst the c.a $305 \Omega \text{ cm}^2 \text{ s}^{0.5}$ produces $1.18 \times 10^{-7} \text{ cm}^2 \text{ s}^{-1}$, a value rather low for limiting ion diffusion and a high value for electron hopping.

In cases where an ion does not interact with a site but merely diffuses through a medium the Warburg co-efficient is not a function of potential [101]. The minima with $E^{0'}$ seen in Figure 4-4 asserts a scenario of coupled ion/electron diffusion limitation, with precedence in the literature, whereby Coowar et al claim that adsorbed anionic oxygen is a charge carrier [194] and the process is influenced by solution anion. A scenario that can occur when diffusivity of the electron is in the region of 1-1000 times greater than that of the ion [101].

7.2.3 AC field phase lag in Nafion/QDPSU air cathodes

At potential proxy to *OCP*, a 10mV AC amplitude produces a double layer current that dwarfs ORR at high and mid frequency. Oxygen concentration is expected to remain

constant throughout the catalyst layer, a feat difficult to achieve with N₂ or O₂ sparging of an air cathode. The aim of EIS investigation on air cathodes is to assess to what degree anion and cation exchange binders limit electrode performance.

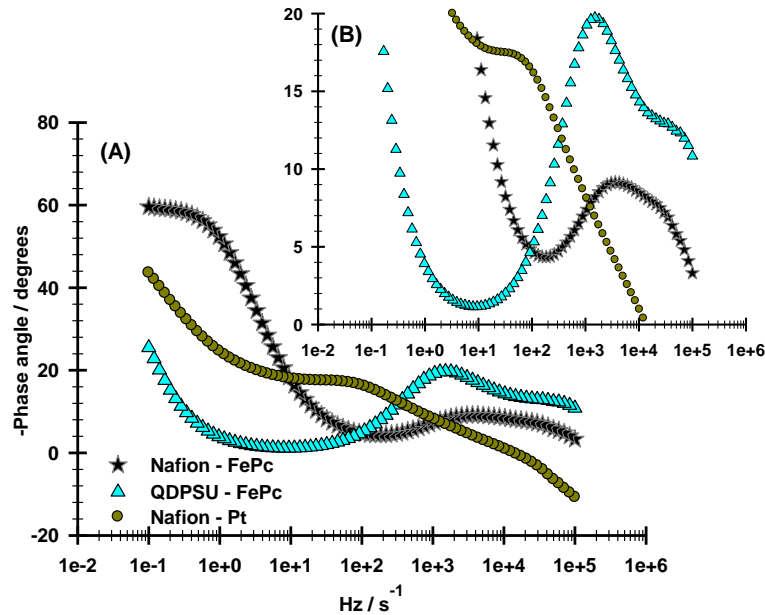


Figure 7-6. Binder influence on $(-\phi)$ as a function of $\log(f)$ in air cathodes.

GDC poised at $E=0.28V$. Inset (B) represents HF region. Electrolyte; air-saturated 50mM PBS, pH 7.0

In Figure 7-6 the phase angle (ϕ) is plotted as function of frequency for each air cathode. QDPSU produces a smaller phase angle over the frequency range $10,000\text{Hz} > f > 0.03\text{Hz}$. A response of $\phi=45^\circ$ is anticipated for limiting ion diffusion, the electric field permeation requires the movement of charge carriers to maintain electro-neutrality this indicates the movement of H_2PO_4^- , HPO_4^{2-} , OH^- , H^+ and Na^+ ions does not control the phase lag in PBS buffer.

7.2.4 High frequency ion diffusion in pores of Nafion and QDPSU

To resolve whether the phase lag is purely capacitive or mixed diffusive-capacitive a linear relationship was sought between; 1) total impedance (Z) vs. $\tilde{\omega}^{-1}$, or 2) (Z) vs. $\tilde{\omega}^{-0.5}$. A linear $-Z''$ vs. $\tilde{\omega}^{-1}$ correlation was found at very low frequency ($84\text{mHz} > f > 10\text{mHz}$). The lack of linear Z vs. $\tilde{\omega}^{-0.5}$ behaviour at low frequency at $E=-0.3V$ denotes no O₂ mass transport limitation in air cathodes, as anticipated. Table 7-2 contains the gradient of the highest frequency linear aspect in the Z vs $\tilde{\omega}^{-0.5}$ plot, the f_2 range was difficult to report due to obscuring from R_{ct} . The result from applying each

candidate for limiting charge carrier is presented in Table 7-3, molarity in the film or solution is the input. The lower binder loading may be a factor in determination of diffusion co-efficients in air cathodes.

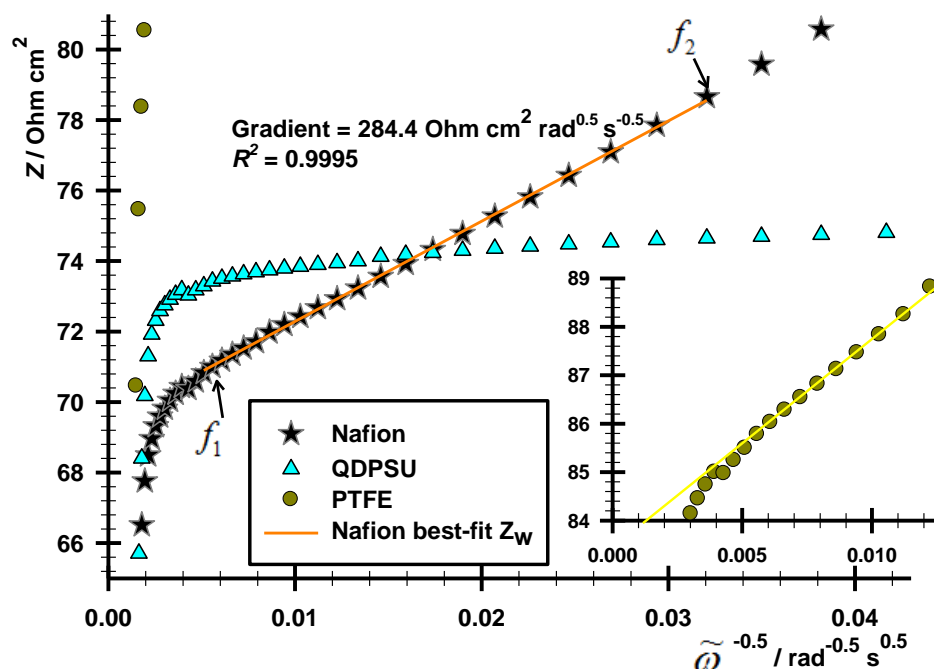


Figure 7-7. Total electrode impedance, Z vs. $\tilde{\omega}^{-0.5}$, for high frequency diffusion related impedance of air cathodes as a function of binder. Example of Nafion binder shown (inset=PTFE). Air cathodes and conditions outlined in Figure 7-6.

Table 7-2. Air cathode binder effect on high frequency Warburg co-efficient. Resulting slopes and linear regions. Calculated film thickness; 0.01cm. Electrolyte; 50mM PBS, pH7.

Binder	linear Z vs. $f^{1/2}$ range		Z at $f^{-0.5}=0$	$\sigma /$
	high f_1 /Hz	low f_2 /Hz	Ohm cm ²	Ω cm ² s ^{-0.5}
QDPSU	1791		73.31	51.9
PTFE	3605		83.42	429.1
Nafion	6093		69.44	284.4

Table 7-3. Utilising data obtained in Table 7-2 and testing various species that may cause a diffusion limiting scenario. The factor d is produced with Eq.2-114 to search for evidence of electron limited diffusion.

Limiting Charge Carrier	n	[X] Mole cm ⁻³	D cm ² s ⁻¹	f_3 / Hz	d / cm	Binder
ΣPO_4	1	5.00E-05	5.09E-09	15.941	1.61E-05	QDPSU
	1	5.00E-05	7.44E-11	22.616	1.64E-06	PTFE
	1	5.00E-05	1.69E-10	2.774	7.05E-06	Nafion
H^+ / OH^-	1	1.00E-07	1.27E-03	15.941	8.06E-03	QDPSU
	1	1.00E-07	1.86E-05	22.616	8.19E-04	PTFE
	1	1.00E-07	4.23E-05	2.774	3.53E-03	Nafion
H_2PO_4^-	1	2.11E-05	2.84E-08	15.941	3.81E-05	QDPSU
	1	2.11E-05	4.16E-10	22.616	3.87E-06	PTFE
	1	2.11E-05	9.46E-10	2.774	1.67E-05	Nafion
HPO_4^{2-}	2	2.88E-05	9.55E-10	15.941	6.99E-06	QDPSU
	2	2.88E-05	1.40E-11	22.616	7.09E-07	PTFE
	2	2.88E-05	3.18E-11	2.774	3.06E-06	Nafion
Na^+	1	7.88E-02	2.05E-15	15.941	1.02E-08	QDPSU
	1	7.88E-02	2.99E-17	22.616	1.04E-09	PTFE
	1	7.88E-02	6.81E-17	2.774	4.47E-09	Nafion
FePc loading (Γ_{FePc})	1	6.25E-05	3.26E-09	15.941	1.29E-05	QDPSU
	1	6.25E-05	4.76E-11	22.616	1.31E-06	PTFE
	1	6.25E-05	1.08E-10	2.774	5.64E-06	Nafion
Electro-active FePc ($\tilde{\Gamma}_{\text{FePc}}$)	1	3.77E-07	8.96E-05	15.941	2.14E-03	QDPSU
	1	3.77E-07	1.31E-06	22.616	2.17E-04	PTFE
	1	3.77E-07	2.98E-06	2.774	9.36E-04	Nafion
O_2 (Not a charge carrier)	4	5.67E-07	1.55E-07	15.941	8.89E-05	QDPSU
	4	5.67E-07	2.26E-09	22.616	9.03E-06	PTFE
	4	5.67E-07	5.15E-09	2.774	3.89E-05	Nafion

After establishing in section 7.2.2. couple ion/electron diffusion resulted in diffusive behaviour various charge carrier scenarios were tested, though contributions are frequently left unseparated in analysis [105] producing a joint diffusion co-efficient. This may appear to be the case in air cathodes aswell as the thin film. Since the transition from Warburg control to capacitance occurs via the relation $\tilde{\omega}_3 \propto D/\delta_f^2$, the transition region could be expected to occur at a frequency x700 higher in the TFE than the Nafion air cathode, considering the layer is x26 thinner [88]. The influence of binder concentration and pore volume will mean relationship between diffusion co-efficient is not exact. It is worth noting this type of analysis would not be possible in ultra-thin films (<0.5 μm) [87].

Scrutinizing the scenarios generated in Table 7-3 with the $\delta_f \tilde{\omega}_3/5.12$ (Eq.2-114) it can be suggested that this equation does not accurately describe the phenomenon or else electrons do not diffuse the whole film thickness (0.01cm). It could be assume that this process is not electron diffusion.

Nb. The $[\text{HPO}_4^{2-}]$ could potentially be considerably lower than bulk concentration at the reaction site. With Nafion binder the linear region occurred over a large frequency range ($6.1\text{kHz} < f < 155\text{Hz}$) with $R^2=0.9995$. In the study by Contamin et al [84], a lower frequency region of 4Hz to 0.24Hz produced a linear response in thin FePc binder-less films in PBS, attributed to electron hopping. The conductive nature of the pores in the carbon supported catalyst layer makes this possibility less likely. They attributed a scenario of $\tilde{\Gamma}_{\text{FePc}}$ being the charge carrier, splitting the response of diffusion of holes and electrons by applying Eq.2-98 to the $\text{Fe}^{3+}/(\text{Fe}^{3+}+\text{Fe}^{2+})$ and $\text{Fe}^{2+}/(\text{Fe}^{3+}+\text{Fe}^{2+})$ ratio respectively. The ratio cannot be established at $E=0.28\text{V}$ in aerobic air cathodes, the diffusion co-efficient cannot be split in such a fashion. It is clear from Figure 6-21 that $\text{Fe(III)} > \text{Fe(II)}$ at $E=0.28\text{V}$. The amalgamated diffusion co-efficient being 4 and 6 orders of magnitude larger than that for electrons and holes respectively in [84], as would be anticipate for the addition of the carbon support.

In Table 7-2, the σ value occurred in the order $\text{PTFE} > \text{Nafion} > \text{QDPSU}$. The upper frequency limit could only be reliable obtained with QDPSU ($1790 > f > 890\text{Hz}$). With Nafion ($6093 > f > 155\text{Hz}$) the detectable low frequency limit was increased, being linked to anion retardation as opposed to cation selectivity [258].

For QDPSU, “ σ ” is in the order of magnitude of an ion diffusing through a film of a redox active material of the opposing charge immobilised on graphite in an aqueous systems [98]. Using Eq.2-114 at $d|Z'|/dZ'=2$ the diffusion distance (d) is obtained. This equation is derived for a sharp transition for Warburg to reflective finite limit. In the case of porous electrodes where the low frequency limit $d|Z'|/dZ' \neq \infty$, the maximum value was 2.12 (PTFE) and 2.16 (Nafion). This behaviour is well documented with porous electrodes [87, 88]. The transition frequency (f_3 or $\tilde{\omega}_3$) occurs at different points, close to f_2 or at significantly lower frequency. This uncertainty introduces a potential

source of error in reporting d or δ_f using this equation. The number of electrical charge transferred " n " was set at 1 [94, 96], the charge on most carriers in the electrolyte.

To summarise the effect of binder, thickness and anion, the findings are presented in Table 7-4 and evaluated in following sections.

Table 7-4. Summary of linear regions in Z vs. $f^{-0.5}$ plots at high frequency, EIS of half-cells at potentials approximate to *OCF*.

Experiment	Binder / % wt.	Electrolyte / Dissolved Gas	Poised E (V) / Amplitude (V)	Linear range in Z vs. $f^{-1/2}$		σ / $\Omega \text{ cm}^2 \text{ s}^{-0.5}$	$\sigma = f(E)$? yes/no	Change in $dZ/d f^{-0.5}$ gradient (m) at f_1 of linear region Z increase / Z plateau
				high f_1 /Hz	low f_2 /Hz			
Thin film	Nafion / 156%	PBS / O_2	0.22 / 0.01	8260	2060	268	NO	Plateau m
Thin film	Nafion / 156%	PBS / N_2	0.22 / 0.01	8260	2060	300	NO	Plateau m
Thin film	Nafion / 156%	PBS / O_2	0.22 / 0.01	204	40	39.1	YES	Increase m
Thin film	Nafion / 156%	PBS / N_2	0.22 / 0.01	204	40	39.1	NO	Increase m
GDC	Nafion / 10%	PBS / Air	0.28 / 0.01	6100	155	284	N/A	Increase m
GDC	QDPSU / 10%	PBS / Air	0.28 / 0.01	1800	900	51.9	N/A	Plateau m
GDC	PTFE / 10%	PBS / Air	0.28 / 0.01	3600	1260	429	N/A	Increase m
Air cathode	QDPSU / 10%	PBS / Air	0.20 / 0.01	12260	4300	290	YES	Increase m
Air cathode	QDPSU / 10%	NaCl / Air	0.20 / 0.01	10300	5115	128.6	YES	Plateau m
Air cathode	QDPSU / 10%	WW+PBS / Air	0.20 / 0.01	24700	890	9810	YES	Plateau m
Air cathode	Nafion / 10%	WW+PBS / Air	0.20 / 0.01	110	23	187	YES	Increase m

In Figure 7-6 the final column, "change in gradient at frequencies lower than linearity", indicates whether capacitance is present at low frequency (increase m), meaning that f_2 may be inaccurate, or whether a finite diffusion barrier has been reached at low f (decrease m), indicating an accurate f_2 . Thickness and binder content of the thin film differs from the air cathode, thus frequency (f_1) is not as comparable as σ .

7.2.5 Phosphate and Chloride effect on diffusive resistance

The role of counter-anion was examined in FePcKJB QDPSU air cathodes and the properties of the Warburg parameter presented in Figure 7-8.

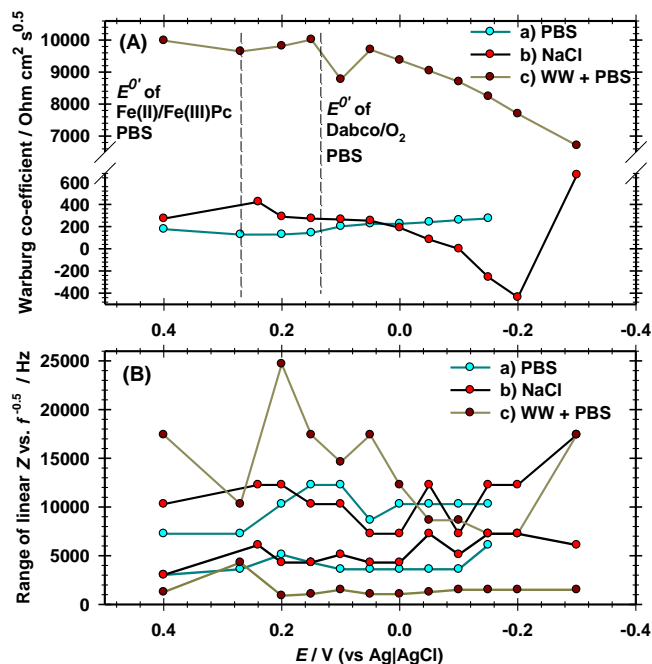


Figure 7-8. HF warburg parameter (A) σ vs E , and (B) f_1 vs. E and f_2 vs. E , in FePc/KJB QDPSU air cathodes in electrolytes of a) 50mM PBS, pH 7.0 b) 50mM NaCl, pH 7.0 or c) Primary clarifier influent with 50mM PBS, pH 7.0.

At OCP , the σ is x3.3 larger with Chloride than Phosphate. At $E < OCP$ polarisation in NaCl, σ decreased from $\sigma = 423$ to $\sigma = 290 \Omega \text{ cm}^2 \text{ s}^{0.5}$ at OCP and $E = 0.2 \text{ V}$ respectively. This could be interpreted as generation of a more motile charge carrier (such as OH^-). Z' vs $\omega^{-0.5}$ slope inversion was seen in NaCl at $0 \text{ V} > E > -0.2 \text{ V}$, this phenomenon cannot be explained in terms of rapid alkalination. With PBS buffering a σ minima occurred at OCP , contrary to NaCl. This would indicate the divalent anion (HPO_4^{2-}) did improve charge compensation over H_2PO_4^- resulting from alkalinity.

In Figure 7-8(A) the similarity in σ for PBS and NaCl shows initial molarity of the charge carrier is within an order of magnitude. In Table 7-4, the Z' vs $\omega^{-0.5}$ frequency range is largest for Nafion > PTFE > QDPSU. Therefore limitation from cationic diffusion (ie. Na^+) is not the case.

The σ vs E plot in PBS is similar for Nafion thin film, Figure 4-4 as for air cathode, Figure 7-8(A), indicating chemistry relating FePc with Phosphate. In Table 7-4, σ values are within 40-430 $\Omega \text{ cm}^2 \text{ s}^{0.5}$ across all electrodes with different binders. A notable exception is the addition of wastewater to the QDPSU air cathode, data from

Figure A-21 is converted from Hz and displayed in Figure 7-8(A). A minima at 0.1V overlaps the Dabco redox from $\sigma=10,000-7,000 \text{ Ohm cm}^2 \text{ s}^{0.5}$, equating to a rise of electrode resistance of $100-120 \Omega \text{ cm}^2$ which is not present in PBS alone. This shows another pollutant from wastewater is interacting with Dabco, which is likely redox active, according to the presence of a minima [101]. A drastic loss of ion diffusivity appears to be indicated for QDPSU in wastewater when relating Figure 7-8(A) to Eq.2-98.

7.2.6 Impedance spectra of QDPSU and Nafion air cathodes in PBS

In Figure 7-9, FePc/KJB air cathodes are mounted in a GDC. Binder loading is 10% wt. is applied for QDPSU, PTFE and Na-Nafion. The important aspects of nyquist impedance spectra are displayed. The entire frequency spectrum is examined.

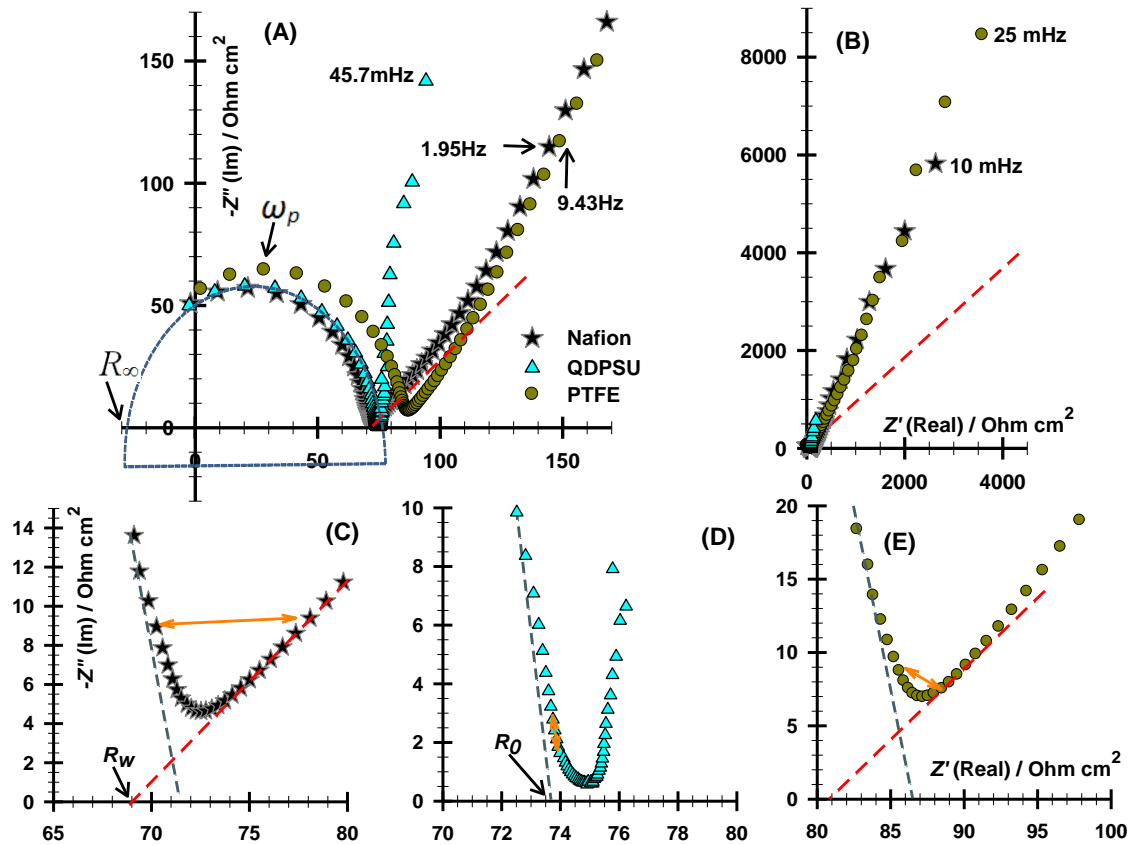


Figure 7-9. $-Z''$ vs. Z' plots of air cathodes in Figure 7-6. HF region (A), LF region (B) and Mid freq. region (C), (D) and (E) of Nafion, QDPSU and PTFE binder respectively. Red line=Warburg gradient ($m=1$), orange=linear Z vs. $\omega^{-0.5}$ range.

Table 7-5. Characteristics of high and mid frequency region displayed in Figure 7-9

$$A=0.2826\text{cm}^2$$

Binder	$R_{\infty} / \Omega \text{ cm}^2$	$R_0 / \Omega \text{ cm}^2$	f_p / Hz	$Y^0 / \Omega^{-1} \text{ cm}^{-2}$	$C_{\text{HF}} / \text{F cm}^{-2}$	$R_{w,\infty} / \Omega \text{ cm}^2$
Nafion	-56.24	70.59	70484	1.45E-08	1.78E-08	68.6
PTFE	-57.52	85.49	70484	1.32E-08	1.58E-08	80.7
QDPSU	-62.10	73.53	70484	1.34E-08	1.66E-08	74.4

The HF response of the air cathodes produced an arc that extrapolated to negative Z' value at $f > 1\text{MHz}$, a capacitance which appeared to be in parallel with solution resistance. As this feature is not a source of internal resistance it is not evaluated but discussed in the appendix section 10.6.2.

From Figure 7-9, R_0 of the HF time constant was linked to the Warburg co-efficient by ($R_{w,\infty}-R_0$) as in (see Figure A-18). Application of Eq.2-110 and Eq.2-111, using the HF capacitance rather C_{dl} found that values for σ were dissimilar when compared to the Z vs $\omega^{-0.5}$ plot in Table 7-2. Using this method the σ values for PTFE were larger than Nafion. For a $R_{w,\infty}-R_0 \propto \sigma^2$ relationship [35] $\sigma=3\text{-}5 \times 10^4 \text{ Ohm cm}^2 \text{ s}^{-0.5}$ is followed as opposed to a $R_{w,\infty}-R_0 \propto \sigma$ relationship ($\sigma=8\text{-}24 \times 10^8 \text{ Ohm cm}^2 \text{ s}^{-0.5}$), so was deemed an unreliable method for σ determination. This indicated the HF arc was not linked to the diffusion process and could be neglected as a source of electrode impedance.

As a result of convolution from this capacitance in parallel with R_s the HF and LF regions were treated separately; an equivalent circuit was applied to the LF only, Figure 7-10(C). This approach produced the lowest χ^2 of any equivalent circuit fit, and has been used before with FePc films [84]. A fixed value of $R_{w,\infty}$ from Table 7-5 was placed in equivalent circuit 4-9 (C) as R_s . This approach allowed accurate determination of R_{ct} as a priority. This was evaluated from the %error report for R_{ct} in the Nova programme.

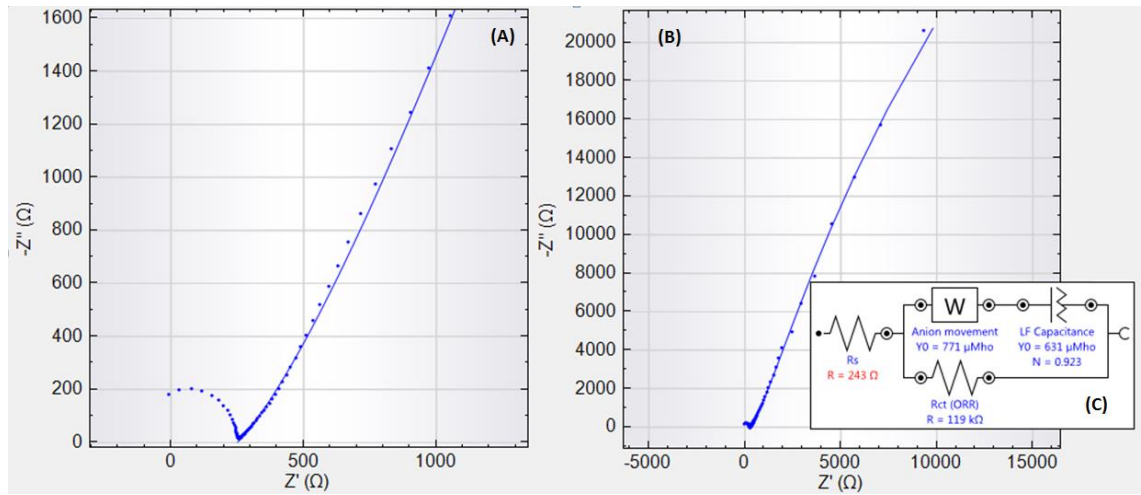


Figure 7-10. Equivalent circuit (C) fit to mid frequency (A) or low frequency (B) data in NOVA software for FePc/KJB (Nafion) air cathodes poised at $E=0.28V$.
Electrolyte; 50mM PBS, pH 7.0.

Table 7-6. Characteristics of LF region displayed in Figure 7-10. $A=0.2826cm^2$

Binder	$C_{\Sigma}^{(10)}$ / F cm ⁻²	CPE Y^0 / S s ^N	CPE N	Z_w Y^0 / S s ^{0.5}	R_w+R_{ion} Ohms	R_{ct} / Ohms
Na-Nafion	1.10E-02	6.31E-04	0.923	7.71E-04	214.3	1.19E+05
PTFE	2.25E-03	1.53E-04	0.804	4.61E-01	85.6	5.41E+06
QDPSU	3.85E-02	6.31E-03	0.927	6.21E-02	20.6	2.74E+04

For the data in Figure 7-10 various equivalent circuit fits were attempted. These included; R_{ct} leading to a parallel split between $R_{dl}+Z_w$ (series) and CPE, in standard notation $[R(Q[RW])]$ [184], also $[R([RW]Q[RQ])]$ [84], and $[R(CCR)(RC)R]$ [208]. A point of inflexion in the LF response indicated a very slow charge transfer reaction at $E=0.28V$. Accordingly the $[R(R[QW])]$ circuit in Figure 7-10(C) produced the smallest χ^2 . The decision to include a HF Warburg element shows consistency with the $N=c.a.$ 0.5 seen at OCP in Yu et al [184] and by Alcaide et al [341].

Several factors of the LF response are noted;

- Using Eq.2-103 the CPE capacitance and correcting for area produces C_{dl} , and $C_{dl}<C_{\Sigma}$ from CV.
- The CPE exponent (N) was equivalent for Nafion and QDPSU, with near perfect capacitance (0.923 and 0.927 respectively), producing transitory behaviour in

¹⁰ Obtained at $E=0.28V$ with Eq.2-16 during CV ($v=20mV/s$)

PTFE (0.804) with the most uneven surface. This explanation fits the trend in total non-faradic current observed during CV (C_s in Table 7-5).

- Using Eq.2-104 the geometric J_0 of the QDPSU air cathode is, $J_0=8.15 \times 10^{-7} \text{ A cm}^{-2}$, similar to that of the thin films (Table 6-1).

The Warburg co-efficients from the EC fit were a relatively minor source of impedance in the QDPSU electrode, therefore generating Z_w from the Nova iteration, A/Y^0 (Eq.2-99), produced a less accurate fit than the Z vs $\omega^{-0.5}$ plot. Nafion produced the most accurate fit, iteration produced $259 \Omega \text{ cm}^2 \text{ s}^{0.5}$ (Eq.2-99) vs. $284.4 \Omega \text{ cm}^2 \text{ s}^{0.5}$ from Z vs. $\omega^{-0.5}$. QDPSU produced $32.2 \Omega \text{ cm}^2 \text{ s}^{0.5}$ with circuit iteration and $51.9 \Omega \text{ cm}^2 \text{ s}^{0.5}$ in Table 7-3. With PTFE, the iteration result was exactly three orders of magnitude lower than that in Table 7-3. It can be concluded that equivalent circuit fitting was found to be a poor method for estimating R_{ct} in FePc/KJB binder air cathodes in PBS and Z' vs. $\omega^{-0.5}$ regression should be used instead.

7.3 Nafion and QDPSU binders for MFC air cathodes

7.3.1 Impedance of QDPSU air cathodes in buffered wastewater

The impedance study herein aims to show how binder influences components of resistance in the FePc/KJB air cathode in the presence of wastewater. Figure 7-11 depicts the Nyquist response of half-cell air cathodes in 50mM PBS wastewater.

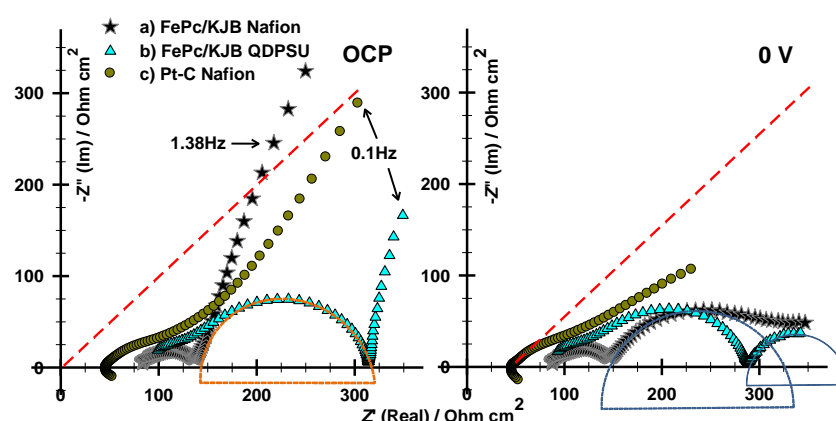


Figure 7-11. Nyquist plot of air cathodes described in legend, in a WW-PBS filled cube half-cell. Auxiliary Electrode; Pt mesh. (A) $E=OCP$, (B) $E=0 \text{ V}$. Red line=Warburg impedance ($m=1$), blue semi-circle; parallel R_{ct}/C_{diff} related to ORR, orange semi-circle R_{dl}/C_{dl} parallel. Electrolyte; air saturated Wastewater+PBS(50mM), pH 7.0.

In Figure 7-11 the constant phase element is clearly applicable from depression of the semi-circle. This is due to inhomogeneity on the surface presented to the electrolyte. With QDPSU the R_{dl} produced $150\Omega\text{ cm}^2$ with wastewater addition (Figure 7-11), analogous to the relaxation of accumulated countercharges at the IHP. This indicates strong bonds between QDPSU and numerous countercharges. C_{dl} was largely invariant with potential and occurred in parallel with this component. The response of Pt-Nafion was convoluted due to the non-specificity of Pt for oxidation/reduction reactions of wastewater contaminants. The time constants were amalgamated for these processes and total AC impedance (R_{AC}) or equivalent circuit fits could not be obtained.

As anticipated, O_2 permeation to the reaction site was not impeded by accumulation of wastewater pollutants; the QDPSU LF response at $E=0V$ in Figure 7-11 did not represent transmissive diffusion boundary resistance. The LF semi-circle could be manually measured for R_{ct} [342].

7.3.2 Wastewater pollutant and R_{ct} of QDPSU and Nafion air cathodes

Figure 7-12 shows manual arc fits at low frequency ($R_0-R_\infty=R_{ct}$) in wastewater PBS. $\log_{10}(R_{ct}^{-1})$ vs E is akin to a tafel plot ($R_{ct}^{-1} \propto i_k$) [343], provided all other resistances are successfully removed.

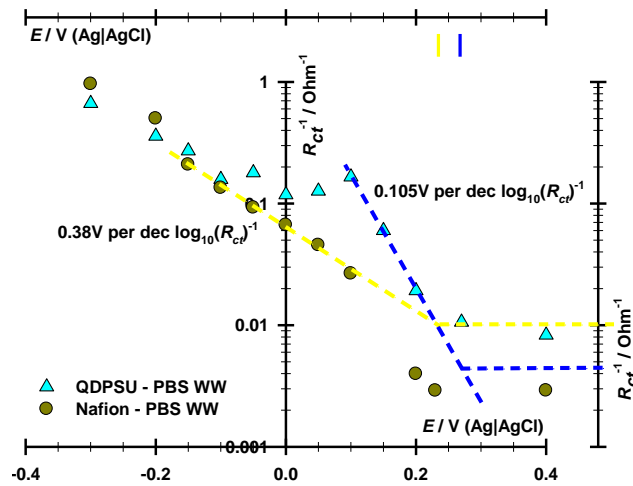


Figure 7-12. (R_{ct}^{-1}) vs E plot for FePc/KJB air cathodes with binders of a) QDPSU or b) Nafion in WW-PBS. Setup as in Figure 7-11. Least square fit; yellow-nafion and dark blue-QDPSU. Extrapolated to stable OCP (markers on top offset axis).

The circle diameter represents R_{ct} of oxygen reduction in a PBS wastewater environment. Maximum R_{ct} only corresponds to the $E^{0'}$ of the RDS couple when $\alpha=0.5$ and the reaction is nernstian and it is the only reaction occurring on the electrode. Electroanalysis of this type cannot be applied to chemically diverse electrolytes. Several observations can be made;

- At $E > -0.2V$, R_{ct} is lower with QDPSU than Nafion.
- With QDPSU electrodes in PBS a linear fit occurred at $0.197V \log_{10}(R_{ct})^{-1}$ ($-0.05 < E < 0.1V$) with an extremely accurate fit ($R^2=0.99993$). In NaCl this linear region is $-0.15 < E < 0V$ at $3.98V \log_{10}(R_{ct})^{-1}$ ($R^2=0.973$).
- A 'noisy' R_{ct} response from $-0.1 < E < 0.1V$ was not observed in PBS or NaCl and may indicate complex adsorption processes. The QDPSU redox with O_2 (section 6.2.1.) is unlikely to account for the result at $0.1V$ as it was not observed in PBS.
- Using Eq.2-104 (and assuming $n=4$), the corresponding geometric J_0 values for R_{ct} recorded at OCP is $1.45 \times 10^{-6} A \text{ cm}^{-2}$ with Nafion and $5.3 \times 10^{-6} A \text{ cm}^{-2}$ with QDPSU in PBS-Wastewater.

It is perhaps unusual that the magnitude in difference in J_0 with Nafion and QDPSU air cathodes in wastewater, x3.5 larger with QDPSU, is similar to that of thin films in PBS, ca. x2.5 larger with QDPSU (Table 6-1 and Table 5-1). Especially considering the Nafion electrode displayed a lower $OCP=0.23V$ while QDPSU produced an OCP similar to that in PBS; $OCP=0.27V$.

7.3.3 Equivalent circuit in PBS WW for QDPSU and Nafion

It was established that it would be impossible for the resistance element at high frequency (Figure 7-11) to relate to R_{ct} due to 1) the unfeasible J_0 values (c.a. $3.5 \times 10^{-5} A \text{ cm}^{-2}$) that would correspond to this at OCP and, 2) the Z' value is consistent at all potentials above and below $\eta=0V$ ($\pm 20\%$). This was the case in every system tested using the FePc/KJB catalyst, both thin film and air cathode, Nafion and QDPSU.

Due to the result in Figure A-21 a semi-infinite Warburg element was placed in series with a capacitance. This capacitance was established to be the double layer capacity (C_{dl}) [84] from the consistent values $1-1.5 \mu F \text{ cm}^{-2}$ for all potentials and binders (Table 7-7). The two components were connected in parallel to the resistance offered by the double-layer (R_{dl}). The fit at low frequency was very accurate, yet the presence of a

UHF arc ($>50,000\text{Hz}$) meant iteration produced an electron diffusion impedance dissimilar to that obtained by Z vs. $f^{-0.5}$ analysis, the latter being the more accurate representation. None of the values were constrained, and the C_{diff} consistently produced an exponent ($N>0.86$) suggesting capacitance in an in-homogenous surface.

The $R_{dl}[C_{dl}W]$ components could also be substituted (Table 7-3) with an open ended diffusion element ($\chi^2=0.227$) or Gerischer impedance [344] ($\chi^2=1.02$), both producing 1.65-1.25mMho. However, the need to identify C_{dl} required these components to be separated. It was theorised that resistance to O_2 adsorption may increase in the presence of wastewater, but no such feature could be identified on the nyquist plots (Figure 7-11 which would call for a parallel $R_{ads}[C_{ads}]$ component. A slight depression in the arc did not fit the bounded adsorbing Warburg unit modelled in Figure 2-22, and no physical explanation can be found for a Gerischer unit (electrolyte reaction). The equivalent circuit presented in Figure 7-13 was valid for FePc/KJB air cathodes with QDPSU binder in PBS amended wastewater at all potentials in the range $0.4>E>-0.3\text{V}$.

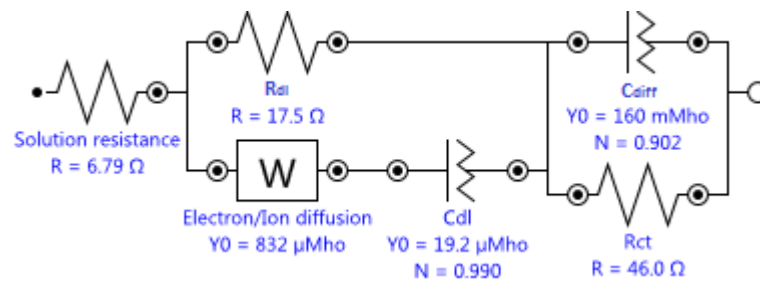


Figure 7-13. Equivalent circuit used to model FePc/KJB QDPSU air cathodes with contamination and blocking from adsorption of species in PBS buffered wastewater.

Table 7-7 contains the results of manual arc fitting of the components in equivalent circuit 4-14 to the iteration stabilised values of this equivalent circuit.

Table 7-7. FePc QDPSU electrodes in WW-PBS, parameters of fitted circuit Figure 7-13, comparison of fitting high and low frequency arc manually with both FePc Nafion and FePc QDPSU electrodes.

$E /$ V (Ag AgCl)	$R_s /$ $\Omega \text{ cm}^2$	$R_{dl} /$ $\Omega \text{ cm}^2$	e^- diffusion $Y^0 / S \text{ s}^{0.5} \text{ cm}^{-2}$ $\Omega^{-1} \text{ cm}^{-2}$	C_{dl} $Y^0 / S \text{ s}^N \text{ cm}^{-2}$ $\Omega^{-1} \text{ cm}^{-2}$	C_{dl} N	C_{diff} $Y^0 / S \text{ s}^N \text{ cm}^{-2}$ $\Omega^{-1} \text{ cm}^{-2}$	C_{diff} N	$R_{ct} /$ $\Omega \text{ cm}^2$	χ^2
EC circuit fit - QDPSU FePc/KJB									
0.4	84.99	217.0	6.52E-05	1.40E-06	0.990	6.76E-03	0.962	540.1	0.0647
0.27	88.03	228.9	6.66E-05	1.37E-06	0.990	8.91E-03	0.982	718.4	0.0648
0.2	85.26	219.2	6.63E-05	1.53E-06	0.990	1.27E-02	0.902	578.2	0.0502
0.15	84.38	224.9	6.43E-05	1.48E-06	0.990	1.27E-02	0.944	186.5	0.0553
0.1	79.55	189.7	6.57E-05	1.69E-06	0.990	1.25E-02	0.855	59.9	0.0383
0.05	82.21	215.0	6.45E-05	1.53E-06	0.990	1.28E-02	0.907	115.0	0.0488
0	81.27	208.5	6.46E-05	1.58E-06	0.990	1.21E-02	0.873	88.4	0.0455
-0.05	80.63	199.5	6.54E-05	1.64E-06	0.990	1.29E-02	0.860	71.7	0.0413
-0.1	79.55	189.7	6.57E-05	1.69E-06	0.990	1.25E-02	0.855	59.9	0.0383
-0.15	78.66	178.8	6.69E-05	1.74E-06	0.990	1.33E-02	0.872	43.2	0.0319
-0.2	77.41	163.6	6.89E-05	1.69E-06	0.990	1.48E-02	0.895	31.4	0.0293
-0.3	75.81	135.7	7.61E-05	2.00E-06	0.990	1.50E-02	0.922	19.7	0.0184
Manual arc fit - QDPSU FePc/KJB									
0.4	N/A	166.4	N/A	1.11E-06	0.998	1.05E-03	0.999	1511.6	N/A
0.27	N/A	178.5	N/A	1.08E-06	0.998	1.34E-03	0.999	1183.8	N/A
0.2	N/A	171.7	N/A	1.09E-06	0.998	2.44E-03	0.998	652.8	N/A
0.15	N/A	176.1	N/A	1.07E-06	0.998	7.61E-03	0.998	209.3	N/A
0.1	N/A	147.2	N/A	1.12E-06	0.997	1.27E-02	0.995	75.8	N/A
0.05	N/A	166.6	N/A	1.10E-06	0.998	1.41E-02	0.999	99.1	N/A
0	N/A	160.8	N/A	1.12E-06	0.997	1.28E-02	0.996	106.2	N/A
-0.05	N/A	155.0	N/A	1.13E-06	0.997	1.25E-02	0.997	70.0	N/A
-0.1	N/A	146.1	N/A	1.15E-06	0.997	1.29E-02	0.994	79.5	N/A
-0.15	N/A	135.5	N/A	1.20E-06	0.997	1.07E-02	0.997	46.3	N/A
-0.2	N/A	123.0	N/A	1.24E-06	0.997	1.13E-02	0.996	35.0	N/A
-0.3	N/A	96.5	N/A	1.52E-06	0.998	1.06E-02	0.999	18.9	N/A
Manual arc fit - Nafion FePc/KJB									
0.4	N/A	55.8	N/A	1.18E-06	0.995	3.67E-04	0.997	4332.8	N/A
0.24	N/A	59.6	N/A	1.12E-06	0.995	3.67E-04	0.997	4341.0	N/A
0.2	N/A	59.2	N/A	1.19E-06	0.996	5.03E-04	0.996	3163.6	N/A
0.1	N/A	62.8	N/A	1.13E-06	0.995	7.48E-04	0.996	473.4	N/A
0.05	N/A	64.1	N/A	1.09E-06	0.995	5.70E-04	0.995	276.1	N/A
0	N/A	65.5	N/A	1.03E-06	0.994	4.72E-04	0.995	188.6	N/A
-0.05	N/A	63.9	N/A	1.05E-06	0.995	5.17E-04	0.995	135.6	N/A
-0.1	N/A	62.7	N/A	1.08E-06	0.995	9.65E-04	0.991	93.4	N/A
-0.15	N/A	57.7	N/A	1.22E-06	0.995	1.18E-03	0.990	60.2	N/A
-0.2	N/A	52.2	N/A	1.24E-06	0.995	1.83E-03	0.993	25.2	N/A
-0.3	N/A	42.6	N/A	1.38E-06	0.995	1.49E-03	0.994	13.1	N/A

The admittance (Y^0) of the C_{diff} component was x10 lower with Nafion than QDPSU. In QDPSU electrodes, the resistance due to surface states is extremely large (c.a 220-150 Ω

cm²). By comparison, in 50mM PBS the typical performance of an anion exchange membrane is 12.4Ω cm² [254] and that of all aspects of the anode biofilm in a sandwich MFC can be 340Ω cm² [264]. Applying Eq.2-107 to R_{ss} produced unfeasibly high rate constants (3×10^3 cm s⁻¹) for O₂ adsorption, indicating convolution with R_{dl} and inseparable time constants.

An LF impedance was observed for Nafion at all potentials 0.4> E >-0.1V and absent in QDPSU (Figure 7-14). This appeared to be the reason behind the superior performance of QDPSU in wastewater.

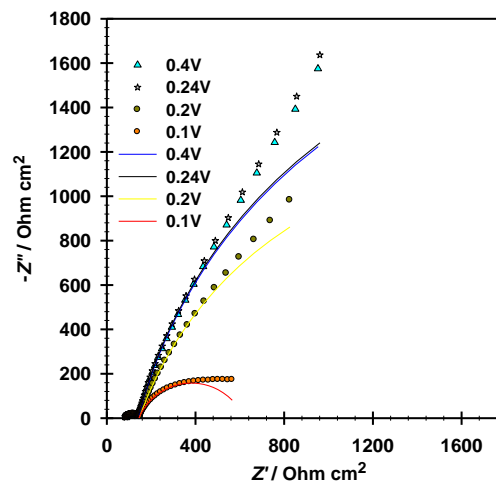


Figure 7-14. Nafion FePc/KJB air cathode, low frequency impedance in wastewater.

Data with manual $R_{ct}[C_{diff}]$ circuit arc applied.

The absence at low potential excluded O₂ diffusion limitation, Z' vs $\omega^{-0.5}$ and Z' vs ω^{-1} plots were non-linear and convective effects were not present in QDPSU. A cationic pollutant such as Mg²⁺ has previously impeded ORR on FePc [176], via adsorption onto the pyrrole ring. Mg²⁺ is present at 3mM in Wastewater (Table 1-1) and is capable of transport in a Nafion film, a process blocked by exclusion with QDPSU, indicating a benefit of anion exchange.

7.3.4 MFCs polarisation with QDPSU air cathodes in artificial wastewater

Two MFCs with established biofilms were run continuously for over a year. Initial inoculation was from acetate supplemented primary clarifier influent with PBS buffer. The MFCs were used to analyse the anticipated improvements with QDPSU binder by swapping electrodes across both MFCs. All phosphate buffered wastewater inoculum was consistent in conductivity, 6.6 ± 0.2 mS cm⁻¹ and pH, 7.0-7.1. Steady state

polarisation minimises power “overshoot” over potentiostat [345]. Example polarisations from 20 minute interval changes in Ω_{ext} can be seen in Figure 7-15 and the average of all tests summarised in Table 7-8.

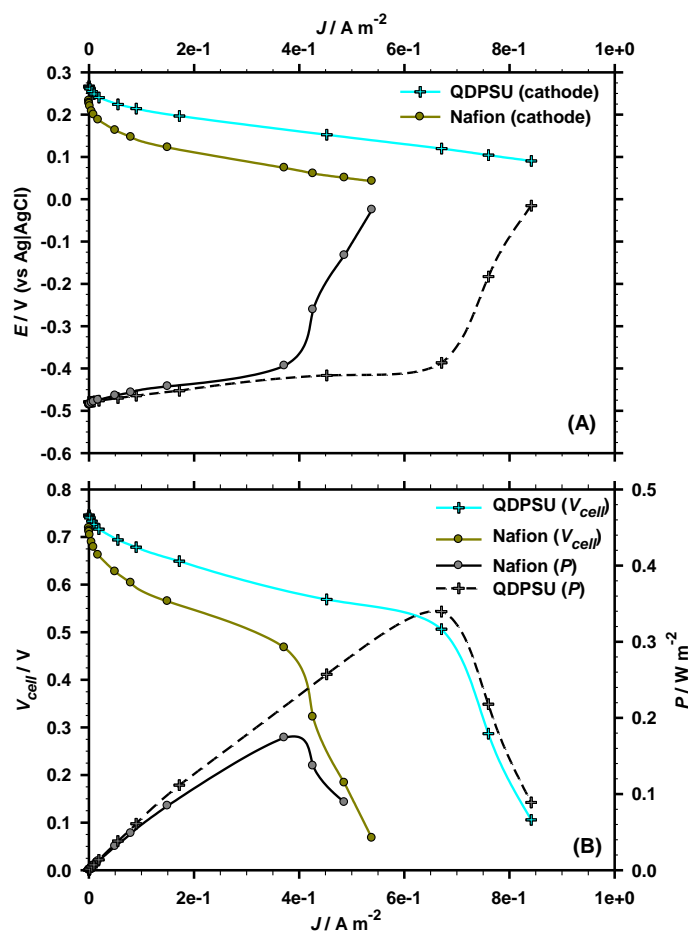


Figure 7-15. Steady state polarisation curves of MFCs with FePc/KJB air cathodes containing QDPSU or Nafion binders.(A) E_{cat} and E_{an} vs J and (B) V_{cell} - J and P - J power curved. Electrolyte; wastewater amended with 50 mM PBS, $\kappa=6.6mS cm^{-1}$, pH 7.0

Table 7-8. Summary of repeated MFC performance at fixed external load (left column) or steady-state polarisation (right column).Electrolyte; wastewater amended with 50mM PBS, $\kappa=6.6mS cm^{-1}$, pH 7.0

$P\ (\Omega_{ext}=1k\Omega)\ /\ W\ m^{-2}$				$P_{max}\ /\ W\ m^{-2}$		
Old/New	FePc <i>QDPSU</i>	FePc <i>Nafion</i>	Pt <i>Nafion</i>	FePc <i>QDPSU</i>	FePc <i>Nafion</i>	Pt <i>Nafion</i>
New	0.210	0.131		0.340	0.124	
New	0.173		0.201	0.201		0.297
New		0.155	0.210		0.174	0.215
Old	0.189	0.140		0.235	0.158	
Average	0.191	0.142	0.205	0.259	0.152	0.256

In every polarisation QDPSU FePc consistently outperformed Nafion FePc, obtaining an average over three experiments of P_{max} of 0.259 W m^{-2} vs. 0.152 W m^{-2} respectively ($A=12.56 \text{ cm}^2$). The performance was comparable to Pt, average $P_{max}=0.256 \text{ W m}^{-2}$.

In Figure 7-15 the anode potential is consistent until metabolic limitation from the viable exoelectrogen population size of the biofilm is reached. Higher surface area materials, such as carbon brush used in several studies [169, 261], could be used to resolve this issue. As such, the difference in cathode potential prior to this point is used to highlight the improvement with QDPSU binder. The biofilm variance was mitigated by rotating cathodes across cells.

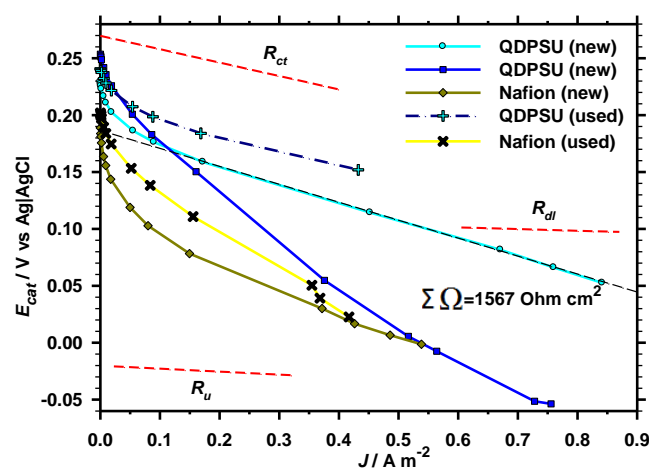


Figure 7-16. E_{cat} of QDPSU or Nafion binder. Obtained during polarisation curves of MFC's. FePc/KJB catalyst. Red dashed lines; R_{dl} and R_{ct} at $E=0.1 \text{ V}$ and OCP respectively.

Electrolyte; wastewater amended, 50 mM PBS , 6.6 mS cm^{-1} , $\text{pH } 7.0$

The data represented in Figure 7-16 was overlaid with parameters recorded in Table 7-7. Before the anode potential reaches limiting current $E_{an} = -0.410 \pm 0.015 \text{ V}$, the average cathode potential for this E_{an} is highest for FePc QDPSU (0.096 V) followed by Pt Nafion (0.078 V) then FePc Nafion (-0.012 V). In all instances the cathode potential was higher with QDPSU.

OCP was consistently higher for QDPSU ($0.229\text{--}0.254 \text{ V}$) than Nafion ($0.189\text{--}0.216 \text{ V}$), showing agreement with the EIS experiments; QDPSU (0.27 V), Nafion (0.24 V). Variance in ohmic drop is due to absence of a current collector and connection with Ti wire via a thick TiO_2 layer. This approach was taken to allow improved sealing and remove surface of active metal (ie. stainless steel) from electrolyte contact.

The uncompensated solution resistance (R_u) was calculated using Eq.1-4 for $\kappa=6.6 \text{ mS cm}^{-1}$ solution and a WE-RE i -R drop of $R_u=20.26\Omega$ was and represented on Figure 7-16. With QDPSU electrodes a large portion of non-potential dependent resistance remained unaccounted for. Voltage loss at low current is not exclusively R_{ct} (Figure 7-16), accounting for a comparison of the R_{dl} value obtained from section 7.3.3 and the actual drop shows this resistance to be minor (11.7Ω at $E=0.1\text{V}$). The linearity of this region reflects the fact that admittance for the C_{diff} unit is x10 larger for QDPSU than Nafion. In contrast the unidentified low frequency impedance of the Nafion electrode drops after OCF and so the line curves upwards. As such the non-linear result of the Nafion is due to the capacitive effect, which decreases below OCF .

7.3.5 MFCs polarisation using QDPSU FePc air cathodes in wastewater

In Figure 7-17 polarisation curves of MFC using new or old air cathodes of Pt/Nafion or FePcKJB/QDPSU are presented. The peak power densities of the same electrodes over the following batch cycle are presented in Table 7-9.

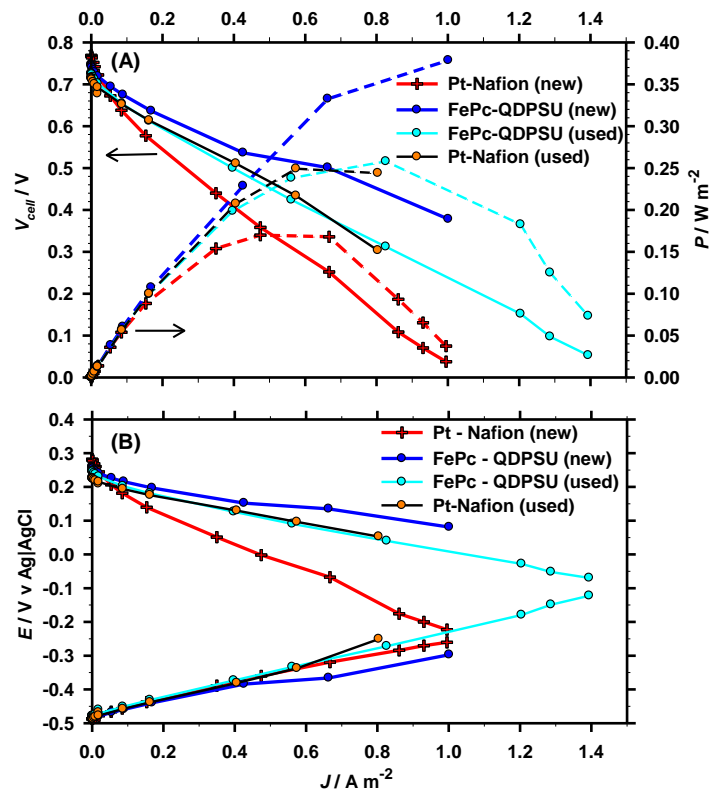


Figure 7-17. (A) V_{cell} and Power density vs J and (B) E_{an} and E_{cat} vs J in polarisation of SCMFC's with air cathodes of Pt/C (Nafion), or FePc/KJB (QDPSU). Electrolyte; primary clarifier influent, pH 7.2. $\kappa=1.82\text{mS cm}^{-1}$.

Table 7-9. MFC performance in batch mode ($\Omega_{ext}=300\Omega$) or steady-state polarisation. Electrolyte; Unbuffered Wastewater, $\kappa=1.82\text{mS cm}^{-1}$. pH; 7.2.

Old/New	$P (\Omega_{ext}=300\Omega)$		$P_{max} / \text{W m}^{-2}$	
	FePc QDPSU	Pt Nafion	FePc QDPSU	Pt Nafion
New	0.158	0.113	0.379	0.170
Old	0.180		0.255	
Old	0.211	0.103	0.258	0.249
Average	0.183	0.108	0.297	0.210

The average P_{max} for FePc/KJB QDPSU air cathodes was larger in wastewater without phosphate supplementation, 0.297W m^{-2} vs. 0.259W m^{-2} . A superior biofilm was cultivated without phosphate presence. However, the FePc/KJB QDPSU cathodes outperformed Pt Nafion in unbuffered wastewater (0.297 vs. 0.21W m^{-2}) with a similar limiting solution resistance and biofilm conditions.

Using Eq.1-4 the internal solution resistance is 140Ω , ($R_u=0.263\text{V}$ in 1.5A m^{-2}). From Figure 7-17 the linear E vs. J response of both electrodes show the cell is limited by ohmic loss, which can be countered by reducing electrode separation [264]. The cathode response is less consistent than with PBS owing to electrode fixation.

Applying iR -correction with Eq.1-4 on the lateral distances shown in Figure 4-1 for RE-frit produces $R_u=73.5\Omega$ and for RE-biofilm $R_u=56.87\Omega$. After i -R loss subtraction linear E vs. J response is observed for Pt, the best Pt polarisation producing $1\text{k}\Omega\text{cm}^2$ in wastewater. In this current range the best FePc/KJB QDPSU polarisation produced the maximum resistance at $0.84\text{k}\Omega\text{cm}^2$ ($J=0.1\text{-}0.5\text{ A m}^{-2}$). With FePc/KJB QDPSU the resistance was not consistent with potential, in-line with the findings in Table 7-7. The same observation is made in un-buffered wastewater.

7.3.6 Batch performance of MFCs with QDPSU air cathodes

Batch performance of MFCs with cathodic biofilm contaminated air cathodes were air dried until totally dry in-between batches, then re-inserted with fresh media to evaluate the effect of biofilm sterilisation (Figure 7-18). At the end of a batch cycle the acetate is

depleted and the reaction on the anode ceases, power output drops rapidly as $E_{an} \rightarrow 0.2V$ (OCP of E_{cat}).

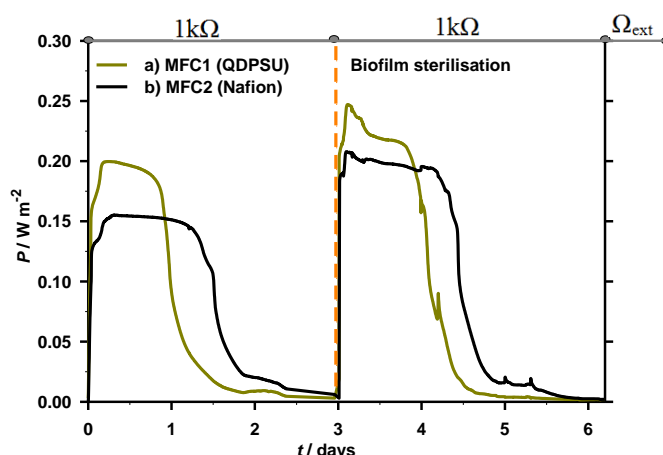


Figure 7-18. Batch performance of FePc/KJB in single chamber MFCs using air cathodes with a) QDPSU or b) Nafion ionomer. Air cathodes with dried cathode biofilm reinserted at $t=3$ days. Electrolyte; Wastewater-PBS, ($6.6mS\ cm^{-1}$) pH 7.0.

The batch performance of new, aged and biofilm contaminated QDPSU electrodes was consistently higher than Nafion, with and without Phosphate supplementation. Cathode biofilm sterilisation by evaporation ($30^{\circ}C$) regenerated the performance of both Nafion and QDPSU electrodes (Figure 7-18), suggesting any damage chemical decomposition of QDPSU in wastewater was minor and did not irreversibly affect electrodes.

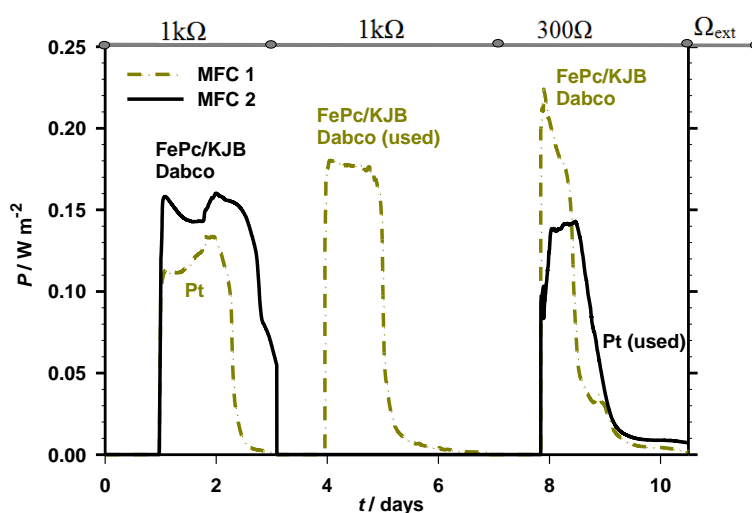


Figure 7-19. Batch performance of single chamber MFCs using Pt/C-Nafion or FePc/KJB-QDPSU air cathodes. Electrolyte; Unbuffered Wastewater, ($1.82mS\ cm^{-1}$) pH; 7.2.

MFCs were dismantled, components and biofilm gently rinsed with de-ionised water, new air cathodes inserted to remove entrained phosphate then loaded with un-supplemented primary clarifier influent. Figure 7-19 shows the results immediately thereafter. For new electrodes, FePc/KJB QDPSU ($P_{max}=0.178\text{W m}^{-2}$) outperformed Pt/C ($P_{max}=0.136\text{W m}^{-2}$).

Comparison of maximum power densities obtained over all FePc/KJB (QDPSU) batch tests were $P_{max}=0.224\text{W m}^{-2}$ (un-supplemented) and $P_{max}=0.243\text{W m}^{-2}$ (+PBS). By comparison, Pt/C Nafion produced $P_{max}=0.166\text{W m}^{-2}$ (un-supplemented) and $P_{max}=0.199\text{mW m}^{-2}$ (+PBS, not shown).

The result is perhaps surprising, considered FePc/KJB QDPSU performance was established to be higher in PBS than other mediums. Therefore unbuffered wastewater may be expected to perform significantly worse in FePc.

7.3.7 QDPSU/FePc interaction with organics in wastewater

The coulombic efficiency (ε_c) reported in Figure 7-20 for Pt/C or FePc/KJB air cathodes.

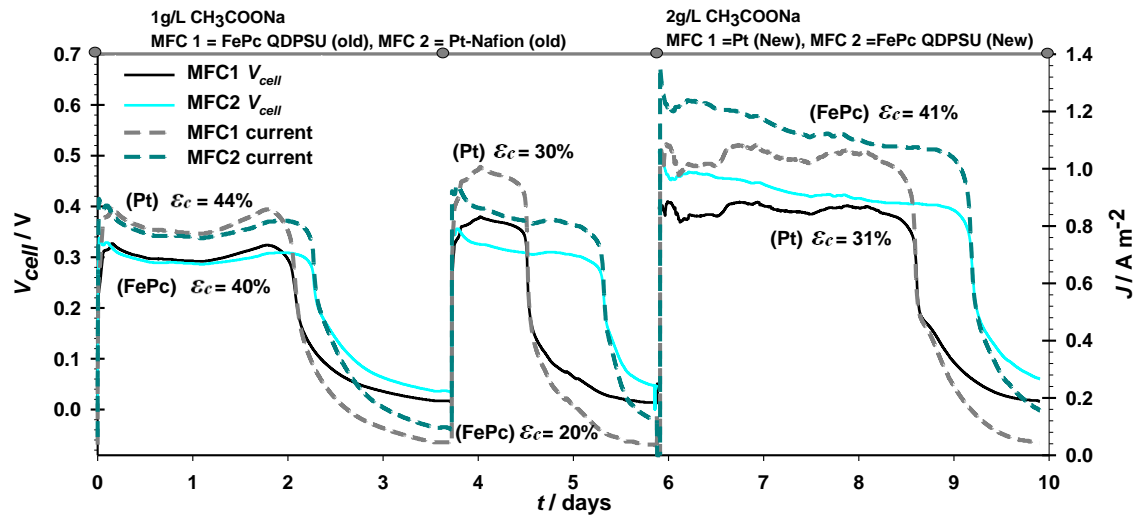


Figure 7-20. Batch performance of MFCs fed with acetate (1 or 2g/L).

$\Omega_{ext}=300\Omega$. Electrolyte; 50mM PBS + Acetate, pH 7.0.

The ε_c values of 20-40% for CH_3COONa electrolyte is largely a function of biofilm population vs. reactor volume as opposed to a cathode effect. Similar ε_c values were obtained for wastewater. The FePc/KJB QDPSU electrodes still produced a superior performance over Pt Nafion even with the presence of large quantities of CH_3COO^- .

anion. Pt performance is affected by CH_3COO^- [113, 346], though FePc QDPSU electrodes continually outperform Pt. This suggests oxygen reduction adopts the kinetics observed for PBS electrolytes when occurring in mixed PBS/ CH_3COO^- . It would not be possible for FePc/KJB QDPSU to outperform Pt if the reaction kinetics seen in pure CH_3COO^- electrolyte (Table 6-3) were apparent in PBS/ CH_3COO^- . This result shows good agreement with that seen for pyrolysed FePc/C [113].

In light of the oxygen fixing properties of QDPSU, evidence was sought for organic oxidation on the cathode surface in phosphate amended wastewater. Chemical oxygen demand (COD) content was measured for two consecutive batch cycles with a fixed external resistor ($1\text{k}\Omega$). A degree of error is anticipated on the concentration axis, due to organic solute diversity and interfering Hg complexes during titration, this error is estimated at 2.3% (g m^{-3}) at highest concentration [281], error bars have not been added so data can be easily read. As COD removal is primarily an anodic issue, biofilms were numbered and electrodes rotated across both cells. Cathode effect on COD removal has only been investigated with biocathodes, though oxidation of fermented organics can occur on Pt [28].

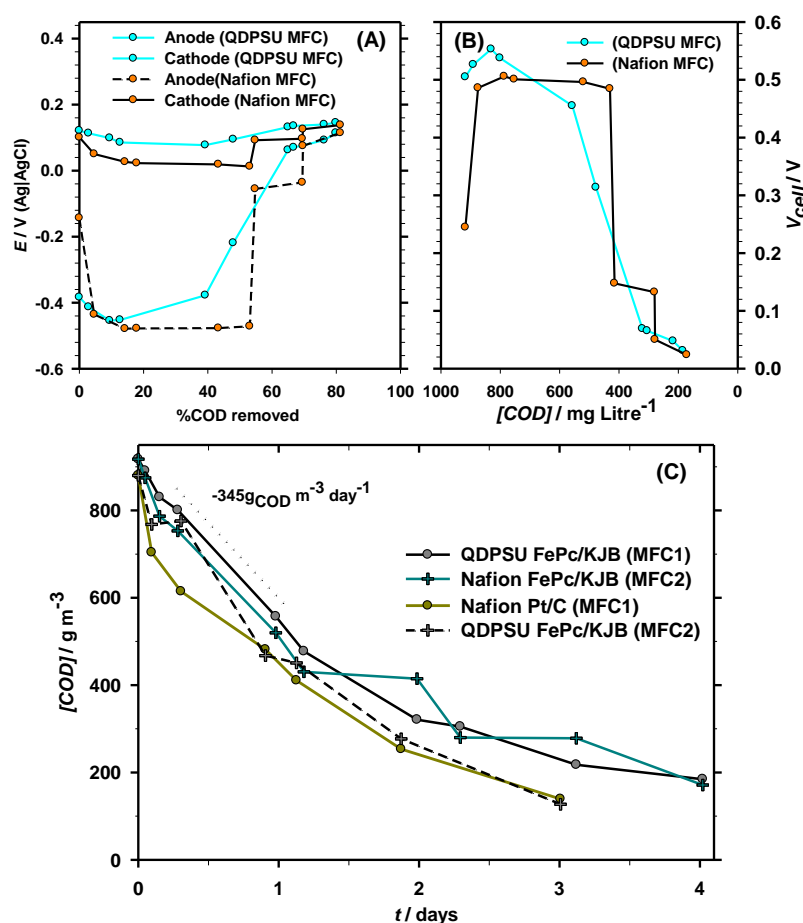


Figure 7-21. Binder and catalyst effect on COD removal. Single Chamber MFC in batch mode, open air membrane-less cathodes, $\Omega_{ext}=1k\Omega$. Graph (A) E vs. %COD removed (FePc/KJB), (B) V_{cell} vs. $[COD]$ (FePc/KJB). (C) $[COD]$ vs. time (t) for FePc/KJB and Pt. Electrolyte; wastewater amended with 50mM PBS, $6.6mS\ cm^{-1}$, pH 7.0.

At a point c.a. 50% COD removal V_{cell} decreases rapidly, this is consistent with the idea that volatile fatty acids must be replenished by hydrolysis organisms [2], and consumption by the biofilm outstrips production causing the concentration to be negligible at this point. Difference in batch time from the first cycle to second cycle can be explained by an increased degree of hydrolysis and fermentation occurring in the sealed wastewater sample container.

Initial COD removal rates were largest, reflective of initial fermented organic concentration being the highest. In the first 70 minutes removal rates ranged from $2.125\ kg_{COD}\ m^{-3}\ day^{-1}$ to $0.46\ kg_{COD}\ m^{-3}\ day^{-1}$, the highest being with Pt. The removal rate is being higher than the potential margin of error, suggesting Pt cathodes have a significant organic oxidation effect in MFCs [347]. With FePc/KJB no relation between QDPSU and COD removal could be established.

The average *OCP* of air cathodes in PBS buffered wastewater was; FePc QDPSU (0.27V), FePc Nafion (0.24V) and Pt-Nafion (0.34V). The *OCP* recorded in PBS; FePc QDPSU (0.28V), FePc Nafion (0.235V) and Pt-Nafion (0.43-0.4V). The disparity between these electrolytes with Pt/C is consistent proclivity to organic oxidation demonstrated herein.

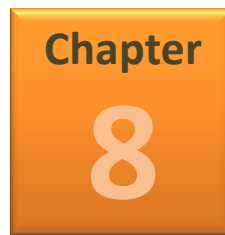
7.4 Conclusions

This study provides the first analysis of coupled electron/counter-ion diffusion rates in MFC air cathodes. Many of the conclusion are specific to semi-conductive polymer electro-catalysts and some are specific to only to FePc. However, the methodology allows a comparable means for MFC researchers to quantitatively assess process bottle-necks in real wastewater.

It was demonstrated that anion's were able to move through the catalyst layer more freely with QDPSU than Nafion or PTFE binders. This resulted in a faster diffusion of electrons from GC surface to the active sites, where reduced Fe(II)Pc is required for oxygen reduction to occur.

This approach is highly focused on kinetics and modelling for an engineering project, but the importance of electron and ion diffusion for FePc was tantamount to electrode performance producing additional resistances of $100\text{-}230\Omega\text{cm}^2$, a resistance larger than R_{ct} at potentials below 0.15V, being approximately 20% of internal resistance of the SCMFC under external load. With removal of the 3cm electrode separation this feature may comprise the majority of cell resistance. Poisoning of anion exchange groups is likely to be a severe issue even with membrane introduction. Functional anion exchange groups designed for alkali fuel cells may not compatible in MFC's. This electron propagation resistance was not observed with Nafion, showing sulfonate groups to be less susceptible to ion exchange blocking than methyl dabco. However, with Nafion R_{ct} was x6 larger at low over-potential and accounted for the poor performance in PBS half-cell tests. Thus the QDPSU anion exchange material is highly recommended for non-precious redox polymer ORR catalysts in pH7.

Conventional wisdom on air cathode design may need to be dispelled when considering the case of non-precious redox polymer catalyst air cathode design for neutral media; ultra-thin catalyst layers may be required (ie. 0.1 mg cm^{-2}), with relatively high loadings of selective anion exchange ionomers. The layer thickness and catalyst loading should be explored to balance reduced electron diffusion distance with R_{ct} and stability, with a reasonably high initial loading of catalyst required to counter catalyst de-activation. Particular attention should be paid to the interface of current collector and catalytic film. More work is recommended using this approach on thin films and air cathodes to demonstrate the stability of QDPSU relative to quaternary ammonium for MFC's.



**Chapter 8. Results - Cation and anion exchange membranes for
Microbial Fuel Cells**

8.1 Background – Factors affecting membranes in MFCs

The purpose and benefits of MFC membranes is briefly discussed in chapter 3. In this section experimental techniques for their analysis are addressed. Typically membranes are assessed with EIS by using a two chamber electrolyte system and either Pt wire's placed either side of the membrane or two reference electrodes measuring potential drop across a fixed current [254]. An important aspect of this approach is the removal of solution resistance or R_u . The membrane is usually modelled in an equivalent circuit as an impedance in series with R_u . Where specific adsorption occurs a capacitive term C_{ads} can become significant [92]. In some instances RC time constants associated with double layer ion resistance and the diffusion boundary layer are added in series to the basic membrane resistance [348]. Ohmic resistances are typically of the order 1-10 $\Omega \text{ cm}^2$ [248].

Two chambered systems are also used to analyse ion diffusion from one reservoir to another. In this chapter, the membrane has been pressed against air cathodes developed in chapter 4 and analysed with EIS. This approach aims to assess the finished MEA configuration and suitability for MFC air cathodes.

Despite the extra cost to an MFC unit, a membrane ensures the degree of biofouling present in appendix Figure A-25 can be largely avoided. Therefore in extended operation the air cathode displays the rest potential of the catalyst and not the periplasmic redox enzymes present in an aerobic biofilm.

8.2 Results - Analysis of MEA impedance spectra

8.2.1 General Nyquist plot response of MEA in pure electrolyte

In Figure 8-1 the AC impedance response of all MEA half cells is shown under cathodic polarisation.

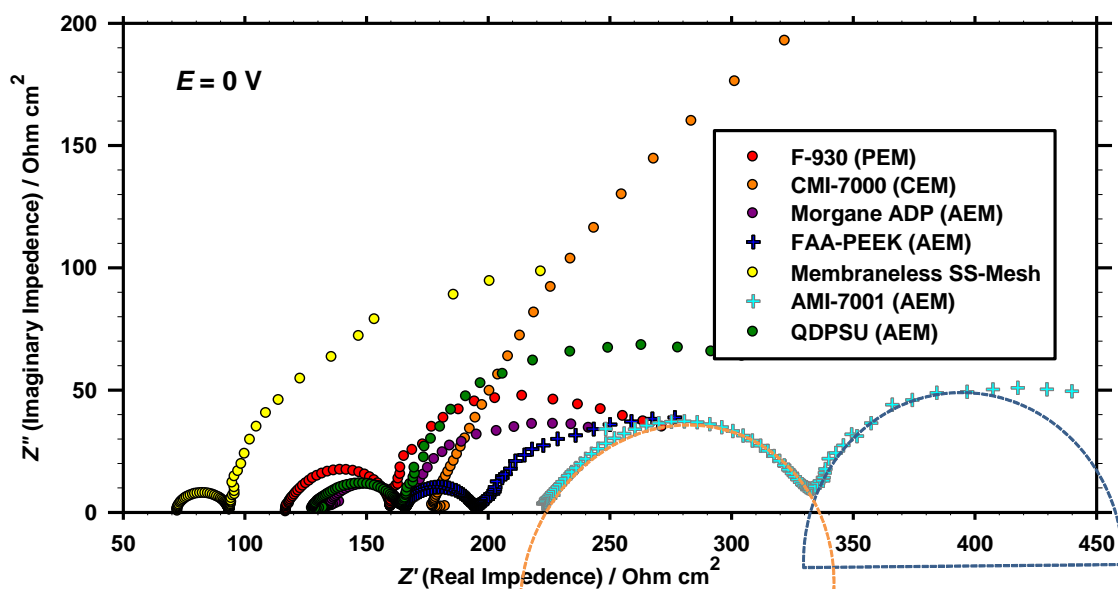


Figure 8-1. Nyquist plot of typical MEA impedance data. FePc/KJB (QDPSU) air cathodes. Orange semi-circle; HF arc. Blue semi-circle; LF arc (ORR). Electrolyte; 50mM PBS, pH 7.0.

The main features of the complex plane response are two arcs in all cases. A potential dependent LF arc was attributed to Oxygen reduction, the R_{ct} only becoming measurable with manual arc fit at potential low enough for ORR to be observed in $i-E$ plots. The HF arc was largely invariant of potential. In Figure 8-1 the Morgane ADP membrane produced the best result in PBS as the total electrode AC resistance (R_{AC}) was smallest. An annotated example of the interfacial and boundary resistances is shown in Figure 8-2 with manual arcs applied.

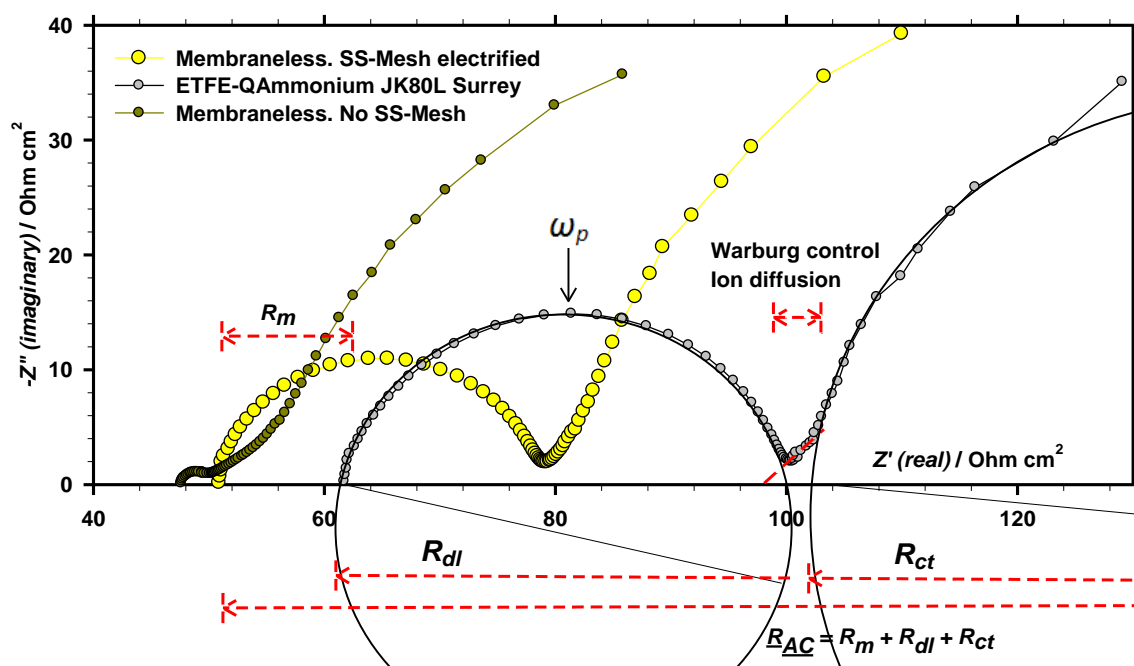


Figure 8-2. Nyquist plot of typical MEA impedance data. FePc/KJB (QDPSU) air cathodes. Red line; Warburg gradient. Orange semi-circle; high frequency arc. Blue semi-circle; low frequency ORR arc. Electrolyte; 50mM PBS, pH 7.0.

Usually R_m was determined under OCP to avoid changes in the relative presence of di-basic and mono-basic anions in the membrane. In Figure 8-2 an example of how ionic resistance (R_m) is calculated relative to the membraneless stainless steel mesh electrode. This is done as the mesh presents a similar face to the reference electrode. All other parameters (R_{dl} , R_{dbl} , R_{ct}) are compared to the meshless FePcKJB-QDPSU electrode as a $f(E)$, as an electrified mesh surface would be capable of performing faradic reactions. In the case of the meshless FePcKJB-QDPSU electrode and all MEA the mesh is unelectrified.

8.2.2 Membrane ionic resistance (R_m)

The ionic resistance in the membrane phase could be determined with Arrhenius plot. Yet the temperature sensitivity of some of the AEM ($>60^\circ\text{C}$) reduce the range from which a linear range can be obtained. Instead the half-cell MEA method (Figure 4-3) was used to obtain the values according to the data treatment illustrated in Figure 8-2. The results are compared to manufacturer reported area specific resistance ($\Omega \text{ cm}^2$) in 0.5M NaCl in Figure 8-3(A). It was established in section 8.2.1 and previous works [252, 255] that the ionic resistance is devoid of interfacial resistances, moreover that the

concentration profile is similar throughout the bulk membrane phase [255]. Therefore the area specific resistance was normalised by hydrated membrane thickness (μm) in Figure 8-3(B). The thickness was measured in dry (delivered) and hydrated states for each ion with a digital Vernier (Table A-9). The resulting term ($\Omega \text{ cm}^2 \mu\text{m}^{-1}$) exacerbated the relative difference between conductivity of each anion across the trend in membranes.

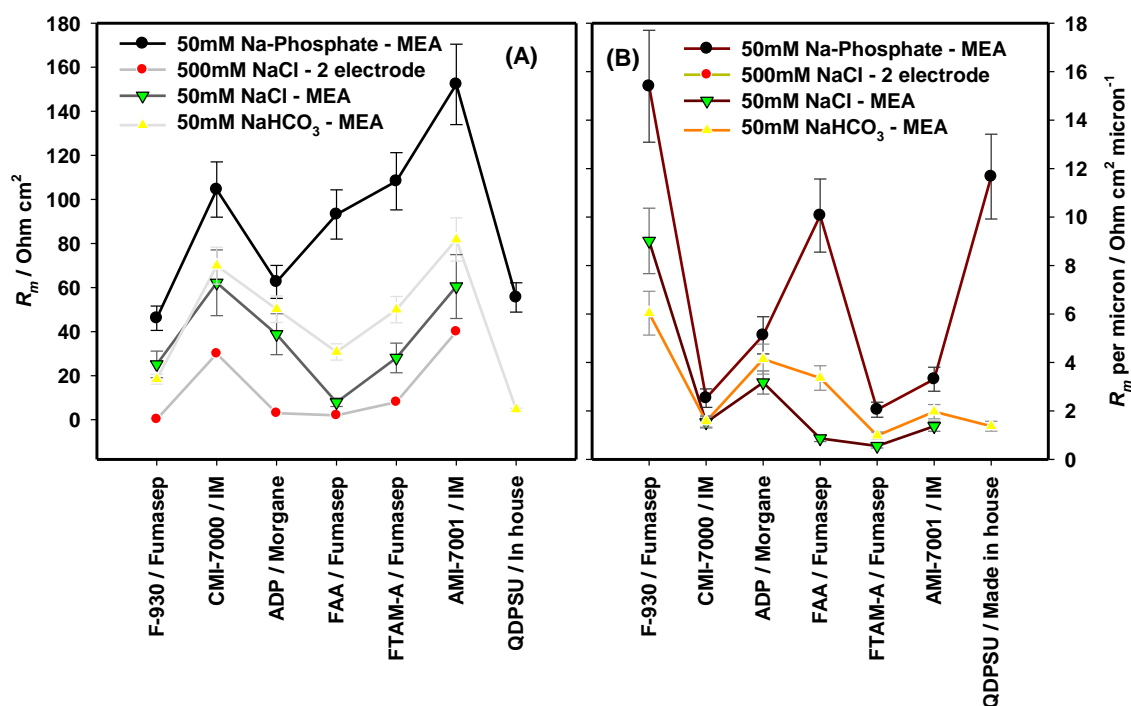


Figure 8-3. Area specific resistances and thickness normalised ASR of several membranes. Obtained from HF impedance data. Electrolyte; air sat. 50mM Na-Phosphate (pH 7.0), NaCl (pH 7.0) or NaHCO₃ (pH 7.81).

The relative trend in ionic phase conductivity (A) is the same across most membranes, in line with anticipated behaviour. A notable exception can be seen in Figure 8-3(B) in which FAA shows low chloride and bicarbonate normalised ASR but an abnormally high resistance to Phosphate ($10 \Omega \text{ cm}^2 \mu\text{m}^{-1}$) compared to the trend. As the anion exchange group (Q-Ammonium) is also used in the other membranes, the only feature unique to FAA is the PEEK backbone. The degree of through plane swelling was compared to the dry state. For FAA this was c.a. 0%, as reported by the manufacturer. The PEEK reinforcement produces a rigid polymer lattice though the 24.1% weight increase in NaCl suggests constrained diffusion channels did not produce the disproportionately high $R_m/d=10 \Omega \text{ cm}^2 \mu\text{m}^{-1}$. An alternative explanation could be the

backbone ether linkage, this is the only chemical moiety present in PEEK and absent in the other membranes. It could be hypothesised that Hydrogen bonding between H_2PO_4^- and the ether group may retard ion diffusion in the membrane.

8.2.3 *High Frequency response of MEA in pure electrolyte*

The HF arc possessed the following aspects;

- The arc width was found to be a function of ion exchange type and membrane thickness. The smallest arc was observed for FePc with and SS-mesh. And without the mesh disappeared.
- The first arc covered at larger frequency range when the membrane was added.

Plotting the intercept of the $Z''=0$ axis at different potentials conclusively proved that the $Z''=0$ intercept did not represent R_s+R_m as 1) Using the Membranes International as a comparison with a similar backbone showed the R_s+R_m value to be larger for Q-Ammonium functional groups than for Sulfonate, counter to previous works in PBS [288]. The results of the first arc were analysed as a function of bias potential to explain the response, the term infinity denotes the HF intercept and the 0 subscript the LF intercept of the arc (orange on Figure 8-1);

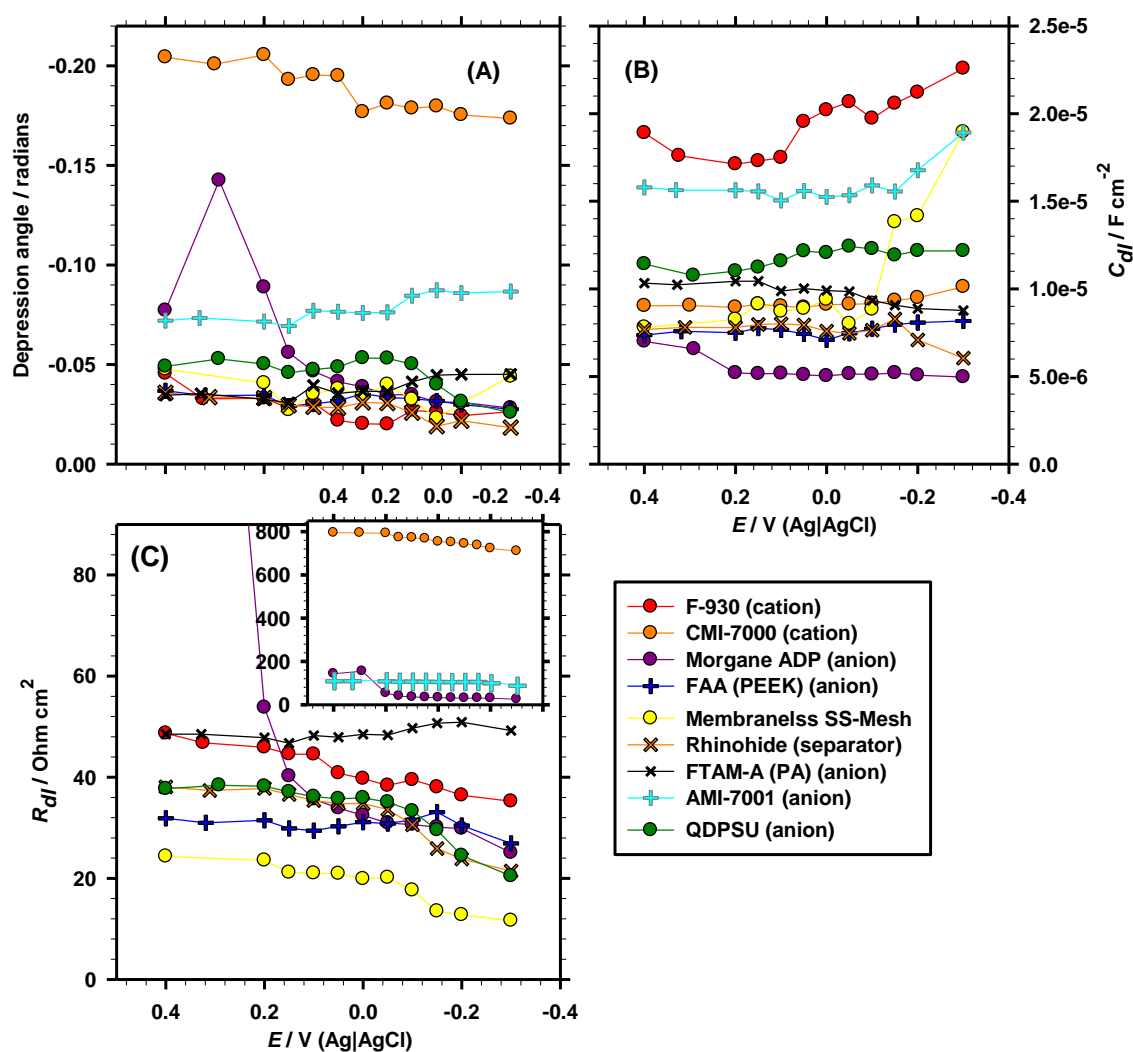


Figure 8-4. Characteristics of HF arc of MEA as a function of applied potential (x-axis in all graphs). (A) depression of the arc below $Z'=0$ axis, (B) capacitance, (C) semi-circle width at $Z''=0 \Omega$ (inset is high Y-axis values). FePc/KJB (QDPSU) air cathodes in air saturated PBS. Electrolyte; 50mM PBS, pH 7.0.

The results of the first arc as a function of E showed the following characteristics;

- The 'smoothest' membrane produced the lowest capacitance, Morgane ADP.
- The diameter of the HF arc remained largely unchanged w.r.t potential. The only membrane that was an exception was Morgane ADP. Some change was noted low potential with QDPSU-PTFE membrane.
- In the case of the F-930 membrane the MEA high frequency arc behaved as a near perfect capacitor ($N=0.999$).
- In the case of the Stainless steel mesh only the arc was heavily depressed, possibly owing to non-uniformity in the double-layer.

- The Morgane ADP membrane behaved unusually, with resistance increasing x5 between 0.1 to 0.3V and capacitance remaining relatively unchanged.

It appears as if the double layer capacitance comprises the majority of the capacitance in Figure 8-4(B). The smoother membranes produce the lowest capacitances and the lowest arc depression angle. This is borne out by the fact that the stainless steel mesh becomes electrically connected to the cathode when the membrane is removed and the depression angle is higher than many membranes.

The unusual behaviour of the Morgane ADP membrane appeared as if the R_{ct} element where somehow incorporated in the high frequency arc, the only membrane for which this was the case. The capacitive element of the high frequency arc did not significantly change with potential.

Amongst anion exchange membrane materials the R_{∞} - R_0 resistance followed the general trend of the resistance for Cl^- by manufacturers. In terms of Ω , the trend was; $\text{FAA} \approx \text{Morgane} < \text{FTAM-A} < \text{AMI-7001}$. The resistance in Table 4-1 also following this trend. However, the cation exchange membranes appear to possess significantly less selectivity to Phosphate than Cl^- . For instance the R_{∞} - R_0 value is marginally lower for F-930 in Phosphate than for FTAM-A, whereas in Cl^- it is reported as x40 smaller in F-930 due to the F-930 membrane being thin.

Direct comparison of CMI-7000 and AMI-7001 allows the effect of the anion exchange group on the HF arc to be assessed as the backbone and thickness are identical. The Q-ammonium increases capacitance by 40-60%, reduces resistance x7-8, decreases CPE depression angle by x2-2.7 closer to Warburg and further from an ideal capacitor.

This was not the case, for instance the FTAM-A membrane was the thickest membrane (500-600 μm) but performed well in comparison to the thinner anion exchange membrane AMI-7001 despite having a larger conductivity in NaCl. As information on pore volume is not provided in the products this cannot be discounted as a potential explanation. However, it did appear that Poly-styrene/divinyl benzene was not conductive to $\text{HPO}_4^{2-} / \text{H}_2\text{PO}_4^-$ diffusion.

It was found that a portion of the high frequency arc response was related to the stainless steel mesh. Adding the mesh to a bare FePc/KJB QDPSU air cathode caused an arc of $24.54 \text{ Ohm cm}^{-2}$ (OCP), invariant at potentials above $0V$ (not shown). The associated parallel CPE produced $Y^0=8.197 \text{ } \mu\text{F cm}^{-2}$. Though this capacitive arc large it is significantly increased with the introduction of a membrane (Figure 8-2). Addition of the SS-mesh reduces the R_{ct} of the oxygen reduction reaction from c.a. 430 Ohm cm^2 to only 194 Ohm cm^2 at a potential of $0V$. No significant linear Z vs. $f^{-0.5}$ region existed with or without the mesh.

8.2.4 Resistance from diffusive elements in MEA

As van Sleutels et al report ion transport may limit membrane MFC systems [249], diffusive elements were sought by plotting Z' vs. $f^{-0.5}$ as in chapter 6. This Warburg plot of the transition region between the high and low frequency arc is shown in Figure 8-5.

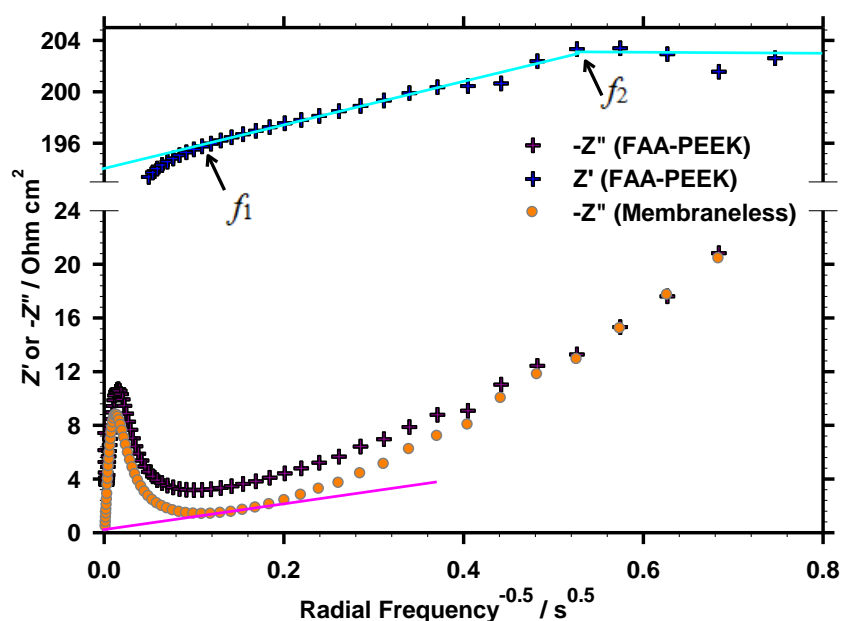


Figure 8-5. Example Warburg plot for MEA of FAA (crosses) or capacitance response without a membrane (dot). $E=0.2V$. Conditions as in Figure 8-1.

Figure 8-5 depicts an example of bounded finite diffusion occurring in the linear process as a capacitive element. The open ended diffusion element applied ubiquitously to two chamber models [251, 252, 255] is not apparent in the air cathode setup; The model depicted in Figure 2-22 shows an upward inflexion in the Z' vs $\omega^{-0.5}$ plot which is clearly not present in Figure 8-5 or any other membranes tested in this configuration.

This is to be expected considering a sustained DC flow of ions into the catalyst layer is clearly not possible. The physical interpretation of diffusion in redox films followed by adsorption holds for the membrane system. This feature was present with NaCl, Na₁₋₂PO₄ and NaHCO₃ across the majority of the 0.4>E>-0.4V potential range. The factor f_2 increases in the trend of $(D_i/f_2)^{0.5}$ being proportional to diffusion length in the thin film system. Increasing the thickness of the FePc/KJB film from 1.5μm (TFE) to c.a. 100μm (Air Cathode) results in f_2 decreasing from c.a. 500-2000 rad s⁻¹ to 14.63 rad s⁻¹ depending on ionomer. The knee frequency f_2 is in the same range for all MEA 0.63< ω <14.63 rad s⁻¹ (in PBS), differences in diffusion co-efficient can be interpreted as counter-ion diffusion through the membrane. This resistance is comparatively low (Z' =9Ω cm²) in this FAA example (PBS) but could significantly increase in MFC wastewater system where membrane or ionomer ion selectivity is lost from poisoning of the fixed charge.

8.2.5 General Equivalent Circuit

The generalised equivalent circuit (B) for FePcKJB-QDPSU AEM membrane electrode assemblies is shown in Figure 8-6. This circuit was applicable for all mono-anionic experiments Cl⁻, H₂PO₄⁻/HPO₄²⁻ and HCO₃⁻ at all potentials at which ORR is observed. An example fit using the iteration programme in Nova software is displayed (A).

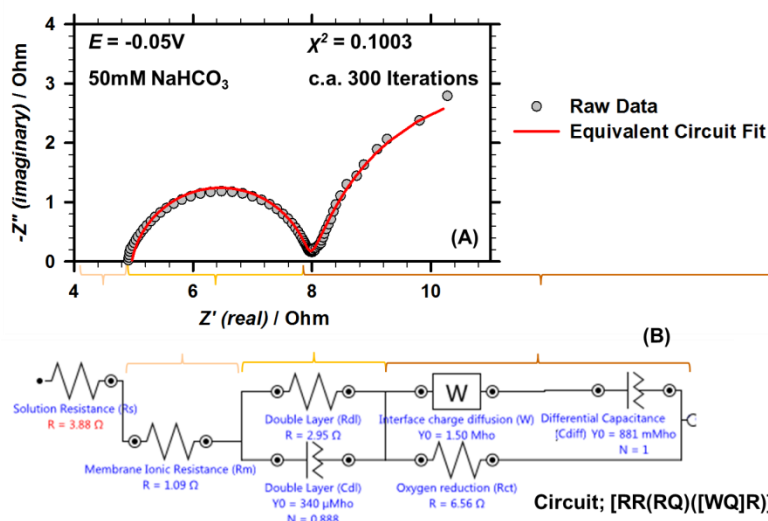


Figure 8-6. Equivalent circuit (B) and fit of data (A) of FePcKJB-QDPSU air cathodes. Example is for FAA membrane. Electrolyte; air saturated 50mM NaHCO₃, pH7.91.

It is clear from Figure 8-6 that the two time constants in (A) are separated and an additional unit must be applied. The linearity of this region $-dZ'/dZ=1$ in the nyquist plot again lends itself to a diffusive process as in the previous chapter. Open ended diffusion element behaviour could occur as the test is not performed under de-aerated conditions. If so this unit is obscured by the charge transfer element (R_{ct}) which is the only component that is strongly potential dependent. The low value of the C_{dl} 'N' exponent (<0.95) did not occur when mesh was not used or thicker membranes. Compression from the stainless steel mesh must then disrupt this boundary resistance on the electrolyte interface.

8.3 MEA performance in artificial wastewater

8.3.1 Polarisation curves

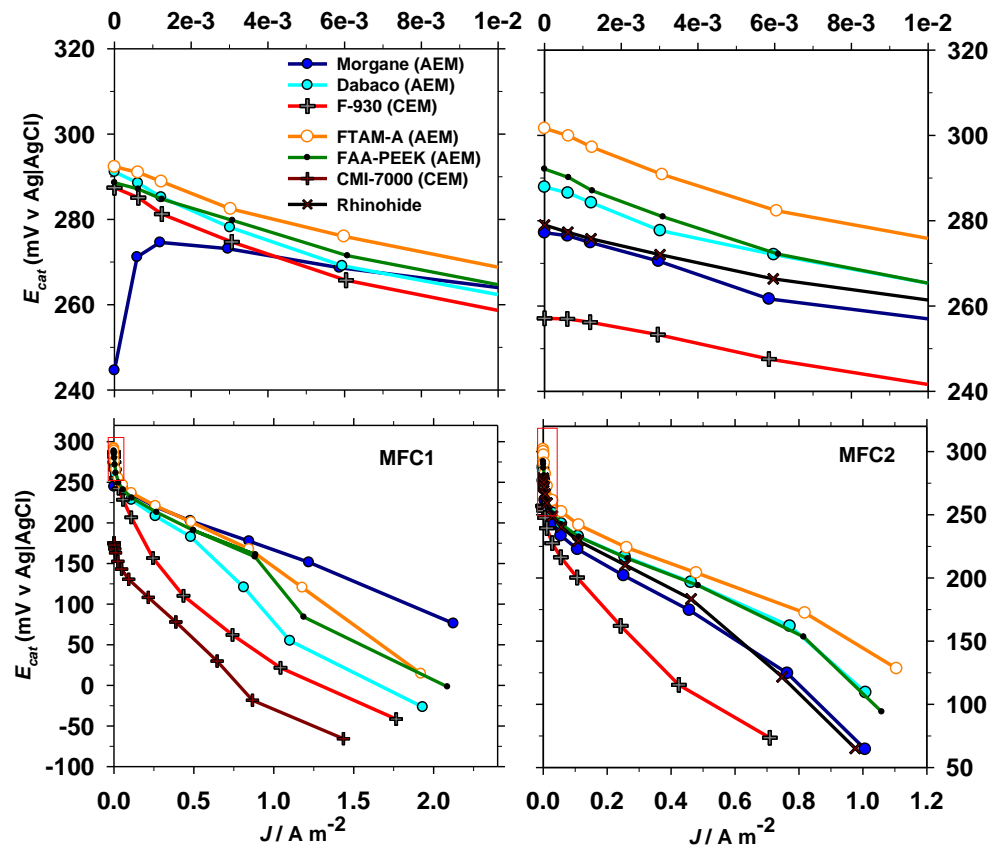


Figure 8-7. E_{cat} vs J polarisation curves of MFC utilising MEA listed in Table 4-1 and FePc/KJB QDPSU air cathodes. Polarisations over two MFCs, activation region in red box enlarged (top). Electrolyte; 50mM PBS + 1g/L CH₃COONa, pH7.

In Figure 8-7 it is apparent that the initial cathode potential drop from activation ($<2 \times 10^{-3} \text{ A m}^{-2}$ on Figure 8-7) appeared not to be significantly affected by the membrane. As current marginally increased the CEM membranes incurred a large degree of overpotential. This drop was not linear in CEM and weakly linear in AEM, suggesting an effect other than ion diffusion resistance was present, such as a space charge capacitance. It was noted that the cathode potential of the cation exchange membranes was still marginally decreasing after 20 minutes of stabilisation. This was not previously observed with membraneless electrodes (ie. Figure 7-16) and was not observed with anion exchange membranes. As this is a low frequency capacitance it is not described in Figure 8-4. The linear E - J responses at $J > 0.1 \text{ A m}^{-2}$ seen with membraneless air cathodes in Figure 7-16 were not observed with membranes.

8.3.2 *EIS spectra of batch fed MFC*

Single Chamber MFC were constructed operated with a permanent reference electrode and fed with artificial wastewater as per Figure 4-1(B) with the addition of a membrane and steel mesh. This cathode configuration produced an identical MEA to those used to obtain Half-Cell EIS data Figure 4-3. Cells were injected with fresh AWW and left at OCP for 30min to attain a stable E_{an} prior to EIS characterization (Figure 8-8). At the end of the same batch cycle ($V_{cell} < 0.05 \text{ V}$) the cells were left at 30 min to attain OCP and the spectra in (C) and (D) recorded.

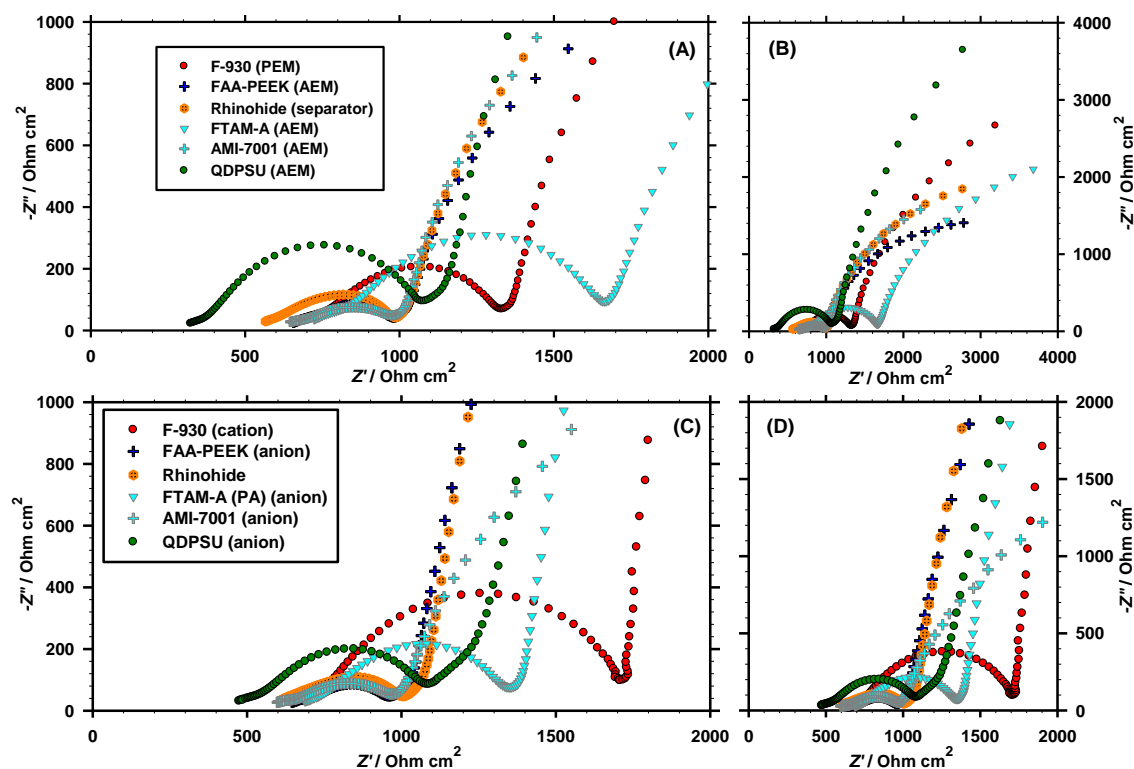


Figure 8-8. Nyquist plot of full MFC utilising MEA.

$E=OCP$. EIS spectra taken at (A) and (B) start of batch cycle, or (C) and (D) end of same batch cycle. (A) and (C) HF response, (B) and (D) LF response. Electrolyte; 50mM PBS+1g/L CH_3COONa , pH7.

In comparison to R_{dl} values obtained in the half cell experiment (Figure 8-4) it is clear that the interfacial impedance in Figure 8-8 has increased for each cell. The effect of $[CH_3OOO^-]=1g/L$ on the HF response (A) was a 0-20% increase in R_{dl} using MEA of Quaternary Ammonium or Dabco relative to acetate depleted conditions (C). This indicates acetate co-ordination to the positive charges at the membrane interface may pose small cell resistance, as ionic conductivity was consistent over the batch. In pure PBS, at open circuit $E_{cat}>0.2V$ was recorded for each MEA. After 30 minutes of stabilization, OCP prior to (A) and (C) was; QDPSU (0.1V), Rhinohide (0.09V), AMI-7001 (0.19V), FTAM-A (0.13V), F-930 (0.13V), FAA (0.19V), indicating varying degrees of acetate cross-over and local alkalinity. The LF response in (B) and (D) is less useful to analyse as a result.

8.3.3 Membrane SCMFC batch performance

During periods of 24 illumination a red microbe appeared to thrive under acetate-nutrient inoculum [349], as seen in previous single chamber MFC studies [350]. As these microbes are capable of photoheterotrophic and photoautotrophic growth [349] then they may use acetate or photosynthesise depending on conditions. The bacteria were found to have an extremely detrimental effect on COD. The usual 80-90% COD observed in single chamber MFCs loaded with acetate decreased with long batch cycles.

Table 8-1. Peak E_{cat} and V_{cell} obtained under fixed external resistance with FePc/KJB (QDPSU) air cathodes and a membrane strapped down with SS304 mesh. Information obtained following polarisation curves. Electrodes connected by fixed resistors of a) 308 Ω and b) 330 Ω . Electrolyte; 50mM PBS+1g/L CH₃COONa, pH 7.0.

Membrane / Manufacturer	MFC1 - 308 Ω		MFC2 - 330 Ω	
	E_{cat} / mV	V_{cell} / mV	E_{cat} / mV	V_{cell} / mV
Cation Exchange Membranes				
F-930 / Fumatech	-28	344	50	268
CMI-7000 / Membranes International	-27	301	-19	306
Anion Exchange Membranes				
AMI-7001 / Membranes International	16	350	49	282
FTAM-A (PA) / Fumatech	54	389	91	267
FAA (PEEK) / Fumatech	27	379	82	256
Morgane ADP® / Solvay	127	440	-	-
QDPSU / made in house	48	402	142	310
Separator				
Rhinohide / Entek	-	-	58	400

Table 8-2. Averaged peak E_{cat} and V_{cell} obtained over batch cycles over two MFC.MFC with FePc/KJB (QDPSU) air cathodes and membrane. Fixed external resistor of 308 Ω or 330 Ω . Electrolyte; 50mM PBS+1g/L CH₃COONa, pH 7.0.

Membrane / Manufacturer	E_{cat}	V_{cell}	#batch cycles	Standard Deviation (σ)	
	/ mV	/ mV		E_{cat} / mV	V_{cell} / mV
Cation Exchange Material					
F-930 / Fumatech	-49	302	14	30	47
CMI-7000 / National Membranes	N/A	N/A	0	N/A	N/A
Anion Exchange Material					
FTAM-A (PA) / Fumatech	-23	289	13	31	20
FAA (PEEK) / Fumatech	0	324	12	50	49
AMI-7001 / National Membranes	-54	309	6	33	31
Morgane ADP® / Solvay	N/A	N/A	0	N/A	N/A
QDPSU / made in house	-63	307	13	33	40
Separator					
Rhinohide / Entek	-121	257	13	74	89

In Table 8-2 the peak stabilised V_{cell} over a batch cycle and the corresponding cathode potential reported [265]. Average and standard deviation of the sample size over all batch cycles make the results less subjective than peak E_p and V_{cell} in the single cycle recorded in Figure 8-5. In most results the standard deviation for E_{cat} is approximate to that for V_{cell} , indicating biofilm variance is negated over repeated batch cycles.

From this data it can be seen that the rank of performance is FAA>FTAM-A>F-930 \approx QDPSU \approx AMI-7000>Rhinohide. With the exception of the QDPSU membrane which performed marginally worse than anticipated an improved performance with thin anion exchange membranes can be seen.

It was observed that the Rhinohide membranes were relatively slow to reach equilibrium. In other words, after inserting fresh electrolyte maximum V_{cell} was attained before E_{cat} had finished decreasing. This can be explained by the low distribution of pores on the surface of the Rhinohide (25nm diameter) causing a long time for the electroneutrality to be established. Interestingly this was not observed for F-930, where the V_{cell} max corresponded to a relatively stable cathode potential. As such, the V_{cell} values for Rhinohide membranes may be over approximated by 50-60mV in Table 8-2, this effect was less than 30mV in all other membranes. For instance in AMI-7000 the

average value of the minimum cathode potential corresponded to an average cell voltage only 17mV lower.

The presence of CH_3COO^- providing an alternate charge carrier, thought diffusion of this species is anticipated to be sluggish in comparison to OH^- and monobasic Phosphate. This may be the reason why the result shows good comparability with the EIS and Polarisation curve results.

8.3.4 EIS half-cell as a predictor of MFC batch performance

The data taken from Table 8-2 for repeat batch cycles in acetate phosphate buffered artificial wastewater was expressed as peak current density and plotted against total impedance recorded during AC Impedance spectroscopy (R_{AC}) in PBS. The graphical representation is seen in Figure 8-9 is obtained. R_{AC} was obtained from extrapolation of the LF arc to $-Z''=0$ Ohms at an applied potential approximate to P_{max} in 8.2.1 ($E=-0.05\text{V}$).

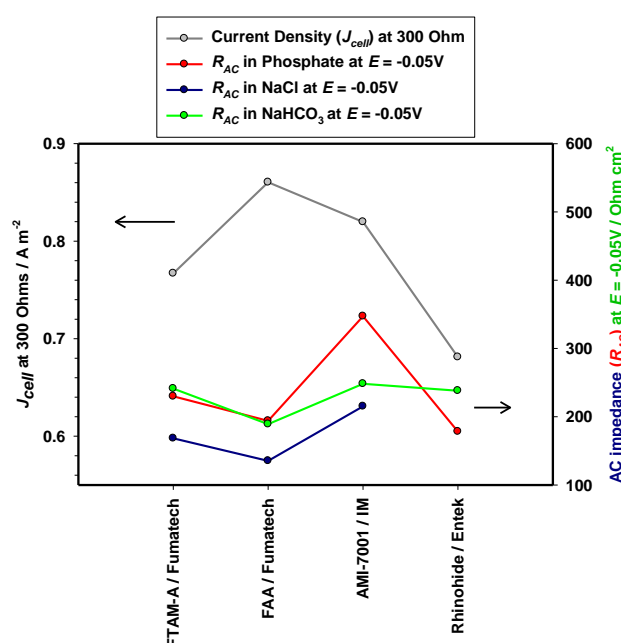


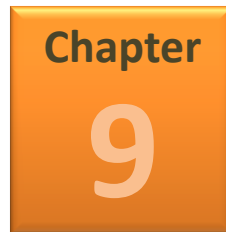
Figure 8-9. Comparison of half-cell R_{AC} obtained from EIS and the batch MFC performance using identical MEA. R_{AC} at $E=-0.05\text{V}$.

No comparison to full MFC can be made as EIS data was collected at *OCP*. The comparison with half-cell EIS allows biofilm variance to be discounted.

8.4 Conclusion

With the thin cation exchange membranes a significant space charge capacitance produced polarisation curves without an ohmic drop region. The EIS data showed that the high frequency response of the thin F-930 membrane was relatively in-exorbitant in terms of resistance. By contrast the thick Polystyrene-Divinyl benzene membranes produced a significant low frequency response suggesting significant inhibitory adsorption and blocking with this back-bone material. As such it's use is not recommended.

More work should be done to assess whether the cation exchange membrane is simply incompatible with an anion exchange ionomer catalyst layer. It must be conceded that the interface between QDPSU ionomer catalyst layer and a cation exchange membrane may cause a charge interface and 'trapped' deposits in a real wastewater MFC system.



Chapter 9. Conclusions and recommendations for further work

9.1 Recommendations for further work

While the ligand itself was not improved in this thesis, it has been demonstrated that the nature of polymeric redox catalysts can be increased without altering the chemistry, but improving the ion and charge transfer throughout the catalyst layer. The work on optimal ionomer loadings and catalyst layer thickness established for nano-particles in PEMFC and AFC is possibly not applicable to polymeric electrocatalysts and most certainly not applicable to their implementation in MFC's with low ionic concentration electrolytes. It has been demonstrated that superior anion exchange materials will be susceptible to decrease of trans-membrane ion diffusion rates with wastewater. Other more established anion exchange ionomers (eg. Quaternary Ammonium) can feasibly be equally susceptible to wastewater pollutants. Therefore the author recommends EIS study on cathodes exposed to continuous flow of wastewater to ascertain whether this process is irreversible and these superior anion selective materials could be used in a finalised design.

In general, materials that scavenge oxygen by O_2 co-ordination may become a promising avenue of ORR research. If the dioxygen bond strength is decreased by coating a metal surface with a planar O_2 chelating molecule (such as Dabco), reaction kinetics can be improved. This could provide an alternative to bi-metallic catalysts for obtaining the optimum binding energy point in a volcano plot, as suggested from the promising result on Platinum in this thesis (Table 5-1 vs Table 6-1). Combination of oxygen scavengers with activated carbon may produce cheap and simple air cathodes. The influence of planar O_2 chelator covering pure metal surfaces could be analysed from the perspective of volcano plots as a new avenue of ORR research, as suggested by the promising results for Pt.

The interest in reaction pathways expressed in this thesis was evolved from the discovery of H_2O_2 release at high potential in neutral media. With specific ligand design and systematic testing of film preparation a polymer configuration may be produced that exclusively yields H_2O_2 at potentials higher still than Cobalt Phthalocyanine. The effect of solution anion will be important to such a process. In certain settings (eg. Medical), H_2O_2 is required to be generated in-situ due to its short shelf-life. An electrocatalyst that would generate oxidative sterilant's with microelectrodes could prove useful.

9.2 Capital cost of materials

Rozendal et al state that 85% of the MFC capital cost is currently (2008) incurred by the membrane and cathode [351], stating a predicted cost of optimised membrane and electrodes of €10 m⁻² and €5 m⁻² respectively. While the FePc/KJB QDPSU catalyst layer of the non-precious metal cathode is within this target range (£1.24 m⁻²), the membrane is still outside.

Table 9-1. Cost analysis of materials discussed in this thesis. Price estimates (£ m⁻²) for catalysts, ionomers and ancillary equipment. Key (s) solid, (l) liquid form.

Material / <i>Supplier</i>	Lab-scale material price / £ kg ⁻¹ (s) or £ L ⁻¹ (l)	Bulk-scale material price ^a / £ kg ⁻¹ (s) or £ L ⁻¹ (l)	Required Use / g m ⁻²	Price / £ m ⁻²	<i>F_{improv.}</i> / <i>Control</i>	Factor	Figure / <i>Table</i>
Catalyst							
Pt/C (20% wt.) / <i>Alfa Aesar</i>	618000	20000 °	25	200	8.8 / <i>KJB</i> [‡]	<i>J at E = -0.1V</i>	Table 5-1.
KJB Carbon / <i>Cabot</i>	N/A	47	10	0.47	N/A		
FePc / <i>Alfa Aesar</i>	6140	6	10	0.06	1.28 / <i>Pt/C</i> [‡]		
Membrane/Ionomer							
Nafion ionomer / <i>Sigma</i>	3852 _(l)	N/A	2 [‡]	3.85	1.86 / <i>PTFE</i> [‡]	<i>J at E = 0.15V</i>	Figure 6-16.
PTFE resin / <i>Sigma</i>		4.97 _(s)	2 [‡]	0.11	N/A		
QDPSU / <i>Made in house</i>	8 _(s)		2 [‡]	0.016	7.37 / <i>Nafion</i> [‡]		
Ancillary equipment							
Carbon Paper (20% PTFE) / <i>Toray</i>	N/A	N/A	N/A	481	N/A		
Carbon Paper (P75T Hydrophobic) / <i>Avcarb</i>	N/A	N/A	N/A	323	N/A		
Generic Activated Carbon paper + PTFE	N/A	N/A	N/A	4	N/A		
Membrane Electrode Assembly							
(Membraneless) FePc QDPSU / <i>In house</i>	N/A	N/A	N/A	482	2.4 / <i>FePc Nafion</i>	<i>R_{dl}+R_{ct} at E=0.1V</i>	Figure A-21
(AMI-7001) FePc QDPSU / <i>In house</i>	N/A	N/A	N/A	543	0.777 / <i>PEM</i>	<i>R_m+R_{dl}+R_{ct} at E=0.1V</i>	Figure 8-9
(Rhinohide) FePc QDPSU / <i>In house</i>	N/A	N/A	N/A	495	1.4 / <i>PEM</i>		
(FTAM-A) FePc QDPSU / <i>In house</i>	N/A	N/A	N/A	759	1.28 / <i>PEM</i>		

Alibaba.com was used to source a bulk price of a generic lead/acid battery separator, H₂Pc pigment (Fe²⁺ chelation), PTFE and generic activated carbon paper. Industrial pigments being the cheapest source of Phthalocyanine, FePc is not as widely used as H₂Pc is widely available. Dissolving in DMSO with FeSO₄ until saturated will cause FePc crystals to deposit.

9.3 Closing comments on cathode development

The development of non-precious cathode catalysts attracts a large amount of research funding. The development is the charge primarily of chemical engineers as opposed to chemists. The common approach is in bimetallic synthesis and non-precious pyrolysis precursors and conditions. With a few exceptions [32, 195, 196, 352], very little effort is expended in the direction of controlled ligand design. This is in part due to the limited stability reported for these moieties, and in part due to the limited stability of chelating complexes in nucleophilic (OH^-) or oxidising (H^+) environments. The primary aim of chelation is to increase the oxidation potential and stabilise the metal.

9.4 Closing comments on balance of the MFC

In consideration of a finalised design for MFCs an eye must always be kept on the cost. The appeal of sophisticated control systems for maximal power output may not be justifiable if the MFCs are stacked in series. In this instance a control system requiring a reference electrode would be required for every anode-cathode array, controlling anode potential or O_2 diffusion into the cell. MFCs are primarily a COD treatment technology with the potential to remove pollutants more effectively than even the anaerobic upstream baffled reactor (UASB). It may be deemed that the electricity generated from MFC stacks is not of a 'harvestable' quantity and the cells may be run at a fixed external resistance with no energy recovery. In this instance the anode and cathode may simply be short circuited and oxygen diffusion into the cell controlled until a suitable anode biofilm has developed. If this be the case then MFC designers should be wary of an upper potential limit for the anode [19], beyond which exoelectrogens will not grow during the start-up period when no net reaction occurs on the anode, thus adopting the potential of the cathode in air. As such, a cathode catalyst with an extremely low activation energy (eg. Bilirubin Oxidase, $\text{OCP}=0.65\text{V}$ vs. $\text{Ag}|\text{AgCl}$ [173]) may cause the biofilm never to develop if the anode and cathode are simply short-circuited. Aelterman et al established that 0V ($\text{Ag}|\text{AgCl}$) was not too high to stop formation of an anode biofilm [20]. An extension of this study with increments of up to +0.6V ($\text{Ag}|\text{AgCl}$) will allow MFC scale-up engineers to assess what the maximum potential an anode biofilm could withstand in the initial growth stages, should a superior cathode catalyst be implemented and the cell started at short circuit. Thus they will know

whether design consideration such as oxygen constraint should be factored into the start-up phase.

For a suitable power density the ‘sandwich’ type MFC stack is likely to be applied. In this case, a suitably inexpensive membrane will separate the anode-cathode pairs. For this design a carbon cathode could not be used. The amount of H_2O_2 generated by 2e^- ORR would degrade almost all known polymer materials, causing the need for regular maintenance and replacement. As such an inexpensive and robust 4e^- catalyst is sought. The reaction should be facile with electron transfer incurring the smallest of resistances. As such a superior tafel slope ($25 < |b_c| < 35 \text{ mV dec}^{-1}$) should be associated with the 4e^- ORR reaction. This gives macrocycles the edge over carbon or alloy catalysts where the rate determining step involves a H^+ or complex cleavage of a bond ($50 < |b_c| < 120 \text{ mV dec}^{-1}$). Combining this edge with a stabilising chemistry or MFC architecture will ensure its implementation into a commercial scale MFC plant.

Chapter

10

Chapter 10. Appendices

10.1 Derivations

10.1.1 Derivation of tafel slope equation

Relating to Eq.2-8 it is clear that the symmetry factor of the rate determining reaction is produced by Eq.A-1.

$$\beta_c = \Delta\phi_{VT} / \Delta\phi_{VW} \quad (\text{Eq.A-1})$$

Using this equation in Eq.2-8 the single rate determining step portion of the Eq.2-8 becomes Eq.A-2

$$\Delta\overline{G}^0 = \sum_i Z_{RV} F \Delta\phi_{RV} + Z_{VW} F \beta_c \phi_{VT} \quad (\text{Eq.A-2})$$

Which is re-organised to relate the inner potentials to the metal surface ϕ_m , using the term n_c to describe the no. of electrons transferred prior to the RDS and considering only electrons yields Eq.A-3. In this equation the terms n_{RV}/n_c and n_{VW}/n_c describe the number of electrons transferred before and during the RDS respectively from surface to bulk solution. Then substituting with Eq.2-9 generates Eq.A-4. It is this equation which simplifies to Eq.2-18, provided all electrons and charges traverse the total double layer [36].

$$\Delta\overline{G}^0 = \frac{n_{RV}}{n_c} F(\phi_s - \phi_{bulk}) + \frac{n_{VW}}{n_c} F \beta_c (\phi_s - \phi_{bulk}) \quad (\text{Eq.A-3})$$

$$\frac{n_{RV}}{n_c} F(\phi_s - \phi_{bulk}) + \frac{n_{VW}}{n_c} F \beta_c (\phi_s - \phi_{bulk}) = -RT \ln(i) + C \quad (\text{Eq.A-4})$$

The term $(\phi_s - \phi_{bulk})/\ln i$ is not akin to $|b_c|$ which uses \log_{10} as opposed to the natural logarithm (\ln). Hence the multiplication factor of 2.303 is applied to convert $(\phi_s - \phi_{bulk})/\ln(i)$ to $(\phi_s - \phi_{bulk})/\log_{10}(I)$.

10.1.2 Derivation of Cottrell equation

After a step in applied potential sufficient to initiate a reaction, the concentration of electroactive species (C) at a given distance (x) from the electrode surface is a function

of time (t) produces the linear diffusion equation $\partial C_0(x,t)/\partial t = D \partial^2 C(x,t)/\partial x^2$. The three boundary conditions of t , x and C are...

$$C(0,t)=0 \text{ (for } t > 0) \quad \text{semi-infinite diffusion} \quad (\text{Eq.A-5})$$

$$C_0 = C(x,0) \quad \text{initial condition} \quad (\text{Eq.A-6})$$

$$\lim_{x \rightarrow \infty} C(x,t) = C_0 \quad \text{after E step} \quad (\text{Eq.A-7})$$

Performing Laplace transform on (t) we obtain

$$s\bar{C}(x,s) - C_0 = D \frac{d^2 \bar{C}(x,s)}{dx^2} \quad (\text{Eq.A-8})$$

$$\frac{d^2 \bar{C}(x,s)}{dx^2} - \frac{s}{D} \bar{C}(x,s) = \frac{C_0}{D} \quad (\text{Eq.A-9})$$

The ordinary differential equations above can be solved using a boundary condition derived in [35] from a similar circuit where “ s ” is set to zero. In this derivation A' and B' are obtained from expanded Laplace transform treatment of constant A and B .

$$C(x) = \frac{b}{a^2} + A'e^{-ax} + B'e^{ax} \quad (\text{Eq.A-10})$$

Inputting this equation into Eq.A-9 produces Eq.A-11

$$\bar{C}(x,s) = \frac{C_0}{s} + A'(s) \exp\left[-(s/D)^{0.5} x\right] + B'(s) \exp\left[(s/D)^{0.5} x\right] \quad (\text{Eq.A-11})$$

The limit of semi-infinite diffusion becomes

$$\lim_{x \rightarrow \infty} \bar{C}(x,s) = C_0/s \quad (\text{Eq.A-12})$$

Inputting $B'(s)=0$ for the conditions at hand.

$$\bar{C}(x,s) = \frac{C_0}{s} + A'(s) \exp\left[-(s/D)^{0.5} x\right] \quad (\text{Eq.A-13})$$

The conditions $\bar{C}(x,s)$ and $C(x,t)$ depend on the third boundary condition. The application of conditions $\lim_{x \rightarrow \infty} C(x,t) = C_0$ produces Eq.A-14.

$$\bar{C}(x,s) = \frac{C_0}{s} - \frac{C_0}{s} \exp\left[-x(s/D)\right] \quad (\text{Eq.A-14})$$

A Laplace transform of the term relating proportionality of flux of material to the electrode to current (Eq.2-35) produces Eq.A-15.

$$\frac{\bar{i}(s)}{nFA} = D \left[\frac{\partial \bar{C}(x,s)}{\partial x} \right]_{x=0} \quad (\text{Eq.A-15})$$

The derivative term in Eq.A-15 can be evaluated with Eq.A-14 with substitution yielding Eq.A-16.

$$\bar{i}(s) = \frac{nFAD^{0.5}C_0}{s^{0.5}} \quad (\text{Eq.A-16})$$

The Inverse produces the current-time response of the Cottrell equation (Eq.2-34) applicable for a potential sweep on a planar electrode under diffusion control.

10.1.3 Derivation of the Levich equation

The velocity of fluid approaching the disc is given by the sum of laminar velocity in each direction according to Eq.A-17.

$$V = \mu_1 v_r + \mu_2 v_y + \mu_3 v_\phi \quad (\text{Eq.A-17})$$

In this instance μ_1 , μ_2 , μ_3 are unit vectors in the positive direction of r , y and ϕ respectively at a certain co-ordinate relative to the centre of the disc surface. “ y ” is the distance from the RDE/RRDE surface (cm), v_x , v_y and v_z are fluid velocities (cm s^{-1}) in

the 3D plane of x, y and z. “ r ” is the radial distance from the centre of the electrode (cm), and ϕ is the electrical potential. C does not vary with ϕ provided the flow is symmetrical and perpendicular to the electrode. After a potential step at steady state ($\omega=0$ rpm) in the mass transfer control region, the transient decays to a steady value, contrary to unstirred solution, $\partial C / \partial t = 0$. The steady state laplacian operator is derived at length elsewhere, but the result is Eq.A-18 in the case of a reduction.

$$\frac{\partial C_{Ox}}{\partial t} = D_{Ox} \nabla^2 C_{Ox} - v \cdot \nabla C_{Ox} \quad (\text{Eq.A-18})$$

Where ∇^2 is the laplacian operator $\partial^2 / \partial x^2$, where x is the distance in the plane of the diffusion band. Writing Eq.A-18 in terms of reaction cylindrical co-ordinates for steady state Eq.A-19 is obtained.

$$v_r \left(\frac{\partial C}{\partial r} \right) + \frac{v_\theta}{r} \left(\frac{\partial C}{\partial \phi} \right) + v_y \left(\frac{\partial C}{\partial y} \right) = D \left[\frac{\partial^2 C}{\partial y^2} + \frac{\partial^2 C}{\partial r^2} + \frac{1}{r} \frac{\partial C}{\partial r} + \frac{1}{r^2} \left(\frac{\partial^2 C}{\partial \phi^2} \right) \right] \quad (\text{Eq.A-19})$$

The limiting current condition at $y = 0$, $C=0$ and $\lim_{y \rightarrow \infty} C = C_0$. Assuming that $C \neq f(\phi)$ and $v_y \neq f(r)$. so the portion $\partial C / \partial \phi = \partial^2 C / \partial \phi^2 = 0$ the situation across the face of the disc is $\partial C / \partial r = 0$, in other words reactant concentration does not change across the face of the disc or at any point the same distance from the disc centre, allowing significant simplification in (Eq.A-20).

$$v_y = \left(\frac{\partial C}{\partial y} \right) = D \frac{\partial^2 C}{\partial y^2} \quad (\text{Eq.A-20})$$

Kármán and Cochran's [353] treatment was described by Levich [55], in which laminar velocities are reported for the y and r ordinate, Eq.A-22 and Eq.A-23. This approach is based on the Schmidt number (S_c) for a known substrate in a known solute (section 10.2.5.) and is an approximation of Eq.A-21 [54], where only the first term has been expanded.

$$v_y = (\tilde{\omega} \nu)^{0.5} \left(-0.51023 \left(\left(\frac{\tilde{\omega}}{\nu} \right)^{0.5} y \right)^2 + \frac{1}{3} \left(\frac{\tilde{\omega}}{\nu} \right)^{3/2} y^3 - 0.10265 \left(\frac{\tilde{\omega}}{\nu} \right)^2 y^4 \right) \quad (\text{Eq.A-21})$$

$$v_y = (\tilde{\omega}v)^{0.5} \left(-0.51023 \left((\tilde{\omega}/v)^{0.5} y \right)^2 \right) = -0.51 \tilde{\omega}^{3/2} v^{-1/2} y^2 \quad (\text{Eq.A-22})$$

$$v_r = r \tilde{\omega} \left(-0.51023 \left((\tilde{\omega}/v)^{0.5} y \right) \right) = 0.51 \tilde{\omega}^{3/2} v^{-1/2} r y \quad (\text{Eq.A-23})$$

Substituting Eq.A-22 into Eq.A-20 produces Eq.A-24. Where $B = D_0 \omega^{-3/2} v^{1/2} / 0.51$

$$\frac{\partial^2 C}{\partial y^2} = \frac{-y^2}{B} \frac{\partial C}{\partial y} \quad (\text{Eq.A-24})$$

Letting $M = \partial C / \partial y$ to make $\partial M / \partial y = \partial^2 C / \partial y^2$ at $y=0$, $M=M_0 = (\partial C / \partial y)_{y=0}$, then Eq.A-24 becomes..

$$\frac{\partial M}{\partial y} = \left(\frac{-y^2}{B} \right) M \quad (\text{Eq.A-25})$$

$$\int_{M_0}^M \left(\frac{dM}{M} \right) = \left(\frac{-1}{B} \right) \int_0^y y^2 dy \quad (\text{Eq.A-26})$$

$$\frac{M}{M_0} = \exp \left(\frac{-y^3}{3B} \right) \quad (\text{Eq.A-27})$$

$$\frac{\partial C}{\partial y} = \left(\frac{\partial C}{\partial y} \right)_{y=0} \exp \left(\frac{-y^3}{3B} \right) \quad (\text{Eq.A-28})$$

$$\int_0^{C_0} dC = \left(\frac{\partial C}{\partial y} \right)_{y=0} \int_0^\infty \exp \left(\frac{-y^3}{3B} \right) dy \quad (\text{Eq.A-29})$$

Setting the limits as limiting current conditions $C(y=0)$. Substituting $z=y^3/3B$ or $0.8934(3B)^{1/3}$ we obtain Eq.A-30.

$$C_0 = \left(\frac{\partial C}{\partial y} \right)_{y=0} 0.8934 \left(\frac{3D \tilde{\omega}^{-3/2} v^{0.5}}{0.51} \right)^{1/3} \quad (\text{Eq.A-30})$$

Expressing in terms of the flux at the electrode surface (current);

$$i = nFAD \left(\frac{\partial C}{\partial y} \right)_{y=0} \quad (\text{Eq.A-31})$$

10.2 Calculations and estimates

10.2.1 *FePc/KJB Nafion film thickness for EIS calculation on TFE*

Using an assumed density of 0.1325 g cm⁻³ for KJB (assume +50% wt. FePc=0.19875 g cm⁻³ FePc/KJB) and the density of dry Nafion ionomer=2.1 g cm⁻³ [354]. Loadings are; FePc/KJB; 71 μg cm⁻² + Nafion; 111 μg cm⁻². Producing loading of FePc/KJB; 17.55 μg + Nafion; 27.4368 μg. Dividing by density produces volumes of FePc/KJB; 8.83x10⁻⁵ cm³ + Nafion; 1.3x10⁻⁵ cm³. The void fraction is greatly reduced after FePc incorporation, assuming 50% of the Nafion fills the pores with the remainder forming a surface film. The combined thickness is 9.5x10⁻⁵ cm³/0.24718= 3.8x10⁻⁴ cm (±30%)

Predicted loading of FePc (Γ_{FePc})=23.66 μg cm⁻² of Fe=1.09618x10⁻⁴ Moles cm⁻³

Electro-active FePc ($\tilde{\Gamma}_{FePc}$)=2.26x10⁻¹⁰ Moles cm⁻²

=Volumetric electro-active FePc=5.95x10⁻⁷ Moles cm⁻³

10.2.2 *FePc/KJB QDPSU air cathode thickness for EIS calculation*

0.19875 g cm⁻³ FePc/KJB and the density of dry Nafion ionomer=2.1 g cm⁻³

Applied weights: 2 mg cm⁻² FePc/KJB and 0.2 mg cm⁻² QDPSU.

In air cathodes the ionomer loading is small enough to be completely entrained in the carbon pores, therefore the volume of the ionomer is neglected.

Volume=12.56 cm²*0.002 g cm⁻²/0.19875 g cm⁻³=0.126 cm³

Thickness=0.01 cm (±30%) c.a. the maximum limit deemed efficient for a catalyst layer [355].

10.2.3 *Cost calculation for QDPSU synthesis*

The rough cost ratio between Nafion and DABCO was added. QDPSU was synthesised in our lab. Nafion resin is £127.30/10g¹¹, and DABCO is £12.90/100g¹², PSU around

¹¹ Alfa Aesar

¹² Alfa Aesar

£380/kg¹³ or £10/kg¹⁴ bulk. For the QDPSU, the cost could be around x10 the material cost, approximately £140-300/kg, significantly lower than Nafion. A QDPSU membrane 30µm thick ($\rho_{dry}=1240\text{kg m}^{-3}$) produces a price £110,000m⁻³ or £8 m⁻², though with PTFE cross-linker the price will rise.

10.2.4 Non-precious cathodes and MEA

The charge carrier concentration in the membrane phase is obtained from (Eq.A-32) where C_c is the membrane phase charge carrier concentration (moles of ion per cm³ polymer), IEC is the ion exchange capacity in mMoles of ion per gram of polymer, $\rho_{m,i}$ is the wet density of the membrane for ion “i” (g cm⁻³), V_{x-H2O} is the volume based water uptake (cm³ cm⁻³).

$$C_c = 0.001 * IEC * \rho_{m,i} / (1 + 0.01V_{x-H2O}) \quad (\text{Eq.A-32})$$

For the diffusion of ions in dilute solution (D_0) in cm² s⁻¹, k_B is the Boltzmann constant ($1.3806488 \times 10^{-23} \text{ m}^2 \text{ kg s}^{-2} \text{ K}^{-1}$), T is temperature (K) and z is the ion charge.

$$D_0 = \mu * k_B * T / z \quad (\text{Eq.A-33})$$

The rate of ion diffusion through the membrane at $E=\text{OCP}$ from the Warburg diffusion co-efficient can then be used to express the relative diffusion of an ion compared to dilute solution (D/D_0).

10.2.5 Schmidt number of O₂ in aqueous solution

$$Sc^0 = 1800.6 - 120.1t + 3.7818t^2 - 0.047608t^3 \quad (\text{Eq.A-34})$$

$$Sc = Sc^0 (1 + 3.14 \times 10^{-3} PSU) \quad (\text{Eq.A-35})$$

¹³ Sigma Aldrich

¹⁴ Alibaba.com

Where PSU=practical salinity units=5.3828 for 50mM PBS (6.6mS cm⁻¹), and t is temperature (in °C). Produces a value of $Sc^0=725.123$, and $Sc=737.4$ for 50mM PBS. For H₂O₂ this number is 1561 from Table A-2.

10.3Tables

Table A-1. Preparation procedure for all catalysts prepared in-house.

Catalyst Description							Catalyst Abbreviation	
Unpyrolysed FePc on Monarch	1.2g FePc + 0.8g MON	>	+ conc. H ₂ SO ₄ 20 min agitation	>	Cold DIW added incrementally to suspension (2.5L)	>	20hr stir. Filtered, DIW Washed, Dry 100°C 16hr	FePc/MON
Pyrolysed FePc on Monarch			FePc/MON	>	Pyrolysis in N ₂ @ 800°C for 2hrs 300°C/hr ramp for heating/cooling			FePc/MON pyr
Manganese Oxides on Monarch	118.3g MnSO ₄ • H ₂ O + 70ml DIW +4g MON @80°C	>	40 minutes agitation	>	+300ml of 33mM KMnO ₄ (@80°C and 10ml/min)	>	Filter, DIW wash, dry 100°C 16hr	MnOx/MON
Unpyrolysed FePc and MnOx on Monarch	11.83g MnSO ₄ • H ₂ O + 70ml DIW +400mg FePc/MON (@80°C)	>	40 minutes agitation	>	+30ml of 33mM KMnO ₄ (@80°C and 10ml/min)	>	Filter, DIW wash, dry 100°C 16hr	FePcMnOx/MON
Titanium Oxides on Monarch	20ml Iso-propanol +1g MON sparged 15min N ₂	>	+1.5ml Ti Iso-Propoxide under N ₂ +agitation	>	+10mM HNO ₃ @0.05ml for 30 minutes under N ₂	>	Filter, DIW wash dry 100°C 16hr	TiOx/MON
Pyrolysed TiOx on Monarch			TiOx/MON	>	Pyrolysis in N ₂ @ 600°C for 2hrs 300°C/hr ramp for heating/cooling			TiOx/MON pyr
TiOx and FePc on Monarch	1.2g FePc + 0.8g TiOx/MON	>	(+ conc H ₂ SO ₄) 20 min agitation	>	2.5L Cold DIW added incrementally	>	Filter, DIW wash dry 100°C 16hr	TiOxFePc/MON
FePc on Ketjen Black	1g FePc +1g KJB	>	(+ conc H ₂ SO ₄) 30min agitation - air	>	Added to 1L cold water in one go	>	20hr stir. Filter, DIW wash dry 100°C 16hr	FePc/KJB
Pyrolysed FePc on KJB			FePc/KJB	>	Pyrolysis in Argon @ 750°C for 2hrs 300°C/hr ramp for heating/cooling			FePc/KJB pyr
FePc and MnOx on KJB from KMnO ₄ action	400mg FePc/KJB in 70ml DIW @80°C	>	40 minutes agitation	>	+30ml of 33mM KMnO ₄ (@80°C and 10ml/min)	>	Filter, DIW wash, dry 100°C 16hr	FePcMnOx/KJB (KMnO₄)
Unpyrolysed FePc and MnOx on KJB	11.83g MnSO ₄ • H ₂ O +70ml DIW +400mg FePc/KJB (@80°C)	>	40 minutes agitation	>	+30ml of 33mM KMnO ₄ (@80°C and 10ml/min)	>	Filter, DIW wash, dry 100°C 16hr	FePcMnOx/KJB (+Mn²⁺)
Pyrolysed Monarch Carbon			Monarch	>	Pyrolysis in Argon @ 800°C for 2hrs 300°C/hr ramp for heating/cooling			HT Monarch

Table A-2. Physical constants of 50mM PBS used in this study.

Parameter	Chemical Species			
	O ₂	H ₂ O ₂	OH ⁻	H ⁺
Concentration (saturated) / Mole cm ⁻³	5.67 x 10 ^{-7 15}	-	10 ⁻¹⁰	10 ⁻¹⁰
Diffusivity / m ² s ⁻¹	1.67 x10 ⁻⁹	0.66 x10 ⁻⁹		8.06 x10 ⁻⁹
K_a / Mole dm ⁻³	-	1.5 x10 ⁻¹²	-	-
K_b / Mole dm ⁻³	-	-	-	-
50mM PBS, pH7				
Kinematic Viscosity (ν) / m ² s ⁻¹		1.0304 x10 ⁻⁶		
Density (ρ) / kg m ^{-3s}		1.00479		

The information in Table A-2 is taken from [43] for 20°C for 100mM PBS. Reported values vary from 1mM to 0.22mM.

Table A-3. Dissolved O₂ in air equilibrated 50mM Na⁺PBS, pH 7.0.

Air equilibrated		[O ₂]	
T / °C	T / °K	mg / L	Moles dm ⁻³
14.8	287.95	9.80	3.06E-04
18	291.15	9.37	2.93E-04
19.5	292.65	9.07	2.83E-04
22.1	295.25	9.04	2.83E-04
25	298.15	8.70	2.72E-04
25.9	299.05	8.63	2.70E-04

This data was acquired using a Jenway consumptive dissolved O₂ probe in rapidly agitated air equilibrated solutions. No dissolved bubbles were visible.

¹⁵ The concentration of O_{2(aq)} at 20°C varies significantly (1mM to 0.22mM) across literature, but consensus shows that the phosphate or sodium ions cause no significant difference from that in DIW.

Table A-4. Physical constants of ions in 50mM PBS at T = 20°C. Protons and Hydroxide ions reported at infinite dilution, sodium and phosphates reported at 50mM where possible.

Parameter	Chemical Species					
	$\text{H}_2\text{NaPO}_4 / \text{HNa}_2\text{PO}_4$	Na^+	HPO_4^{2-}	H_2PO_4^-	H^+	OH^-
Concentration / Mole dm^{-3}	0.021147 / 0.028847	0.078841	0.028847	0.021147	10^{-7}	10^{-7}
Diffusivity / $\text{m}^2 \text{s}^{-1}$	n/a	1.29×10^{-9} [356] (¹⁶)	0.86×10^{-9}	1.0×10^{-9}	8.6×10^{-9} [357]	4.78×10^{-9} [357]
Molar Conductivity / $\text{S m}^2 \text{mole}^{-1}$	n/a	50.1	66	57	349.6	200
Electrophoretic mobility (μ) / $\text{m}^2 \text{V}^{-1} \text{s}^{-1}$	n/a	4.98×10^{-8} (¹⁷)		5.9×10^{-8} [358]	36.2×10^{-8} [357]	20.5×10^{-8} [357]
Hydrated Ionic radii / Nm [359]		0.4	0.4	0.4	0.9	0.35

Table A-5. Reported qualities of carbons from manufacturer and academic sources.

Parameter	Ketjen Black EC300J [360]	Monarch 1000	Synthetic Graphite
Specific Density / g cm^{-3}	0.1325		
Pore Volume / $\text{cm}^3 \text{g}^{-1}$	3.1-3.45		
Void fraction (from above) / $\text{cm}^3 \text{cm}^{-3}$	0.4286		
Relative Surface Area (N_2 adsorption) / $\text{m}^2 \text{g}^{-1}$			
Particle diameter / μm			<20
Apparent pH / pH	9-10.5		
Iodine Adsorption / mg g^{-1}	740-840		

Table A-6. Collection Efficiency for Pt ring used in Wroblowa analysis.

Assume 100% H_2O_2	100rpm	200rpm	300rpm	400rpm	600rpm	800rpm	1000rpm	1600rpm	3200rpm
Synth Graphite/Nafion	0.2549	0.2543	0.2455	0.2359	0.2165	0.2016	0.1910	0.1648	0.1155
Assume 100% H_2O_2	100rpm	200rpm	300rpm	400rpm	600rpm	800rpm	1000rpm	1600rpm	3200rpm
Glassy Carbon	0.2328	0.2491	0.2501	0.2228	0.2117	0.2047	0.1910	0.1779	0.1366
% drop from CE=37%	100rpm	200rpm	300rpm	400rpm	600rpm	800rpm	1000rpm	1600rpm	3200rpm
Synth Graphite/Nafion	0.37	0.3691	0.3563	0.3423	0.3142	0.2926	0.2772	0.2391	0.1676
% drop from CE=37%	100rpm	200rpm	300rpm	400rpm	600rpm	800rpm	1000rpm	1600rpm	3200rpm
Glassy Carbon	0.3443	0.3685	0.3700	0.3297	0.3132	0.3029	0.2826	0.2632	0.2021

¹⁶ Infinite dilution, 25°C

¹⁷ Infinite dilution, 25°C

Table A-7. Ingredients of biofilm growth nutrient supplement. x10 concentrated stock solution.

	Stock mg/ <i>L</i>	Final Molarity / M dm ⁻³		Stock mg/ <i>L</i>	Final Molarity / M dm ⁻³
NH ₄ Cl	400	7.47E-04	FeSO ₄ •7H ₂ O	6.25	2.25E-06
MgSO ₄	150	1.25E-04	HBO ₃	Trace	Trace
CaCl ₂ • 2H ₂ O	50	3.40E-05	NiSO ₄ •6H ₂ O	Trace	Trace
MnCl ₂ • 4H ₂ O	1.5	7.58E-07	CoCl ₂ •2H ₂ O	Trace	Trace
CuSO ₄ •5H ₂ O	1	4.00E-07	(NH ₄) ₆ Mo ₇ O ₂₄ •4H ₂ O	Trace	Trace
ZnCl ₂	1	7.34E-07			

Table A-8. Reproducibility of electro-active FePc loading from 6μl aliquots of new catalyst inks. Data from integration of Fe(II)→Fe(III) peak obtained in N₂ sat PBS for separate inks produced from 10mg of FePcKJB catalyst in the presence of different binders.

Binder	H ⁺ Nafion	Na ⁺ Nafion	QDPSU	PTFE
$\tilde{\Gamma}_{FePc} /$	2.9E-09	1.7E-09	3.7E-09	7.5E-09
Moles cm ⁻²	3.7E-09	6.0E-09	3.1E-09	
	3.7E-09			
	5.1E-09			
Mean	3.9E-09	3.9E-09	3.4E-09	7.5E-09
Standard Deviation	8.9E-10			
Co-eff. of variation	0.23			

The co-efficient of variation is obtained from dividing the standard deviation by the mean.

Table A-9. Membranes thickness in NaHCO₃ PBS or NaCl solution and % swelling vs dry state. Standard deviation over 4 repeat Vernier thickness measurements.

Membrane / Manufacturer	Dry		50mM NaCl		50mM PBS			50mM NaHCO ₃		
	Thick / μm	Thick / μm	St. Dev. / μm	% swell vs. dry	Thick. / μm	St. Dev. / μm	% swell vs. dry	Thick. / μm	St. Dev. / μm	% swell vs. dry
F-930 / Fumasep	26	35	2.0	35%	38	1.5	45%	38	3.2	47%
CMI-7000 / Membranes Int.	465	511	6.0	10%	520	3.0	12%	561	4.7	21%
Surrey / Surrey	59	80	1.0	36%	77	1.7	31%	83	1.3	40%
ADP / Morgane	146	154	0.6	5%	154	1.3	5%	152	1.5	4%
FAA / Fumasep	119	115	0.6	-3%	116	0.6	-2%	115	1.2	-3%
FTAM-A / Fumasep	557	637	11.4	14%	663	3.3	19%	639	41.5	15%
AMI-7001 / Membranes Int.	503	555	1.7	10%	578	3.2	15%	522	1.3	4%
QDPSU / Made in house	38	54	17.6	43%	60	16.8	57%	43	6.8	13%
ETFE Cranfield / Made out house	37	43	2.5	16%	40	4.1	7%	43	2.5	14%
Rhinohide / Entek		N/A	N/A	N/A	N/A	N/A	N/A	N/A	N/A	N/A
FAB / Fumasep	83	91	1.3	9%	97	2.6	16%	92	1.5	11%
FAD-PET / Fumasep	87	95	0.6	10%	115	1.5	32%	111	4.8	27%

Table A-10. Quantification of random sources of error in thin film experiment. Example is for FePcKJB Nafion film.

	Condition	Error margin (+/-)	Error margin (+/-) %
Catalyst weight (mg)	10	1	10
Pipette - Nafion (μl)	340	1.02	0.3
Pipette - Ethanol (μl)	3000	9	0.3
Pipette - disc aliquot (μl)	6	0.036	0.6
Cumulative error in Γ / %			10.6

10.4 Chemical de-activation of FePc catalyst

The stability of FePc in the presence of H⁺Nafion/Ethanol inks is shown from stabilised CV of the thin films in N₂ saturated PBS (Figure A-1). The aim was to assess whether polarisation was required for de-metallation (Eq.3-8).

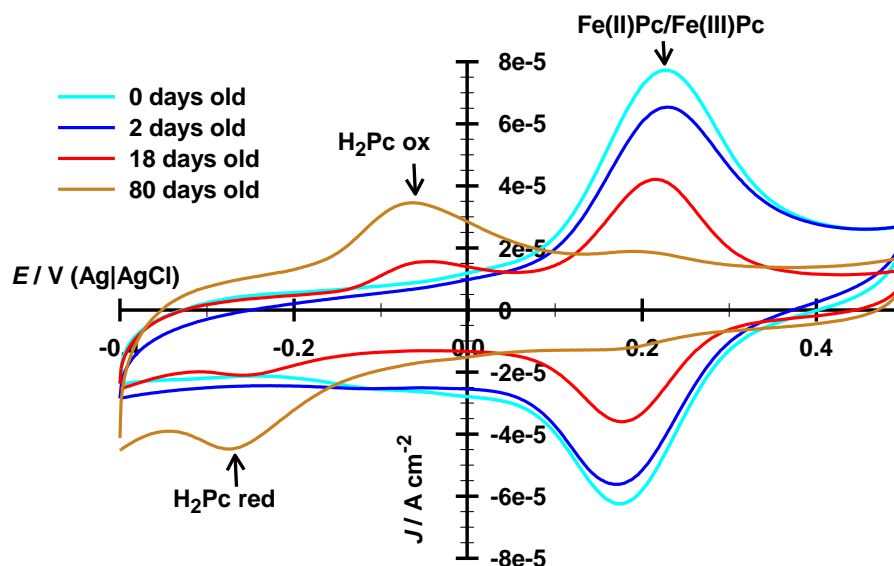


Figure A-1. FePc demetallation during storage in pH2 air sat. H⁺Nafion/ethanol ink. Stable CV response of thin FePc/KJB films from ink age 0, 2, 18 or 80 days. Electrolyte; 50mM PBS (pH7). $\omega=0\text{rpm}$. $\nu=20\text{mV/s}$

As the catalyst aged in the presence of O₂ at pH 2 several observations were made about the redox peak;

1. The main Fe(II)Pc/Fe(III)Pc redox peak reduced in size with age of the ink.
2. The redox peaks at $E_p=-0.264\text{V}$ and $E_p=-0.076\text{V}$ grew with sample age. The mid-point of this redox couple is $E^{0'}=-0.17\text{V}$.

Several possibilities must be eliminated before the $E^{0'}=-0.17\text{V}$ couple can be identified;

- 1) FePc solubility in ethanol (ink) is low, recrystallization of FePc is unlikely.
- 2) Sulfonate (from solvated Nafion) or ethanol may ligate FePc, altering $E^{0'}$. It is implausible that a single sulfonate ligand may cause a large shift in $E^{0'}$ [181].
- 3) The formation of μ -oxo FePc occurs within catalyst ink with O₂. The $E^{0'}=-0.17\text{V}$ redox may be a FePc-O-FePc moiety [179, 361].
- 4) De-metallation of FePc occurs, producing electrochemically detectable H₂Pc.

μ -oxo FePc is generated instantaneously during polarisation [212] yet the Fe(II)/Fe(III) can still be visible in O₂ at approximately the same $E^{0'}$ (Figure 5-22) making (3) an unlikely explanation. Zagal shows the Phthalocyanine ring redox of H₂Pc occurs 0.3V lower than the Co(II)Pc/Co(III)Pc redox in alkali medium [193]. The $W_{1/2}$ and $E_{pa}-E_{pc}$ of this couple suggests pH dependency, as if causing proton dissociation (-59mV pH^{-1}). Using Eq.3-8 would generate a corresponding peak at $E=-0.17\text{V}$ for H₂Pc in pH7 media

[362], close to that observed thus suggesting H₂Pc. the characteristics of the H₂Pc peak are;

- Quasi-reversible with the characteristics of the forward and reverse being -0.049 ($W_{1/2}=0.0862V$) and $E_p=-0.250$ ($W_{1/2}=0.0786V$) respectively. A catalyst layer applied from 80 day old ink had a H₂Pc peak 28.5% the size of the initial Fe(II)Pc/Fe(III)Pc peak, while the Fe(II)/Fe(III)Pc peak was 6-7% the original size after 80days.
- At $t=80$ days deterioration in Fe(II)Pc→Fe(III)Pc is >90% but the increase in H₂Pc only 28.5% suggesting H₂Pc decomposition or solvation has occurred.
- The oxidation peak of H₂Pc is Gaussian and the reduction peak slightly Lorentzian as if charge insertion were impeded during Fe(III)Pc reduction.

The Fe(III)Pc↔Fe(II)Pc peak shape is initially Gaussian from new ink while it becomes Lorentzian in 80 day ink suggesting resistance to electron propagation.

10.5 Method Justification

10.5.1 Iron Phthalocyanine films, deposition solvent and support

FePc is readily solvated in concentrated H₂SO₄ or several organic solvents that reversibly complex with iron, namely Pyridine, CHCl₃, CH₂Cl₂, DMSO and DMF (insoluble in THF [363]). Thermal treatment or ligand substitution is required to remove some of these ligands. DMSO could not be used due to low volatility, requiring potentially harmful heating for removal. Deposition on GC disc from H₂SO₄ may result in thermal decomposition from enthalpy of solution. Low FePc solubility in non-polar aliphatic and aromatic solvents, with additional problems of graphite pore entrainment (eg. Benzene) prevent consideration of this deposition method.

Therefore FePc was deposited from DMF, a relatively strong ligand solvent (though FePc complexing is reversible). Establishing DMF removal is an important aspect of the validity of this mechanism study. The FePc-DMF adduct displays a different electrochemistry than FePc-H₂O. Chen et al show FePc to form self-assembled π -bond lattices from a DMF solution [70], displacing axial ligands with H₂O. Axial DMF ligands (Figure 3-5, position X) will remain after evaporation at ambient temperature, [275]. O₂ did not displace the DMF ligand in acid electrolyte (SO₄²⁻ anion) [275]. If

FePc was co-ordinated by two mono dentate DMF ligands, O₂ binding and ORR would not be possible without ligand substitution, yet the O₂ reduction wave is observed (Section 5.2.3). This may be due to Phosphate binding strongly compared to SO₄²⁻ allowing DMF substitution to occur.

As seen in Table 5-1, deposition on KJB (BET=795m² g⁻¹ [218]) provided a larger FePc than on Monarch (BET=292m² g⁻¹ [364]), as the Brunauer Emmett Teller surface area is larger. Though the data is not presented in Table 5-1, FePc (50%wt.) was deposited on Vulcan XC-72R carbon (BET=250m² g⁻¹ [364]) with equilibrium adsorption from FePc-DMF solution (C:FePc=50:50 wt.) to produce 43.6x10¹³ sites cm⁻². The area of the two carbons is comparable but loading from DMF is slightly higher than that from concentrated H₂SO₄ (FePc/MON). This validates the assertion that FePc was not blocked by axial DMF ligands at the point of polarisation in N₂ (Figure 5-3). Deposition in hydrophobic areas (via non-aqueous solvent) may influence effective loading. Deposition on carbon support increased the geometric loading of FePc in electrolytic contact by x9.2 for FePc/KJB at 223x10¹³ redox active sites cm⁻² compared to $\bar{\Gamma}$ =6.77x10⁻⁸ Moles cm⁻² unsupported FePc layer in Figure 5-2 at 25.4x10¹³ redox active sites cm⁻². If uniformly ordered, this crystalline form produces an expected thickness equating to 647 layers of FePc, using the molecule dimensions outlined by Baker et al [213] for an α -FePc film.

10.5.2 *Electroanalysis of redox polymer catalyst*

Two methods of concentration polarisation correction are reviewed in Figure A-2. From K-L plot intercepts of v =5mV/s data and from applying Eq.2-52 to unstirred solutions with v =1mV/s LSV data.

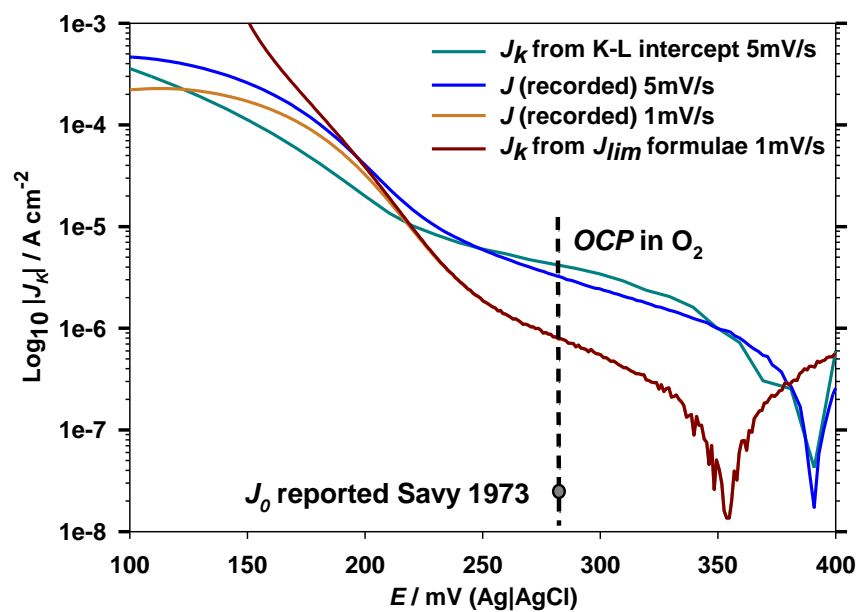


Figure A-2. Effect of concentration polarisation and scan rate on tafel behaviour of an FePc/KJB film and correction techniques. Key; J =Recorded Current density, J_k =Kinetic Current Density.

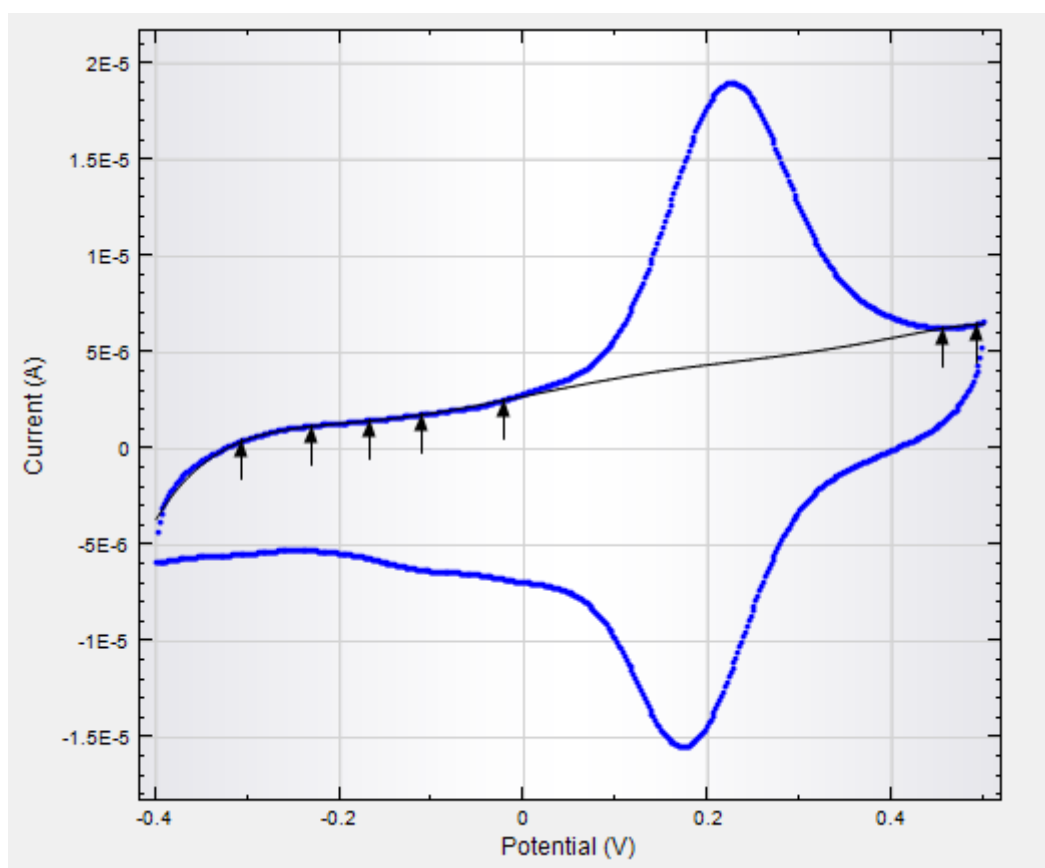


Figure A-3. Fitting a polynomial baseline (6-order) to obtain integratable charge of Fe(II)Pc/Fe(III)Pc redox

This method has been adapted from the one used by Baker et al [179] and a study on the redox of immobilised proteins of Hirst et al [365]. The difference being that this group used a baseline of the current response by an electrode with the support carbon with no FePc. The integration of the peak was constrained to a 50mV range either side of the peak potential. As observed in Figure A-3 the higher surface loading in carbon black supported FePc causes the peak to cover a 0.4V potential range when using $v=20\text{mV/s}$. As such the high and low potential limit for charge integration was established as the point where deflection from linear i - E response (capacitive current). The passed charge was integrated on both forward and reverse scans and a match ($\pm 0.5\%$) demonstrated accurate baseline fitting of this finite and surface controlled process.

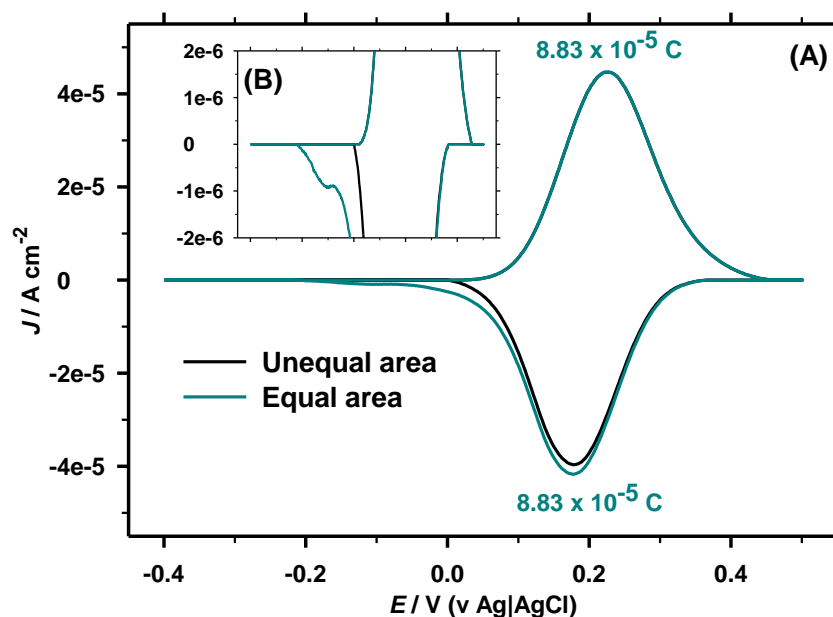


Figure A-4. Fe(II) \leftrightarrow Fe(III) redox peaks (A) with adjustment of cathodic scan baseline.
(B) Enlarged Y-axis

When the peaks are checked for charge conservation ($Q_{\text{Fe(II)}\rightarrow\text{Fe(III)}}=Q_{\text{Fe(III)}\rightarrow\text{Fe(II)}}$) it is seen that cathodic tailing is present in carbon supported FePc in Figure A-4. This is consistent with the finding in Figure 5-2(A) which shows resistance to Fe(III) \rightarrow Fe(II) in thick adsorbed multilayers.

For irreversible electrocatalytic reactions a linear E_p vs $\log_{10}(v)$ is also anticipated [366]. In comparison, As a control, Figure 2-4 (B) shows that continual CV at the same scan rate causes no shift in E_{pc} for 40 scans. The cathodic shift $-0.03/\alpha n \text{ V } v_{\text{decade}}^{-1}$ in Eq.2-30 may not be applicable unless $n_c=0$ but the fit was attempted. The recorded slope is $-0.02016 \text{ V per } \log_{10}(\text{V s}^{-1})$, which equates to $\alpha=0.744$ for a k_2 mechanism ($n=2$) or

$\alpha=0.372$ for a k_1 mechanism ($n=4$). The n -value for ORR is taken for FePc/KJB at 0.15V (c.a. $n=3.94$).

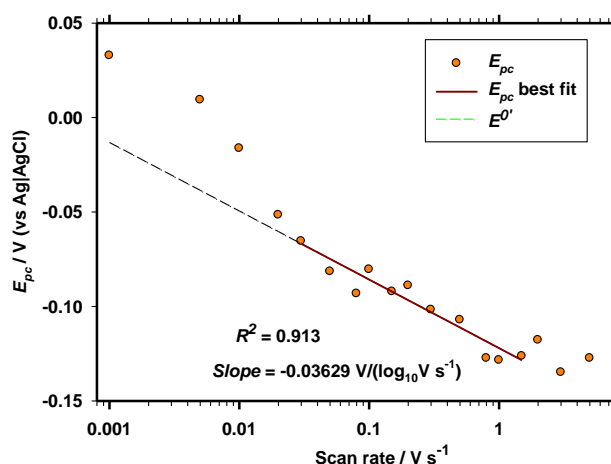


Figure A-5. Trumpet plot unsupported FePc film. Cathodic peak relates to $\text{ORR}/\Gamma_{\text{FePc}} = 6.77 \times 10^{-8} \text{ Moles cm}^{-2}$. Electrolyte; air saturated PBS, pH 7.0

The unsupported FePc film was evaluated within the range of $-0.75 < E < 0.35 \text{ V}$ (orange) and $-0.4 < E < 0.35 \text{ V}$ (red), selected to avoid H_2 evolution ($E < -0.75 \text{ V}$) and aryl-aryl bond formation catalysed by Fe(III). The slope corresponds to a value of $\alpha=0.413$ for k_2 mechanism ($n=2$) or $\alpha=0.207$ for k_1 mechanism ($n=4$) if Eq.2-39 is applied. However, this equation is only applicable in the case of 1^{st} e^- heterogeneous ET, showing poor comparability with the carbon supported case.

10.5.3 RRDE methodology

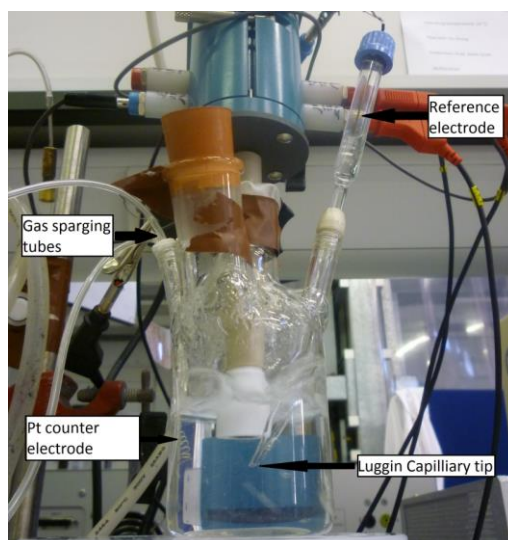


Figure A-6. RRDE experimental apparatus

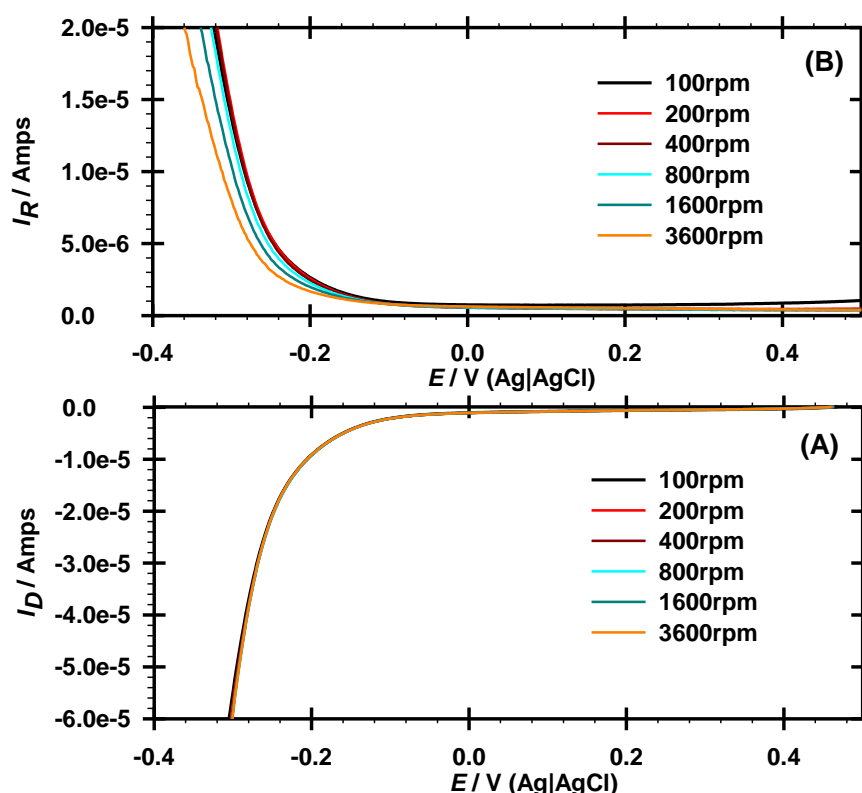


Figure A-7. The (A) i_D vs. E and (B) i_R vs. E profile for RRDE experiments on Synthetic Graphite/Nafion thin films. Electrolyte; 50mM PBS, pH 7.0. $E_{disc} = -0.4V$, $E_{ring} = +0.6V$

RRDE work with ORR is typically performed in KOH or H_2SO_4 , several fundamental assumptions on oxygen electrochemistry [367] needed to be confirmed in PBS. This could not be achieved with the $K_3Fe(CN)_6 / K_4Fe(CN)_6$ method of determining CE . The most suitable approach was selecting $2e^-$ active materials. Synthetic Graphite (particle size $<20\mu m$) has received no surface functionalization and so was used to assess the influence of rotation on $\%H_2O_2$ when a film is present. This proved a good selection of material for calibration of the cell because $i_D = f(\omega)$ for KJB and Monarch. For synthetic graphite at $E = -0.4V$ disc current was $i_D \neq f(\omega)$ showing strict kinetic limitation. For $\omega = 100rpm$ $i_D = 2.88 \times 10^{-6} A cm^{-2}$ and $\omega = 3600rpm$ $i_D = 2.99 \times 10^{-6} A cm^{-2}$. The data is represented as collection efficiency in Figure A-8.

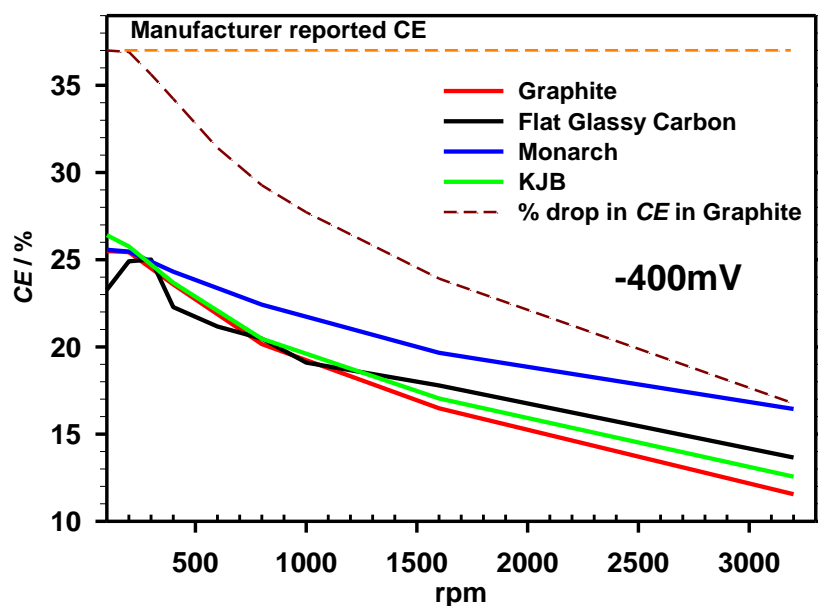


Figure A-8. Effect of RRDE tip rotation speed on experimentally determining ring CE. Following PtO formation Carbon(71 $\mu\text{g cm}^{-2}$)/Nafion thin films Electrolyte; 50mM PBS, pH 7.0. $E(\text{disc})=-0.4\text{V}$, $E(\text{ring})=+0.6\text{V}$ (Glassy Carbon only).

With synthetic graphite, i_R decreased drastically, at $\omega=200\text{rpm}$ $CE=25\%$ while at $\omega=3200\text{rpm}$ $CE=11.5\%$. Two possibilities are present; 1) disproportionation (k_4) increases significantly with rotation or 2) the flow regime of H_2O_2 rich disc product veers away from the ring at high rotation. If $k_3=f(\omega)$ or $k_5=f(\omega)$ ($\text{H}_2\text{O}_{2(\text{aq})}$ reduction) was true then i_D is anticipated to increase with ω which is not seen in would change.

It is assumed that E_D does not affect CE once solvated H_2O_2 has left the inner Helmholtz plane of the disc catalyst layer. This model assumes that the catalyst layer is aerated being under kinetic control, therefore the consistent i_D does not prove $k_4=f(\omega)$, this would only be proved under diffusion limitation.

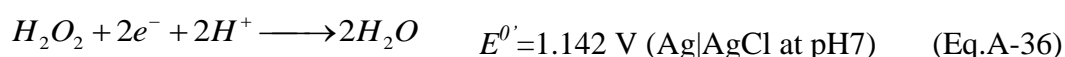
k_7 and k_8 are assumed negligible.

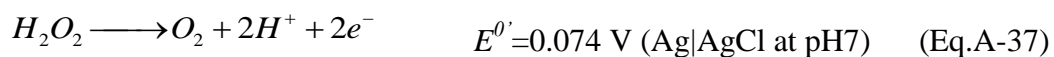
$CE=f(\omega)$

$k_3 \neq f(\omega)$, cannot assume for macrocycles

$k_5 \neq f(\omega)$, assume this holds for macrocycles, though it cannot be assumed QDPSU does not catalyse k_5 .

$k_6 \neq f(\omega)$, for Graphite only, adsorbing as an isotherm.





Though collection efficiency of metallic Pt and PtO layer should be identical, the kinetics of H_2O_2 oxidation may differ at low overpotential. Pine Research Instrumentation calculate $CE=37\%$ based on ring-disc geometry. At $E=0.6V$ the potential is anodic enough for significant PtO coverage and does not influence H_2O_2 oxidation kinetics at comparatively low concentrations being studied. The mixed potential of the reactions in Eq.A-36 and Eq.A-37 mean J_0 is large, though the anodic reaction is more facile at $E=0.6V$ in pH 7.0 PBS [368]. In this work, the potential of zero current on a polycrystalline PtO surface was not affected by $[H_2O_2]_{\text{bulk}}$ and found to be 0.244V from linear regression of i - E plots at various $[H_2O_2]_{\text{bulk}}$.¹⁸

A potential window of $0.244 < E_{\text{ring}} < 0.6V$ is identified, encompassing the OCP of the O_2/H_2O couple 0.4V $[H_2O_2]_{\text{bulk}}=0\text{mM}$ and the OCP of the mixed O_2/H_2O_2 and H_2O_2/H_2O couple in $[O_2]_{\text{bulk}}= \text{c.a } 0\text{mM}$ in the Khudaish study (0.244V) and a desire to avoid any kinetic limitation of H_2O_2 oxidation. $E_{\text{ring}}=0.6V$ was picked as a trade-off between trace Oxygen Evolution current and totally mass transfer limited H_2O_2 oxidation.

Khudaish found that 2mM H_2O_2 oxidation on polycrystalline PtO/PtOH reaches diffusion limitation plateau at $E=0.6V$ vs. Ag|AgCl (1000rpm) of 7mA cm^{-2} . In O_2 saturated solution $[O_2]_{\text{bulk}}=5.67 \times 10^{-4} \text{ Mole dm}^{-3}$, for the RRDE E7R9 the area ratio of ring/disc = $0.1859/0.2472=0.752$. The study of Khudaish confirms that $H_2PO_4^-$ reversibly binds to Pt [43]. The kinetic control of H_2O_2 oxidation on Pt in PBS occurs at $b_a=58.5 \text{ mV dec}^{-1}$ [368]. Trace Pt dissolution (Pt^{2+}) was disregarded as a significant current at $E=0.6V$ [369] in pH 7.28 PBS.

Collection efficiency (CE) may vary for substrate and electrolyte. For porous electrodes it is expected the CE may vary with electrode rotation (ω) [370]. The profile and magnitude of change in CE with rotation in Figure A-8 is similar to that observed by Bouwkamp-Wijnoltz [63]. Therefore the CE data is collected for GC and Porous carbon films. The data represented in Figure A-8 is shown in Table A-6. Converting the % drop from that seen at the rotation of highest H_2O_2 detection from the factory reported

¹⁸ Due to the limitation of the RRDE unit ($\omega_{\text{max}}=3000\text{rpm}$) similar experiments were not performed

$CE=37\%$ was frequently applied. For example, with synthetic graphite if 100% of the O_2 is converted to H_2O_2 and 25.49% of the H_2O_2 was detected by the ring if this value drops to 20.16% at 800rpm the % drop is calculated and subtracted from a $CE=37\%$ value, producing anticipated collection efficiencies listed in the bottom two rows of Table A-6.

Although H_2O_2 residence time in the catalyst layer is anticipated to be smaller at high rpm it can be seen from Figure A-8 that the % H_2O_2 was highest and most comparable at 200rpm. Film thickness is less of an issue than electrode rotation speed as the results from glassy carbon are comparable to KJB and Graphite, the two carbons without HNO_3 treatment that generates a small proportion of $4e^-$ ORR active sites.

Therefore % H_2O_2 vs. E plots a rotation speed of 200rpm was selected as % H_2O_2 was relatively uniform at this rotation speed. While K-L plots are verified as accurate by this experiment, the Wroblowa plots ($CE*i_D/i_R$ vs. $\omega^{-0.5}$) can be expected to produce inaccurate results high rpm unless collection efficiency adjustment is very accurate. Omitting these points produced noise in the J vs. C plots, suggesting the data was valid if accurately compensated.

With GPES software continual ring polarisation is not possible (unlike Nova). Therefore components of the current other than H_2O_2 oxidation require subtraction in order to plot accurate % H_2O_2 vs. E plots at high potential. An approximated example of i_R decay profile encountered over an LSV is depicted in Figure A-9. Transients and surface oxidation kinetics have not been used to model decay in charging current, the point of H_2O_2 oxidation current is apparent after overlaying i_D .

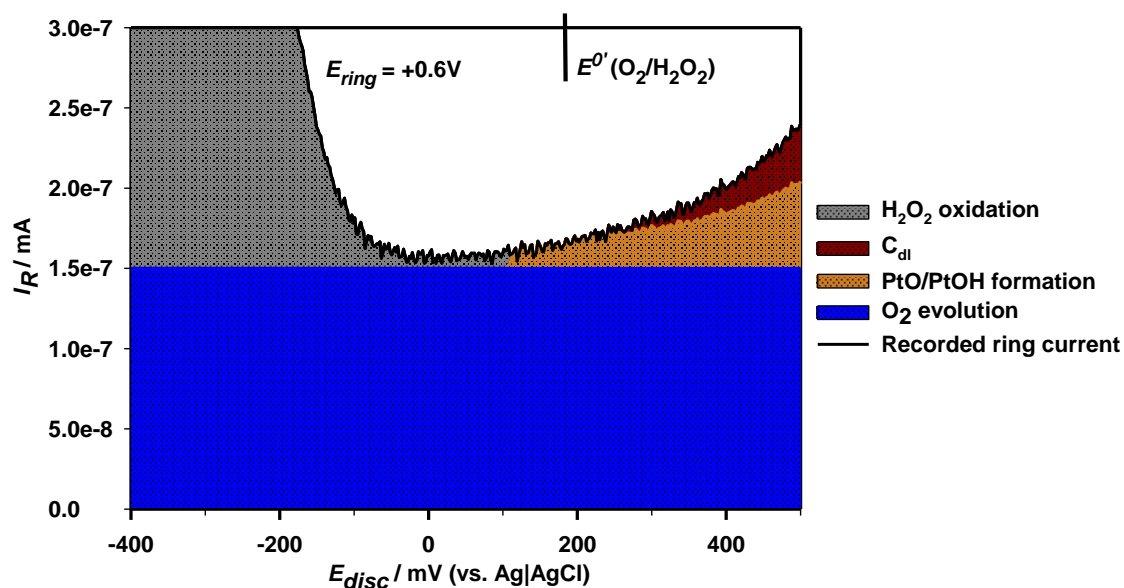


Figure A-9. I_R vs E_{disc} recorded during LSV scan. Components of current Thin film of synthetic graphite/Nafion on GC disc. Electrolyte; O_2 saturated 50mM PBS. $\nu=5mV/s$, $\omega=200rpm$. $E(ring)=+0.6V$

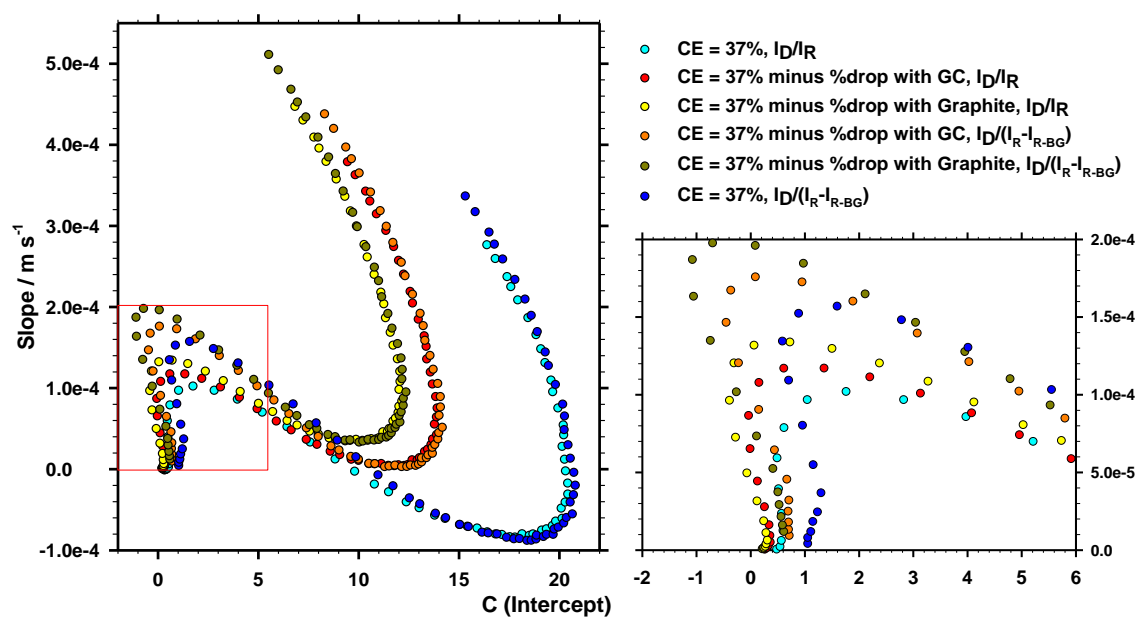


Figure A-10. S vs. C plot of $CE \cdot i_D/i_R$ vs. $k_{D,H_2O_2}^{-1}$ data of FePc film (4×10^{-9} Moles cm^{-2}) on GC disc. Data treated with different means (see key). Data from $E=0.25$ to $E=-0.4V$ displayed at 10mV intervals. Best fit applied to all rotation speeds. $\nu=5mV/s$. Electrolyte; 50mM PBS, pH7.

Examples of the S vs. C plot produced by application of different CE vs ω data. The $i_D/(i_R-i_{R-BG})$ with $CE=37\%$ at all ω data appears most accurate at low η but highly inaccurate at moderate-high overpotential.

10.5.4 RRDE data

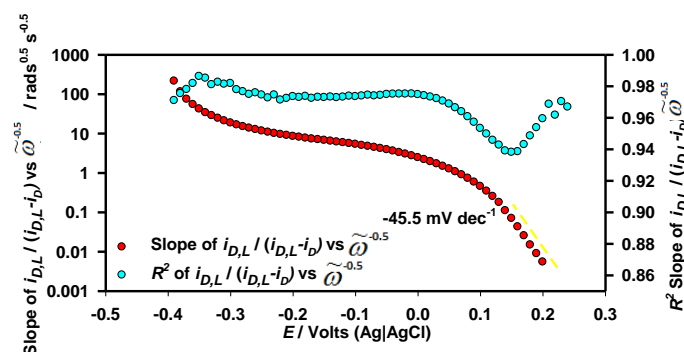


Figure A-11. Slope and R^2 fit of data from Figure 5-16.

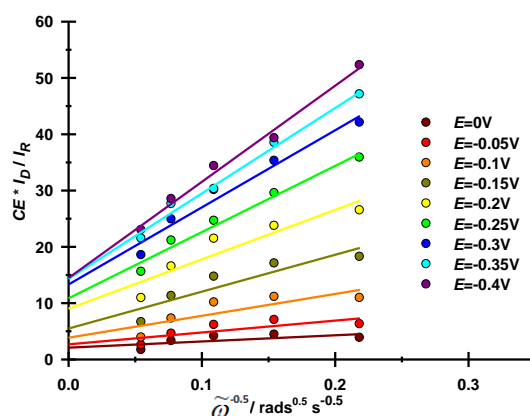


Figure A-12. $CE \cdot i_D/i_R$ over $\tilde{\omega}^{-1/2}$ plot for FePc/KJB film with QDPSU binder, CE adjusted to CE of Synthetic Graphite response. $v=5\text{mV/s}$.

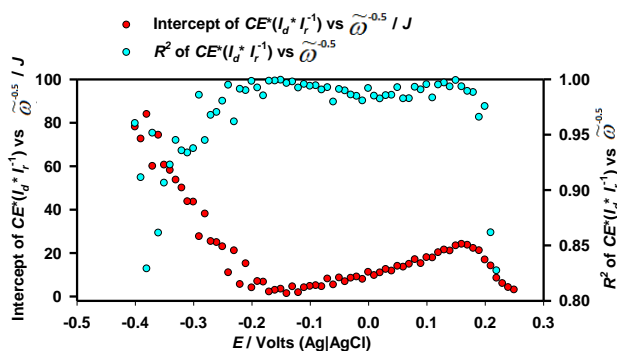


Figure A-13. Intercept and R^2 fit of data from Figure A-12.

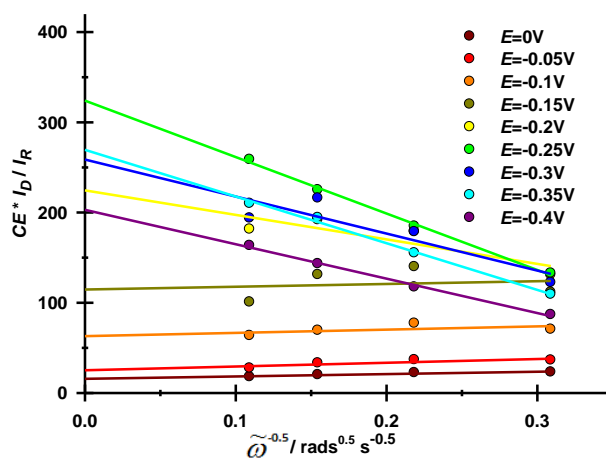


Figure A-14. CE^*i_D/i_R over $\tilde{\omega}^{-1/2}$ plot for pyrolysed (750°C) FePc/KJB film with Nafion binder, CE adjusted to CE of Synthetic Graphite response. $v=5\text{mV/s}$.

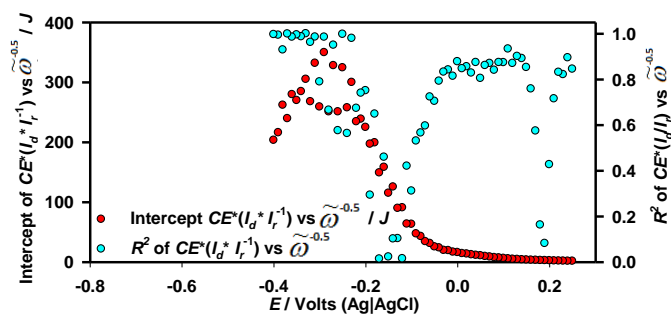


Figure A-15. Intercept and R^2 fit of data from Figure A-14.

It is apparent from Figure A-14 and Figure A-15 that the large at higher potential shows that pyrolysis drastically changes the nature of the active site.

10.5.5 QDPSU interaction with Pt and carbon surface

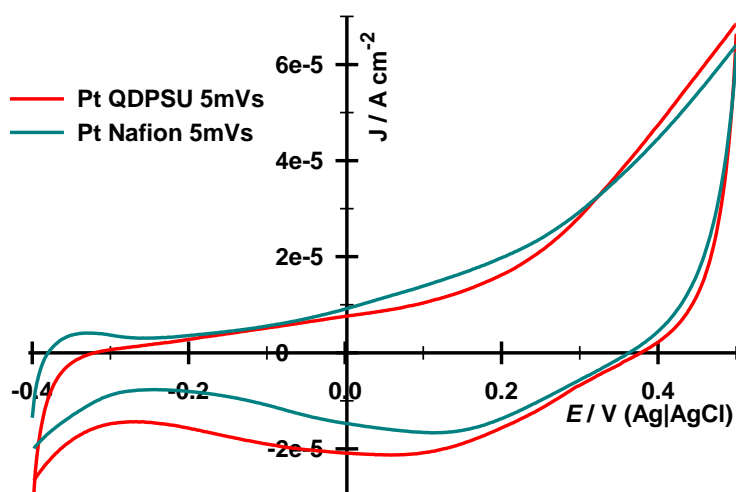


Figure A-16. CV of Pt/C-surface chemistry with Nafion or QDPSU. $\nu=5\text{mV/s}$. Electrolyte; N_2 saturated 50mM PBS, pH 7.0.

QDPSU-Pt surface interactions that present a redox active moiety are not detected.

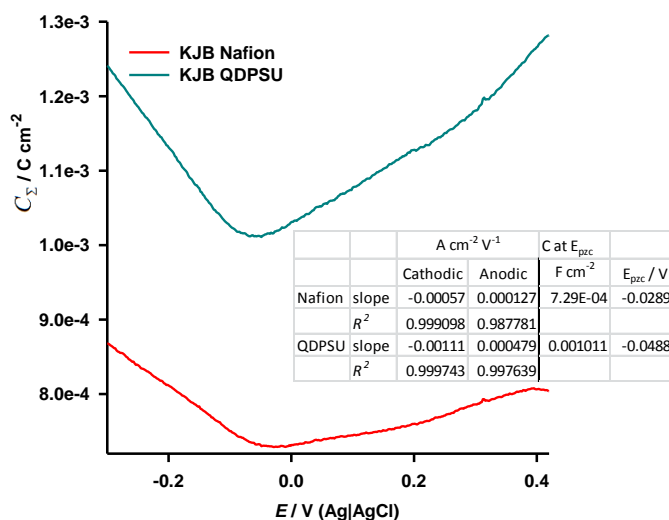


Figure A-17. CV of Pt/C-surface chemistry with Nafion or QDPSU. $\nu=5\text{mV/s}$. Electrolyte; N_2 saturated 50mM PBS, pH 7.0.

An analysis of the type in Figure 2-6 was performed on KJB Nafion and KJB QDPSU films. The result of C_d vs E plot is shown in Figure A-17. The C_d/E gradient is reported anodic and cathodic of E_{pzc} in the potential ranges $0.2 > E > 0\text{V}$ and $-0.13 > E > -0.28\text{V}$ respectively.

10.6 EIS

10.6.1 Nova arc fitting software for EIS

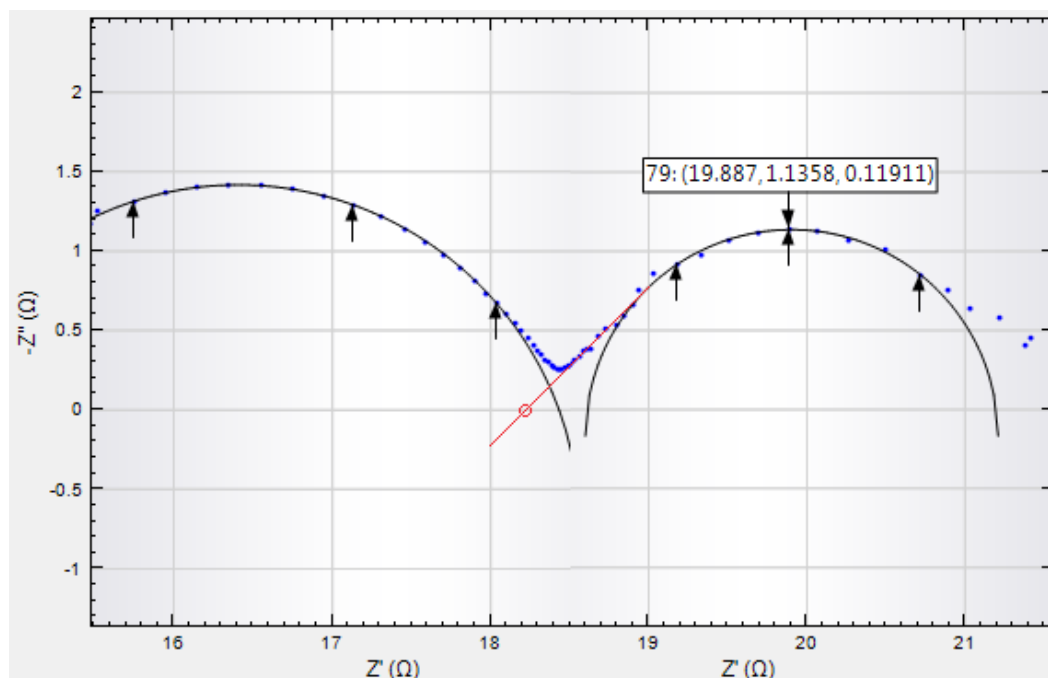


Figure A-18. Arc fitting and linear regression of Warburg element in Nova software. MEA of FTAM-A membrane fixed to FePc/KJB QDPSU air cathode with SS-mesh. $E = -0.2V$. Red line is extrusion of ion transfer resistance. Electrolyte; 50mM PBS, pH 7.0.

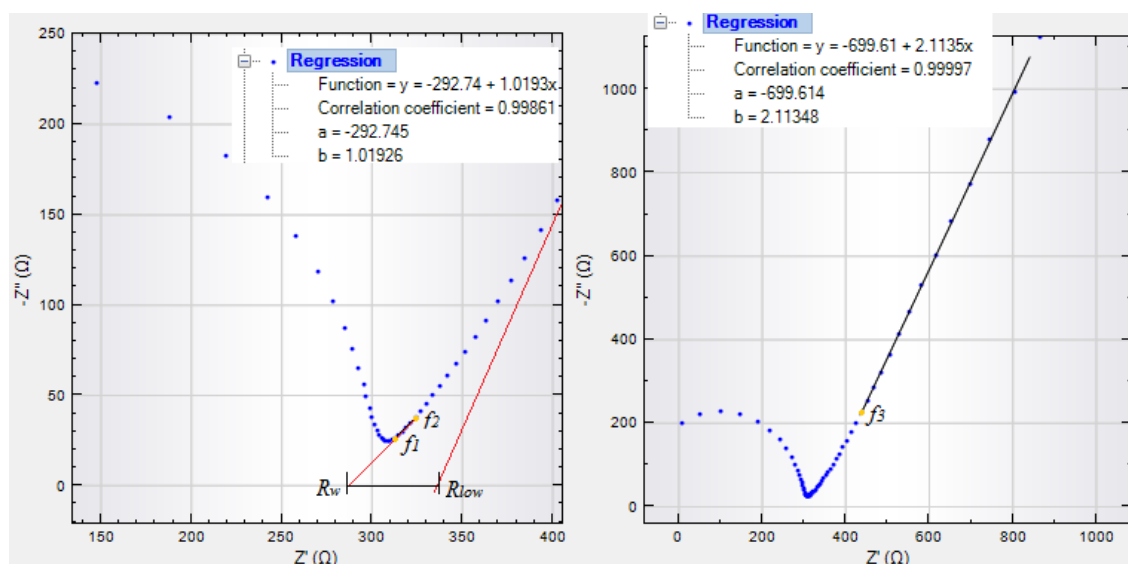


Figure A-19. Example of determination of Electron/Ion hopping/diffusion resistance in reflective finite diffusion. FePcKJB air cathodes with PTFE binder in GDC. $E = 0.28V$. Electrolyte; 50mM PBS, pH 7.0.

Note; f_3 does not mark the start of the C_{diff} region, only in this instance. f_3 corresponds to the point $\tilde{\omega}_3$ where $-\delta Z'/\delta Z'=2$.

10.6.2 High frequency arc with FePc films/air cathodes

The HF arc feature observed in Figure 7-9 and Figure 7-2 is a process linked to the presence of FePc with PBS or bicarbonate ion, with or without a current collector [331]. The C_{HF} values are reported in Table 7-5 are associated f_p with time constant $RC_{HF}=c.a.$ $2.2\mu s$. Figure 7-9 illustrates how the LF limit of this HF time constant is the start warburg control.

Two explanations for the HF arc response were explored;

- Di-electric relaxation arc with negative Z' intercepts [371]. This geometric capacitance is typically placed in parallel with R_s [102].
- Constricted water dipole rotation at the IHP on FePc surface.
- A change in charge gradient along the thickness of the electrode [372]. This can be discounted from the 2hrs wetting time and stabilised *OCP* recorded.

In Figure 7-2 the HF arc ($f>100kHz$) is also visible in thin film, discounting capacitances arising from grain boundaries that may arise from the current collector/catalyst layer or compression gasket interface.

10.6.3 Warburg impedance of QDPSU FePc/KJB air cathode in wastewater

Figure A-20 depicts the bode plot when real wastewater is added to PBS.

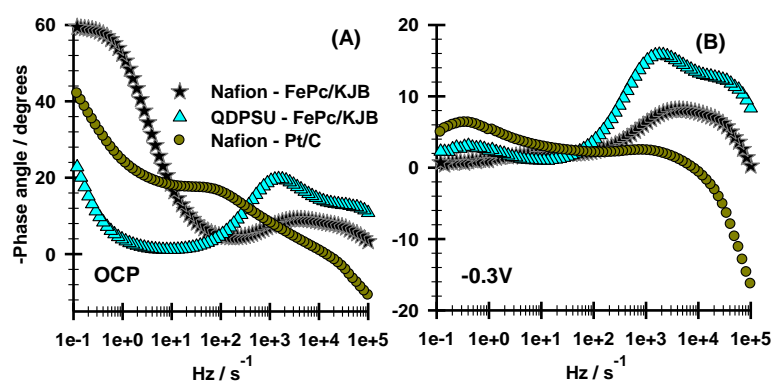


Figure A-20. Effect of wastewater on Bode Plot ($-\phi$ vs. f) of Nafion and QDPSU binders. Air cathodes of FePc/KJB or Pt/C with 10% wt. binder. Polarisation at $E=OCP$ or $E=-0.3V$. Electrolyte; air saturated Wastewater + PBS (at 50mM), pH 7.0.

In Figure A-20 the ($-\phi$) increase is seen HF in QDPSU is non-potential dependent, (1790-1500Hz), corresponding to Z vs. $\omega^{-0.5}$ type resistance (Figure A-21). This is also the case for Nafion (3.6-4.3kHz). With Nafion a large phase angle ($-\phi$) is retained at low frequency, as in NaCl and PBS. The LF phase angle is largest c.a. *OCP*, negligible at low potential but crucially is partially mitigated with QDPSU binder.

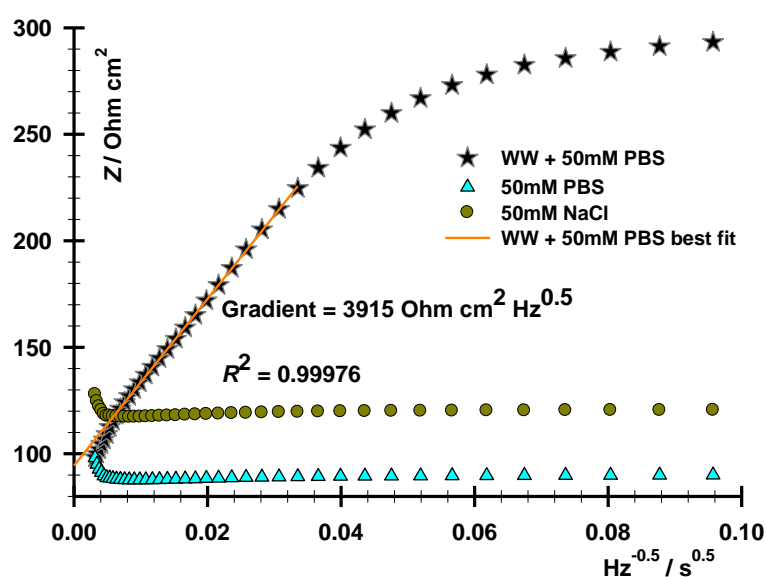


Figure A-21. $|Z|$ vs. $\omega^{-0.5}$ plot illustrating the effect of solution electrolytes on diffusion control at mid frequency. Conditions outlined Figure 7-8.

10.7 Physical characterisation data

10.7.1 X-ray Photoemission Spectroscopy of FePc catalyst

When depositing from concentrated H_2SO_4 the N1s signal dominates the other nitrogen groups in carbon. The XPS spectra of the catalyst FePc/MON is seen in Figure A-22 for the N1s signal. No peak splitting is observed for the primary peak indicating no large binding energy shift from the influence of the carbon support, as if deposited primarily on graphite [373].

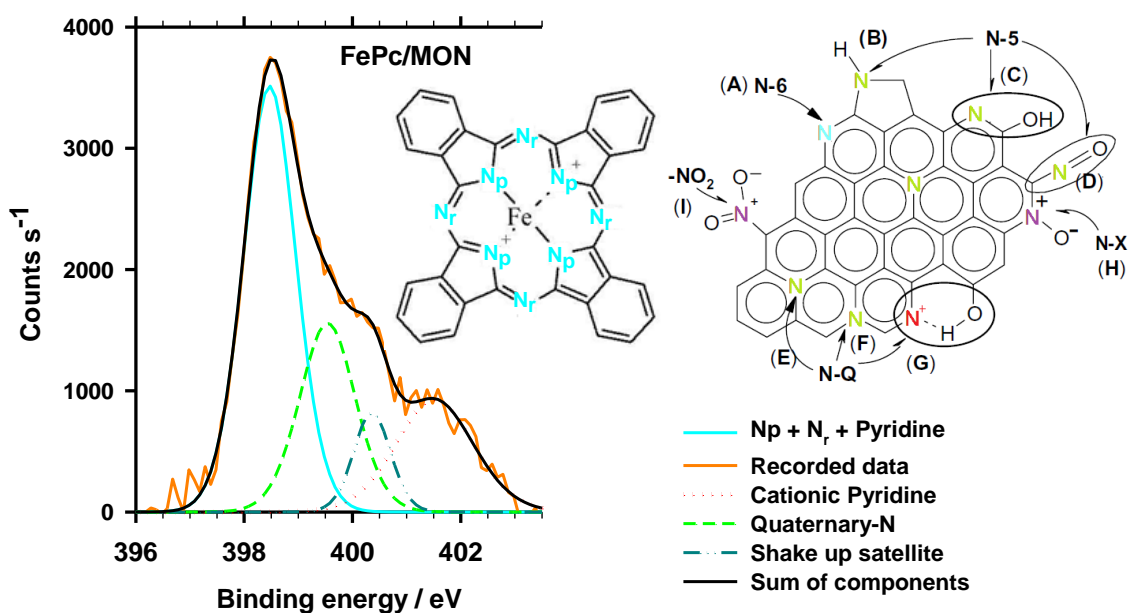


Figure A-22. XPS N1s spectra of FePc/MON. Demonstration of effective loading or Nitrogen signal in support relative to FePc. Figure on the left colour coded to N1s type. Shirley baseline subtracted, Monochromatic Al K α radiation, Pass energy; 50eV. Analysed with CASA XPS. Carbon support diagram modified from García et al [374].

10.7.2 Confocal microscopy on thin film

The surface roughness is depicted in the imaging software AnalySIS in Figure A-23 with $x=0\mu\text{m}$ set as the GC disc surface.

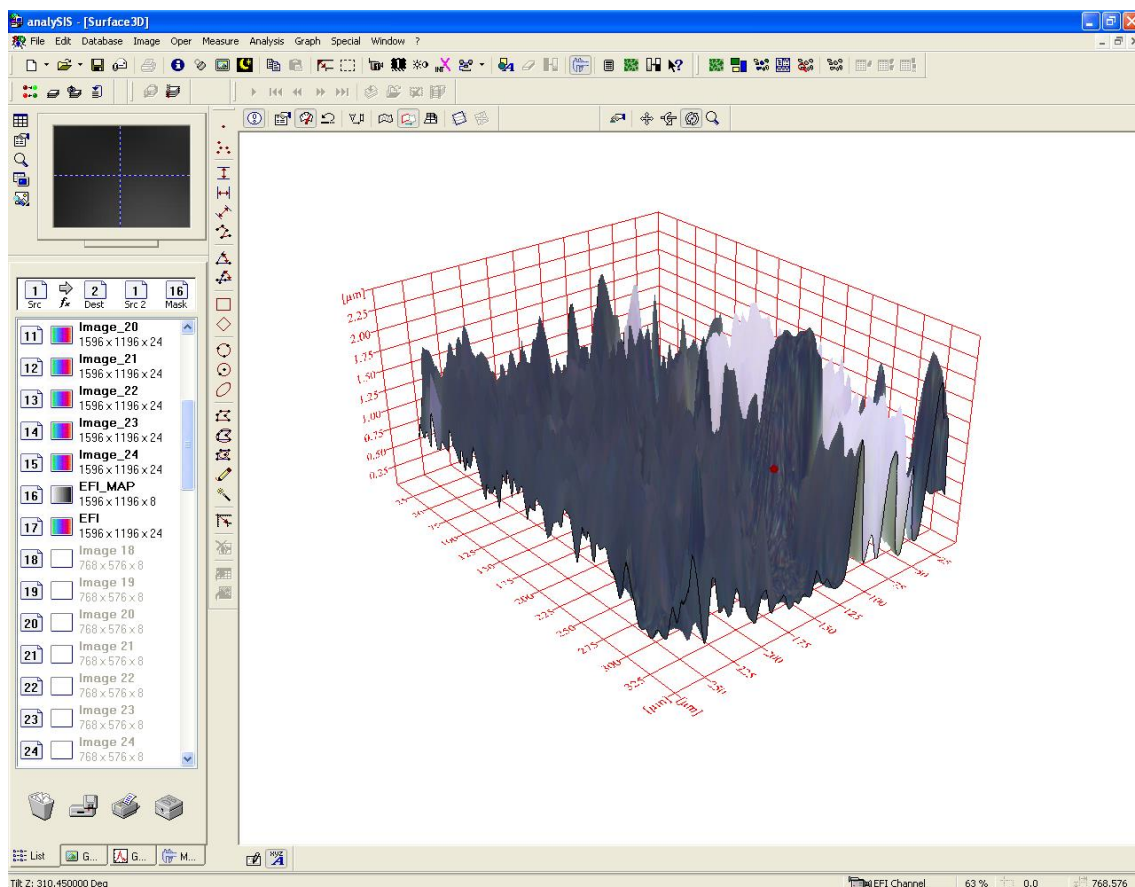


Figure A-23. Confocal microscope surface image of FePcKJB QDPSU film on GC disc. X and Y axis are microns, taken near film edge.

It is anticipated that the transparency of the Nafion would not provide a focal surface and the presented surface be smoother than that shown in Figure A-23 which possess a resolution large enough to detect graphitic edges.

10.8 Stability of Ag|AgCl reference electrodes

All reference electrodes were stored in 3M NaCl when not in use. For voltammetry in pure electrolyte the RE-5B (BASi) was used with Vycor tip. For operation in wastewater/biotic artificial wastewater the RE-6 was modified with a NaCl/Agar salt bridge as in Figure A-24.

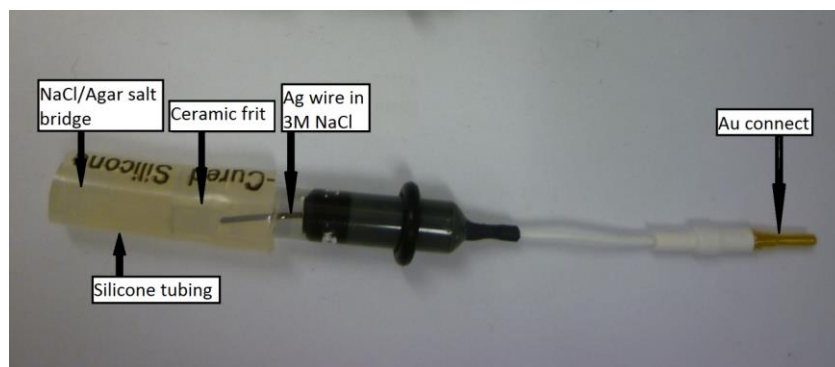
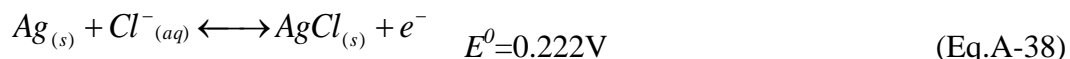


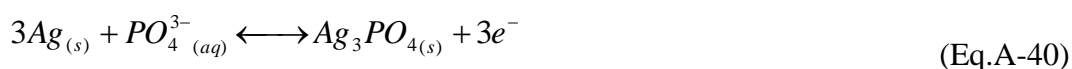
Figure A-24. Ag|AgCl reference electrode protected from wastewater bacteria and chemical poisoning by salt bridge tip. Model RE-6 (BASi).

The Agar/NaCl bridge was made from 2g Agarose, 0.5g NaCl in 50ml deionised water, heated to 95°C till Agar melted then injected into the Silicone tubing and the RE pushed through and left to cool. The $E^{0'}$ of Ag|AgCl is a function of Temperature and $[Cl^-]$ via Eq.A-39. In wastewater $[Cl^-]$ =c.a. 220 mg/L [24] (6.2mM). This would correspond to a drift of $E=0.365V$ vs NHE from $E=0.208V$ were equilibrium allowed to be established. Despite Cl^- diffusion through H_2O and 3% polymerised agar being approximately the same [375], the electrodes in Figure A-24 were consistently +30mV vs a new Ag|AgCl, showing AgCl layer integrity was maintained. Additionally bacterial colonisation in the frit is not possible.



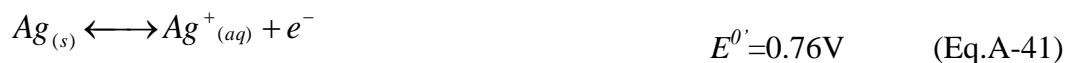
$$E^{0'} = E^0 - \log[Cl^-] 2.303RT/F \quad (Eq.A-39)$$

In this thesis, mono-anionic solutions possess a lower chemical potential and higher $E^{0'}$ of the Ag|AgX couple than Ag|AgCl. This predicts no significant drift in rest potential in solutions where X is; Phosphate (Eq.A-40), Sulphate ($E^0=0.449V$), Nitrate (no surface reaction, $AgNO_3$ soluble), Nitrite ($E^0=0.564V$), Carbonate ($E^0=0.47V$) or Acetate (no reaction, $AgCH_3COO$ soluble). Silver sulphate is semi-soluble and Silver Nitrate are highly soluble.

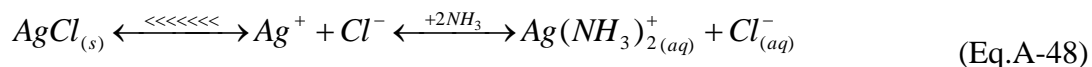
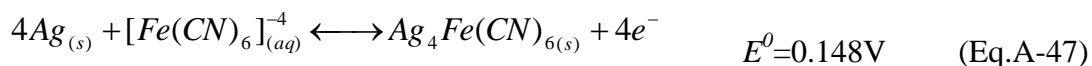


$$E^{0'}(pH7, 50mM PBS)=0.328V \text{ vs } Ag|AgCl^{19} [376]$$

¹⁹ MFC cell alkalination increases $[PO_4^{3-}]$ meaning electrode life is reduced only at high pH.



The Ag|AgCl redox is poisoned by the reaction of AgCl and anions possessing lower E^0 (pH7) than the Ag|AgCl couple. Dissolution of solid AgCl surfaces begins in the presence of ammonia above pH6.8 [377]. Common poisoning reactions of Ag|AgCl reference electrodes;



The concentration of these pollutants is relatively low in wastewater making potential drift and anion substitution of AgCl relatively slow. NH_3/NH_3OH is one of the primary pollutants in aerated wastewater, while in anoxic wastewater S^{2-} may not permeate the agar tip with the salt bridge in place. The drift was <30mV with the agar bridge in place over repeated cycles with wastewater.

10.9 MFC components

The air reservoir created by the non-stretched parafilm cover was 8ml in volume. The oxygen permeability of the parafilm is unknown but aims to avoid aerobic conditions during *OCP* or start-up. For mature biofilm at $P=P_{max}$, O_2 constriction from parafilm causes $V_{cell} < 0.01V$ in 40mins, due to a drop in E_{cat} .



Figure A-25. Parasitic biofilm growth on air cathode. 17 day exposure to wastewater

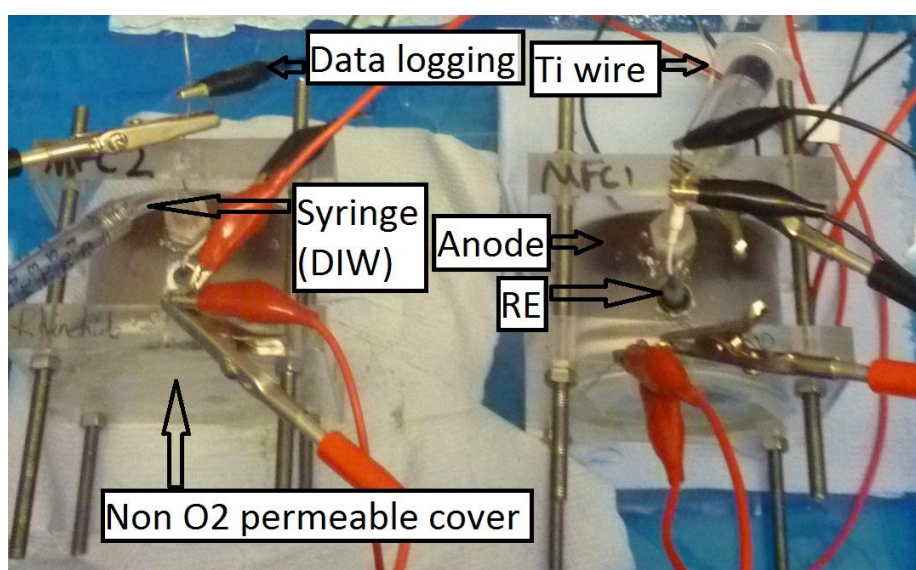


Figure A-26. SCMFC with parafilm covered to control oxygen flux at OCP and start-up.

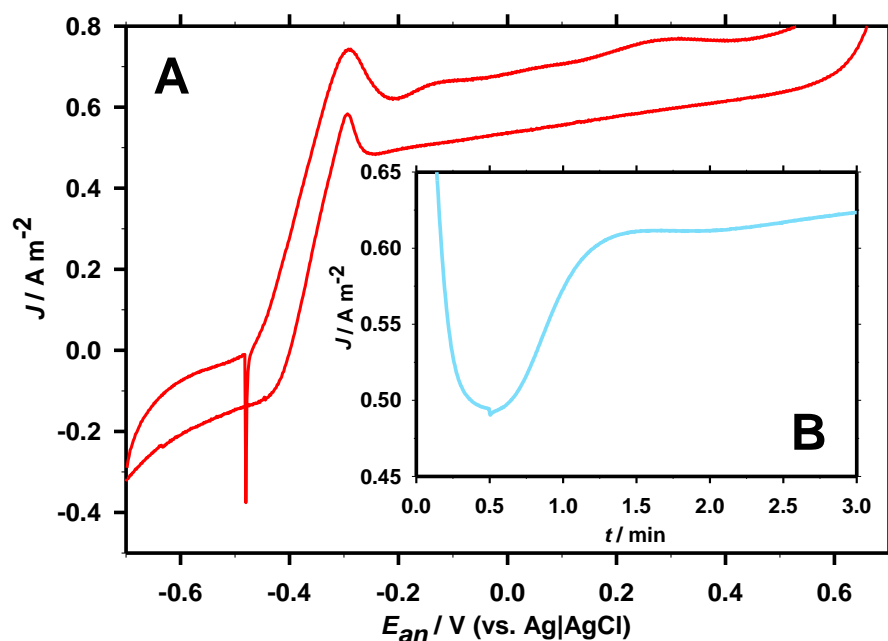


Figure A-27. Carbon felt supported biofilm (A); CV, $\nu=2\text{mV/s}$. (B); Potentiostatic $E=-0.3\text{V}$. Electrolyte; anaerobic WW-PBS, pH 7.0.

The lag in response after E is stepped from OCP to $E=-0.3\text{V}$ is initially a capacitive response. The increase in current after equilibrium is established ($t=1.5\text{min}$) is minimised by the 20minute stabilisation time of polarisation curves, a factor that cannot be discounted when using potentiostat analysis for power curves.

Conferences and Publications

Aspects of this work were reported in;

Burkitt, R., and Yu, Eileen Hao. (2010). *Application of Anion Exchange Membranes in Microbial Fuel Cells*. Oral Presentation. Anion-Exchange Membranes for Energy Generation Technologies, Surrey University. 25th-26th July 2013

R, Burkitt. *Low Cost Oxygen Reduction Catalysts for Microbial Fuel Cells*, 61st Annual Meeting of International Society of Electrochemistry. Nice, France [378]

R, Burkitt. *Low Cost Oxygen Reduction Catalysts for Microbial Fuel Cells*, Electrochem 2010: Electrochemistry and Sustainability, SCI annual UK meet. Wolverhampton, UK.

Eileen Hao Yu, Richard Burkitt, Xu Wang, Keith Scott. *Application of anion exchange ionomer for oxygen reduction catalysts in microbial fuel cells*. *Electrochemistry Communications*, 2012. **21** : p. 30–35

Poster competition of ICheme Catalysis Subject Group, 2009 meeting, Bath university.
1st prize (£250).

References

1. Logan, B.E. and J.M. Regan, *Microbial Fuel Cells—Challenges and Applications*. Environmental Science & Technology, 2006. **40**(17): p. 5172-5180.
2. Velasquez-Orta, S.B., *Bioelectricity production from simple and complex organic compounds using microbial fuel cells*, in *School of Civil Engineering and Geosciences 2010*, Newcastle University: Newcastle upon Tyne, UK. p. 145.
3. Brar, M.S., S.S. Malhi, A.P. Singh, C.L. Arora, and K.S. Gill, *Sewage water irrigation effects on some potentially toxic trace elements in soil and potato plants in northwestern India*. Canadian Journal of Soil Science, 2000. **80**(3): p. 465-471.
4. D'Ascenzo, G., A. Di Corcia, A. Gentili, R. Mancini, R. Mastropasqua, M. Nazzari, and R. Samperi, *Fate of natural estrogen conjugates in municipal sewage transport and treatment facilities*. Science of The Total Environment, 2003. **302**(1-3): p. 199-209.
5. Petrovic, M., M. Solé, M.J. López De Alda, and D. Barceló, *Endocrine disruptors in sewage treatment plants, receiving river waters, and sediments: Integration of chemical analysis and biological effects on feral carp*. Environmental Toxicology and Chemistry, 2002. **21**(10): p. 2146-2156.
6. Lindqvist, N., T. Tuhkanen, and L. Kronberg, *Occurrence of acidic pharmaceuticals in raw and treated sewage and in receiving waters*. Water Research, 2005. **39**(11): p. 2219-2228.
7. Foley, J.M., R.A. Rozendal, C.K. Hertle, P.A. Lant, and K. Rabaey, *Life Cycle Assessment of High-Rate Anaerobic Treatment, Microbial Fuel Cells, and Microbial Electrolysis Cells*. Environmental Science & Technology, 2010. **44**(9): p. 3629-3637.
8. O'Hayre, R., S.W. Cha, W. Colella, and F.B. Prinz, *Fuel Cell fundamentals*. 2nd ed 2008: John Wiley & Sons.
9. Potter, M.C. *Electrical effects accompanying the decomposition of organic compounds*. in *Proceedings of the royal society*. 1911. London: RSC.
10. Pant, D., G. Van Bogaert, L. Diels, and K. Vanbroekhoven, *A review of the substrates used in microbial fuel cells (MFCs) for sustainable energy production*. Bioresource Technology, 2010. **101**(6): p. 1533-1543.
11. Liu, H. and B.E. Logan, *Electricity Generation Using an Air-Cathode Single Chamber Microbial Fuel Cell in the Presence and Absence of a Proton Exchange Membrane*. Environmental Science & Technology, 2004. **38**(14): p. 4040-4046.
12. Huang, L., J.M. Regan, and X. Quan, *Electron transfer mechanisms, new applications, and performance of biocathode microbial fuel cells*. Bioresource Technology, 2011. **102**(1): p. 316-323.
13. Rosenbaum, M., F. Aulenta, M. Villano, and L.T. Angenent, *Cathodes as electron donors for microbial metabolism: Which extracellular electron transfer mechanisms are involved?* Bioresource Technology, 2011. **102**(1): p. 324-333.
14. Pons, L., M.L. Délia, and A. Bergel, *Effect of surface roughness, biofilm coverage and biofilm structure on the electrochemical efficiency of microbial cathodes*. Bioresource Technology, 2011. **102**(3): p. 2678-2683.
15. Wagner, R.C., D.F. Call, and B.E. Logan, *Optimal Set Anode Potentials Vary in Bioelectrochemical Systems*. Environmental Science & Technology, 2010. **44**(16): p. 6036-6041.
16. Hamelers, H.V.M., A. ter Heijne, N. Stein, R.A. Rozendal, and C.J.N. Buisman, *Butler-Volmer-Monod model for describing bio-anode polarization curves*. Bioresource Technology, 2011. **102**(1): p. 381-387.
17. Logan, B.E., P. Aelterman, B. Hamelers, R. Rozendal, U. Schröder, J. Keller, S. Freguia, W. Verstraete, and K. Rabaey, *Microbial fuel cells: Methodology and technology*. Environmental Science & Technology, 2006. **40**(17): p. 5181 - 5192.
18. Zagal, J.H., F. Bedioui, and J.-P. Dodelet, *N₄ Macrocyclic Metal Complexes*, ed. J.H. Zagal, F. Bedioui, and J.-P. Dodelet. Vol. 1. 2009: Springer. 814.
19. Wei, J., P. Liang, X. Cao, and X. Huang, *A New Insight into Potential Regulation on Growth and Power Generation of Geobacter sulfurreducens in Microbial Fuel Cells Based on Energy Viewpoint*. Environmental Science & Technology, 2010. **44**(8): p. 3187-3191.
20. Aelterman, P., S. Freguia, J. Keller, W. Verstraete, and K. Rabaey, *The anode potential regulates bacterial activity in microbial fuel cells*. Applied Microbiology and Biotechnology, 2008. **78**(3): p. 409-418.
21. Busalmen, J.P., A. Esteve-Núñez, and J.M. Feliu, *Whole Cell Electrochemistry of Electricity-Producing Microorganisms Evidence an Adaptation for Optimal Exocellular Electron Transport*. Environmental Science & Technology, 2008. **42**(7): p. 2445-2450.
22. Torres, C.S.I., R. Krajmalnik-Brown, P. Parameswaran, A.K. Marcus, G. Wanger, Y.A. Gorby, and B.E. Rittmann, *Selecting Anode-Respiring Bacteria Based on Anode Potential: Phylogenetic,*

- Electrochemical, and Microscopic Characterization*. Environmental Science & Technology, 2009. **43**(24): p. 9519-9524.
23. Ahn, Y. and B.E. Logan, *Effectiveness of domestic wastewater treatment using microbial fuel cells at ambient and mesophilic temperatures*. Bioresource Technology, 2010. **101**(2): p. 469-475.
 24. Krauter, P.W., J.E. Harrar, and S.P. Orloff, *Effect of CO₂-Air Mixtures on the pH of Air-Stripped Water at Treatment Facility D*. Technical Report, 1998.
 25. Fan, Y., H. Hu, and H. Liu, *Enhanced Coulombic efficiency and power density of air-cathode microbial fuel cells with an improved cell configuration*. Journal of Power Sources, 2007. **171**(2): p. 348-354.
 26. Ozkan, U.S., *Bridging Heterogeneous Catalysis and Electro-catalysis: Catalytic Reactions Involving Oxygen*. Topics in Catalysis, 2013. **56**: p. 1603-1610.
 27. Wieckowski, A. and M. Neurock, *Contrast and Synergy between Electrocatalysis and Heterogeneous Catalysis*. Advances in Physical Chemistry, 2011.
 28. Harnisch, F., S. Wirth, and U. Schröder, *Effects of substrate and metabolite crossover on the cathodic oxygen reduction reaction in microbial fuel cells: Platinum vs. iron(II) phthalocyanine based electrodes*. Electrochemistry Communications, 2009. **11**(11): p. 2253-2256.
 29. Tian, F. and A.B. Anderson, *Effective Reversible Potential, Energy Loss, and Overpotential on Platinum Fuel Cell Cathodes*. The Journal of Physical Chemistry C, 2011. **115**(10): p. 4076-4088.
 30. Tsou, Y.-M. and F.C. Anson, *Shifts in Redox Formal Potentials Accompanying the Incorporation of Cationic Complexes in Perfluoro Polycarboxylate and Polysulfonate Coatings on Graphite Electrodes*. Journal of The Electrochemical Society, 1984. **131**(3): p. 595-601.
 31. Léger, C. *An introduction to electrochemical methods for the functional analysis of metalloproteins*. 2012; Available from: bip.cnrs-mrs.fr/bip06/pdf/louvain-CL-2011.pdf.
 32. Zagal, J.H., S. Griveau, J.F. Silva, T. Nyokong, and F. Bedioui, *Metallophthalocyanine-based molecular materials as catalysts for electrochemical reactions*. Coordination Chemistry Reviews, 2010. **254**(23-24): p. 2755-2791.
 33. Treimer, S., A. Tang, and D.C. Johnson, *A Consideration of the Application of Koutecký-Levich Plots in the Diagnoses of Charge-Transfer Mechanisms at Rotated Disk Electrodes*. Electroanalysis, 2002. **14**(3): p. 165-171.
 34. Petrii, O.A., R.R. Nazmutdinov, M.D. Bronshtein, and G.A. Tsirlina, *Life of the Tafel equation: Current understanding and prospects for the second century*. Electrochimica Acta, 2007. **52**(11): p. 3493-3504.
 35. Bard, A.J. and L.R. Faulkner, *Electrochemical methods; Fundamentals and Applications* 2001: John Wiley and Sons, Inc.
 36. Gnanamuthu, D.S. and J.V. Petrocelli, *Closure to 'Discussion of 'A Generalized Expression for the Tafel Slope and the Kinetics of Oxygen Reduction on Noble Metal and Alloys' [D. S. Gnanamuthu and J. V. Petrocelli (pp. 1036--1041, Vol. 114, No. 10)]'*. Journal of The Electrochemical Society, 1968. **115**(6): p. 625.
 37. Hurlen, T., Y.L. Sandler, and E.A. Pantier, *Reactions of oxygen and hydrogen peroxide at silver electrodes in alkaline solutions*. Electrochimica Acta, 1966. **11**(10): p. 1463-1473.
 38. Danilov, F. and V. Protzenko, *Actual activation energy of electrochemical reactions at stage charge transfer*. Russian Journal of Electrochemistry, 2010. **46**(2): p. 188-195.
 39. Appleby, A. and J. Zagal, *Free energy relationships in electrochemistry: a history that started in 1935*. Journal of Solid State Electrochemistry, 2011. **15**(7): p. 1811-1832.
 40. Song, C. and J. Zhang, *Electrocatalytic Oxygen Reduction Reaction*, in *PEM Fuel Cell Electrocatalysts and Catalyst Layers* 2008. p. 89-134.
 41. Cheng, S., H. Liu, and B.E. Logan, *Increased Power Generation in a Continuous Flow MFC with Advective Flow through the Porous Anode and Reduced Electrode Spacing*. Environmental Science & Technology, 2006. **40**(7): p. 2426-2432.
 42. Appleby, A.J. and M. Savy, *Kinetics of oxygen reduction reactions involving catalytic decomposition of hydrogen peroxide: Application to porous and rotating ring-disk electrodes*. Journal of Electroanalytical Chemistry, 1978. **92**(1): p. 15-30.
 43. Khudaish, E.A., *The electrochemical oxidation of hydrogen peroxide on platinum electrodes at phosphate buffer solutions* 1999, Massey University: Palmerston.
 44. Hsueh, K.L., D.T. Chin, and S. Srinivasan, *Electrode kinetics of oxygen reduction: A theoretical and experimental analysis of the rotating ring-disc electrode method*. Journal of Electroanalytical Chemistry and Interfacial Electrochemistry, 1983. **153**(1-2): p. 79-95.
 45. Dalton Jr. I, A.A., PA), Bauer, Jeffery V. (Macungie, PA), *Method of stabilizing hydrogen peroxide solutions*, 1982, Air Products and Chemicals, Inc. (Allentown, PA): United States.
 46. Bray, R., C., *Free-Radical Intermediates in the Reduction of Oxygen*. PROCEEDINGS OF THE BIOCHEMICAL SOCIETY, 1970: p. 13P.
 47. Xu, Y., *Comparative studies of the Fe³⁺/Fe²⁺-UV, H₂O₂-UV, TiO₂-UV/vis systems for the decolorization of a textile dye X-3B in water*. Chemosphere, 2001. **43**(8): p. 1103-1107.

48. Wilke, C.R., M. Eisenberg, and C.W. Tobias, *Correlation of Limiting Currents under Free Convection Conditions*. Journal of The Electrochemical Society, 1953. **100**(11): p. 513-523.
49. Schütz, G., *Natural convection mass-transfer measurements on spheres and horizontal cylinders by an electrochemical method*. International Journal of Heat and Mass Transfer, 1963. **6**(10): p. 873-879.
50. G. H. Sedahmed, M. Z. El-abd, I. A. S. Mansour, A. M. Ahmed, and A.A. Wragg, *The role of natural convection mass transfer in the kinetics of electropolishing of horizontal surfaces*. Journal of Applied Electrochemistry, 1979. **9**(1): p. 1-6.
51. G. H. Sedahmed, M. Z. El-Abd, I. A. S. Mansour, A. M. Ahmed, and A.A. Wragg, *The role of natural convection mass transfer in the kinetics of electropolishing of horizontal surfaces*. Journal of Applied Electrochemistry. **9**: p. 1-6.
52. Artyushkova, K., S. Pylypenko, T.S. Olson, J.E. Fulghum, and P. Atanasov, *Predictive Modeling of Electrocatalyst Structure Based on Structure-to-Property Correlations of X-ray Photoelectron Spectroscopic and Electrochemical Measurements*. Langmuir, 2008. **24**(16): p. 9082-9088.
53. Holdcroft, S., *Charge Transfer in Electroactive Polymer Films in Department of Chemistry* 1987, Simon Fraser University: Vancouver.
54. Newman, J., *Current Distribution on a Rotating Disk below the Limiting Current*. Journal of The Electrochemical Society, 1966. **113**(12): p. 1235-1241.
55. Levich, V.G., *Physicochemical Hydrodynamics*, 1962: Prentice-Hall, Englewood Cliffs, NJ.
56. Vargas, R., C. Borrás, J. Mostany, and B.R. Scharifker, *Kinetics of surface reactions on rotating disk electrodes*. Electrochimica Acta, 2012. **80**(0): p. 326-333.
57. Durand, R.R., C.S. Bencosme, J.P. Collman, and F.C. Anson, *Mechanistic aspects of the catalytic reduction of dioxygen by cofacial metalloporphyrins*. Journal of the American Chemical Society, 1983. **105**(9): p. 2710-2718.
58. Gottesfeld, S., I.D. Raistrick, and S. Srinivasan, *Oxygen Reduction Kinetics on a Platinum RDE Coated with a Recast Nafion Film*. Journal of The Electrochemical Society, 1987. **134**(6): p. 1455-1462.
59. Andrieux, C.P. and J.M. Savéant, *Kinetics of electrochemical reactions mediated by redox polymer films: Pre-activation (CE) mechanisms*. Journal of Electroanalytical Chemistry and Interfacial Electrochemistry, 1984. **171**(1-2): p. 65-93.
60. Andrieux, C.P. and J.M. Savéant, *Kinetics of electrochemical reactions mediated by redox polymer films: Irreversible cross-exchange reactions: Formulation in terms of characteristic currents for stationary techniques*. Journal of Electroanalytical Chemistry and Interfacial Electrochemistry, 1982. **134**(1): p. 163-166.
61. Wroblowa, H.S., P. Yen Chi, and G. Razumney, *Electroreduction of oxygen: A new mechanistic criterion*. Journal of Electroanalytical Chemistry and Interfacial Electrochemistry, 1976. **69**(2): p. 195-201.
62. Jovancicevic, V. and J.O.M. Bockris, *The Mechanism of Oxygen Reduction on Iron in Neutral Solutions*. Journal of The Electrochemical Society, 1986. **133**(9): p. 1797-1807.
63. Bouwkamp-Wijnoltz, A.L., W. Visscher, and J.A.R. van Veen, *The selectivity of oxygen reduction by pyrolysed iron porphyrin supported on carbon*. Electrochimica Acta, 1998. **43**(21-22): p. 3141-3152.
64. Prakash, J., D.A. Tryk, and E.B. Yeager, *Kinetic Investigations of Oxygen Reduction and Evolution Reactions on Lead Ruthenate Catalysts*. Journal of The Electrochemical Society, 1999. **146**(11): p. 4145-4151.
65. Olson, T.S., S. Pylypenko, J.E. Fulghum, and P. Atanasov, *Bifunctional Oxygen Reduction Reaction Mechanism on Non-Platinum Catalysts Derived from Pyrolyzed Porphyrins*. Journal of The Electrochemical Society, 2010. **157**(1): p. B54-B63.
66. Wang, F. and S. Hu, *Studies of electrochemical reduction of dioxygen with RRDE*. Electrochimica Acta, 2006. **51**(20): p. 4228-4235.
67. Van Den Brink, F., W. Visscher, and E. Barendrecht, *Electrocatalysis of cathodic oxygen reduction by metal phthalocyanines: Part IV. Iron phthalocyanine as electrocatalyst: Mechanism*. Journal of Electroanalytical Chemistry, 1984. **175**(1-2): p. 279-289.
68. Zečević, S., D.M. Dražić, and S. Gojković, *Oxygen reduction on iron—IV. The reduction of hydrogen peroxide as the intermediate in oxygen reduction reaction in alkaline solutions*. Electrochimica Acta, 1991. **36**(1): p. 5-14.
69. Paliteiro, C., A. Hamnett, and J.B. Goodenough, *The electroreduction of dioxygen on thin films of gold in alkaline solution*. Journal of Electroanalytical Chemistry and Interfacial Electrochemistry, 1987. **234**(1-2): p. 193-211.
70. Chen, R., H. Li, D. Chu, and G. Wang, *Unraveling Oxygen Reduction Reaction Mechanisms on Carbon-Supported Fe-Phthalocyanine and Co-Phthalocyanine Catalysts in Alkaline Solutions*. The Journal of Physical Chemistry C, 2009. **113**(48): p. 20689-20697.

71. Appleby, A.J. and J. Marie, *Kinetics of oxygen reduction on carbon materials in alkaline solution*. *Electrochimica Acta*, 1979. **24**(2): p. 195-202.
72. Damjanovic, A., M.A. Genshaw, and J.O.M. Bockris, *The Role of Hydrogen Peroxide in the Reduction of Oxygen at Platinum Electrodes*. *The Journal of Physical Chemistry*, 1966. **70**(11): p. 3761-3762.
73. van den Brink, F., E. Barendrecht, and W. Visscher, *Hydrogen Peroxide as an Intermediate in Electrocatalytic Reduction of Oxygen. A New Method for the Determination of Rate Constants*. *Journal of The Electrochemical Society*, 1980. **127**(9): p. 2003-2006.
74. Anastasijević, N.A., V. Vesović, and R.R. Adžić, *Determination of the kinetic parameters of the oxygen reduction reaction using the rotating ring-disk electrode: Part I. Theory*. *Journal of Electroanalytical Chemistry and Interfacial Electrochemistry*, 1987. **229**(1-2): p. 305-316.
75. Zečević, S., D.M. Dražić, and S. Gojković, *Oxygen reduction on iron: Part III. An analysis of the rotating disk-ring electrode measurements in near neutral solutions*. *Journal of Electroanalytical Chemistry and Interfacial Electrochemistry*, 1989. **265**(1-2): p. 179-193.
76. Toupin, M., D. Bélanger, I.R. Hill, and D. Quinn, *Performance of experimental carbon blacks in aqueous supercapacitors*. *Journal of Power Sources*, 2005. **140**(1): p. 203-210.
77. Anson, F.C., J.M. Saveant, and K. Shigehara, *Self-exchange reactions at redox polymer electrodes. A kinetic model and theory for stationary voltammetric techniques*. *The Journal of Physical Chemistry*, 1983. **87**(2): p. 214-219.
78. Lyons, M.E.G., *Electrocatalysis using electroactive polymers, electroactive composites and microheterogeneous systems*. *Analyst*, 1994. **119**(5): p. 805-826.
79. Andrieux, C.P. and J.M. Saveant, *Electroneutrality coupling of electron hopping between localized sites with electroinactive counterion displacement. I. Potential-step plateau currents*. *The Journal of Physical Chemistry*, 1988. **92**(23): p. 6761-6767.
80. Laviron, E., *The use of linear potential sweep voltammetry and of a.c. voltammetry for the study of the surface electrochemical reaction of strongly adsorbed systems and of redox modified electrodes*. *Journal of Electroanalytical Chemistry and Interfacial Electrochemistry*, 1979. **100**(1-2): p. 263-270.
81. Hirst, J., *Elucidating the mechanisms of coupled electron transfer and catalytic reactions by protein film voltammetry*. *Biochimica et Biophysica Acta (BBA) - Bioenergetics*, 2006. **1757**(4): p. 225-239.
82. Laviron, E. and L. Roullier, *General expression of the linear potential sweep voltammogram for a surface redox reaction with interactions between the adsorbed molecules: Applications to modified electrodes*. *Journal of Electroanalytical Chemistry and Interfacial Electrochemistry*, 1980. **115**(1): p. 65-74.
83. Laviron, E., *A.C. polarography and faradaic impedance of strongly adsorbed electroactive species: Part I. Theoretical and experimental study of a quasi-reversible reaction in the case of a Langmuir isotherm*. *Journal of Electroanalytical Chemistry and Interfacial Electrochemistry*, 1979. **97**(2): p. 135-149.
84. Contamin, O., E. Levart, and M. Savy, *Inhibition of oxygen reduction on iron phthalocyanine layers by glutathione in buffered neutral media: Investigation by potentiometry, cyclic voltammetry and operational impedance techniques*. *Journal of Electroanalytical Chemistry and Interfacial Electrochemistry*, 1980. **115**(2): p. 267-278.
85. Godwin, J., *Immobilized Mediator Electrodes for Microbial Fuel Cells*, in *Department of Chemical and Biological Engineering 2011*, University of Saskatchewan.
86. Barsoukov, E. and J.R. Macdonald, *Impedance Spectroscopy* 2005, Hoboken, New Jersey: Wiley & Sons.
87. Láng, G. and G. Inzelt, *Some problems connected with impedance analysis of polymer film electrodes: effect of the film thickness and the thickness distribution*. *Electrochimica Acta*, 1991. **36**(5-6): p. 847-854.
88. Rubinstein, I., J. Rishpon, and S. Gottesfeld, *An AC-Impedance Study of Electrochemical Processes at Nafion-Coated Electrodes*. *Journal of The Electrochemical Society*, 1986. **133**(4): p. 729-734.
89. Mamuru, S.A. and K.I. Ozoemena, *Heterogeneous Electron Transfer and Oxygen Reduction Reaction at Nanostructured Iron(II) Phthalocyanine and Its MWCNTs Nanocomposites*. *Electroanalysis*, 2010. **22**(9): p. 985-994.
90. Komura, T., Y. Ito, T. Yamaguti, and K. Takahasi, *Charge-transport processes at poly-o-aminophenol film electrodes: electron hopping accompanied by proton exchange*. *Electrochimica Acta*, 1997. **43**(7): p. 723-731.
91. Schiewe, J., J. Házi, V.A. Vicente-Beckett, and A.M. Bond, *A unified approach to trace analysis and evaluation of electrode kinetics with fast Fourier transform electrochemical instrumentation*. *Journal of Electroanalytical Chemistry*, 1998. **451**(1-2): p. 129-138.
92. Holze, R. and W. Vielstich, *Double-layer capacity measurements as a method to characterize porous fuel cell electrodes*. *Electrochimica Acta*, 1984. **29**(5): p. 607-610.

93. Vedalakshmi, R., V. Saraswathy, H.-W. Song, and N. Palaniswamy, *Determination of diffusion coefficient of chloride in concrete using Warburg diffusion coefficient*. Corrosion Science, 2009. **51**(6): p. 1299-1307.
94. Armstrong, R.D., B. Lindholm, and M. Sharp, *Impedance characteristics of a modified electrode*. Journal of Electroanalytical Chemistry and Interfacial Electrochemistry, 1986. **202**(1-2): p. 69-74.
95. Contamin, O., E. Levart, G. Magner, R. Parsons, and M. Savy, *Restricted diffusion impedance: Theory and application to the reaction of oxygen on a hydrogen phthalocyanine film*. Journal of Electroanalytical Chemistry and Interfacial Electrochemistry, 1984. **179**(1-2): p. 41-52.
96. Contamin, O., E. Levart, and D. Schuhmann, *Study of the concentration impedance on a thin-layer cell: Part III. Diffusion coupled to a fast first-order chemical reaction*. Journal of Electroanalytical Chemistry and Interfacial Electrochemistry, 1978. **88**(1): p. 49-56.
97. Gabrielli, C., O. Haas, and H. Takenouti, *Impedance analysis of electrodes modified with a reversible redox polymer film*. Journal of Applied Electrochemistry, 1987. **17**(1): p. 82-90.
98. Kahlert, H., U. Retter, H. Lohse, K. Siegler, and F. Scholz, *On the Determination of the Diffusion Coefficients of Electrons and of Potassium Ions in Copper(II) Hexacyanoferrate(II) Composite Electrodes*. The Journal of Physical Chemistry B, 1998. **102**(44): p. 8757-8765.
99. Komura, T., G.Y. Niu, T. Yamaguchi, and M. Asano, *Redox and ionic-binding switched fluorescence of phenosafranine and thionine included in Nafion® films*. Electrochimica Acta, 2003. **48**(6): p. 631-639.
100. Lindholm, B., *Ac-impedance studies of charge transport and redox capacities at poly-4-vinylpyridine films on electrode surfaces*. Journal of Electroanalytical Chemistry and Interfacial Electrochemistry, 1990. **289**(1-2): p. 85-101.
101. Mathias, M.F. and O. Haas, *An alternating current impedance model including migration and redox-site interactions at polymer-modified electrodes*. The Journal of Physical Chemistry, 1992. **96**(7): p. 3174-3182.
102. Cameron, C.G., *Enhanced Rates of Electron Transport in Conjugated-Redox Polymer Hybrids* in Department of Chemistry 2010, Memorial University, Newfoundland: St. John's.
103. Armstrong, R.D., *Impedance plane display for an electrode with diffusion restricted to a thin layer*. Journal of Electroanalytical Chemistry and Interfacial Electrochemistry, 1986. **198**(1): p. 177-180.
104. Wang, H. and L. Pilon, *Intrinsic limitations of impedance measurements in determining electric double layer capacitances*. Electrochimica Acta, 2012. **63**(0): p. 55-63.
105. Komura, T., Y. Funahashi, T. Yamaguchi, and K. Takahashi, *Dependence of redox-kinetic parameters at poly(o-phenylenediamine)-modified electrodes upon the oxidation and protonation levels of the polymer*. Journal of Electroanalytical Chemistry, 1998. **446**(1-2): p. 113-123.
106. Mao, Y., L. Zhang, D. Li, H. Shi, Y. Liu, and L. Cai, *Power generation from a biocathode microbial fuel cell biocatalyzed by ferro/manganese-oxidizing bacteria*. Electrochimica Acta, 2010. **55**(27): p. 7804-7808.
107. Chung, K., I. Fujiki, and S. Okabe, *Effect of formation of biofilms and chemical scale on the cathode electrode on the performance of a continuous two-chamber microbial fuel cell*. Bioresource Technology, 2011. **102**(1): p. 355-360.
108. Virdis, B., K. Rabaey, R.A. Rozendal, Z. Yuan, and J. Keller, *Simultaneous nitrification, denitrification and carbon removal in microbial fuel cells*. Water Research, 2010. **44**(9): p. 2970-2980.
109. Rodrigo, M.A., P. Cañizares, and J. Lobato, *Effect of the electron-acceptors on the performance of a MFC*. Bioresource Technology, 2010. **101**(18): p. 7014-7018.
110. Rhoads, A., H. Beyenal, and Z. Lewandowski, *Microbial Fuel Cell using Anaerobic Respiration as an Anodic Reaction and Biomineralized Manganese as a Cathodic Reactant*. Environmental Science & Technology, 2005. **39**(12): p. 4666-4671.
111. Butler, C.S., P. Clauwaert, S.J. Green, W. Verstraete, and R. Nerenberg, *Bioelectrochemical Perchlorate Reduction in a Microbial Fuel Cell*. Environmental Science & Technology, 2010. **44**(12): p. 4685-4691.
112. ter Heijne, A., H.V.M. Hamelers, and C.J.N. Buisman, *Microbial Fuel Cell Operation with Continuous Biological Ferrous Iron Oxidation of the Catholyte*. Environmental Science & Technology, 2007. **41**(11): p. 4130-4134.
113. Birry, L., P. Mehta, F. Jaouen, J.P. Dodelet, S.R. Guiot, and B. Tartakovsky, *Application of iron-based cathode catalysts in a microbial fuel cell*. Electrochimica Acta, 2011. **56**(3): p. 1505-1511.
114. Wang, X., S. Cheng, X. Zhang, X.-y. Li, and B.E. Logan, *Impact of salinity on cathode catalyst performance in microbial fuel cells (MFCs)*. International Journal of Hydrogen Energy, 2011. **36**(21).
115. Wang, L., P. Liang, J. Zhang, and X. Huang, *Activity and stability of pyrolyzed iron ethylenediaminetetraacetic acid as cathode catalyst in microbial fuel cells*. Bioresource Technology, 2011. **102**(8): p. 5093-5097.

116. Li, X., B. Hu, S. Suib, Y. Lei, and B. Li, *Electricity generation in continuous flow microbial fuel cell (MFCs) with manganese dioxide (MnO₂) cathodes*. Biochemical Engineering Journal, 2011. **54**(1): p. 10-15.
117. Li, X., B. Hu, S. Suib, Y. Lei, and B. Li, *Manganese dioxide as a new cathode catalyst in microbial fuel cells*. Journal of Power Sources, 2010. **195**(9): p. 2586-2591.
118. Lefebvre, O., W.K. Ooi, Z. Tang, M. Abdullah-Al-Mamun, D.H.C. Chua, and H.Y. Ng, *Optimization of a Pt-free cathode suitable for practical applications of microbial fuel cells*. Bioresource Technology, 2009. **100**(20): p. 4907-4910.
119. Roche, I., K. Katuri, and K. Scott, *A microbial fuel cell using manganese oxide oxygen reduction catalysts*. Journal of Applied Electrochemistry, 2010. **40**(1): p. 13-21.
120. Zhang, L., C. Liu, L. Zhuang, W. Li, S. Zhou, and J. Zhang, *Manganese dioxide as an alternative cathodic catalyst to platinum in microbial fuel cells*. Biosensors and Bioelectronics, 2009. **24**(9): p. 2825-2829.
121. Duteanu, N., B. Erable, S.M. Senthil Kumar, M.M. Ghangrekar, and K. Scott, *Effect of chemically modified Vulcan XC-72R on the performance of air-breathing cathode in a single-chamber microbial fuel cell*. Bioresource Technology, 2010. **101**(14): p. 5250-5255.
122. Wang, H., Z. Wu, A. Plaseied, P. Jenkins, L. Simpson, C. Engtrakul, and Z. Ren, *Carbon nanotube modified air-cathodes for electricity production in microbial fuel cells*. Journal of Power Sources, 2011. **196**(18): p. 7465-7469.
123. Feng, C., F. Li, H. Liu, X. Lang, and S. Fan, *A dual-chamber microbial fuel cell with conductive film-modified anode and cathode and its application for the neutral electro-Fenton process*. Electrochimica Acta, 2010. **55**(6): p. 2048-2054.
124. Deng, Q., X. Li, J. Zuo, A. Ling, and B.E. Logan, *Power generation using an activated carbon fiber felt cathode in an upflow microbial fuel cell*. Journal of Power Sources, 2010. **195**(4): p. 1130-1135.
125. Yuan, Y., S. Zhou, and L. Zhuang, *Polypyrrole/carbon black composite as a novel oxygen reduction catalyst for microbial fuel cells*. Journal of Power Sources, 2010. **195**(11): p. 3490-3493.
126. Xiao, L., J. Damien, J. Luo, H.D. Jang, J. Huang, and Z. He, *Crumpled graphene particles for microbial fuel cell electrodes*. Journal of Power Sources, 2012. **208**(0): p. 187-192.
127. Kong, X., Y. Sun, Z. Yuan, D. Li, L. Li, and Y. Li, *Effect of cathode electron-receiver on the performance of microbial fuel cells*. International Journal of Hydrogen Energy, 2010. **35**(13): p. 7224-7227.
128. Momoh, O., *A novel electron acceptor for microbial fuel cells: Nature of circuit connection on internal resistance*. Journal of Biochemical Technology, 2010. **2**(4): p. 216-220.
129. Li, J., Q. Fu, Q. Liao, X. Zhu, D.-d. Ye, and X. Tian, *Persulfate: A self-activated cathodic electron acceptor for microbial fuel cells*. Journal of Power Sources, 2009. **194**(1): p. 269-274.
130. Borole, A.P., C.Y. Hamilton, and T.A. Vishnivetskaya, *Enhancement in current density and energy conversion efficiency of 3-dimensional MFC anodes using pre-enriched consortium and continuous supply of electron donors*. Bioresource Technology, 2011. **102**(8): p. 5098-5104.
131. Zhuang, L., S. Zhou, Y. Li, T. Liu, and D. Huang, *In situ Fenton-enhanced cathodic reaction for sustainable increased electricity generation in microbial fuel cells*. Journal of Power Sources, 2010. **195**(5): p. 1379-1382.
132. Zhang, B., C. Feng, J. Ni, J. Zhang, and W. Huang, *Simultaneous reduction of vanadium (V) and chromium (VI) with enhanced energy recovery based on microbial fuel cell technology*. Journal of Power Sources, 2012. **204**(0): p. 34-39.
133. Zhang, B., H. Zhao, C. Shi, S. Zhou, and J. Ni, *Simultaneous removal of sulfide and organics with vanadium(V) reduction in microbial fuel cells*. Journal of Chemical Technology & Biotechnology, 2009. **84**(12): p. 1780-1786.
134. Morris, J.M., S. Jin, J. Wang, C. Zhu, and M.A. Urynowicz, *Lead dioxide as an alternative catalyst to platinum in microbial fuel cells*. Electrochemistry Communications, 2007. **9**(7): p. 1730-1734.
135. Heijne, A.T., F. Liu, R.v.d. Weijden, J. Weijma, C.J.N. Buisman, and H.V.M. Hamelers, *Copper Recovery Combined with Electricity Production in a Microbial Fuel Cell*. Environmental Science & Technology, 2010. **44**(11): p. 4376-4381.
136. Fu, L., S.-J. You, G.-Q. Zhang, F.-L. Yang, X.-H. Fang, and Z. Gong, *PB/PANI-modified electrode used as a novel oxygen reduction cathode in microbial fuel cell*. Biosensors and Bioelectronics, 2011. **26**(5): p. 1975-1979.
137. Amutha, R., J. Josiah, J. Adriel Jebin, P. Jagannathan, and S. Berchmans, *Chromium hexacyanoferrate as a cathode material in microbial fuel cells*. Journal of Applied Electrochemistry, 2010. **40**(11): p. 1985-1990.
138. Feng, Y. and N. Alonso-Vante, *Nonprecious metal catalysts for the molecular oxygen-reduction reaction*. physica status solidi (b), 2008. **245**(9): p. 1792-1806.
139. Tang, D., J. Pan, S. Lu, L. Zhuang, and J. Lu, *Alkaline polymer electrolyte fuel cells: Principle, challenges, and recent progress*. SCIENCE CHINA Chemistry, 2010. **53**(2): p. 357-364.

140. Prieto, A., J. Hernández, E. Herrero, and J. Feliu, *The role of anions in oxygen reduction in neutral and basic media on gold single-crystal electrodes*. Journal of Solid State Electrochemistry, 2003. **7**(9): p. 599-606.
141. Martin, E., B. Tartakovsky, and O. Savadogo, *Cathode materials evaluation in microbial fuel cells: A comparison of carbon, Mn₂O₃, Fe₂O₃ and platinum materials*. Electrochimica Acta, 2011. **58**(0): p. 58-66.
142. Nilekar, A.U. and M. Mavrikakis, *Improved oxygen reduction reactivity of platinum monolayers on transition metal surfaces*. Surface Science, 2008. **602**(14): p. L89-L94.
143. Zhang, F., T. Saito, S. Cheng, M.A. Hickner, and B.E. Logan, *Microbial Fuel Cell Cathodes With Poly(dimethylsiloxane) Diffusion Layers Constructed around Stainless Steel Mesh Current Collectors*. Environmental Science & Technology, 2010. **44**(4): p. 1490-1495.
144. Chen, S., Y. Chen, G. He, S. He, U. Schröder, and H. Hou, *Stainless steel mesh supported nitrogen-doped carbon nanofibers for binder-free cathode in microbial fuel cells*. Biosensors and Bioelectronics, 2012. **34**(1): p. 282-285.
145. Call, D.F., M.D. Merrill, and B.E. Logan, *High Surface Area Stainless Steel Brushes as Cathodes in Microbial Electrolysis Cells*. Environmental Science & Technology, 2009. **43**(6): p. 2179-2183.
146. Goto, H., Y. Hanada, T. Ohno, and M. Matsumura, *Quantitative analysis of superoxide ion and hydrogen peroxide produced from molecular oxygen on photoirradiated TiO₂ particles*. Journal of Catalysis, 2004. **225**(1): p. 223-229.
147. Logan, B.E., B. Hamelers, R. Rozendal, U. Schröder, J. Keller, S. Freguia, P. Aelterman, W. Verstraete, and K. Rabaey, *Microbial Fuel Cells: Methodology and Technology*. Environmental Science & Technology, 2006. **40**(17): p. 5181-5192.
148. Takeno, N., *Atlas of Eh-pH diagrams*. National Institute of Advanced Industrial Science and Technology, Research Center for Deep Geological Environments, 2005.
149. Tengvall, P., I. Lundström, L. Sjöqvist, H. Elwing, and L.M. Bjursten, *Titanium-hydrogen peroxide interaction: model studies of the influence of the inflammatory response on titanium implants*. Biomaterials, 1989. **10**(3): p. 166-175.
150. Arihara, K., L. Mao, P.A. Liddell, E. Marino-Ochoa, A.L. Moore, T. Imase, D. Zhang, T. Sotomura, and T. Ohsaka, *Electrocatalytic Reduction of Oxygen in a Novel Catalytic System with Cobalt Phthalocyanines and Manganese Oxide*. Journal of The Electrochemical Society, 2004. **151**(12): p. A2047-A2052.
151. Kubota, L.T., Y. Gushikem, J. Perez, and A.A. Tanaka, *Electrochemical Properties of Iron Phthalocyanine Immobilized on Titanium(IV) Oxide Coated on Silica Gel Surface*. Langmuir, 1995. **11**(3): p. 1009-1013.
152. Zhang, D., D. Chi, T. Okajima, and T. Ohsaka, *Catalytic activity of dual catalysts system based on nano-manganese oxide and cobalt octacyanophthalocyanine toward four-electron reduction of oxygen in alkaline media*. Electrochimica Acta, 2007. **52**(17): p. 5400-5406.
153. El-Deab, M., S. Othman, T. Okajima, and T. Ohsaka, *Non-platinum electrocatalysts: Manganese oxide nanoparticle-cobaltporphyrin binary catalysts for oxygen reduction*. Journal of Applied Electrochemistry, 2008. **38**(10): p. 1445-1451.
154. Li, X., C. Liu, W. Xing, and T. Lu, *Development of durable carbon black/titanium dioxide supported macrocycle catalysts for oxygen reduction reaction*. Journal of Power Sources, 2009. **193**(2): p. 470-476.
155. Xie, X.-Y., Z.-F. Ma, X. Wu, Q.-Z. Ren, X. Yuan, Q.-Z. Jiang, and L. Hu, *Preparation and electrochemical characteristics of CoTMPP-TiO₂NT/BP composite electrocatalyst for oxygen reduction reaction*. Electrochimica Acta, 2007. **52**(5): p. 2091-2096.
156. Xie, X.-Y., Z.-F. Ma, X.-X. Ma, Q. Ren, V.M. Schmidt, and L. Huang, *Preparation and Electrochemical Characteristics of MnOx--CoTMPP/BP Composite Catalyst for Oxygen Reduction Reaction in Alkaline Solution*. Journal of The Electrochemical Society, 2007. **154**(8): p. B733-B738.
157. Lu, M., S. Kharkwal, H.Y. Ng, and S.F.Y. Li, *Carbon nanotube supported MnO₂ catalysts for oxygen reduction reaction and their applications in microbial fuel cells*. Biosensors and Bioelectronics, 2011. **26**(12): p. 4728-4732.
158. Banks, C.E., T.J. Davies, G.G. Wildgoose, and R.G. Compton, *Electrocatalysis at graphite and carbon nanotube modified electrodes: edge-plane sites and tube ends are the reactive sites*. Chemical Communications, 2005(7): p. 829-841.
159. Jenkins, G.M. and K. Kawamura, *Structure of Glassy Carbon*. Nature, 1971. **231**(5299): p. 175-176.
160. Feng, L., Y. Chen, and L. Chen, *Easy-to-Operate and Low-Temperature Synthesis of Gram-Scale Nitrogen-Doped Graphene and Its Application as Cathode Catalyst in Microbial Fuel Cells*. ACS Nano, 2011.
161. Chattopadhyay, D., I. Galeska, and F. Papadimitrakopoulos, *Complete elimination of metal catalysts from single wall carbon nanotubes*. Carbon, 2002. **40**(7): p. 985-988.

162. Zheng, J.-S., X.-S. Zhang, P. Li, X.-G. Zhou, D. Chen, Y. Liu, and W.-K. Yuan, *Oxygen reduction reaction properties of carbon nanofibers: Effect of metal purification*. *Electrochimica Acta*, 2008. **53**(10): p. 3587-3596.
163. Sarapuu, A., K. Helstein, K. Vaik, D.J. Schiffrin, and K. Tammeveski, *Electrocatalysis of oxygen reduction by quinones adsorbed on highly oriented pyrolytic graphite electrodes*. *Electrochimica Acta*, 2010. **55**(22): p. 6376-6382.
164. Valarselvan, S. and P. Manisankar, *Electrocatalytic reduction of oxygen at glassy carbon electrode modified by polypyrrole/anthraquinones composite film in various pH media*. *Electrochimica Acta*, 2011. **56**(20): p. 6945-6953.
165. Larsen, M.J. and E.M. Skou, *ESR, XPS, and thin-film RRDE characterization of nano structured carbon materials for catalyst support in PEM fuel cells*. *Journal of Power Sources*, 2012. **202**(0): p. 35-46.
166. Erable, B., N. Duteanu, S.M.S. Kumar, Y. Feng, M.M. Ghangrekar, and K. Scott, *Nitric acid activation of graphite granules to increase the performance of the non-catalyzed oxygen reduction reaction (ORR) for MFC applications*. *Electrochemistry Communications*, 2009. **11**(7): p. 1547-1549.
167. Pirjamali, M. and Y. Kiros, *Effects of carbon pretreatment for oxygen reduction in alkaline electrolyte*. *Journal of Power Sources*, 2002. **109**(2): p. 446-451.
168. Jahnke, H., M. Schönborn, and G. Zimmermann, *Organic dyestuffs as catalysts for fuel cells*, 1976. p. 133-181.
169. HaoYu, E., S. Cheng, K. Scott, and B. Logan, *Microbial fuel cell performance with non-Pt cathode catalysts*. *Journal of Power Sources*, 2007. **171**(2): p. 275-281.
170. Harnisch, F., N.A. Savastenko, F. Zhao, H. Steffen, V. Brüser, and U. Schröder, *Comparative study on the performance of pyrolyzed and plasma-treated iron(II) phthalocyanine-based catalysts for oxygen reduction in pH neutral electrolyte solutions*. *Journal of Power Sources*, 2009. **193**(1): p. 86-92.
171. Herrmann, I., V. Bruser, S. Fiechter, H. Kersten, and P. Bogdanoff, *Electrocatalysts for Oxygen Reduction Prepared by Plasma Treatment of Carbon-Supported Cobalt Tetramethoxyphenylporphyrin*. *Journal of The Electrochemical Society*, 2005. **152**(11): p. A2179-A2185.
172. Mizutani, K., M. Toyoda, K. Sagara, N. Takahashi, A. Sato, Y. Kamitaka, S. Tsujimura, Y. Nakanishi, T. Sugiura, S. Yamaguchi, K. Kano, and B. Mikami, *X-ray analysis of bilirubin oxidase from *Myrothecium verrucaria* at 2.3 Å resolution using a twinned crystal*. *Acta Crystallographica Section F*, 2010. **66**(7): p. 765-770.
173. Gupta, G., C. Lau, V. Rajendran, F. Colon, B. Branch, D. Ivnitski, and P. Atanassov, *Direct electron transfer catalyzed by bilirubin oxidase for air breathing gas-diffusion electrodes*. *Electrochemistry Communications*, 2011. **13**(3): p. 247-249.
174. Erable, B., I. Vandecandelaere, M. Faimali, M.-L. Delia, L. Etcheverry, P. Vandamme, and A. Bergel, *Marine aerobic biofilm as biocathode catalyst*. *Bioelectrochemistry*, 2010. **78**(1): p. 51-56.
175. You, S.J., N.Q. Ren, Q.L. Zhao, J.Y. Wang, and F.L. Yang, *Power Generation and Electrochemical Analysis of Biocathode Microbial Fuel Cell Using Graphite Fibre Brush as Cathode Material*. *Fuel Cells*, 2009. **9**(5): p. 588-596.
176. Kozawa, A., V.E. Zilionis, and R.J. Brodd, *Effects of Various Additives in the Electrolyte on Oxygen Reduction at Ferric Phthalocyanine-Catalyzed Graphite Electrode*. *Journal of The Electrochemical Society*, 1971. **118**(10): p. 1705-1709.
177. Hanack, M., S. Deger, and A. Lange, *Bisaxially coordinated macrocyclic transition metal complexes*. *Coordination Chemistry Reviews*, 1988. **83**(0): p. 115-136.
178. Evans, D.R. and C.A. Reed, *Reversal of H₂O and OH⁻ Ligand Field Strength on the Magnetochemical Series Relative to the Spectrochemical Series. Novel 1-equiv Water Chemistry of Iron(III) Tetraphenylporphyrin Complexes*. *Journal of the American Chemical Society*, 2000. **122**(19): p. 4660-4667.
179. Baker, R., D.P. Wilkinson, and J. Zhang, *Electrocatalytic activity and stability of substituted iron phthalocyanines towards oxygen reduction evaluated at different temperatures*. *Electrochimica Acta*, 2008. **53**(23): p. 6906-6919.
180. Lever, A.B.P., S.R. Pickens, P.C. Minor, S. Licoccia, B.S. Ramaswamy, and K. Magnell, *Charge-transfer spectra of metallophthalocyanines: correlation with electrode potentials*. *Journal of the American Chemical Society*, 1981. **103**(23): p. 6800-6806.
181. Burgess, J. and M.V. Twigg, *Iron: Inorganic & Coordination Chemistry*, in *Encyclopedia of Inorganic Chemistry* 2006, John Wiley & Sons, Ltd.
182. Savy, M., P. Andro, C. Bernard, and G. Magner, *Etude de la reduction de l'oxygene sur les phtalocyanines monomeres et polymeres--I. principes fondamentaux, choix de l'ion central*. *Electrochimica Acta*, 1973. **18**(2): p. 191-197.

183. Lalande, G., G. Faubert, R. Côté, D. Guay, J.P. Dodelet, L.T. Weng, and P. Bertrand, *Catalytic activity and stability of heat-treated iron phthalocyanines for the electroreduction of oxygen in polymer electrolyte fuel cells*. Journal of Power Sources, 1996. **61**(1-2): p. 227-237.
184. Yu, E., S. Cheng, B. Logan, and K. Scott, *Electrochemical reduction of oxygen with iron phthalocyanine in neutral media*. Journal of Applied Electrochemistry, 2009. **39**(5): p. 705-711.
185. Li, W., A. Yu, D.C. Higgins, B.G. Llanos, and Z. Chen, *Biologically Inspired Highly Durable Iron Phthalocyanine Catalysts for Oxygen Reduction Reaction in Polymer Electrolyte Membrane Fuel Cells*. Journal of the American Chemical Society, 2010. **132**(48): p. 17056-17058.
186. Zagal, J., M. Pérez, A.A. Tanaka, J.R. dos Santos Jr, and C.A. Linkous, *Electrocatalytic activity of metal phthalocyanines for oxygen reduction*. Journal of Electroanalytical Chemistry, 1992. **339**(1-2): p. 13-30.
187. Kozawa, A., V.E. Zilionis, and R.J. Brodd, *Oxygen and Hydrogen Peroxide Reduction at a Ferric Phthalocyanine-Catalyzed Graphite Electrode*. Journal of The Electrochemical Society, 1970. **117**(12): p. 1470-1474.
188. Kozawa, A., V.E. Zilionis, and R.J. Brodd, *Electrode Materials and Catalysts for Oxygen Reduction in Isotonic Saline Solution*. Journal of The Electrochemical Society, 1970. **117**(12): p. 1474-1478.
189. Blomquist, J., U. Helgeson, L.C. Moberg, L.Y. Johansson, and R. Larsson, *Simultaneous electrochemical and mössbauer measurements on polymeric iron phthalocyanine oxygen electrodes*. Electrochimica Acta, 1982. **27**(10): p. 1453-1460.
190. Jaouen, F.d.r., *O₂ Reduction Mechanism on Non-Noble Metal Catalysts for PEM Fuel Cells. Part II: A Porous-Electrode Model To Predict the Quantity of H₂O₂ Detected by Rotating Ring-Disk Electrode*. The Journal of Physical Chemistry C, 2009. **113**(34): p. 15433-15443.
191. Savy, M., C. Bernard, and G. Magner, *Etude de la reduction de l'oxygene sur les phthalocyanines monomeres et polymeres--III. Phthalocyanines monomeres de fer en couche mince sur l'or*. Electrochimica Acta, 1975. **20**(5): p. 383-391.
192. Savy, M., P. Andro, and C. Bernard, *Etude de la reduction de l'oxygene sur les phthalocyanines monomeres et polymeres--II: Polyphthalocyanines de fer impregnees sur noir d'acetylene Y*. Electrochimica Acta, 1974. **19**(7): p. 403-411.
193. Zagal, J.H., *Metallophthalocyanines as catalysts in electrochemical reactions*. Coordination Chemistry Reviews, 1992. **119**: p. 89-136.
194. Coowar, F., O. Contamin, M. Savy, and G. Scarbeck, *Electrocatalysis of O₂ reduction to water in different acid media by iron naphthalocyanines*. Journal of Electroanalytical Chemistry and Interfacial Electrochemistry, 1988. **246**(1): p. 119-138.
195. Frémond, L., *Catalysis of the Electroreduction of Dioxygen by Cobalt(III) Corrole. Reactivity of Monocorrole, Biscorrole and Porphyrin-Corrole Dyads.*, in *the Faculty of the Department of Chemistry 2007*, University of Houston: Houston.
196. Van Der Putten, A., A. Elzing, W. Visscher, E. Barendrecht, and R.D. Harcourt, *Increased valence theory and the four electron reduction of O₂ to H₂O*. Journal of Molecular Structure: THEOCHEM, 1988. **180**: p. 309-318.
197. Linares, C., D. Geraldo, M. Paez, and J. Zagal, *Non-linear correlations between formal potential and Hammett parameters of substituted iron phthalocyanines and catalytic activity for the electro-oxidation of hydrazine*. Journal of Solid State Electrochemistry, 2003. **7**(9): p. 626-631.
198. Lever, A.B.P., *Derivation of metallophthalocyanine redox potentials via Hammett parameter analysis*. Inorganica Chimica Acta, 1993. **203**(2): p. 171-174.
199. Zagal, J.H., M. Gulppi, M. Isaacs, G. Cárdenas-Jirón, and M.J.s. Aguirre, *Linear versus volcano correlations between electrocatalytic activity and redox and electronic properties of metallophthalocyanines*. Electrochimica Acta, 1998. **44**(8-9): p. 1349-1357.
200. Charbonnière, L.J., R. Schurhammer, S. Mameri, G. Wipff, and R.F. Ziessel, *Photophysical and Structural Impact of Phosphorylated Anions Associated to Lanthanide Complexes in Water*. Inorganic Chemistry, 2005. **44**(20): p. 7151-7160.
201. Harding, M. *The Geometry of Metal-Phosphate Links in Metalloproteins - a Brief Survey 2005*; Available from: tanna.bch.ed.ac.uk/mphos/mphos3w.htm.
202. Appleby, A.J., J. Fleisch, and M. Savy, *Correlation between the spectroscopic properties of iron phthalocyanines and their activities for electrodic reduction of oxygen in alkaline media*. Journal of Catalysis, 1976. **44**(2): p. 281-292.
203. Appleby, A.J. and M. Savy, *Oxygen reduction on ultra thin carbon supported polymeric phthalocyanine electrodes in 6N KOH*. Electrochimica Acta, 1976. **21**(8): p. 567-574.
204. Appleby, A.J. and M. Savy, *Effect of thermal treatments of low microporosity graphite supports on the activity of Fe polyphthalocyanine for oxygen reduction in 6N KOH*. Electrochimica Acta, 1977. **22**(11): p. 1315-1323.
205. van Veen, J.A.R. and C. Visser, *Oxygen reduction on monomeric transition metal phthalocyanines in acid electrolyte*. Electrochimica Acta, 1979. **24**(9): p. 921-928.

206. Behret, H., H. Binder, G. Sandstede, and G.G. Scherer, *On the mechanism of electrocatalytic oxygen reduction at metal chelates : Part III. Metal phthalocyanines*. Journal of Electroanalytical Chemistry, 1981. **117**(1): p. 29-42.
207. van Veen, J.A.R., *On the use of rotating paste (ring-) disc electrodes in mechanistic studies*. Electrochimica Acta, 1982. **27**(10): p. 1401-1407.
208. Van Den Brink, F., W. Visscher, and E. Barendrecht, *Electrocatalysis of cathodic oxygen reduction by metal phthalocyanines: Part III. Iron phthalocyanine as electrocatalyst: experimental part*. Journal of Electroanalytical Chemistry, 1984. **172**(1-2): p. 301-325.
209. Van Der Putten, A., A. Elzing, W. Visscher, and E. Barendrecht, *Oxygen reduction on pyrolysed carbon-supported transition metal chelates*. Journal of Electroanalytical Chemistry, 1986. **205**(1-2): p. 233-244.
210. van Veen, J.A.R., H.A. Colijn, and J.F. van Baar, *On the effect of a heat treatment on the structure of carbon-supported metalloporphyrins and phthalocyanines*. Electrochimica Acta, 1988. **33**(6): p. 801-804.
211. Baranton, S., C. Coutanceau, C. Roux, F. Hahn, and J.M. Léger, *Oxygen reduction reaction in acid medium at iron phthalocyanine dispersed on high surface area carbon substrate: tolerance to methanol, stability and kinetics*. Journal of Electroanalytical Chemistry, 2005. **577**(2): p. 223-234.
212. Baranton, S., C. Coutanceau, E. Garnier, and J.M. Léger, *How does [alpha]-FePc catalysts dispersed onto high specific surface carbon support work towards oxygen reduction reaction (orr)?* Journal of Electroanalytical Chemistry, 2006. **590**(1): p. 100-110.
213. Baker, R., *Substituted iron phthalocyanines: Electrocatalytic activity towards O₂ reduction in a proton exchange membrane fuel cell cathode environment as a function of temperature*, 2008, The University of British Columbia: Vancouver.
214. Tarasevich, M.R., K.A. Radiyschkina, and S.I. Androuseva, *Electrocatalysis of oxygen reduction on organic metallic complexes*. Bioelectrochemistry and Bioenergetics, 1977. **4**(1): p. 18-29.
215. Behret, H., H. Binder, W. Clauberg, and G. Sandstede, *Comparison of the reaction mechanisms of electrocatalytic oxygen reduction using transition metal thiospinels and chelates*. Electrochimica Acta, 1978. **23**(10): p. 1023-1029.
216. Yuan, Y., J. Ahmed, and S. Kim, *Polyaniline/carbon black composite-supported iron phthalocyanine as an oxygen reduction catalyst for microbial fuel cells*. Journal of Power Sources, 2011. **196**(3): p. 1103-1106.
217. Morozan, A., S. Campidelli, A. Filoramo, B. Jusselme, and S. Palacin, *Catalytic activity of cobalt and iron phthalocyanines or porphyrins supported on different carbon nanotubes towards oxygen reduction reaction*. Carbon, 2011. **49**(14): p. 4839-4847.
218. Mamlouk, M., X. Wang, K. Scott, J.A. Horsfall, and C. Williams, *Characterization and application of anion exchange polymer membranes with non-platinum group metals for fuel cells*. Proceedings of the Institution of Mechanical Engineers, Part A: Journal of Power and Energy, 2011. **225**(2): p. 152-160.
219. Xu, G., Z. Li, S. Wang, and X. Yu, *Planar polyphthalocyanine cobalt absorbed on carbon black as stable electrocatalysts for direct methanol fuel cell*. Journal of Power Sources, 2010. **195**(15): p. 4731-4735.
220. Tanaka, A.A., C. Fierro, D. Scherson, and E.B. Yeager, *Electrocatalytic aspects of iron phthalocyanine and its .mu.-oxo derivatives dispersed on high surface area carbon*. The Journal of Physical Chemistry, 1987. **91**(14): p. 3799-3807.
221. Van Der Putten, A., A. Elzing, W. Visscher, and E. Barendrecht, *Oxygen reduction on vacuum-deposited and absorbed transition-metal phthalocyanine films*. Journal of Electroanalytical Chemistry, 1986. **214**(1-2): p. 523-533.
222. Zagal, J., P. Bindra, and E. Yeager, *A Mechanistic Study of O₂ Reduction on Water Soluble Phthalocyanines Adsorbed on Graphite Electrodes*. Journal of The Electrochemical Society, 1980. **127**(7): p. 1506-1517.
223. Fujishima, A., T.N. Rao, and D.A. Tryk, *Titanium dioxide photocatalysis*. Journal of Photochemistry and Photobiology C: Photochemistry Reviews, 2000. **1**(1): p. 1-21.
224. Stefan, I.C., Y. Mo, S.Y. Ha, S. Kim, and D.A. Scherson, *In Situ Fe K-Edge X-ray Absorption Fine Structure of a Nitrosyl Adduct of Iron Phthalocyanine Irreversibly Adsorbed on a High Area Carbon Electrode in an Acidic Electrolyte*. Inorganic Chemistry, 2003. **42**(14): p. 4316-4321.
225. van Veen, J.A.R., J.F. van Baar, and J. Kroese, *Effect of Heat Treatment on the Performance of Carbon-supported Transition-metal Chelates in the Electrochemical Reduction of Oxygen*. Journal of the chemical society, faraday transactions 1, 1981. **77**: p. 2827-2843.
226. Serov, A., M. Min, G. Chai, S. Han, S. Seo, Y. Park, H. Kim, and C. Kwak, *Electroreduction of oxygen over iron macrocyclic catalysts for DMFC applications*. Journal of Applied Electrochemistry, 2009. **39**(9): p. 1509-1516.
227. Beck, F., *The redox mechanism of the chelate-catalysed oxygen cathode*. Journal of Applied Electrochemistry, 1977. **7**(3): p. 239-245.

228. Beck, F., *Voltammetrische untersuchungen an elektrokatalytisch wirksamen Phthalocyaninen und Tetraazaannulenen in konzentrierter schwefelsaure*. Berichte der Bunsen-Gesellschaft, 1973. **77**(5): p. 353-364.
229. Birry, L., J.H. Zagal, and J.-P. Dodelet, *Does CO poison Fe-based catalysts for ORR?* Electrochemistry Communications, 2010. **12**(5): p. 628-631.
230. Savy, M., F. Coowar, J. Riga, J.J. Verbist, G. Bronoël, and S. Besse, *Investigation of O₂ reduction in alkaline media on macrocyclic chelates impregnated on different supports: influence of the heat treatment on stability and activity*. Journal of Applied Electrochemistry, 1990. **20**(2): p. 260-268.
231. Elzing, A., A. van der Putten, W. Visscher, and E. Barendrecht, *Models for the adsorption of dioxygen on metal chelates*. Recueil des Travaux Chimiques des Pays-Bas, 1990. **109**(2): p. 31-39.
232. Saito, T., M.D. Merrill, V.J. Watson, B.E. Logan, and M.A. Hickner, *Investigation of ionic polymer cathode binders for microbial fuel cells*. Electrochimica Acta, 2010. **55**(9): p. 3398-3403.
233. Clouser, S.J., J.C. Huang, and E. Yeager, *Temperature dependence of the Tafel slope for oxygen reduction on platinum in concentrated phosphoric acid*. Journal of Applied Electrochemistry, 1993. **23**(6): p. 597-605.
234. Wei, Y., G.N. Sastry, and H. Zipse, *Methyl Cation Affinities of Commonly Used Organocatalysts*. Journal of the American Chemical Society, 2008. **130**(11): p. 3473-3477.
235. Gorman, A.A., I. Hamblett, K. Smith, and M.C. Standen, *Strychnine : A fast physical quencher of singlet oxygen (1Δg)*. Tetrahedron Letters, 1984. **25**(5): p. 581-584.
236. Bitá, B., *1,4-Diazabicyclo[2.2.2]octane (DABCO) as a useful catalyst in organic synthesis*. European Journal of Chemistry, 2010. **1**(1): p. 54-60.
237. Altmeier, P.D., 66822 Lebach, DE), *Strongly alkaline anion exchange membranes and process for producing the same*, 1998: United States.
238. Altmeier, P.D., 66822 Lebach, DE), *Strongly basic anion-exchanging molded bodies and a method of manufacturing the same*, 1999: United States.
239. Koo, J.-y.A., MA), Yoon, Young Seo (Seoul, KR), *Composite polyamide reverse osmosis membrane and method of producing the same*, 2000, Saehan Industries Inc. (KR): United States.
240. Ogryzlo, E.A. and C.W. Tang, *Quenching of oxygen(1.DELTA.8) by amines*. Journal of the American Chemical Society, 1970. **92**(17): p. 5034-5036.
241. Guzonas, D.A., D.E. Irish, and G.F. and Atkinson, *The surface enhanced raman scattering of the protonated forms of DABCO at a silver electrode*. OFFICE OF NAVAL RESEARCH, 1988.
242. Lesch, B., J. Toräng, S. Vanderheiden, and S. Bräse, *Base-Catalyzed Condensation of 2-Hydroxybenzaldehydes with α,β-Unsaturated Aldehydes – Scope and Limitations*. Advanced Synthesis & Catalysis, 2005. **347**(4): p. 555-562.
243. Takewaki, T., L.W. Beck, and M.E. Davis, *Zeolite synthesis using 1,4-diazabicyclo[2,2,2]octane (DABCO) derivatives as structure-directing agents*. Microporous and Mesoporous Materials, 1999. **33**(1-3): p. 197-207.
244. Rao, C.N.R., S. Natarajan, and S. Neeraj, *Building Open-Framework Metal Phosphates from Amine Phosphates and a Monomeric Four-Membered Ring Phosphate*. Journal of Solid State Chemistry, 2000. **152**(1): p. 302-321.
245. Maras, N., S. Polanc, and M. Kocivar, *Ring-opening reactions of 1,4-diazabicyclo[2.2.2]octane (DABCO) derived quaternary ammonium salts with phenols and related nucleophiles*. Organic & Biomolecular Chemistry, 2012. **10**: p. 1300-1310.
246. Iojoiu, C., F. Chabert, M. Maréchal, N.E. Kissi, J. Guindet, and J.Y. Sanchez, *From polymer chemistry to membrane elaboration: A global approach of fuel cell polymeric electrolytes*. Journal of Power Sources, 2006. **153**(2): p. 198-209.
247. Rozendal, R.A., H.V.M. Hamelers, R.J. Molenkamp, and C.J.N. Buisman, *Performance of single chamber biocatalyzed electrolysis with different types of ion exchange membranes*. Water Research, 2007. **41**(9): p. 1984-1994.
248. Rozendal, R., T.H.J.A. Sleutels, B. Hamelers, and C.J. Buisman, *Effect of the type of ion exchange membrane on performance, ion transport, and pH in biocatalyzed electrolysis of wastewater*. Water Science and Technology, 2008. **57**(11): p. 1757-1762.
249. Sleutels, T.H.J.A., H.V.M. Hamelers, R.A. Rozendal, and C.J.N. Buisman, *Ion transport resistance in Microbial Electrolysis Cells with anion and cation exchange membranes*. International Journal of Hydrogen Energy, 2009. **34**(9): p. 3612-3620.
250. Fan, Y., H. Hu, and H. Liu, *Sustainable Power Generation in Microbial Fuel Cells Using Bicarbonate Buffer and Proton Transfer Mechanisms*. Environmental Science & Technology, 2007. **41**(23): p. 8154-8158.
251. Harnisch, F., R. Warmbier, R. Schneider, and U. Schröder, *Modeling the ion transfer and polarization of ion exchange membranes in bioelectrochemical systems*. Bioelectrochemistry, 2009. **75**(2): p. 136-141.

252. Długołęcki, P., P. Ogonowski, S.J. Metz, M. Saakes, K. Nijmeijer, and M. Wessling, *On the resistances of membrane, diffusion boundary layer and double layer in ion exchange membrane transport*. Journal of Membrane Science, 2010. **349**(1–2): p. 369-379.
253. Ji, E., H. Moon, J. Piao, P.T. Ha, J. An, D. Kim, J.-J. Woo, Y. Lee, S.-H. Moon, B.E. Rittmann, and I.S. Chang, *Interface resistances of anion exchange membranes in microbial fuel cells with low ionic strength*. Biosensors and Bioelectronics, 2011. **26**(7): p. 3266-3271.
254. Harnisch, F., U. Schröder, and F. Scholz, *The Suitability of Monopolar and Bipolar Ion Exchange Membranes as Separators for Biological Fuel Cells*. Environmental Science & Technology, 2008. **42**(5): p. 1740-1746.
255. Nikonenko, V.V. and A.E. Kozmai, *Electrical equivalent circuit of an ion-exchange membrane system*. Electrochimica Acta, 2011. **56**(3): p. 1262-1269.
256. Gu, S., R. Cai, T. Luo, Z. Chen, M. Sun, Y. Liu, G. He, and Y. Yan, *A Soluble and Highly Conductive Ionomer for High-Performance Hydroxide Exchange Membrane Fuel Cells*. Angewandte Chemie International Edition, 2009. **48**(35): p. 6499-6502.
257. Cosofret, V.V., T.M. Nahir, E. Lindner, and R.P. Buck, *New neutral carrier-based H⁺ selective membrane electrodes*. Journal of Electroanalytical Chemistry, 1992. **327**(1–2): p. 137-146.
258. Nguyen, P.H. and G. Paasch, *Transfer matrix method for the electrochemical impedance of inhomogeneous porous electrodes and membranes*. Journal of Electroanalytical Chemistry, 1999. **460**(1–2): p. 63-79.
259. Zhao and Li, *Dielectric Characterization of a Nanofiltration Membrane in Electrolyte Solutions: Its Double-Layer Structure and Ion Permeation*. The Journal of Physical Chemistry B, 2006. **110**(6): p. 2755-2763.
260. Picioreanu, C., M.C.M. van Loosdrecht, T.P. Curtis, and K. Scott, *Model based evaluation of the effect of pH and electrode geometry on microbial fuel cell performance*. Bioelectrochemistry, 2010. **78**(1): p. 8-24.
261. Logan, B., S. Cheng, V. Watson, and G. Estadt, *Graphite Fiber Brush Anodes for Increased Power Production in Air-Cathode Microbial Fuel Cells*. Environmental Science & Technology, 2007. **41**(9): p. 3341-3346.
262. Velasquez-Orta, S.B., I.M. Head, T.P. Curtis, and K. Scott, *Factors affecting current production in microbial fuel cells using different industrial wastewaters*. Bioresource Technology, 2011. **102**(8): p. 5105-5112.
263. Fornero, J.J., M. Rosenbaum, and L.T. Angenent, *Electric Power Generation from Municipal, Food, and Animal Wastewaters Using Microbial Fuel Cells*. Electroanalysis, 2010. **22**(7-8): p. 832-843.
264. Liang, P., X. Huang, M.-Z. Fan, X.-X. Cao, and C. Wang, *Composition and distribution of internal resistance in three types of microbial fuel cells*. Applied Microbiology and Biotechnology, 2007. **77**(3): p. 551-558.
265. Cheng, S., H. Liu, and B.E. Logan, *Power Densities Using Different Cathode Catalysts (Pt and CoTMP) and Polymer Binders (Nafion and PTFE) in Single Chamber Microbial Fuel Cells*. Environmental Science & Technology, 2005. **40**(1): p. 364-369.
266. Cheng, S., H. Liu, and B.E. Logan, *Increased performance of single-chamber microbial fuel cells using an improved cathode structure*. Electrochemistry Communications, 2006. **8**(3): p. 489-494.
267. Zhu, F., W. Wang, X. Zhang, and G. Tao, *Electricity generation in a membrane-less microbial fuel cell with down-flow feeding onto the cathode*. Bioresource Technology, 2011. **102**(15): p. 7324-7328.
268. Zhang, F., M.D. Merrill, J.C. Tokash, T. Saito, S. Cheng, M.A. Hickner, and B.E. Logan, *Mesh optimization for microbial fuel cell cathodes constructed around stainless steel mesh current collectors*. Journal of Power Sources, 2011. **196**(3): p. 1097-1102.
269. Cheng, S. and B.E. Logan, *Increasing power generation for scaling up single-chamber air cathode microbial fuel cells*. Bioresource Technology, 2011. **102**(6): p. 4468-4473.
270. Fornero, J.J., M. Rosenbaum, M.A. Cotta, and L.T. Angenent, *Carbon Dioxide Addition to Microbial Fuel Cell Cathodes Maintains Sustainable Catholyte pH and Improves Anolyte pH, Alkalinity, and Conductivity*. Environmental Science & Technology, 2010. **44**(7): p. 2728-2734.
271. Zhuang, L., S. Zhou, Y. Wang, C. Liu, and S. Geng, *Membrane-less cloth cathode assembly (CCA) for scalable microbial fuel cells*. Biosensors and Bioelectronics, 2009. **24**(12): p. 3652-3656.
272. Zhang, X., S. Cheng, X. Wang, X. Huang, and B.E. Logan, *Separator Characteristics for Increasing Performance of Microbial Fuel Cells*. Environmental Science & Technology, 2009. **43**(21): p. 8456-8461.
273. Shimoyama, T., S. Komukai, A. Yamazawa, Y. Ueno, B. Logan, and K. Watanabe, *Electricity generation from model organic wastewater in a cassette-electrode microbial fuel cell*. Applied Microbiology and Biotechnology, 2008. **80**(2): p. 325-330.
274. Chong, S., T.K. Sen, A. Kayaalp, and H.M. Ang, *The performance enhancements of upflow anaerobic sludge blanket (UASB) reactors for domestic sludge treatment – A State-of-the-art review*. Water Research, 2012. **46**(11): p. 3434-3470.

275. Kreja, L. and A. Plewka, *The influence of some factors on the electrochemical activity of the oxygen cathode activated with iron polyphthalocyanine*. *Electrochimica Acta*, 1982. **27**(2): p. 251-255.
276. Wang, X., M. Li, B.T. Golding, M. Sadeghi, Y. Cao, E.H. Yu, and K. Scott, *A polytetrafluoroethylene-quaternary 1,4-diazabicyclo-[2.2.2]-octane polysulfone composite membrane for alkaline anion exchange membrane fuel cells*. *International Journal of Hydrogen Energy*, 2011. **36**(16): p. 10022-10026.
277. Wang, X., C. Xu, B.T. Golding, M. Sadeghi, Y. Cao, and K. Scott, *A novel phosphoric acid loaded quaternary 1,4-diazabicyclo-[2.2.2]-octane polysulfone membrane for intermediate temperature fuel cells*. *International Journal of Hydrogen Energy*, 2011. **36**(14): p. 8550-8556.
278. Wang, J.X., F.A. Uribe, T.E. Springer, J. Zhang, and R.R. Adzic, *Intrinsic kinetic equation for oxygen reduction reaction in acidic media: the double Tafel slope and fuel cell applications*. *Faraday Discuss.*, 2008. **140**: p. 347-362.
279. Liu, H.Y., I. Abdalmuhdi, C.K. Chang, and F.C. Anson, *Catalysis of the electroreduction of dioxygen and hydrogen peroxide by an anthracene-linked dimeric cobalt porphyrin*. *The Journal of Physical Chemistry*, 1985. **89**(4): p. 665-670.
280. Di Lorenzo, M., K. Scott, T.P. Curtis, K.P. Katuri, and I.M. Head, *Continuous Feed Microbial Fuel Cell Using An Air Cathode and A Disc Anode Stack for Wastewater Treatment*. *Energy & Fuels*, 2009. **23**(11): p. 5707-5716.
281. Greenberg, A., L.S. Clesceri, and A.D. Eaton, *Standard Methods for the Examination of Water and Wastewater* 1992, Washington: American Public Health Association.
282. Zhang, F., D. Pant, and B.E. Logan, *Long-term performance of activated carbon air cathodes with different diffusion layer porosities in microbial fuel cells*. *Biosensors and Bioelectronics*, 2011. **30**(1): p. 49-55.
283. Macdonald, J., *Impedance spectroscopy*. *Annals of Biomedical Engineering*, 1992. **20**(3): p. 289-305.
284. *A Perfect Carbon Nanotube with Two Closed Ends*. *Journal of Nanoscience and Nanotechnology*, 2002. **2**: p. 33-35.
285. Alcaide, F., E. Brillas, and P.-L. Cabot, *An Impedance Study of the O_2/HO_2^- System in Equilibrium on a Gas Diffusion Electrode*. *Journal of The Electrochemical Society*, 2003. **150**(1): p. E52-E58.
286. Vinodh, R. and D. Sangeetha, *Comparative study of composite membranes from nano-metal-oxide-incorporated polymer electrolytes for direct methanol alkaline membrane fuel cells*. *Journal of Applied Polymer Science*, 2012. **128**(3): p. 1930-1938.
287. Xu, T., *Ion exchange membranes: State of their development and perspective*. *Journal of Membrane Science*, 2005. **263**(1-2): p. 1-29.
288. Zhang, X., S. Cheng, X. Huang, and B.E. Logan, *Improved performance of single-chamber microbial fuel cells through control of membrane deformation*. *Biosensors and Bioelectronics*, 2010. **25**(7): p. 1825-1828.
289. Logan, B., *Simultaneous wastewater treatment and biological electricity generation*. *Water Science and Technology*, 2005. **52**(1-2): p. 31-37.
290. Dai, H.-P. and K.-K. Shiu, *Voltammetric studies of electrochemical pretreatment of rotating-disc glassy carbon electrodes in phosphate buffer*. *Journal of Electroanalytical Chemistry*, 1996. **419**(1): p. 7-14.
291. Szymanski, G.S., Z. Karpinski, S. Biniak, and A. Swiatkowski, *The effect of the gradual thermal decomposition of surface oxygen species on the chemical and catalytic properties of oxidized activated carbon*. *Carbon*, 2002. **40**(14): p. 2627-2639.
292. Laviron, E., L. Roullier, and C. Degrand, *A multilayer model for the study of space distributed redox modified electrodes: Part II. Theory and application of linear potential sweep voltammetry for a simple reaction*. *Journal of Electroanalytical Chemistry and Interfacial Electrochemistry*, 1980. **112**(1): p. 11-23.
293. Laviron, E., *A multilayer model for the study of space distributed redox modified electrodes: Part I. Description and discussion of the model*. *Journal of Electroanalytical Chemistry and Interfacial Electrochemistry*, 1980. **112**(1): p. 1-9.
294. Armstrong, F.A., *Insights from protein film voltammetry into mechanisms of complex biological electron-transfer reactions*. *Journal of the Chemical Society, Dalton Transactions*, 2002(5): p. 661-671.
295. Amini, M.K., S. Shahrokhian, and S. Tangestaninejad, *Thiocyanate-selective electrodes based on nickel and iron phthalocyanines*. *Analytica Chimica Acta*, 1999. **402**(1-2): p. 137-143.
296. Taylor, R.J. and A.A. Humffray, *Electrochemical studies on glassy carbon electrodes: III. Oxygen reduction in solutions of low pH ($pH < 10$)*. *Journal of Electroanalytical Chemistry and Interfacial Electrochemistry*, 1975. **64**(1): p. 85-94.

297. Shteinberg, G.V., A.V. Dribinsky, I.A. Kukushkina, L.N. Mokrousov, and V.S. Bagotzky, *Investigation of the carbon-oxygen (air) electrode*. Journal of Electroanalytical Chemistry, 1984. **180**(1-2): p. 619-637.
298. Heusler, K.E., *Multicomponent electrodes*. Electrochimica Acta, 1996. **41**(3): p. 411-418.
299. Paulus, U.A., A. Wokaun, G.G. Scherer, T.J. Schmidt, V. Stamenkovic, V. Radmilovic, N.M. Markovic, and P.N. Ross, *Oxygen Reduction on Carbon-Supported Pt-Ni and Pt-Co Alloy Catalysts*. The Journal of Physical Chemistry B, 2002. **106**(16): p. 4181-4191.
300. Gara, M. and R.G. Compton, *Activity of carbon electrodes towards oxygen reduction in acid: A comparative study*. New Journal of Chemistry, 2011. **35**(11): p. 2647-2652.
301. Subramanian, N.P., S.P. Kumaraguru, H. Colon-Mercado, H. Kim, B.N. Popov, T. Black, and D.A. Chen, *Studies on Co-based catalysts supported on modified carbon substrates for PEMFC cathodes*. Journal of Power Sources, 2006. **157**(1): p. 56-63.
302. de Groot, M.T., *Electrochemistry of Immobilized Hemes and Heme Proteins*, 2007, Universiteit Eindhoven: Eindhoven.
303. Bagotzky, V.S., M.R. Tarasevich, K.A. Radyushkina, O.A. Levina, and S.I. Andrusyova, *Electrocatalysis of the oxygen reduction process on metal chelates in acid electrolyte*. Journal of Power Sources, 1978. **2**(3): p. 233-240.
304. Gharibi, H. and R.A. Mirzaie, *Fabrication of gas-diffusion electrodes at various pressures and investigation of synergetic effects of mixed electrocatalysts on oxygen reduction reaction*. Journal of Power Sources, 2003. **115**(2): p. 194-202.
305. Leddy, J., A.J. Bard, J.T. Maloy, and J.M. Savéant, *Kinetics of film-coated electrodes: Effect of a finite mass transfer rate of substrate across the film—solution interface at steady state*. Journal of Electroanalytical Chemistry and Interfacial Electrochemistry, 1985. **187**(2): p. 205-227.
306. Wu, X., Y. Li, B. Gründig, N.-T. Yu, and R. Renneberg, *A novel iron-porphyrin-derived oxygen sensor working near 0 V (vs. Ag/AgCl) in neutral solution*. Electroanalysis, 1997. **9**(16): p. 1288-1290.
307. Lei, Y. and F.C. Anson, *Mechanistic aspects of the electroreduction of dioxygen as catalyzed by copper-phenanthroline complexes adsorbed on graphite electrodes*. Inorganic Chemistry, 1994. **33**(22): p. 5003-5009.
308. Rozendal, R.A., H.V.M. Hamelers, and C.J.N. Buisman, *Effects of Membrane Cation Transport on pH and Microbial Fuel Cell Performance†*. Environmental Science & Technology, 2006. **40**(17): p. 5206-5211.
309. Yu, E.H., R. Burkitt, X. Wang, and K. Scott, *Application of anion exchange ionomer for oxygen reduction catalysts in microbial fuel cells*. Electrochemistry Communications, 2012. **21**(0): p. 30-35.
310. Bauer, B., H. Strathmann, and F. Effenberger, *Anion-exchange membranes with improved alkaline stability*. Desalination, 1990. **79**(2-3): p. 125-144.
311. Varcoe, J.R., R.C.T. Slade, E. Lam How Yee, S.D. Poynton, D.J. Driscoll, and D.C. Apperley, *Poly(ethylene-co-tetrafluoroethylene)-Derived Radiation-Grafted Anion-Exchange Membrane with Properties Specifically Tailored for Application in Metal-Cation-Free Alkaline Polymer Electrolyte Fuel Cells*. Chemistry of Materials, 2007. **19**(10): p. 2686-2693.
312. Benoit, R.L., D. Lefebvre, and M. Fréchette, *Basicity of 1,4-bis(dimethylamino)naphthalene and 1,4-diazabicyclo[2.2.2]octane*. Can. J. Chemistry, 1986. **65**: p. 996.
313. Boguslavskiy, A.E., M.S. Schuurman, D. Townsend, and A. Stolow, *Non-Born-Oppenheimer wavepacket dynamics in polyatomic molecules: vibrations at conical intersections in DABCO*. Faraday Discussions, 2011. **150**(0): p. 419-438.
314. Brochsztain, S., M.A. Rodrigues, G.J.F. Demets, and M.J. Politi, *Stabilization of naphthalene-1,8:4,5-dicarboximide radicals in zirconium phosphonate solid materials and thin films*. Journal of Materials Chemistry, 2002. **12**(5): p. 1250-1255.
315. Olejniczak, A. and A. Katrusiak, *Pressure induced transformations of 1,4-diazabicyclo[2.2.2]octane (dabco) hydroiodide: diprotonation of dabco, its N-methylation and co-crystallization with methanol*. CrystEngComm, 2010. **12**(9): p. 2528-2532.
316. Parker, D.H. and P. Avouris, *Multiphoton ionization spectra of two caged amines*. Chemical Physics Letters, 1978. **53**(3): p. 515-520.
317. Sehlotho, N., *Phthalocyanines: Photochemical, electrochemical and biomimetic catalytic behaviour*, in Chemistry 2007, Rhodes University.
318. Stoica, D., L. Ogier, L. Akrou, F. Alloin, and J.F. Fauvarque, *Anionic membrane based on polyepichlorhydrin matrix for alkaline fuel cell: Synthesis, physical and electrochemical properties*. Electrochimica Acta, 2007. **53**(4): p. 1596-1603.
319. Watson, V.J., T. Saito, M.A. Hickner, and B.E. Logan, *Polymer coatings as separator layers for microbial fuel cell cathodes*. Journal of Power Sources, 2011. **196**(6): p. 3009-3014.
320. Nelsen, S.F., *Ionization potential, oxidation potential comparisons for compounds containing amino nitrogen*. Israel journal of chemistry, 1979. **18**: p. 45-55.

321. Darmanyan, A.P., W.S. Jenks, and P. and Jardon, *Charge-Transfer Quenching of Singlet Oxygen O₂ by Amines and Aromatic Hydrocarbons*. Journal of Physical Chemistry A, 1998. **102**: p. 7420-7426.
322. Laviron, E., *General expression of the linear potential sweep voltammogram in the case of diffusionless electrochemical systems*. Journal of Electroanalytical Chemistry and Interfacial Electrochemistry, 1979. **101**(1): p. 19-28.
323. Gorton, L., A. Torstensson, H. Jaegfeldt, and G. Johansson, *Electrocatalytic oxidation of reduced nicotinamide coenzymes by graphite electrodes modified with an adsorbed phenoxazinium salt, meldola blue*. Journal of Electroanalytical Chemistry and Interfacial Electrochemistry, 1984. **161**(1): p. 103-120.
324. Laviron, E., *Adsorption, autoinhibition and autocatalysis in polarography and in linear potential sweep voltammetry*. Journal of Electroanalytical Chemistry and Interfacial Electrochemistry, 1974. **52**(3): p. 355-393.
325. Elmgren, M., S.-E. Lindquist, and G. Henriksson, *Cellobiose oxidase crosslinked in a redox polymer matrix at an electrode surface—a new biosensor*. Journal of Electroanalytical Chemistry, 1992. **341**(1–2): p. 257-273.
326. Lange, K.J., P.-C. Sui, and N. Djilali, *Pore Scale Simulation of Transport and Electrochemical Reactions in Reconstructed PEMFC Catalyst Layers*. Journal of The Electrochemical Society, 2010. **157**(10): p. B1434-B1442.
327. Maruyama, J. and I. Abe, *Cathodic oxygen reduction at the interface between Nafion® and electrochemically oxidized glassy carbon surfaces*. Journal of Electroanalytical Chemistry, 2002. **527**(1–2): p. 65-70.
328. Kawai, T., M. Soma, Y. Matsumoto, T. Onishi, and K. Tamaru, *XPS and UPS study on the chemisorptive bond of formic acid, pyridine and water over metal-phthalocyanines*. Chemical Physics Letters, 1976. **37**(2): p. 378-382.
329. James Watkins, E. and P.H. Pfromm, *Capacitance spectroscopy to characterize organic fouling of electro dialysis membranes*. Journal of Membrane Science, 1999. **162**(1–2): p. 213-218.
330. Ghaedi, M., M. Montazerzohori, M. Behfar, and F. Marahel, *Influence of Multiwalled Carbon Nanotubes on the Response Performance of Carbon Paste Iodide Ion Selective Electrode Based on Iron (II) Phthalocyanine*. International Journal of Electrochemical Science, 2011. **6**: p. 6074 - 6084.
331. Minhat, N.A., *Effects of electrolyte and materials for microbial fuel cell cathode*, in *Chemical engineering and advanced materials 2012*, Newcastle University.
332. Rocha, G.O., R.A.W. Johnstone, B.F. Hemming, P.J.C. Pires, and J.P. Sankey, *Rates of formation of peroxyacetic acid from hydrogen peroxide and acetic acid in the presence of metal(IV) phosphates*. Journal of Molecular Catalysis A: Chemical, 2002. **186**(1–2): p. 127-133.
333. Duarte, J.C., R.C.S. Luz, F.S. Damos, A.A. Tanaka, and L.T. Kubota, *A highly sensitive amperometric sensor for oxygen based on iron(II) tetrasulfonated phthalocyanine and iron(III) tetra-(N-methyl-pyridyl)-porphyrin multilayers*. Analytica Chimica Acta, 2008. **612**(1): p. 29-36.
334. Shahrokhian, S., M. Ghalkhani, and M.K. Amini, *Application of carbon-paste electrode modified with iron phthalocyanine for voltammetric determination of epinephrine in the presence of ascorbic acid and uric acid*. Sensors and Actuators B: Chemical, 2009. **137**(2): p. 669-675.
335. Hassan, S.S.M., W.H. Mahmoud, M.A.F. Elmosallamy, and M.H. Almarzooqi, *Iron(II)-phthalocyanine as a novel recognition sensor for selective potentiometric determination of diclofenac and warfarin drugs*. Journal of Pharmaceutical and Biomedical Analysis, 2005. **39**(1–2): p. 315-321.
336. Kuang, F., D. Zhang, Y. Li, Y. Wan, and B. Hou, *Electrochemical impedance spectroscopy analysis for oxygen reduction reaction in 3.5% NaCl solution*. Journal of Solid State Electrochemistry, 2009. **13**(3): p. 385-390.
337. Havránek, A. and K. Wippermann, *Determination of proton conductivity in anode catalyst layers of the direct methanol fuel cell (DMFC)*. Journal of Electroanalytical Chemistry, 2004. **567**(2): p. 305-315.
338. Contamin, O. and E. Levart, *Characterization and identification of partially blocked electrodes*. Journal of Electroanalytical Chemistry and Interfacial Electrochemistry, 1982. **136**(2): p. 259-270.
339. Coowar, F., M. Savy, G. Scarbeck, D. Van den Ham, J. Riga, and J.J. Verbist, *Effect of the nature of iron naphthalocyanine supports on their activity for O₂ reduction in acid media*. Journal of Electroanalytical Chemistry and Interfacial Electrochemistry, 1989. **259**(1-2): p. 241-264.
340. Albery, W.J., C.M. Elliott, and A.R. Mount, *A transmission line model for modified electrodes and thin layer cells*. Journal of Electroanalytical Chemistry and Interfacial Electrochemistry, 1990. **288**(1–2): p. 15-34.
341. Alcaide, F., E. Brillas, and P.-L.s. Cabot, *EIS analysis of hydroperoxide ion generation in an uncatalyzed oxygen-diffusion cathode*. Journal of Electroanalytical Chemistry, 2003. **547**(1): p. 61-73.

342. Roberge, P.R. and R. Beaudoin, *Evaluation of charge transfer resistance by geometrical extrapolation of the centre of semicircular impedance diagrams*. Journal of Applied Electrochemistry, 1988. **18**(1): p. 38-42.
343. Vrubel, H., T. Moehl, M. Gratzel, and X. Hu, *Revealing and accelerating slow electron transport in amorphous molybdenum sulphide particles for hydrogen evolution reaction*. Chemical Communications, 2013. **49**(79): p. 8985-8987.
344. González-Cuenca, M., W. Zipprich, B.A. Boukamp, G. Pudmich, and F. Tietz, *Impedance Studies on Chromite-Titanate Porous Electrodes under Reducing Conditions*. Fuel Cells, 2001. **1**(3-4): p. 256-264.
345. Velasquez-Orta, S.B., T.P. Curtis, and B.E. Logan, *Energy from algae using microbial fuel cells*. Biotechnology and Bioengineering, 2009. **103**(6): p. 1068-1076.
346. Savizi, I.S.P. and M.J. Janik, *Acetate and phosphate anion adsorption linear sweep voltammograms simulated using density functional theory*. Electrochimica Acta, 2011. **56**(11): p. 3996-4006.
347. Harnisch, F. and U. Schröder, *Selectivity versus Mobility: Separation of Anode and Cathode in Microbial Bioelectrochemical Systems*. ChemSusChem, 2009. **2**(10): p. 921-926.
348. Długołęcki, P.E., *Mass transport in reverse electrodialysis for sustainable energy generation*, 2009, University of Twente: Enschede.
349. Le-Hoang, A., *Study of Rhodopseudomonas Palustris toward Photoautotrophic Growth via the Media*, 2008, Swiss Federal Institute of Technology: Lausanne.
350. Xing, D., Y. Zuo, S. Cheng, J.M. Regan, and B.E. Logan, *Electricity Generation by Rhodopseudomonas palustris DX-1*. Environmental Science & Technology, 2008. **42**(11): p. 4146-4151.
351. Rozendal, R.A., H.V.M. Hamelers, K. Rabaey, J. Keller, and C.J.N. Buisman, *Towards practical implementation of bioelectrochemical wastewater treatment*. Trends in Biotechnology, 2008. **26**(8): p. 450-459.
352. Choi, Y.-k., S. Jeon, J.-K. Park, and K.-H. Chjo, *Electrocatalytic reduction of dioxygen by quadruply aza bridged closely interfaced cofacial bis(5,10,15,20-tetraphenylporphyrin)s in various pH solutions*. Electrochimica Acta, 1997. **42**(8): p. 1287-1293.
353. Cochran, W.G., *The flow due to a rotating disc*. Mathematical Proceedings of the Cambridge Philosophical Society, 1934. **30**(03): p. 365-375.
354. Petrina, S., *Properties of Sub-micron NAFION® Thin Films*, 2012.
355. Jaouen, F.d.r., J. Herranz, M. Lefèvre, J.-P. Dodelet, U.I. Kramm, I. Herrmann, P. Bogdanoff, J. Maruyama, T. Nagaoka, A. Garsuch, J.R. Dahn, T. Olson, S. Pylypenko, P. Atanassov, and E.A. Ustinov, *Cross-Laboratory Experimental Study of Non-Noble-Metal Electrocatalysts for the Oxygen Reduction Reaction*. ACS Applied Materials & Interfaces, 2009. **1**(8): p. 1623-1639.
356. Koneshan, S., J.C. Rasaiah, R.M. Lynden-Bell, and S.H. Lee, *Solvent Structure, Dynamics, and Ion Mobility in Aqueous Solutions at 25 °C*. The Journal of Physical Chemistry B, 1998. **102**(21): p. 4193-4204.
357. Lee, S.H. and J.C. Rasaiah, *Proton transfer and the mobilities of the H^{+} and OH^{-} ions from studies of a dissociating model for water*. The Journal of Chemical Physics, 2011. **135**(12): p. 124505-10.
358. Hunter, R.J. and A.E. Alexander, *Surface properties and flow behavior of kaolinite. Part II. Electrophoretic studies of anion adsorption*. Journal of Colloid Science, 1963. **18**(9): p. 833-845.
359. Kielland, J., *Individual Activity Coefficients of Ions in Aqueous Solutions*. Journal of the American Chemical Society, 1937. **59**(9): p. 1675-1678.
360. Hsu, R.S., *Nanostructured Non-Precious Metal Catalysts for Polymer Electrolyte Fuel Cell in Chemical Engineering 2010*, University of Waterloo: Waterloo, Ontario, Canada.
361. Kuzmann, E., Z. Homonnay, A. Vértes, S. Li, H. Yin, Y. Wei, A. Nath, X. Chen, and J. Li, *Mössbauer studies of the interaction of oxygen with solid β -FeII-phthalocyanine*. Journal of Solid State Chemistry, 2003. **170**(1): p. 118-123.
362. Nyokong, T. and S. Vilakazi, *Phthalocyanines and related complexes as electrocatalysts for the detection of nitric oxide*. Talanta, 2003. **61**(1): p. 27-35.
363. Nezel, T., *Investigation and development of selective polymeric liquid membranes for the optical detection of NO₂ with chemical sensors*, 2002, ETH Zurich: Zurich.
364. Medina, F.A., J.W. Larsen, and H.H. Schobert, *Carbon as catalyst for organic electron-transfer reactions*. Fuel Chemistry Division Preprints, 2003. **48**(1).
365. Hirst, J. and F.A. Armstrong, *Fast-Scan Cyclic Voltammetry of Protein Films on Pyrolytic Graphite Edge Electrodes: Characteristics of Electron Exchange*. Analytical Chemistry, 1998. **70**(23): p. 5062-5071.
366. Laviron, E. and L. Roullier, *Electrochemical reactions with adsorption of the reactants and electrosorption. Simple analytical solutions for a Henry isotherm*. Journal of Electroanalytical Chemistry, 1998. **443**(2): p. 195-207.

367. Paulus, U.A., T.J. Schmidt, H.A. Gasteiger, and R.J. Behm, *Oxygen reduction on a high-surface area Pt/Vulcan carbon catalyst: a thin-film rotating ring-disk electrode study*. Journal of Electroanalytical Chemistry, 2001. **495**(2): p. 134-145.
368. Hall, S., E.A. Khudaish, and A.L. Hart, *Electrochemical oxidation of hydrogen peroxide at platinum electrodes. Part IV: phosphate buffer dependence*. Electrochimica Acta, 1999. **44**(25): p. 4573-4582.
369. Zeitler, S., E. Wendler-Kalsch, W. Preidel, and V. Tegeder, *Corrosion of platinum electrodes in phosphate buffered saline solution*. Materials and Corrosion, 1997. **48**(5): p. 303-310.
370. Balbuena, P. and V. Subramanian, *Theory and experiment in electrocatalysis*, ed. R.E. White and c.g. vayenas 2010.
371. Franceschetti, D.R. and J.R. Macdonald, *Electrode kinetics, equivalent circuits, and system characterization: Small-signal conditions*. Journal of Electroanalytical Chemistry and Interfacial Electrochemistry, 1977. **82**(1-2): p. 271-301.
372. Pasta, M., F. La Mantia, L. Hu, H.D. Deshazer, and Y. Cui, *Aqueous Supercapacitors on Conductive Cotton*. Nano Research, 2010. **3** p. 452-458.
373. Isvoranu, C., *Metal-Organic Complexes at Surfaces*, in *Division of Synchrotron Radiation Research* 2010, Lund University: Lund, Sweden.
374. García, P., J.F. Espinal, C. Salinas Martínez de Lecea, and F. Mondragón, *Experimental characterization and molecular simulation of nitrogen complexes formed upon NO-char reaction at 270 °C in the presence of H₂O and O₂*. Carbon, 2004. **42**(8-9): p. 1507-1515.
375. Shao, X.M. and J.L. Feldman, *Micro-agar salt bridge in patch-clamp electrode holder stabilizes electrode potentials*. Journal of Neuroscience Methods, 2007. **159**(1): p. 108-115.
376. Vermes, I. and E.W. Grabner, *A phosphate sensor based on silver phosphate-modified electrodes*. Journal of Electroanalytical Chemistry and Interfacial Electrochemistry, 1990. **284**(2): p. 315-321.
377. Gryboś, R. and A. Samotus, *Potential-ph diagrams for the silver-water-ammonia-sulphuric acid system at elevated temperatures*. Journal of the Less Common Metals, 1984. **98**(1): p. 131-140.
378. Burkitt, R. and E. Yu. *Low Cost Oxygen Reduction Catalysts for Microbial Fuel Cells*. in *61st Annual Meeting of International Society of Electrochemistry*. 2010. Nice, France.